

RADC-TR-87-10, Vol I (of tw/o) In-House Report February 1987



AD-A181 536

PROCEEDINGS OF THE 1986 ANTENNA APPLICATIONS SYMPOSIUM

Daniel T. McGrath, Capt, USAF



Sponsored by
ELECTROMAGNETIC SCIENCES DIVISION
ROME AIR DEVELOPMENT CENTER
HANSCOM AFB, BEDFORD MASS. 01731
AIR FORCE SYSTEMS COMMAND

APPROVED FOR PUBLIC RELEASE; DISTRIBUTION UNLIMITED

ROME AIR DEVELOPMENT CENTER
Air Force Systems Command
Griffiss Air Force Base, NY 13441-5700

This report has been reviewed by the RADC Public Affairs Office (PA) and is releasable to the National Technical Information Service (NTIS). At NTIS it will be releasable to the general public, including foreign nations.

RADC-TR-87-10, Vol I has been reviewed and is approved for publication.

APPROVED:

JOHN K. SCHINDLER

Chief, Antennas & Components Division

Directorate of Electromagnetics

hu K Selindle

APPROVED:

PAUL J. FAIRBANKS, Lt Col, USAF

Call Fabour

Acting Chief

Directorate of Electromagnetics

FOR THE COMMANDER:

JOHN A. RITZ

Directorate of Plans & Programs

If your address has changed or if you wish to be removed from the RADC mailing list, or if the addressee is no longer employed by your organization, please notify RADC (EEAA) Hanscom AFB MA 01731-5000. This will assist us in maintaining a current mailing list.

Do not return copies of this report unless contractual obligations or notices on a specific document requires that it be returned.

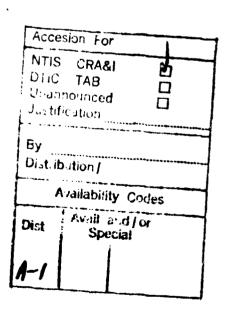


COMPONENT PART NOTICE

THIS PAPER	R IS A COMPONENT PART OF TH	HE FOLLOWING COMPILATION REPORT:			
TITLE:	Proceedings of the Anter	nna Applications Symposium Held in Urbana.			
	Illinois on 17-19 Septem	mber 1986. Volume 1.			
To order 1	THE COMPLETE COMPILATION RE	EPORT, USE _AD_A181_536			
	THE COMPONENT PART IS PROVIDED HERE TO ALLOW USERS ACCESS TO INDIVIDUALLY				
	AUTHORED SECTIONS OF PROCEEDING, ANNALS, SYMPOSIA, ETC. HOWEVER, THE COMPONENT SHOULD BE CONSIDERED WITHIN THE CONTEXT OF THE OVERALL COMPILATION REPORT AND				
NOT AS A S	STAND-ALONE TECHNICAL REPOR	кт.			
THE FOLLOW	WING COMPONENT PART NUMBERS	S COMPRISE THE COMPILATION REPORT:			
AD#: POO	5 39h thru P005 409	AD#:			
AD#:		AD#:			

AD#:





Approved for public released to Distribution Unlimited

DTIC FORM 463

AD#:

OPI: DTIC-TID

	-	
 PERCATION	OF THIS	PAGE

REPORT DOCUMENTATION PAGE					
14 REPORT SECURITY CLASSIFICATION Unclassified		16. RESTRICTIVE M	ARKINGS		
26 SECURITY CLASSIFICATION AUTHORITY		S. DISTRIBUTION/AVAILABILITY OF REPORT			
		Approved for			
25. DECLASSIFICATION/DOWNGRADING SCHED	DULE	Distribution Unlimited.			
4. PERFORMING ORGANIZATION REPORT NUM	8ER(8)	5. MONITORING OR	GANIZATION RE	PORT NUMBER(S)
RADC-TR-87-10, (Volume I)					
SA NAME OF PERFORMING ORGANIZATION	Sh Office Symbol (If applicable)	74 NAME OF MONI	TORING ORGANI	ZATION	
Rome Air Development Center	EEAA				
6c. ADDRESS (City, State and ZIP Code)		7b. ADDRESS (City,	State and ZIP Cod	(e)	
Hanscom AFB					
Massachusetts 01731-5000					
SA NAME OF FUNDING/SPONSORITIG	Sb. OFFICE SYMBOL (If explicable)	9. PROCUREMENT	NSTRUMENT ID	ENTIFICATION NU	IMBER
Rome Air Development Center	EEAA	1			
Sc. ADD RESS (City, State and ZIP Code)		10. SOURCE OF FUR	NDING NOS.		
Hanscom AFB		PROGRAM ELEMENT NO.	PROJECT NO.	TASK NO.	WORK UNIT
Massachusetts, 01731-5000		Ecement No.	140.	1.0.	
11. TITLE (Include Security Classification) Proce		62702F	4600	14	01
1986 Antenna Applications Symp	osium	<u> </u>	<u> </u>		
12, PERSONAL AUTHOR(S)					
134 TYPE OF REPORT 135 TIME C		14. DATE OF REPO			OUNT
In-House FROM	to	1987 Februar	Cy	376	
16. SUPPLEMENTARY NOTATION Volume I Pages 367 through 698	consists of pa	ges 1 through	366; Volum	e II consis	ts of
Daniel T. McGrath, Contract Mo	nitor (RADC/EEA	A)			
	18. SUBJECT TERMS (C				
FIELD GROUP SUB. GR.	Antennas; Satellite Ante	Microsi Reflect	rip,	/ Multibea	m Antennas ntennas, /
	Broadband Anter	nnas HF. VHI	F. UHF	/ ALLAY AL	Leillas
YE. ABSTRACT (Continue on reverse if necessary and	d identify by block number	r)	-		
The Proceedings of the 1986 An	tenna Application	ons Symposium	is a colle	ction of sta	te-of-the-
art papers relating to phased microstrip antennas, reflector	array antennas, antennas. HF. '	multibeam and v VHF. INF and v	tennas, sat	ellite anter	inas,
,		· · · · · · · · · · · · · · · · · · ·	var zous oth	ct ancennas	
				<i>ب</i> ر	
,		1			
	in the suit	(\cdot)			Î
Legue de include.					
'					
					j
20. DISTRIBUTION/AVAILABILITY OF ABSTRA	CT	21. ABSTRACT SEC	URITY CLASSIFI	CATION	
UNCLASSIFIED/UNL:MITED SAME AS RPT.	TIC USERS	Unclassifi			
224 NAME OF RESPONSIBLE INDIVIDUAL		226. TELEPHONE N		22c. OFFICE SYM	BOL
DANIEL T. MCGRATH, Captain, US.	AF	(Include Area Co	-	RADC/EEAA	
DD FORM 1473, 83 APR	EDITION OF 1 JAN 73			lassified	

PREFACE

The Antenna Applications Symposium, held at the University of Illinois' Robert Allerton Park, was cosponsored by Rome Air Development Center's Electromagnetics Directorate (RADC/EEAA), Hanscom AFB, MA and the University of Illinois' Electromagnetics Laboratory under Contract F19628-86-M-0004. Professor Paul Mayes if UI was the symposium chairman. Captain Daniel McGrath of RADC/EEA was the symposium manager for the Air Force.



Accesio	on For	
DTIC	ounced	n n
By Di.t ibutio: /		
Availability Codes		
Dist	Avail a Spec	
A-1		

Contents

Volume 1

Key	note: "A Centennial of Electromagnetics," H. Schrank	1
	Wednesday, September 17, 1986	
	Session 1	
	EHF Antennas	
	Chairman: R. J. Mailloux, Rome Air Development Center	
1.	"V-band Space-Based Rader Antennas," J. A. Kinzel	23
2.	"An Antenna System for an EHF Satellite Earth Terminal and its Calibration," L. W. Rispin	37
3.	"EHF/SHF Satcom Antenna and Radome Test Results," A. L. Johnson and W. O. Fischbach	63
4.	"Simplified MMIC Active Aperture Feeding," J. L. Poirier	93
5.	"APS-Workshop on Characterization of MMIC Devices for Array Antenna," J. Smetana and R. Mittra	119
	Session II	
	Conformal Antennas	
	Chairman: W. C. Chew, University of Illinois	

	C	ontents
6.	"Aperture Coupled Patch Antennas and Arrays," D. K. Schaubert and D. M. Pozar	135
7.	"Phased Array Antenna Pattern Optimization with Failed Elements," B. F. Collins II, Z. H. Lewantowicz, and A. J. Terzuoli	155
8.	"Wideband, Double-Tuned Microstrip Elements," D. Tanner and P. Mayes	173
9.	"Practical Examples of Integral Broadband Matching of Microstrip Antenna Elements, D. A. Paschen	199
10.	"Printed Dipole Radiating Elements for Monolithic Millimeter Wave Phased Arrays," D. B. Rees and B. J. Edward	219
11.	"A Design Concept for an MMIC Microstrip Phased Array," R. Q. Lee, J. Smetana, and R. Acosta	239
12.	"Mutual Admittance Between Slots in Cylinders of Arbitrary Cross Section Shape," A. F. Peterson and R. Mittra	253
	Thursday, September 18, 1986	
	Session III	
	Arrays and Reflectors	
	Chairman: J. L. Poirier, Rome Air Development Center	
13.	"A Technique for Low Sidelobes in Monopulse Planar Array Antennas," A. Derneryd	275
14.	"Phased Array Antenna for Space Shuttle Orbiter," S. E. Davidson	291
15.	"A Hemispherically Scanning X/Ka Band Mirror Antenna," K. Hollenbeck	30.7
16.	"A Lightweight Constrained Lens for Wide Angle Scan in Two Planes," D. T. McGrath	343*
		Volume II
17.	"A High Power Phased Array for Sub-Scale Aerial Target Applications," J. DeVries, K. Doi and F. Lauriente	367
18.	"Design Considerations for the Beamwaveguide Retrofit of a Ground Antenna Stauton," T. Veruttipong, J. Withington,	387

V. Galindo-Israel, W. Imbriale and D. Bathker

Session IV

Broadband Antennas

Chairman: J. D. Dyson, University of Illinois

19.	"A Wideband Ridge Array Feed," C. J. Favoloro and G. Ledonne*	
20.	"An Inexpensive, Relatively Broadband Multi-Purpose Antenna," S. C. Kuo and W. M. Shelton	411
21.	"A Log-Periodic Array of Monopole-Slot Elements," D. J. Tammen and P. E. Mayes	425
22.	"A Shallow-Cavity Unity Gain Notch Radiator," G. J. Monser	457
23.	"Ultra-Broadband Impedance Matching Using Electrically Small Self-Complimentary Structures," K. G. Schroeder	469
24.	"Impedance Inverting Feed Designs for Broadband Endfire Complementary Pairs Using Thin Wire Elements," K. G. Schroeder	491
25.	"Pattern Prediction of Broadband Monopole Antennas on Finite Groundplanes Using the BOR Moment Method," D. E. Baker and L. Botha	521
	Friday, September 19, 1986	
	Session V	
	Analysis, Design and Measurement	
	Chairman: F. Rupp, Hughes Aircraft Company	
26.	"Polarization Measurement," D. L. Hawthorne	547
27.	"Review of Spherical Near-Field Measurements," D. W. Hess	581
28.	"Swept Frequency Technique for Dispersion Measurement of Microstrip Lines," R. Q. Lee	597
29.	"Evaluation of Localized Inhomogeneities in the Reflectivity of Planar Absorber Panels," D. E. Baker and C. A. Van Der Neut	615
30.	"Results of Optimization of Yagi-Uda Arrays of Shaped Dipoles," S. D. Hibbard, S. R. Laxpati and P. D. Wolfe	63

Contents

31.	"Results of Numerical and Physical Modelling Adcock Arrays for VHF DF Applications," D. C. Botha, D. KcNamara and G. W. Reed	OT WITHOUGH	623
32.	"Matrix Formulation of Vector Operations in E Analysis," F. C. Chang	lectromagnetics	687

A CENTENNIAL OF ELECTROMAGNETICS

Helmut E. Schrank, Westinghouse Electric Corporation Baltimore, Maryland

INTRODUCTION

Here we are at another "Antenna Applications Symposium", the tenth in this recent series of annual antenna meetings at Allerton Park - preceded by about 23 similar meetings that were called "Annual Symposium USAF R&D Program." That adds up to 33 such gatherings, which began around 1950 - over a third of a century ago!

Just think how many antenna engineers have been here over the years to present and to near papers on the latest technology, and to enjoy the pleasant surroundings of Allerton Park plus the fine hospitality of the <u>University of Illinois!</u> I think we should express our warmest thanks to all those who have made these worthwhile antenna meetings possible, especially to the fine staff members of the University of Illinois Electrical and Computer Engineering Department.

A third of a century! When you say it that way, it sounds like a long time. To some of you here, it represents your entire life so far, and yet some of us senior citizens have been in the antenna business even longer than that. But what is really remarkable to me is the fact that our field of interest - antennas, or to put it more generically, the business of electromagnetic radiation and reception - is just about one century old!

Next year in Europe and elsewhere there will be many celebrations marking the 100-year anniversary of the first experimental demonstrations proving the validity of Maxwell's (now famous) equations. In 1887, a 30 year old German physicist, Heinrich Rudolf Hertz, with his astonishing insight, opened up the age of electromagnetics (sometimes called the "age of radio") and brought about a turning point in world history. As we examine some of his most noteworthy accomplishments later in this talk, we will see that Hertz was truly the first microwave antenna engineer, and all the amazing advancements in antenna technology that have taken place since 1887 have been built on the firm foundation provided by Hertz, the implementer of Maxwell's theory.

A PLETHORA OF CENTENNIALS

Before reviewing the Hertz contributions to our field of electromagnetics, let me digress for a few moments to note that we have been celebrating a number of centennials (and one half-centennial) in recent years, some related to our field of interest, and some completely unrelated. The point is that for some strange reason, the period around 1880 ± a decade was an unusually fruitful and productive time in the history of our Western civilization.

In 1979, we celebrated the "Centennial of Light" to commemorate the 100th anniversary of Thomas Alva Edison's invention of the incandescent light bulb. Edison's pioneering work in electric lights as well as the generation and distribution of electricity altered the lifestyle of the entire civilized world. Even the appearance of our planet from outer space was altered.

In 1383, the "Centennial of the Transformer" was noted, particularly at Westinghouse, commemorating the invention by Ganlord and Gibbs of this critical component in the eventual success of the Westinghouse-promoted AC (alternating current) electrical system over Edison's competing DC (direct current) system.

In 1984, we celebrated the <u>"IEEE Centennial"</u>, which some thought a little strange since the IEEE was formed in 1362 by merging the AIEE with the IRE. However, the AIEE was founded in 1884, and that is what was really commemorated by this centennial.

In 1985, a half-centennial was commemorated, namely the 50th Anniversary of Radar. This event was best documented by Merrill Skolnik's fine historical review in the IFFE Proceedings of February 1985. Many of us can relate to this subject, because a significant number of notable antenna advancements were made for radar applications. I personally began my antenna career as a Mechanical Engineer at Bell Labs (Whippany) in the early 1940's, designing parts for vintage airborne radar systems including the AN/APS 1 and the AN/APS-4. In those days, the acronym "RADAR" was still classified, and couldn't be used in ordinary conversation.

This year, 1986, marks the 100th Anniversary of the founding of the <u>Westinghouse Electric Corporation</u> by <u>George</u>

<u>Westinghouse</u>, whom we have already mentioned as being the genius and driving force behind the AC electricity system now

being used almost universally. Westinghouse (the corporation) can also be noted for a number of historic firsts, including:

- * The first commercial radio station (KDKA, Pittsburgh)
- * The first production radar with planar array antenna (SCR-270)
- * The first pulse doppler radar
- * The first TV camera on the moon
- The first production radar with ultralow sidelobe antenna (AWACS)

Other Centennials being celebrated in 1986 include the following:

- * The Statue of Liberty
- * Coca Cola
- * Sears Roebuck
- * Moody Bible Institute

While these have little or no relationship to electromagnetics, they show how productive a year 1886 was.

1987 will mark the <u>Hertz Centennial</u> on which we will now focus our attention.

HERTZ BEGINS THE AGE OF ELECTROMAGNETICS

One hundred years ago Heinrich Hertz (Figure 1) began his experiments that proved the validity of Maxwell's equations, and opened up a new world of technology that has directly affected the lives of each one of us.

Hertz had received his doctorate "magna cum laude" from the Berlin Physical Institute in 1880, at the age of 23. His physics professor, Hermann von Helmholtz, was the first on the European continent to study Maxwell's works and to appreciate their significance. Helmholtz tried to influence Hertz to investigate the validity of Maxwell's theory in 1879, the year before Hertz graduated from the Berlin Academy, but Hertz declined. One of the reasons he declined was the lack of a detector for high frequency oscillations, which Hertz knew would be necessary for investigating phenomena involving fractions of a millionth of a second. Galvanometers and other physical instruments available at that time were useless for high frequency observations or measurements.

In 1885, Hertz accepted a position as professor of physics at the <u>Technische Hochschule at Karlsruhe</u>, where he had a well-equipped laboratory and discovered a simple but effective

means for detecting high frequency oscillations — a large wire loop with an adjustable air—gap for observing sparks. The air—gap could be adjusted with a micrometer to measure the intensity or length of sparks, corresponding to the strength of the electrical phenomena. Figure 2 shows the circular loop detector with a small telescope to observe the spark gap. A rectangular loop was sometimes used instead of a circular loop, and worked equally well. Hertz now felt he could proceed with the investigation of Maxwell's theories.

It must be remembered that when Hertz began his experiments, twenty years had passed since the publication of Maxwell's equations (see Figure 3). Few people understood Maxwell's mathematics and fewer still appreciated its significance. Maxwell had essentially expressed the electric and magnetic fields in the space (or dielectric) around the conductors, and included the concept of a <u>displacement</u> <u>current</u>, which ran contrary to most contemporary electrical theories.

Maxwell also predicted that electromagnetic waves propagated in space at the same speed as light travelled, and postulated that light itself was an electromagnetic wave

phenomena. For twenty years, these radical concepts lay dormant and were largely ignored or disputed by the scientific community.

Hertz recognized that if the electromagnetic waves predicted by Maxwell travelled at the speed of light, and he were to investigate these waves within the confines of a laboratory, he had to generate frequencies at least 100 times higher than the highest anyone had achieved up to that time, which was about 1 million cycles per second. Even at that frequency, one wavelength is 300 meters, much longer than the length of any laboratory he could get.

To generate the necessary high frequency oscillations, Hertz used circuits like the one shown schematically in Figure 4, consisting of an induction coil (A) hooked to a wire dipole radiator (B-B) having capacitive end plates (C-C) and a spark discharge gap (G) in the center.

This was the first use of a <u>balanced dipole antenna</u>, a

Hertz innovation, and the length of the dipole was tuned to

resonate at the desired frequency. The detector circuit, shown
as a rectangular loop with a micrometer spark gap (M) at the

bottom of Figure 4, was also tuned to resonance. Figure 5

shows some of the resonance curves plotted by Hertz, in terms of spark length (ordinate) versus total length of the detector loop (abscissa) for a loop detector (top) and a spiral detector (bottom).

Hertz not only had a clear insight into the theoretical implications of Maxwell's equations, but also demonstrated brilliant experimental inventiveness. He formed a directive beam of electromagnetic waves by placing his vertically-oriented dipole radiator at the focal line of a parabolic cylinder reflector, shown diagrammatically in Figure 6. A similar reflector was used with the spark-gap detector circuit, and a photograph of the two reflector antennas is shown in Figure 7 (B and C). Also shown is an octagonal parallel-wire (3 cm spacing) polarization screen (E) and a prism made of pitch (F).

With this and other apparatus, Hertz, operating with wavelengths as short as 25 cm, demonstrated that electromagnetic waves were <u>polarized</u>, and could be <u>reflected</u> and <u>refracted</u> just like light waves.

Hertz summarized his experiments in a paper <u>"On Electric</u>

<u>Radiation"</u> which appeared in December 1888: "We have applied the term rays of electric force to the phenomena which we have

investigated. We may perhaps further designate them as rays of light of very great wavelength. The experiments described appear to me, at any rate, eminently adapted to remove any doubt as to the identity of light, radiant heat and electromagnetic wave motion. I believe that from now on we shall have greater confidence in making use of the advantages which this identify enables us to derive both in the study of optics and electricity."

The experiments that Hertz concluded were among the most notable in the history of electrical science, and were a distinct victory for the field-force theory of Faraday and Maxwell. Hertz showed his skills for analysis as well as for experiments in a paper on "The Forces of Electric Oscillations Treated According to Maxwell's Theory" (1889), in which he constructed the four diagrams of the field lines around a spark-gap oscillator, shown in Figure 8. These four successive diagrams show the radiation of electromagnetic energy through space at four instants of time spaced at quarter-cycle intervals: T=0, 1/4T, 1/2T, and 3/4T. The formation of the radiated fields is clearly depicted.

Convinced of the correctness of Maxwell's theory, Hertz set about to interpret and simplify Maxwell's "Treatise". He and

the British electrical engineer, <u>Oliver Heaviside</u>, were the first to change Maxwell's equations into the form that is now found in most textbooks. Hertz published his papers on electricity in a book <u>"Electric Waves"</u>* which is a model of clarity and thoroughness.

Unfortunately, Hertz developed serious health problems and died on New Years day in 1894 at the age of (almost) 37. In his short life span, he opened up a new <u>electromagnetic</u> <u>spectrum</u> that profoundly changed the world in which we live.

Let us now briefly review the results of his work in terms of our field of interest, <u>antenna engineering</u>, during its first 100 years.

THE FIRST CENTURY OF ANTENNA ENGINEERING

John Kraus, in his plenary session paper at the 1985 IEEE AP-S/URSI Symposium, said, "If a William Proxmire had been around in Hertz's time, Hertz's radio apparatus might have

^{*} Translated into English by D.E. Jones and published in 1893 by Macmillan & Co., London. Reprinted in 1962 by Dover Publications, New York.

received a Golden Fleece Award as a complete waste of money and effort - a toy of absolutely no practical value. Yet from this simple fundamental beginning has come all of wireless, all of radio, all of TV, and all of space communications." And we can add, all of <u>radar</u> and all of <u>radio astronomy</u> have also come from Hertz. And all these applications require the use of <u>antennas</u> to transmit and/or receive signals.

Hertz apparently never considered applying his results to a radio communication system, but the papers he wrote were more readily understood than Maxwell's and therefore stimulated others to do so. One of these was Marconi, who at the age of 20 happened to read a magazine article describing Hertz's experiments, while on a summer vacation in the Alps. Young Marconi became obsessed with the idea of using radio waves to send messages without wires. He cut short his vacation, rushed home to try the idea, and the rest is history.

Early antennas were made of wires, appropriate for the lower frequencies used in those days. In the 1930's, with the development of radar and microwave technology, antennas soon took the form of reflectors, lenses, and other derivatives of optical devices. Array antennas soon followed, and antenna technology as we now know it developed rapidly.

Some of the more spectacular reflector antenna designs are represented by the huge <u>radio astronomy</u> telescopes, including Kraus' Big Ear, the Goldstone Deep Space Cassegrain antennas, the 100 meter Effelsberg dish, and of course the 1000 ft. Arecibo reflector.

More recently, low sidelobe offset Gregorian reflectors have been design d for <u>satellite communication</u> farth stations, and many large unfurlable <u>satellite antennas</u> have been built for the orbiting part of such systems, including the ATS-t and the TORSS antennas for examples.

Array antennas are also too numerous to mention except for some notable examples, including the AN/FPS-85 USAF Spacetrack antennas, the huge arrays for the Pave Paws and Cobra Dane radar systems and perhaps the most impressive array of all, the VLA (Very Large Array) of 27 eighty-four ft. dishes for radio astronomy in Socorro, New Mexico. Not nearly as impressive, but of importance for future airborne systems are the conformal (non-planar) arrays being developed, including cylindrical, conical, and spherical examples.

<u>Lens antennas</u> have not been as popular in recent years, but notable exceptions are the multiple beam lens antennas used in DSCS-III (Defense Satellite Communication System). A complete discussion of the thousands of diverse antennas that have been invented, designed, and used in this first century since Hertz would take many days or even months to cover. Just look at this symposium - we are about to devote two and a half days to a review of some three dozen antenna papers, and by the time this year ends, there will have been at least four other symposia devoted to antennas and related electromagnetic topics in this country alone.

we are all part of a great scientific and technological community, building a body of knowledge on the foundations given to us by Faraday, Maxwell, Hertz, Marconi, and many other contributors, some of whom are still alive and active today.

THE CHALLENGES AHEAD

The challenges ahead for antenna engineers, scientists, and educators are as diverse and exciting as they were 100 years ago. Antennas for spacebased radar, global and interplanetary communications, the space station, strategic defense initiative, a lunar colony, a manned mission to Mars, all present opportunities for innovative design. We need smarter antennas, with the ability to adapt instantly to changes in

mission or environmental conditions. We need active arrays that generate coherent RF power in each element with high efficiency to minimize heat generation. A remotely controlled radio telescope on the moon could gather data from the farthest corners of our Universe and relay the pre-processed images to laboratories here on Farth.

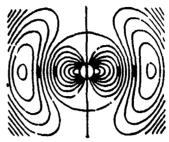
When the attendees of the Allerton symposia of the next century look back at our 1986 meeting, I'm sure they'll find a number of notable contributors to their successes among our generation. Who knows, we may have another Heinrich Hertz right here in this distinguished group!

RFFFRENCES

- John D. Kraus, "Antennas Since Hertz and Marconi"
 IEEE Transactions AP-33, No. 2, Feb. 1985, pp. 131-137.
- 2. S.F. Bordeau, "Volts to Hertz, the rise of electricity"

 Burgess Publishing Co., Minneapolis, MN.





HERTZ...

his discoveries opened the age of radio

Figure 1. Heinrich Rudolf Hertz (1857-1894)

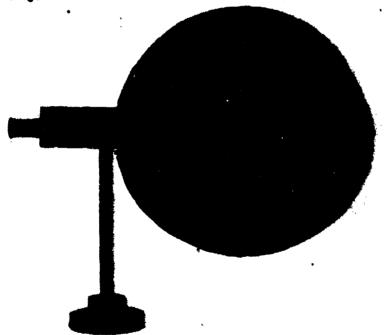


Figure 2. Circular Detector Loop with Telescope for Observing Sparks in Air-Gap

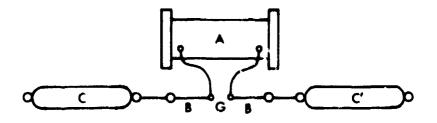
$$\nabla \times \mathbf{E} = \frac{1}{c} \frac{d\mathbf{B}}{dt}$$

$$\nabla \times \mathbf{B} = \frac{\mu}{c} \left(4\pi \mathbf{i} + \frac{d\mathbf{D}}{dt} \right)$$

$$\nabla \cdot \mathbf{D} = 4\pi \rho$$

$$\nabla \cdot \mathbf{B} = 0$$

Figure 3. Maxwell's Equations



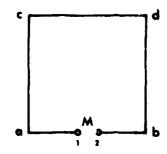


Figure 4. Hertz's Oscillator and Detector Circuits

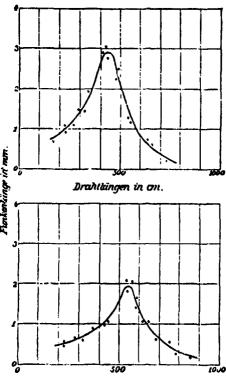


Figure 5. Measured Resonance Curves Plotted by Hertz

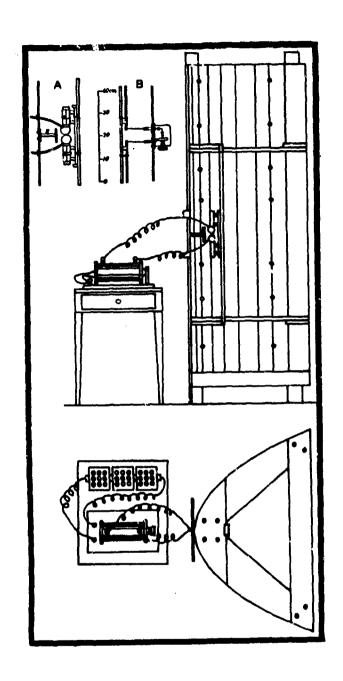


Figure 6. Hertz's Parabolic Cylinder Reflector Antenna with Dipole Feed

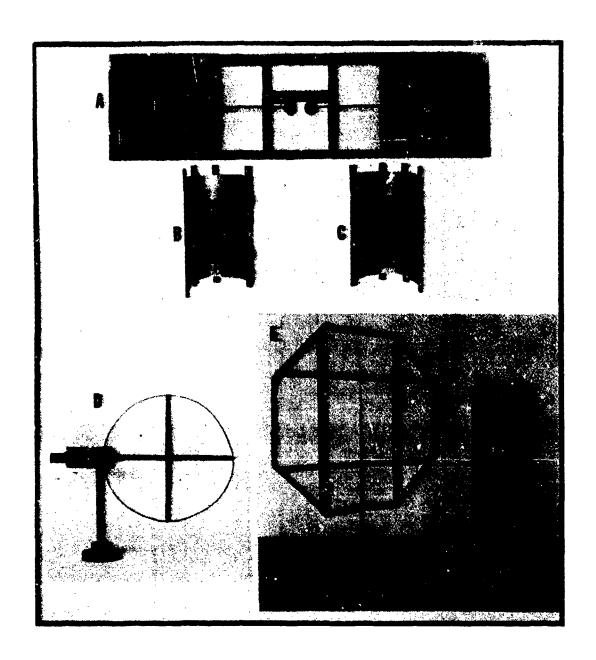


Figure 7. Apparatus used by Hertz (from Deutsches Museum, Munich)

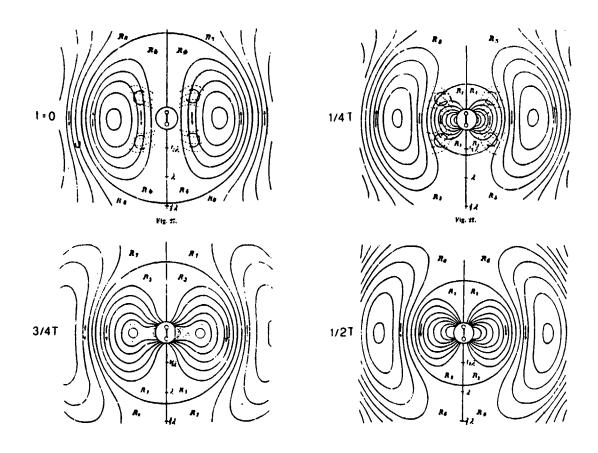


Figure 8. Hertz's Plots of Theoretical Radiation Fields at Four Instants



V-BAND SPACE-BASED RADAR ANTENNAS

Joseph A. Kinzel

Electronics Laboratory

General Electric Company

Syracuse, New York

1.0 ABSTRACT

State-of-the-art technology and the related design considerations for V-band solid-state phased array antennas are presented in this paper. One approach, with highly integrated tray modules comprised of 20-30 transmit/receive monolithic microwave integrated circuits (MMICs), also is discussed as well as the factors involved in configuring such complex modules into arrays.

2.0 INTRODUCTION

The Electronics Laboratory of General Electric has been agressively developing gallium arsenide (GaAs) monolithic technology for phased array antennas since 1980. The program initially concentrated on lower frequency transmit/receive (T/R) modules, such as the C-band modules shown in Figure 1. These 5 watt modules, completed in 1983 and 1984, utilize separate chips for power amplifiers, low noise amplifiers, phase shifters, and driver amplifiers. The module interfaces with a calibration circuit or radiating element at the input and the array beamformer at the output. The overall module has a width of 1.5 inches, which is adequate for C-band array spacing to realize wide-angle scan. Today monolithic microwave circuits for such microwave frequencies are ready for production, and transmit-receive modules are in advanced stages of development.

During the last two years GE has extended its GaAs phased array technology to millimeter-wave frequencies, with emphasis at 60 GHz. The development of a low cost, high performance, solid-state technology presents a real engineering challenge, especially when complex functions (amplifications, phase shifting, amplitude weighting, power conditioning, etc.) must be implemented consistent with grid spacings of 100 mils.

One approach being implemented by General Electric for V-

band phased arrays is applicable to both radar and communications arrays. The present discussion, however, will concentrate on radar applications, and more specifically monostatic radar.

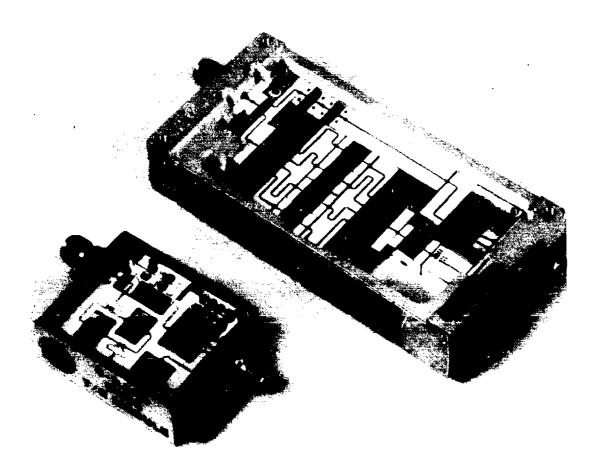


Figure 1. C-Band Modules

3.0 ARRAY APPROACH

The design of millimeter-wave arrays involves a tangle of complex technology issues, as illustrated in Figure 2. Such design

must <u>simultaneously</u> consider each of the requirements represented around the figure's periphery. We emphasize simultaneously since, contrary to lower frequency arrays where electrical, ther-

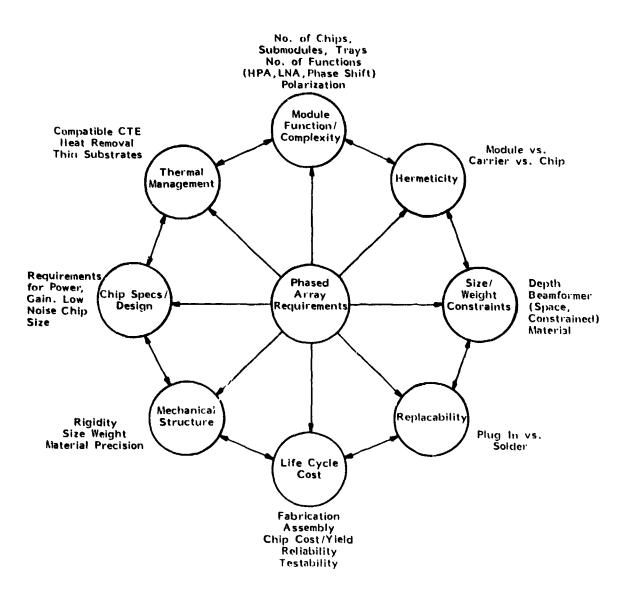


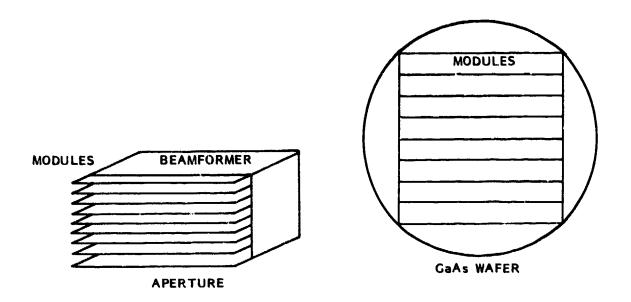
Figure 2. V-Band Array design Presents a Tangle of Complex Technology Requirements

mal, and mechanical requirements can be initially addressed independently and later integrated, such latitude does not exist for the extremely dense structure of a 60 GHz array. For example, the mechanical structure, thermal management, module replacability, and size constraints are highly interdependent. Similarly, module complexity, cost, hermeticity, thermal management, and MMIC design become intertwined.

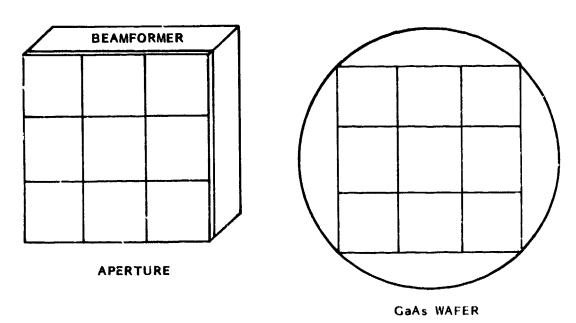
Generally speaking, monolithic array design can be classified into two configurations, which we refer to as "bricks" and "tiles." The two approaches are illustrated in Figure 3. The "tile" concept, similar to bathroom tiles, places the GaAs circuits parallel to the plane of the aperture. The radiating element, often a patch radiator, is in the same plane as the monolithic circuits, hence they share the available aperture space. Alternately the circuits can be stacked on top of or behind the radiators necessitating via or plated-thru hole connections.

The "brick" concept utilizes MMICs formed with wafer strips to realize a module that is orthogonal to the aperture plane. This approach takes advantage of array depth to accommodate the MMIC circuits and avoid compromising radiation efficiency. A comparison of bricks and tiles in relation to these array requirements is shown in Table 1. This table indicates the salient features for V-band implementation involving very densely packed modules.

After balancing the tradeoffs for V-band monostatic radar, the



BRICK CONSTRUCTION



TILE CONSTRUCTION

Figure 3. Brick Vs. Tile Concepts

TABLE 1. V-BAND ARRAY "BRICKS" VS "TILES"

Requirement	Brick	Tãe
Module Function/Complexity	Depth dimension accommodates more functions (T/R possible)	Better accommodates orthogonal polariza- tions
Hermeticity	Can be accomplished at module or tray level	Complicated by radiating element on same surface
Size/Weight	Minimum depth favors constrained feed	Less size and weight for comparable func- tions since smaller depth
Replacability	Space available for mechanical and thermal attachment	Very difficult
Cost	Single layer planar construction lends itself to automatic assembly	Repair more costly
Mechanical Structure	Available volume between rows Accommodate either constrained feed or space feed	Less antenna depth Multilayer construction
Chip Specs/Design	Comparable	Comparable
Thermal Management	More surface area for heat removal	Multilayer construction increases thermal resistance Possibly Accomodates thermal radiation

brick- type construction looks more promising primarily because the depth dimension is desirable to accommodate the required module functions while maintaining a planar structure for low-cost, automatic assembly.

One concept for a V-band brick module is shown in Figure 4.

A large number of T/R circuits can be incorporated in a single module-tray. At 60 GHz as many as 24 radiating elements with associated circuitry can be accommodated in a single tray with dimensions less than 1 in. by 3 in. The T/R circuits in a tray can be controlled by a single module controller, memory chip, and optical receiver/decoder chip. Power conditioning, if needed, also can be incorporated with a fourth circuit chip.

Most importantly, at the heart of the tray module, there is the issue of performance, in particular the radiating element and circuit technology which must achieve the required noise figure, output power, amplifier gains, and phase shift as well as radiating-element gain, efficiency, and patterns.

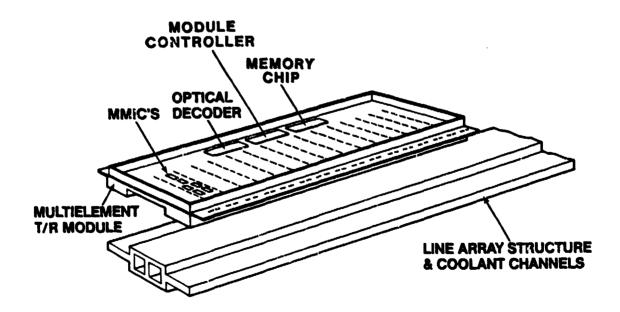


Figure 4. V-Band Brick Module Concept

4.0 CIRCUIT TECHNOLOGY

The submicron device technology has progressed much more rapidly than anyone envisioned two years ago. State-of-the-art advances now make it feasible to develop V-band phased arrays.

Device noise figures as low as 2.5 dB have been measured from General-Electric-fabricated HEMT devices as shown in Figure 5.

Significantly lower noise figure can be expected during the next one to two years. This development means that a 2.5 dB noise figure will be realized from a multistage V-band amplifier using low

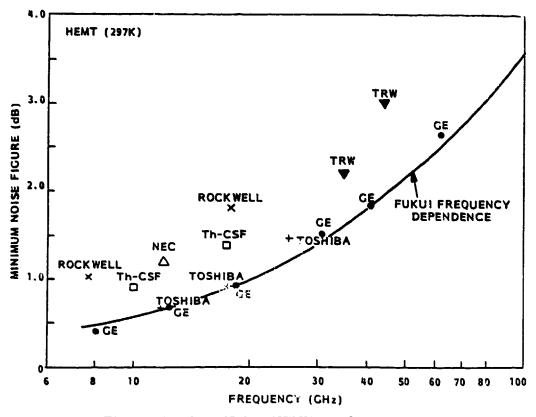


Figure 5. Low Noise HEMT Performance

loss matching circuits with further device improvements. The recently awarded AFWAL V-band technology contracts are expected to advance the technology dramatically.

Achieving millimeter-wave power performance with high efficiency is the most difficult technical challenge. However GE and others are aggressively addressing the state of the art for power. Table 2 presents recent power measurements on GE FET and HEMT devices. A power design of 0.41 w/mm has been achieved with 12% efficiency. Over the next year dramatic increases in power and efficiency performance can be expected from three terminal GaAs devices. New materials and devices, such as indium antimonide (InP) MISFET, alternately may be highly efficient power sources.

TABLE 2. 60 GHz POWER PERFORMANCE

Device	Output Power (mW)	Output Power (W/mm)	Power Gain (dB)	Power- Added Efficiency %
50μm HEMT	21	0.41	3	12
50 μm HEMT	12	0.24	3	9

Solid-state phase shifter developments for 60 GHz continue as well, involving FET, Schottky diode, and PIN diode technology.

Generally speaking, the pin diode is the lower loss option, although it requires a modest amount of DC power. To date, only

a limited amount of data is available on 60 GHz solid-state phase shifters.

In addition, radiating elements at 60 GHz currently are under development. One example of this work is presented at this conference.

5.0 SUBARRAY CONSTRUCTION

For large array applications it is most desirable to configure the aperture using identical subarrays, with each subarray comprised of identical tray modules.

For applications requiring large angular resolution and large bandwidth, the bandwidth is a major factor in determining subarray size, if adopting subarray time-delay compensation. In this situation

$$D < \frac{C}{\sin \theta \Delta f}$$

where D = array diameter; θ_S = maximum scan angle; Δf = signal bandwidth; and C = velocity of light.

For a 2 GHz bandwidth at geosynchronous orbit (\pm 10°), the maximum size is .86 meters. However the maximum size drops to .1732 meters for lower-orbit, wide scan-angle (\pm 60°) systems. The \pm 10° scan array requires element spacing of .0049 meters,

whereas the ±60° scan angle requires .0031 meter spacing, assuming triangular grid spacing. The subarray for ±60° scan then requires 2,842 radiating elements, corresponding to approximately 100 tray modules. A concept for a hexagonal array for a space-feed subarray is shown in Figure 6. Other factors that can affect the subarray size include:

- Beam pattern degradation resulting from any element occasions between subarrays.
- The tray module gain compared to available RF drive power.
- Current handling in the subarray.
- Controller architecture.

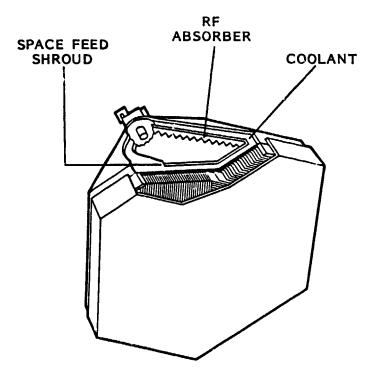


Figure 6. Discrimination Radar Space Feed Concept

- Heat removal from the subarray.
- Assembly/yield issues.

6.0 SUBARRAY VOLUME

As previously shown, tray modules (containing radiating elements, MMIC circuitry, controller chips, optical decoder/amplifier chip, and power management chip), the subarray support structure, and heat-removal spacing can be realized, with the brick construction, in a one-inch depth. Other systems also require volume that tend to increase subarray depth. These include: 1) the RF signal distribution for transmit power as well as receive beamformer for delta azimuth and delta elevation; 2) RF calibration circuits; 3) prime DC power (bias) distribution; 4) control signal distribution to each tray module for phase shift, variable gain, and T/R switching control; 5) heat removal at the subarray level; and 6) mechanical support to tie together all subarrays. The subarray concept thown in Figure 6 uses a space-feed transmissive lens for distribution of all RF signals.

For application where depth is a real premium, the space-feed approach may be replaced by constrained-feeds and fiberoptics technology. However, when looking ahead, it will not be practical or necessary to use one array or subarray for all applications, if and when the components, which are replicated with the number of

radiating elements (namely the active circuitry with its associated packaging), can be made common, and the cost of each phased-array system is dramatically reduced.

ACKNOWLEDGEMENT

The work described in this paper is the result of a team effort at General Electric Electronics Laboratory involving B. Edwards, D. Bates, B. Mitchell, P. Smith, P.C. Chao, to name a few.

395

AN ANTENNA SYSTEM FOR AN EHF SATELLITE EARTH TERMINAL AND ITS CALIBRATION*†

by Lawrence W. Rispin
Lincoln Laboratory, Massachusetts Institute of Technology
Lexington, Massachusetts

ABSTRACT

The antenna system for a 44/20 GHz earth terminal to be used to measure on-orbit satellite performance and the facilities used in its calibration are described. Built around a 8-ft. diameter Cassegrain antenna mounted on a pedestal positioner, the entire system is enclosed within a 17-ft. diameter radome. The antenna uses a frequency-selective-surface to diplex the 44-GHz uplink signal from a scalar horn and the 20-GHz downlink signal to a five-horn tracking feed. Mounted directly to the back of the antenna are a 20-GHz receiver front-end, a 5-W 44-GHz transmitter, and a transmit power attenuator used to precisely control terminal EIRP. Individual calibration of each of these units in conjunction with gain measurements on the radome-enclosed antenna allow a prediction of the overall antenna system performance, in terms of downlink G/T and uplink EIRP.

Gain and pattern measurements were made with the aid of two boresight towers. One tower at a relatively great distance permitted far-field measurements while the much nearer tower required the use of small correction factors. The nearer tower was also instrumented to support rapid, periodic G/T and EIRP measurements on the antenna system as a whole.

The different approaches to calibrating the performance of the EHF antenna system are compared, and the accuracy to which the antenna system can perform its primary function of evaluating the performance of an on-orbit satellite are discussed.

^{*}This work has been sponsored by the Department of the Air Force.

†The views expressed are those of the author and do not reflect
the official policy or position of the U.S. Government.

1. INTRODUCTION

The near-term reality of a 44/20 GHz satellite communication system called for the construction of a cost-effective earth terminal antenna system which would utilize advanced-but-reliable technology with the foremost purpose of evaluating and calibrating satellite on-orbit performance. Basic specifications for the antenna system read as follows:

Uplink EIRP

Variable from 20 to 60 dBW with < 1 dB variation 43.5 to 45.5 GHz

Downlink G/T

Minimum 19 dBi/°K with <±0.5 dB variation 20.2 to 21.2 GHz

In pursuit of these goals, the definition of the antenna system relied upon the anticipated availabilities of the following components for the indicated applications:

Uplink Transmitter

5 Watt, 43.5 to 45.5 GHz solid-state power amplifier

Downlink Receiver

Low noise amplifier > 30 dB gain with 2.8 dB NF, 20.2 to 21.2 GHz

From these starting points and the assumed performance budgets given in Table 1, design of the antenna system was initiated.

The antenna system would be mounted on a steel tower located on the roof (Fig. 1) above the control room where baseband processing would be performed. In addition to a radome and the necessary pedestal-positioner, the major elements would include: the antenna and feeds, transmitter and power attenuator, receiver front-end,

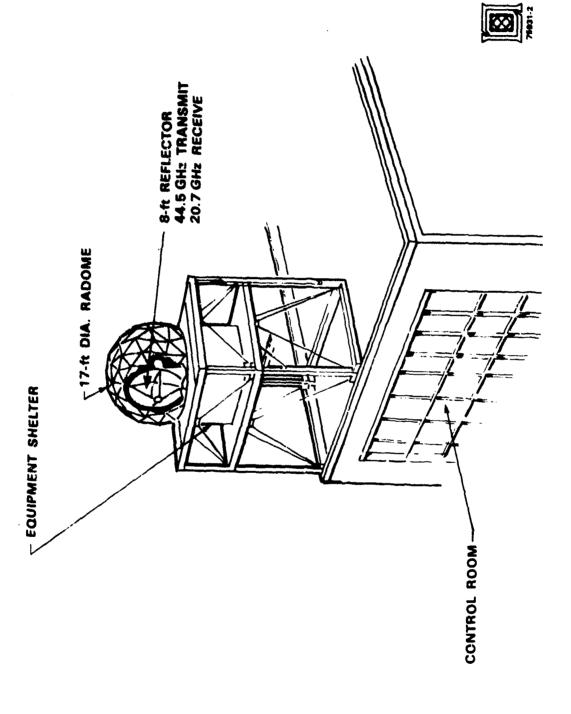


Figure 1. EHF Satellite Earth Terminal Antenna System Installation at Lincoln Laboratory.

digital control system and assorted ancillaries. These elements are indicated in a simplified schematic diagram in Fig. 2. A photograph of the completed antenna system showing these items (Fig. 3) will assist in the discussions to follow. Concise descriptions of the major elements of the antenna system and the measurement of its performance will be given.

2. ANTENNA AND RADOME

An 8 ft, diameter Cossegrain reflector (Fig. 4) satisfied the gain requirements and was judged to be the largest acceptable antenna which could be mounted on a relatively inexpensive pedestal-positioner. The main reflector is of metalized fiberglass construction with an F/D of 1/3. Common use of the reflector by both uplink and downlink signals is realized by a frequencyselective-surface (FSS) featuring Jerusalen cross type elements sandwiched between two dielectric layers (Fig. 5). The downlink signal passes through the FSS to a five-horn tracking feed and pseudo mono-pulse comparator. Two switchable ferrite circulators in the comparator simulate a PI switch (Fig. 2), while a third allows a choice Detween pairs of azimuth and elevation horns which are positioned about the main (center beam) horn. A computer in the control room effects the "dither" of the tracking feed and controls the pedestal-positioner so as to minimize the difference between the signal level received for each of the four beam dither positions. Conversely, the uplink signal from a scalar feed horn is reflected off the FSS to the subreflector and on to the main reflector. Downlink antenna patterns (dithered in azimuth) are shown along with the uplink azimuth pattern in Fig. 6. Elevation Protection from the elements for the patterns are similar. antenna, its feeds and the pedestal-positioner is afforded by a 17 ft. diameter metal-space-frame radome (Fig. 4). Table 2 gives a detailed account of the gains and losses in this section of the antenna system.



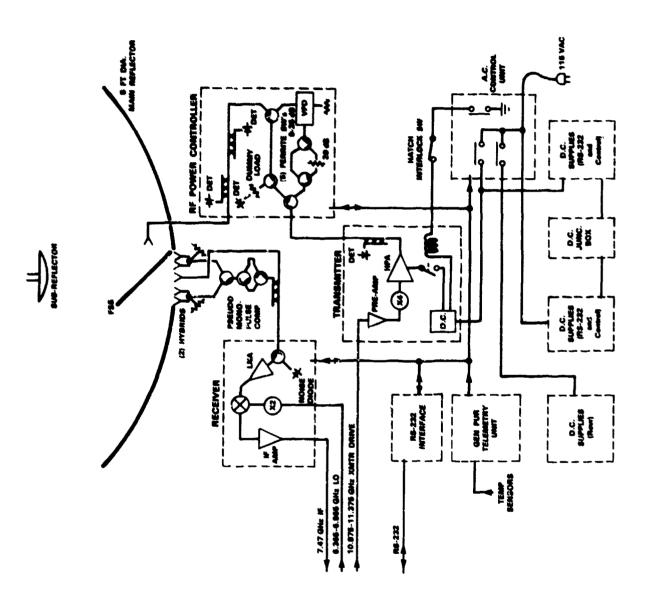


Figure 2. Simplified EHF Antenna System Schematic.

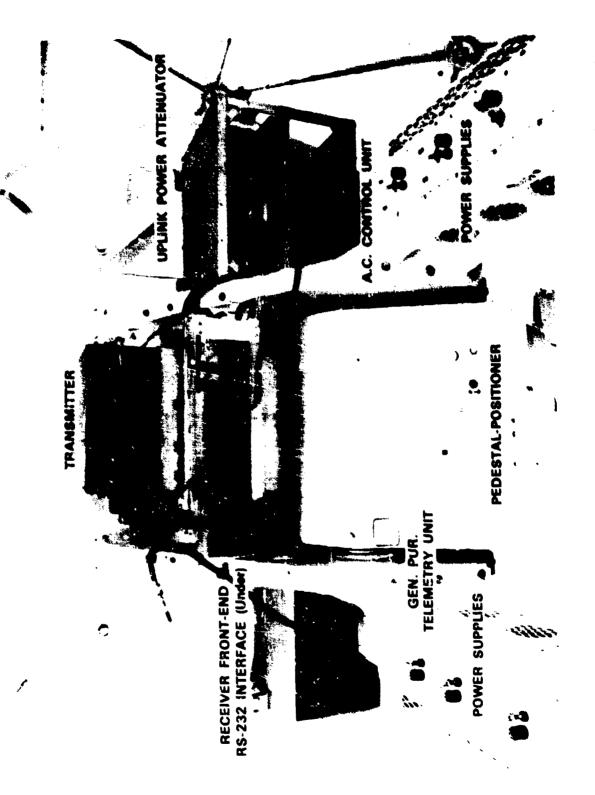
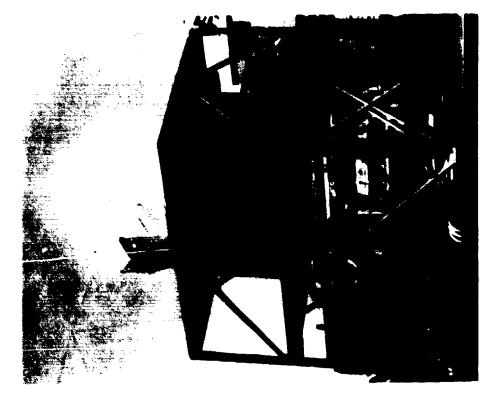
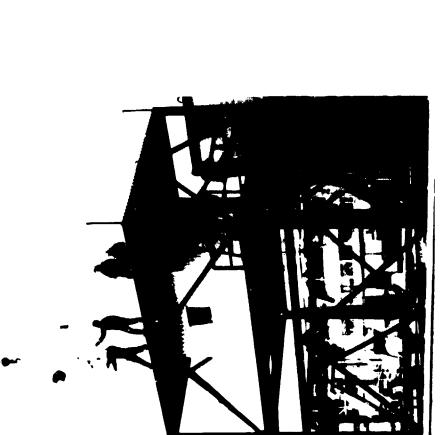


Figure 3. Photograph of the back of the 8 ft. Cassegrain antenna showing the mountings of the RF and control units that are integral parts of the antenna system.





The EHF Antenna Systems Figure 4. ..during installation of the 8-ft. Cassegrain antenna and....

ş

• after installation of the 17-ft. diameter metal-space-frame radome.

d.

1410

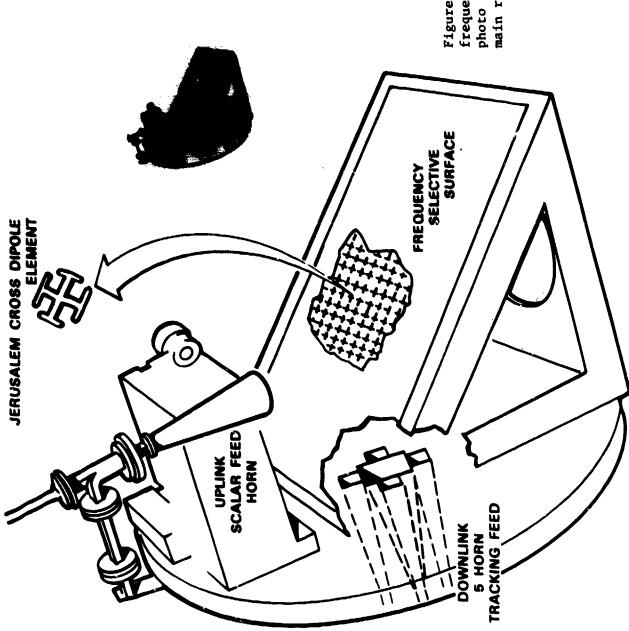


Figure 5. Detail of antenna feeds with frequency-selective-surface (FSS) and photo of some at the vertex of the 8-ft. main reflector.

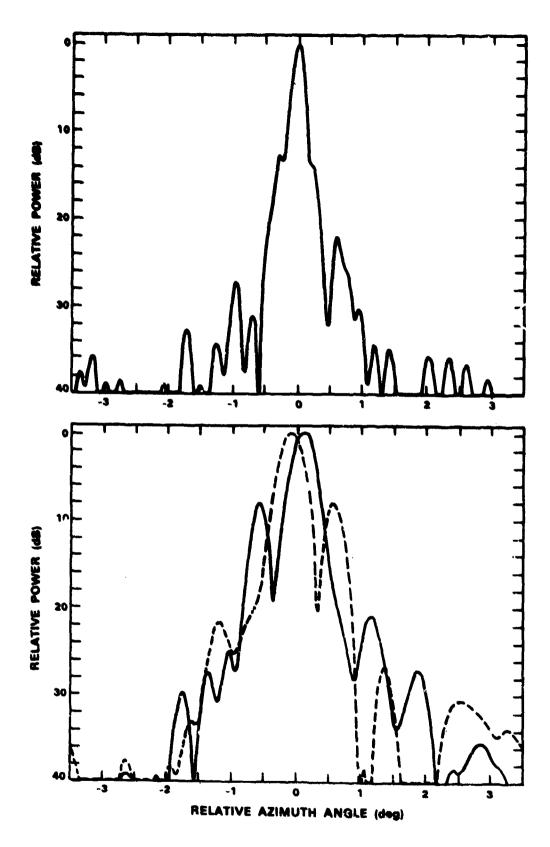




Figure 6. Uplink and Downlink (dithered left and right) azimuth antenna patterns at respective center frequencies, 44.5 and 20.7 GHz.

3. UPLINK TRANSMITTER AND ATTENUATOR

The 5 Watt 44 GHz transmitter resides in a central location behind the main reflector (Fig. 3). It consists basically of a low noise 11 GHz amplifier driving an integral 11 GHz power amplifier/frequency quadrupler/44 GHz impatt diode amplifier and necessary DC power supplies (Fig. 2). Output power from the impatt diode amplifier is a nominal 5 Watts (Fig. 7) across the uplink band. A 44 GHz bandpass filter, cross-guide coupler and waveguide following the amplifier reduce this output power by about 1.1 db.

Mounted on the back of the reflector, to the right of the transmitter (Fig. 3), is a variable attenuator which gives precise control over the uplink EIRP. This attenuator will be used in link tests and bit-error-rate tests on satellites in orbit. Utilizing five switchable ferrite circulators to give three paths for low, medium and high attenuation with a variable power divider (VPD) common to the medium and high paths, this unit offers between 2.0 to 45 dB of attenuation to the uplink signal in approximate 0.1 dB steps. Accuracy with regard to programmed attenuation is about ±1.0 dB for up to 40 dB in attenuation (Fig. 8). Diode detectors are presently used to monitor transmitted power levels.

An estimate of uplink EIRP is available from the product of the power at the uplink antenna port and the effective antenna gain at the same point as indicated in Table 3.

4. DOWNLINK RECEIVER

The receiver front-end (Fig. 2) is built around a low noise amplifier² and a 20 GHz double balanced mixer. Mounted behind the main reflector to the left of the transmitter (Fig. 3), the receiver interfaces immediately to the output of the pseudo mono-pulse comparator. Measured gain is a nominal 59.5 dB with a 3.0 dB noise figure (Fig. 9). A switchable ferrite circulator and "calibrated" noise source (Fig. 2) provide a means of

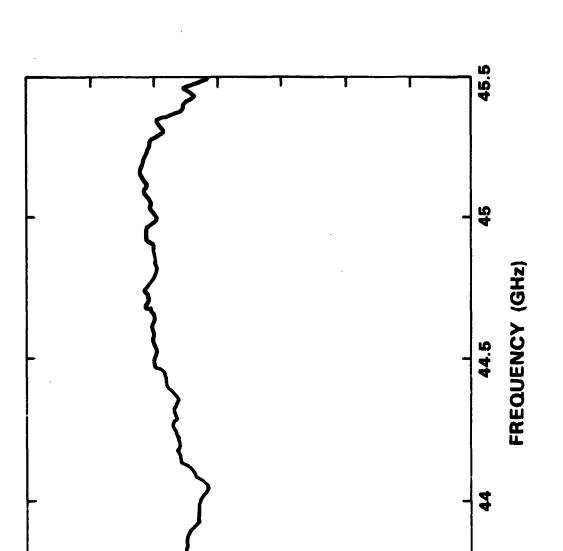


Figure 7. Output power from solid-state transmitter used in the EHF antenna system.

43.5

(W) A3WO9 TU9TUO

9

IJ

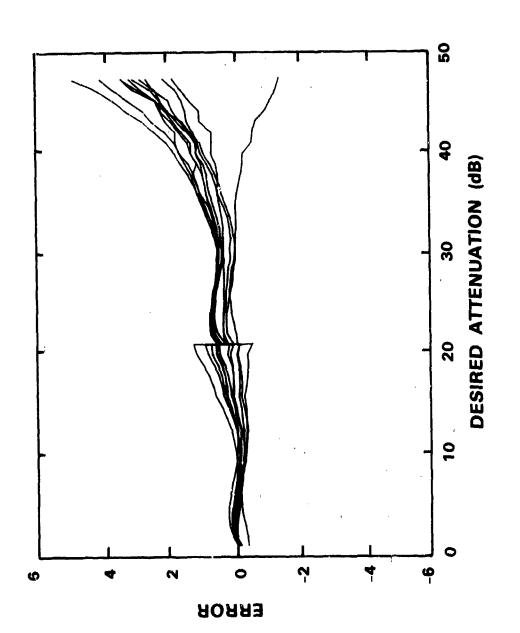


Figure 8. Error in prescribed attenuation introduced by uplink power controller at eleven frequencies (200 MHz steps) across the uplink band. Note the switch-over from medium to high attenuation paths.

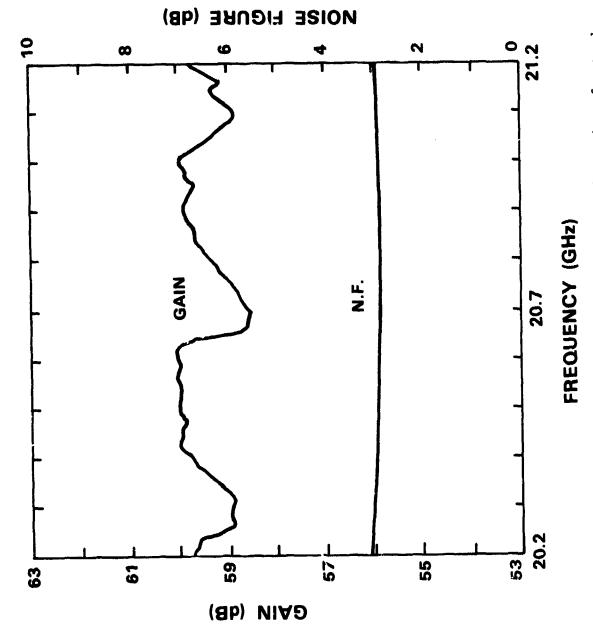


Figure 9. Measured gain and noise figure for downlink receiver frontend.

estimating G/T for the antenna system based upon a determination of antenna system noise temperature T and a separately measured value for downlink antenna gain (see Table 4).

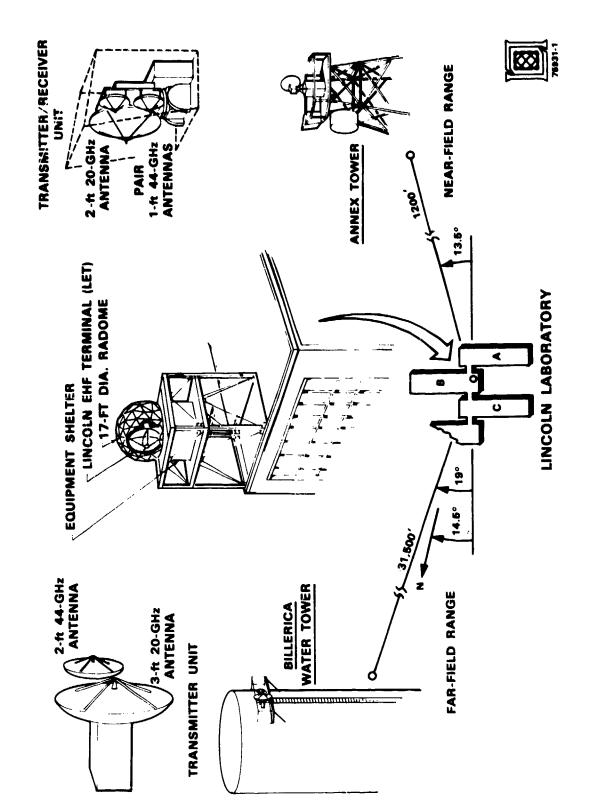
5. DIGITAL CONTROL SYSTEM

Communication between the antenna system and the control room is provided by two RS-232 links. One interfaces directly to the pedestal-positioner. The other interfaces with a specially-built RS-232 interface circuit card which provides two 4-bit data buses and 12 strobe lines for control/telemetry circuits in the receiver, uplink power attenuator, AC control unit, and a general purpose telemetry unit (Fig. 2). The AC control unit distributes AC power to the power supplies for the receiver, transmitter and uplink attenuator.

Primary RS-232 control functions include: turning the receiver and/or transmitter ON and OFF, "dithering" the tracking feed, control of the antenna switch and noise source configuration in the receiver, and setting the attenuation level in the uplink attenuator. Primary telemetry quantities include: receiver LO power; uplink power; various operating system quantities such as voltage, current, and temperature; and readback of all control function commands.

6. BORESIGHT TOWERS

Two boresight towers³ were instrumented (Fig. 10), a temporary one in the far-zone (6 miles) and a more permanent installation much nearer the antenna system. Measured gain of the 8 ft. antenna (via the usual substitution technique with a known standard) from both facilities is shown in Fig. 11. Subsequent measurements using the nearer tower necessitate the inclusion of small correction factors (for uplink only) available from this figure in order to simulate a far-field condition. Both towers are controlled with telephone links from the Laboratory.



Orientation of the EHF Antenna System and the Two Boresight Towers used in its Calibration. Figure 10.



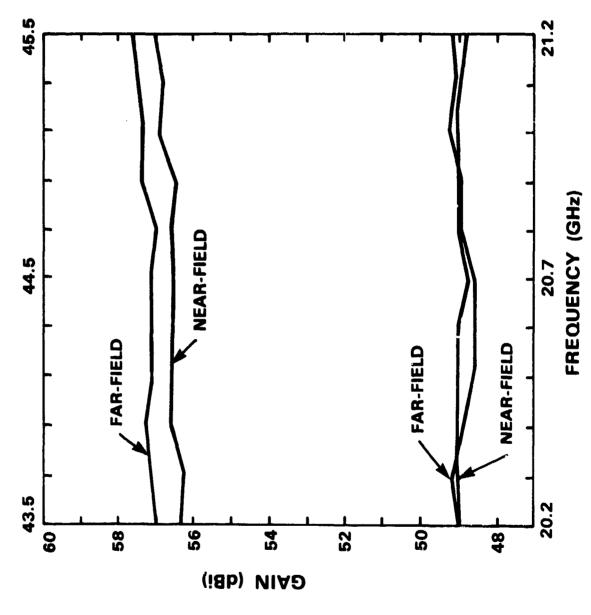


Figure 11. Effective Uplink and Downlink Gain of 8 ft. Cassegrain Antenna Measured using Both the Far and Near Boresight Towers.

The nearer tower (Fig. 12) is also capable of supporting rapid, periodic EIRP and G/T measurements. Uplink EIRP determinations are made in a "direct" manner based upon the power received by a calibrated antenna within the boresight tower. Table 3 illustrates this calculation and gives estimates for the anticipated error.

Precise control and accurate calibration of the amount of downlink power transmitted from the boresight tower allow "direct" G/T measurements to be obtained from signal-to-noise ratio estimates at the output of the downlink receiver. This calculation is detailed in Table 4 and error estimates given.

7. ANTENNA SYSTEM PERFORMANCE

The uplink performance of the EHF antenna system estimated indirectly and measured directly is displayed in Fig. 13. Upper and lower bounds were determined by the estimated accuracies of the quantities involved in the manner indicated in Table 3. Although slightly below the original desired level, the confidence lent by the relatively good agreement seen in Fig. 13 is quite acceptable. Error bars show combined (RSS) uncertainty and accuracy.

Downlink performance of the EHF antenna system estimated by both indirect and direct methods is shown in Fig. 14. Table 4 details the contributions to the determination of the error bounds. Comfortably above the original requirements for G/T, the agreement between the results of the two methods lends credibility to the results of both techniques. At higher elevations, above that of the boresight tower, G/T improves by about 0.5 dB.

8. FUTURE PLANS

Performance calibrations of the EHF antenna system using the boresight tower facility will continue on a periodic, as well as an on-demand, basis. Rain effects and radome surface contamination will also be examined. An opportunity to estimate receiver



Figure 12. Simplified schematic and photograph of the "near" boresight tower used for antenna pattern and gain and "direct" EIRP and G/T measurement.

performance using the sun as a "known" noise source is also on the agenda. The reason for this multiplicity of characterizations, of course, is to know the performance parameters of the antenna system for all plausible conditions, so that an accurate evaluation of satellite on-orbit performance can be made.

Prior to launch, exhaustive measurements and calibrations of satellite performance, both uplink and downlink, will have been made. Necessarily, all such tests are done in conditions which can only simulate the "free-space" environment of the on-orbit situation. After launch, the "calibrated" EHF antenna system will be used to estimate (in much the same manner as the boresight tower had been used to estimate the EHF antenna system performance) satellite EIRP (dowlink) and G/T (uplink). With terminal EIRP and G/T known from the procedures in Tables 3 and 4, satellite G/T and EIRP can be determined in the manner suggested in Table 5.

The term, $Atm(\lambda/4\pi R)^2$, represents the path loss in which Atm expresses the additional loss due to atmospheric attenuation. Over the short distance between the boresight tower and antenna system, the atmospheric attenuation was quite negligible and did not appear in the previous expressions. A detailed account of the factors contributing to the error associated with performance estimates is also given in Table 5.

With the satellite launch scheduled for the not-too-distant future, the opportunity to close the loop between satellite and earth terminal performance will present itself and will complete the system calibration.

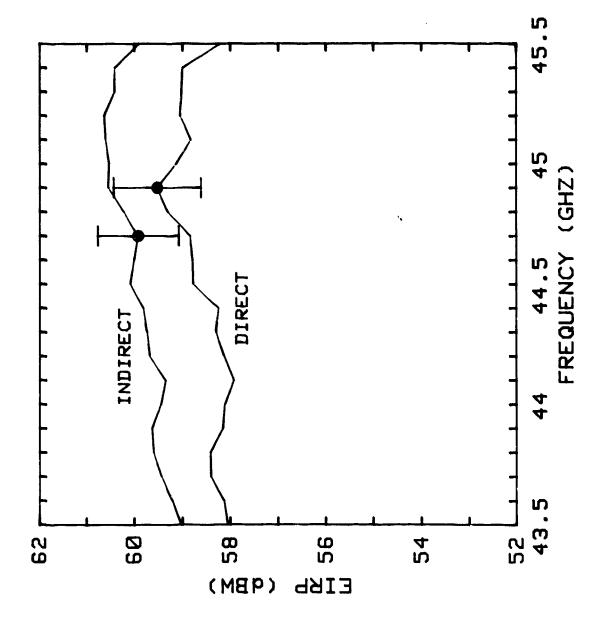


Figure 13. Maximum EIRP from EHF Antenna System Measured; "Directly" Using Boresight Tower "indirectly" Using Product of Transmitted Power and Separately Measured Antenna Gain.

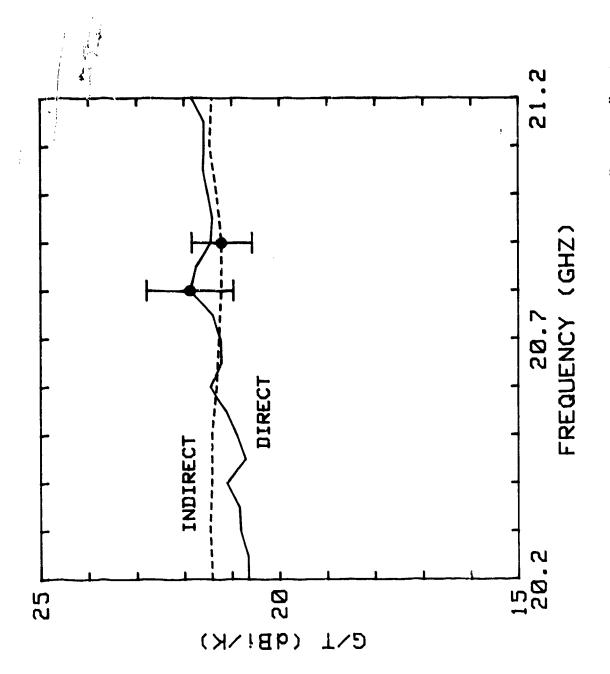


Figure 14. Downlink G/T for EHF Antenna System Measured; "Directly" using Boresight Tower "indirectly" using internal noise source and separately measured antenna gain.

References

- 1. Zolnay, S. L., 5-W, Solid-State EHF Transmitter, Microwave Journal, 28, No. 7 (1985) pp. 103-126.
- Watkins, E. T., T. Q. Ho, and B. M. Post, "FET LNAs designed for advanced EHF systems, Microwave System News, 15, No. 13, pp. 70-80.
- 3. Rispin, L. W., and A. J. Simmons, Calibration of an EHF Satellite Communication Terminal, National Radio Science Meeting, Boulder, CO (1986).

Acknowledgments

The EHF antenna system described herein was the collective result of the efforts of a great many people. A regrettably abbreviated list would include: W. Rotman - reflector specification and feed design, R. J. Burns and R. C. Aucoin - antenna measurements, and D. S. Besse - test and measurement software development. The overall Lincoln EHF Terminal antenna system effort was supervised by W. C. Cummings and A. J. Simmons. Their comments and suggestions in the preparation of this paper are greatfully acknowledged.

TABLE 1

EHF ANTENNA SYSTEM PERFORMANCE BUDGETS

UPLI	<u>NK</u>		DOWNLINK	
Transmitter	7 dBW	Antenna Gain	>50 dBi	290°K
Attenuator	-2 to -42 dB	Tracking Feed	Loss 3 dB	-
Waveguide Loss	2 dB	LNA	>30 dB	260°K
Antenna Gain	>57 dBi	Mixer, IF Amp	_	
EIRP	>60 to 20 dBW	G/T	>19 dBi/°K	

TABLE 2
FACTORS CONTRIBUTING TO EFFECTIVE ANTENNA GAIN

	UPLINK	DOWNLINK
Radome Loss	0.8 (1.0)	0.5 (0.6)
8 ft. Reflector Gain $(\pi D/\lambda)^2$	61.1	54.5
Surface (reflector) Loss	0.2	0.1
Blockage (subreflector and struts)	0.3	0.3
Spill-over plus taper	1.4	1.9
FSS Loss	0.8	0.2
Axial Ratio	0.2 (1.0)	0.2 (0.3)
Tracking Feed and Comparator	-	2.0
Waveguide Loss Inc. Polarizers	0.4	0.4
Predicted Effective Gein	57.0 (57.1)	49.4 (48.6)

Note: Values in parenthesis are based upon subsequent measurements.

TABLE 3
CALCULATIONS AND ERROR ESTIMATE FOR EIRP

INDIRECT ESTIMATE OF UPLINK EIRP	UNCERTAINTY (dB)	ACCURACY (dB)
Effective Antenna Gain, G	±0.3	±0.4
Transmit Power, P	±0.5	±0.5
EIRP = PG	±0.6 (RSS)	±0.6 (RSS)
DIRECT MEASUREMENT OF UPLINK EIRP	UNCERTAINTY (dB)	ACCURACY (dB)
Received Power, PR	±0.5	±0.5
Correction factor, n,	<u>-</u>	±0.2
from Fig. 10 Receive Antenna Gain, GR	±0.3	±0.3
Path Effects, $(\lambda/4\pi R)^2$ & Clutter	-	±0.3
EIRP = $\frac{P_R}{\eta G_R \left(\frac{\lambda}{4\pi R}\right)}$	±0.6 (RSS)	±0.7 (RSS)

TABLE 4
CALCULATION AND ERROR ESTIMATE FOR G/T

INDIRECT ESTIMATE OF DOWNLINK G/T	UNCERTAINTY (dB)	ACCURACY (dB)
Effective Gain, G	±0.3	±0.4
Noise Source Temp, T _{NS}	±0.2	±0.2
Receiver Noise Temp, TREC	±0.2	±0.2
[Noise Source/Antenna Noise] Ra	tio, -	±0.2
[N _{NS} /N _{ANT}]		•
$G/T = \frac{G}{\left(T_{NS} + T_{REC}\right)/\left[N_{NS}/N_{ANT}\right]}$	±0.4 (RSS)	±0.5 (RSS)
DIRECT MEASUREMENT OF DOWNLINK G/T	UNCERTAINTY (dB)	ACCURACY (dB)
K = 198.6 dBm/Hz°K	-	-
B = Noise bandwidth of Receiver	-	-
Signal-to-Noise Ratio (S/N)	-	±0.2
Transmit Power, P _T	±0.5	±0.5
Transmit Antenna Gain, G _T	±0.3	±0.3
Path Effects, $(\lambda/4\pi R)^2$ & Clutter	-	±0.3
$G/T = \frac{KB}{P_T G_T \left(\frac{\lambda}{4\pi R}\right)^2} \left(\frac{S}{N}\right)$	±0.6 (RSS)	±0.7 (RSS)

TABLE 5
CALCULATIONS AND ERROR ESTIMATE FOR SATELLITE PERFORMANCE

UPLINK G/T	UNCERTAINTY (dB)	ACCURACY (dB)
$K = 198.6 \text{ dBm/(}3z^{\circ}K)$	-	-
B _{sat} = Noise Bandwidth of a Satellite Receiver	-	-
Antenna System Uplink (EIRP) _{term}	±0.6	±0.7
Path Effects Atm $(\lambda/4\pi R)^2$	±0.3	••
Signal-to-Noise Ratio (S/N) _{sat}	_	±0.2
$G/T = \frac{K B_{sat}}{(EIRF)_{term} Atm(\frac{\lambda}{4\pi R})^2} (\frac{S}{N})_{sat}$	±0.7 (RSS)	±0.7 (RSS)
DOWNLINK	UNCERTAINTY (dB)	ACCURACY (dB)
K = -198.6 dBm/(Hz°K)	-	•
B _{term} = Noise Bandwidth of Terminal Receiver	-	-
Antenna System Downlink (G/T) _{term}	±0.6	±0.7
Path Effects Atm $(\lambda/4\pi R)^2$	±0.3	-
Signal-to-Noise Ratio (S/N) _{term}	-	±0.2



EHF/SHF SATCOM ANTENNA AND RADOME TEST RESULTS

Allen L. Johnson Wayne O. Fischbach Avionics Laboratory Wright-Patterson AFB, Ohio 45433

ABSTRACT

The current airborne EHF SATCOM system has a RF power output of 100 watts and an antenna beamwidth of less than 1 degree. As the RF beam from the antenna passes through the dielectric radome it will be refracted at each surface. The resulting change in direction of the beam depends on the frequency, the dielectric constant of the radome, and the shape of the radome surfaces. Tests have been performed to evaluate the beam deflection at 20 and 44 Giga-Hertz. Other systems effects which were evaluated included antenna beam distortion, RF heating. and Radio Frequency Interference between two antennas (SHF and EHF) under a single radome. 🌱

INTRODUCTION

Command post aircraft currently use satellite communications (SATCOM) to achieve worldwide connectivity. Early SATCOM systems employed the Ultra High Frequency (UHF) band, with simple aerodynamic blade or overhead-looking antennas (Armstrong, 1978). As the communications systems became more sophisticated, the use of the microwave frequency bands became practical. Antennas now used for SATCOM include Super High Frequency (SHF) and Extremely High

Frequency (EHF) dishes, (Schultz, 1983). These antennas must be placed under radomes to maintain the aerodynamics of the airborne command post. The Avionics Laboratory has investigated the effects of narrow-beam systems since it undertook the development of its first microwave SATCOM system in 1969. We are currently flight testing our fifth generation microwave SATCOM system, (Joyner, 1981).

Some of the operational command post aircraft are already equipped with SHF SATCOM systems to allow operation with the 7-8 GigaHertz (GHz) Defense Satellite Communications System (DSCS II & DSCS III). With the advent of the MILSTAR system, which operates at 20 and 44 GHz, these command post aircraft will require a radome capable of handling 7/8, 20, and 44 GHz: i.e. a tri-band radome.

A tri-band radome has been developed for the Avionics Laboratory's SATCOM system aboard the C-135 testbed aircraft which is maintained and operated by the 4950th Test Wing, (Joyner, 1985). Evaluation of the parameters and effects of the C-135 radome is necessary to validate models used to predict the radome characteristics and reduce the risk associated with future tri-band radome developments.

AN/ASC-30 SATCOM SYSTEM TESTS

The AN/ASC-30 EHF SATCOM system has a Radio Frequency (RF) power output of 100 watts and an antenna beamwidth of less than 1 degree. As the RF beam from the antenna passes through the

dielectric radome it is refracted at each surface. The resulting change in direction of the beam, called beam squint, depends on the frequency, the dielectric constant of the radome, and the shape of the radome surfaces. Tests have been performed to evaluate the beam squint at 20 and 44 GHz.

Other systems effects which were evaluated included radome attenuation, antenna beam shape, RF heating, Radio Frequency Interference (RFI) between two antennas under a single radome, and radome deflection in flight.

RF Beam Squint

Measurements of the RF beam squint were accomplished by comparing the optimum antenna pointing angles with the radome in place and removed. One practical problem in measuring the beam squint of the AN/ASC-30 tri-band radome was the lack of a 20/44 GHz satellite on-orbit to use as a signal source. In place of the satellite, a simulator was used, consisting of a 20 GHz transmitter and a 44 GHz receiver on the tower of building 620 at WPAFB, OH, Figure 1. The AN/ASC-30 with its 44 GHz transmitter and 20 GHz receiver was installed in aircraft C-135/372, which was located on the ground at Patterson Field.

For the beam squint test the 20 GHz tower transmitter and 44 GHz aircraft transmitter were turned on and their antennas pointed toward the respective receivers. The aircraft antenna was moved in 0.1° azimuth steps for $\pm 2.5^{\circ}$, and 0.1° elevation steps for $\pm 1.0^{\circ}$ of

the calculated pointing angle from the aircraft to the tower. In the tower and aircraft, the azimuth antenna beam patterns were received, recorded, and correlated with the transmitter pointing angles. The radome was then removed and the azimuth/elevation steps repeated. Any difference in the pointing angle for the peak of the beam was attributed to radome-induced beam squint. Due to the complex curvature of the radome, various portions were measured from the nose, to broadside, to the tail, Figure 2.

Radome Attenuation

It was possible to measure the absolute attenuation of the radome at 20 and 44 GHz by comparing the received power with and without the radome in the line-of-sight path, using the same test configuration as for beam squint.

Antenna Beam Shape

The pattern of AN/ASC-30 EHF antenna is also of interest. The beam squint measurements provided the information necessary to characterize the affect of the radome and ribs on the three-dimensional beam shape.

Radome RF Heating

When an SHF transmitted beam passes through the radome, local RF heating will occur. For the RF heating tests a special test fixture was constructed to simulate a section of the C-135 aircraft fuselage. The AN/ASC-18 airborne SATCOM antenna was mounted on the fixture and the tri-band radome installed over the antenna,

Figure 3. The AN/ASC-18 terminal, which was installed in the nearby Rooftop Facility, has a power output of 10 kW in the SHF band. To conduct the test, the SHF transmitter was turned on and operated until the radome's inside temperature stabilizes. extent of the heating was measured by attaching a series of heat tabs (which blacken at a specific temperature) around a 15 inch diameter circle inside the radome in the area where the antenna beam intercepted the radome. The test procedures require the SHF transmit power to be raised from a 2 kW level to a maximum of 10 kW in four steps. At a 10 kW transmit power level, the uniform energy density from the antenna would be 12.4 watts/inch². In the near field, the energy distribution is not uniform and it was anticipated that "hot spots" could occur with energy densities of 20 watts/inch². Tests with flat panels of the radome material indicated that at 8 GHz the loss in the radome is approximately 2dB. (60% transmission). In a hot spot it was expected that 8 watts/inch² could be dissipated in the radome skin. temperature was determined for each power level by reading the highest temperature heat tab which had fired (blackened).

RFI/EMI Between Two Antennas Under One Radome

For some airborne command post applications, two dish antennas will be mounted under the same radome. One antenna system operates at 7 and 8 GHz while the other operates at 20 and 44 GHz. For the RFI/EMI test, the 20 GHz noise out of the 8 GHz transmitter that

couples into the 20 GHz antenna/receiver and the 7 GHz noise from the 44 GHz transmitter that couples into the 7 GHz antenna/receiver were measured. Both antennas were mounted on the test fixture, under the tri-band radome. Receiver measurements were made as each transmitter was turned on. The antennas were positioned at various geometrics; both pointed toward the same equal-angle reflection point, both antennas normal to the radome wall, and the antennas pointed almost directly toward each other.

Radome Deflection In Flight

The AN/ASC-30 system employs a 26" parabolic antenna that is mounted on top of a C-135 test aircraft. An aerodynamic radome covers the antenna to reduce the drag, Figure 4. Since the radome has to pass three frequency bands (7-8 GHz, 20-21 GHz, and 43-45 GHz), a special wall thickness design was required. The resulting thin-wall radome design did not have sufficient stiffness to meet deflection limits during maximum erodynamic loading. To improve the stiffness, three ribs were added to the radome, Figure 5. The final design was run on a NASTRAN computer model (WANG, 1984) to calculate the radome wall deflection during an 8° aircraft sideslip, the maneuver specified as providing the maximum dynamic loading to the sides of the radome.

The tri-band radome was constructed by Hitco Inc. under a subcontract with Bell Aerospace Corp. and the Raytheon Company. The radome was then installed on the C-135/372 test aircraft and a

test flown to measure the actual deflection (Hocutt, 1985).

The tri-band radome was modelled by Bell Aerospace Corp. using a NASTRAN finite element computer model. The radome surface was divided into 320 separate panels and pressure levels calculated for the specific maneuver were applied to each panel. After several iterations of different skin thickness and rib placement, a final design was achieved with a skin thickness of 0.145 inches and rib placement shown in Figure 6. The maximum deflection location and value were predicted to be 0.251 inches at node 1056 with the 8° sideslip maneuver. Figure 7.

To measure radome deflection, a fixture was constructed by the 4950th TW to fit over the AN/ASC-30 antenna, Figure 8. Two linear deflection transducers were mounted at the edges of the fixture and the deflection arm attached to buttons cemented to the insides of the radome. The buttons were positioned within a few inches of the predicted maximum deflection point. The linear deflection transducers were connected to a DC power source and to the instrumentation system. The transducers had a travel of ± 1.5 inches from their static position. The transducer position was calibrated over the entire travel range and recorded on a magnetic recorder and a chart recorder to an accuracy of 0.001 inches.

TEST RESULTS

Racome Beam Squint Measurements

A comparison of the antenna azimuth angle with the AN/ASC-30 tri-band radome both in place and removed provided a measurement of

the beam squint. A summary of the beam squint for various portions of the radome (azimuth angles) is shown in Figure 9. One azimuth sweep showing the worst beam squint is presented in Figure 10. The beam squint appears to be approximately 0.4° over the nose and tail and on the order of 0.1° broadside.

Radome Attenuation Measurements

In an effort to evaluate the effect of radome thickness and incidence angles on the radome attenuation, a 36-inch square flat panel was constructed of the same material and thickness as the tri-band radome. Attenuation tests were conducted on the flat panel. The results of the 20 GHz and 44 GHz measurements are shown in Figure 11.

Measurements of the actual radome attenuation were made by comparing the received signal level with the AN/ASC-30 tri-band radome in place and removed. A plot of the attenuation for various portions of the radome is shown in Figure 12. The radome attenuation measurements are in close agreement with the flat panel measurements.

Antenna Pattern

The 44 GHz pattern of the tri-band antenna was measured with the radone in place and removed. The mainbeam portion of the pattern is shown as a 3 dimensional plot, Figure 13. This data shows the effects of the radome and ribs particularly on the sidelobe distribution.

Radome Heating

The AN/ASC-18 SHF transmitter was first operated at 2 kW RF power at 8 GHz. The ambient temperature was approximately 40°F outside the radome and 50°F inside the radome. After 20 minutes of operation, the radome temperature stabilized at less than 100°F at the top and left side of the test circle, 105°F at the right side, and 115°F at the bottom. Following each power leve' setting, the maximum temperatures were recorded, Table 1.

TABLE 1 Temperature Distribution On Tri-Band Radome

Xmit Po	ower Measurement	<u>0°</u>	<u>90°</u>	<u>180°</u>	270°	Time
2 KW	Temp Tabs Thermocouple	100°F	105°F	115°F	100°F	20 Min
5 KW	Temp Tabs Thermocouple	100°	115° 100°	130° 125°	100° 100°	15 Min
8 kW	Temp Tabs Thermocouple	130° 135°	130° 170°	130° 180°	130° 135°	32 Min
10 KW	Temp Tabs Thermocouple	130° 176°	130° 180°	200° 188°	130° 176°	16 Min

With the transmitter operating at 5 kW of power for 15 minutes, the maximum temperature recorded was 130°F. After transmitting 8 kW for 32 minutes, the temperature tabs on the bottom of the circle showed 130° but a thermocouple measured 180°F. The maximum power transmitted was 10 kW for 16 minutes, after which the temperature tabs showed 200°F at the bottom of the circle. Subsequent discoloring of the radome material indicated that the

internal plys of the radome reached a temperature of approximately 500° F during the 10 kW run.

From the measurements, it appears that the current tri-band radome design could withstand between 2 and 5 kW of transmit power at 8 GHz without experiencing an excessive temperature rise. Power levels above 5 kW are likely to cause an excessive temperature build up in the laminated plys which could damage the radome. If the radome loss were reduced, the transmit power could be increased proportionally.

RFI/EMI Test

system encountered no interference at 20.8 GHz, the AN/ASC-30 system encountered no interference at 20.8 GHz except when the transmit antenna was pointed at 225° azimuth where the mainbeam just grazed the AN/ASC-30 antenna. In that configuration, the worst case interference was with the AN/ASC-30 pointing at 180° azimuth and 80° elevation. Approximately a 1 dB rise was noticed in the noise floor of the AN/ASC-30 receiver when the AN/ASC18 was transmitting 10 kW. It was postulated that the interference was caused by energy coupling directly into the RF mixer and downconverter that is mounted on the back of the dish, rather than through the antenna feed. The RF mixer and downconverter were removed, reinstalled, and all connectors properly tightened. A retest showed only 0.1 dB rise in the noise floor. To determine the effect of the interference on link performance, data was

transmitted to the AN/ASC-30 system with the interference source on and off. The Bit Error Rate (BER) performance of the system appeared to be uneffected by the interference, Figure 14.

When the AN/ASC-30 transmitted 100 watts at 44 GHz, no interference was experienced in the AN/ASC-18's 7 GHz receive system, regardless of the orientation of the two antennas.

Radome Deflection Flight Test

During the aircraft's take-off roll, at a speed of approximately 90 knots, both sides of the radome started to deflect outward, Figures 15. As the aircraft reached take-off speed, rotated, and continued to accelerate, both sides of the radome deflected outward approximately 0.09 inches. The aircraft climbed to an altitude of 10,000 feet and the outward deflection remained constant during straight and level flight. The aircraft made a data run at 200 Knots Indicated Air Speed (KIAS) with a 5° side slip. There was no noticeable change in the radome deflection. Several runs were made at 10,000 feet altitude, 200 KlAS, with an 8° side slip. The instrumentation recorded a deflection of one minor division (approximately 0.04 inches) inward on both sides of the radome during those runs, Figure 16.

During the aircraft's approach and landing the radome deflection decreased on both sides as the airspeed decreased, Figure 17. Shortly after touch-down the instrumentation showed the radome had returned to its static width.

It appears the aerodynamic pressure on the front and top of the radome causes both sides to bow outward approximately 0.10 inches at the antenna station. The effect of the side-slip maneuver appears to reduce the front and top pressures, allowing both sides of the radome to move inward 0.04 inches. The effect of the dynamic pressure on the sides of the radome appears to be so small that it is masked by the change in front and top pressures.

inches during the side slip appears to be quite conservative. The model was used previously to predict the deflection on a dual-band radome (Severyn, 1978). A similar flight test of the dual-band radome produced deflections which agreed quite closely with the model (Cummins, 1978). The difference between the tri-band radome prediction and the test results may be due to inaccurate pressure distributions in the model or to the difficulty of correctly modeling the stiffness of the ribs.

REFERENCES

Armstrong, E.L., Maj (USAF), "AFSATCOM," Air Force Magazine, pp 80-85, July 1978.

Cummins, W.S., "Airworthiness Test of Dual Frequency SAICOM Radome," 4950th TW, Wright-Patterson AFB, OH, 2 June 1978.

Hocutt, Capt A.M., "Tri-band Radome Test Plan," AFWAL TM-85-13, Air Force Wright Aeronautical Laboratories, Wright-Patterson AFB, OH, 27 June 1985.

Johnson, A.L., "Airborne EHF Satellite Communications Terminals," Submitted to IEE Proceedings F, Herts England, July 1985.

Joyner, T.E., "AN/ASC-30 EHF/SHF Command Post SATCOM Terminal," NAECON Symposium, Vol 1, pp 124-127, Dayton OH, 19 May 1981.

Joyner, T.E., "AN/ASC-30 Upgrade SATCOM Moderate Gain Antenna/ Radome Subsystem," NAECON Symposium, pp 1192-1197, Dayton OH, 20 May 1985.

Schultz, J.B., "MILSTAR To Close Dangerous C3I Gap." Defence Electronics, Vol 15 No. 3, pp 46-59, March 1983.

Severyn, T., "Aerodynamic Evaluation of Dual Frequency Radome," Flight Test Plan 78-4-3, 4950th TW, Wright-Patterson AFB, OH, 5 May 1978.

Wang, T., "AN/ASC-30 Upgrade Radome Structural Analysis," Bell Aerospace Corp, Buffalo, NY, 13 December 1984.

TRI-BAND RADOME BEAM SQUINT TEST CONFIGURATION Figure 1

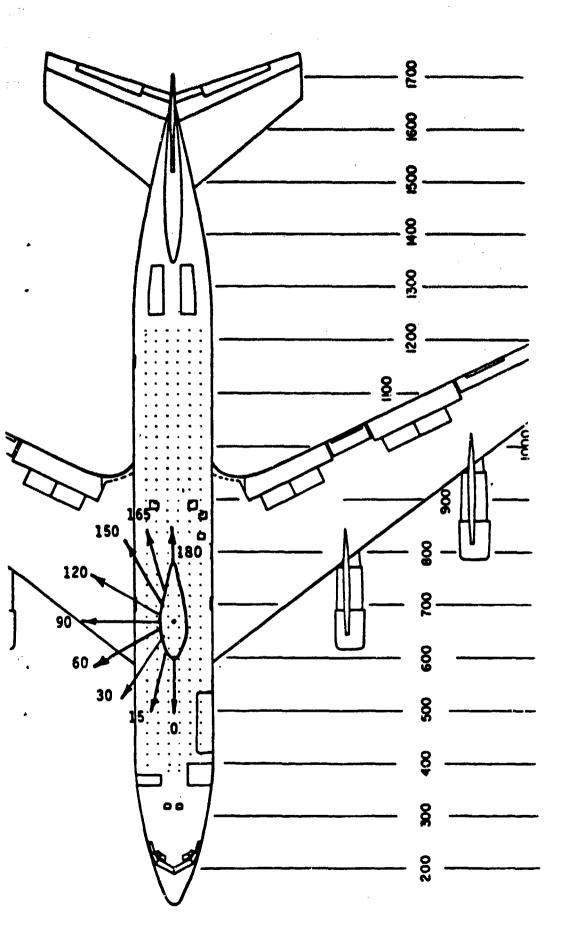
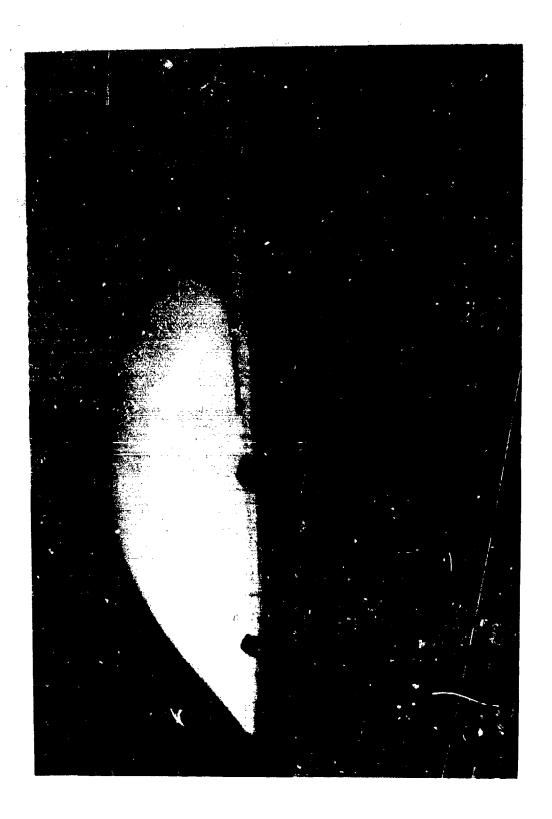


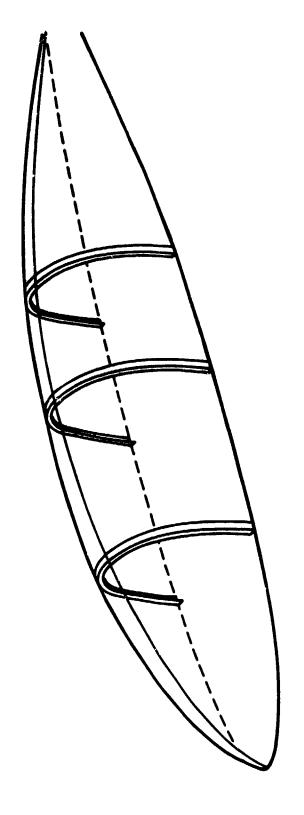
FIGURE 2 ANGLES FOR BEAM SQUINT TEST MEASUREMENTS



ANTENNA/RADOME TEST FIXTURE FOR TEMPERATURE & RFI TEST FIGURE 3



FIGURE 4 AN/ASC-30 RADOME ON C-135 AIRCRAFT



RIB PLACEMENT FOR AFWAL TRI-BAND RADOME FIGURE 5

AN/ASC-30 UPGRADE RADOME STRUCTURAL ANALYSIS RECOMMENDED 3 RIB CONFIGURATION

FINITE ELEMENT MODEL

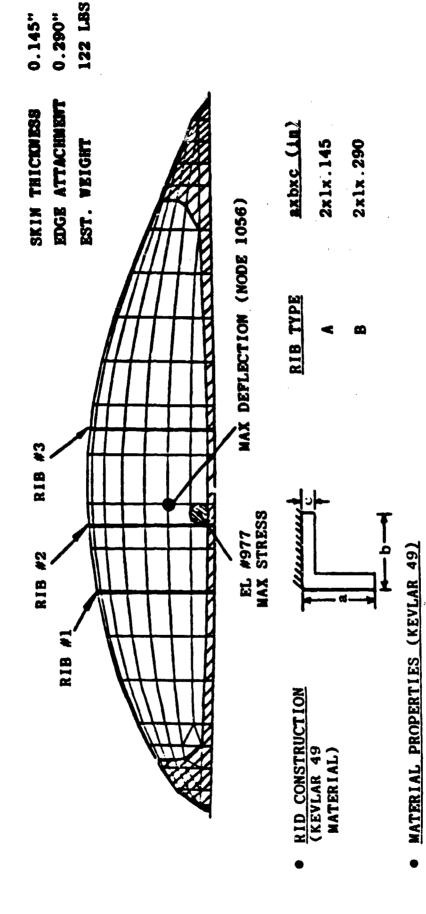


Figure 6 NASTRAN FINITE ELEMENT MODEL

0.05 #/IN³

 $4.5 \times 10^6 \text{ PSI}$

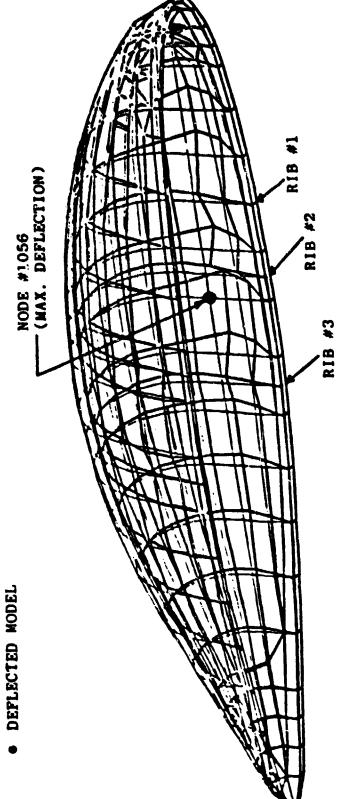
M

 $0.3 \times 10^6 \text{ PSI}$

Ç

AERODYNAMIC LOAD - PER 6475-950001



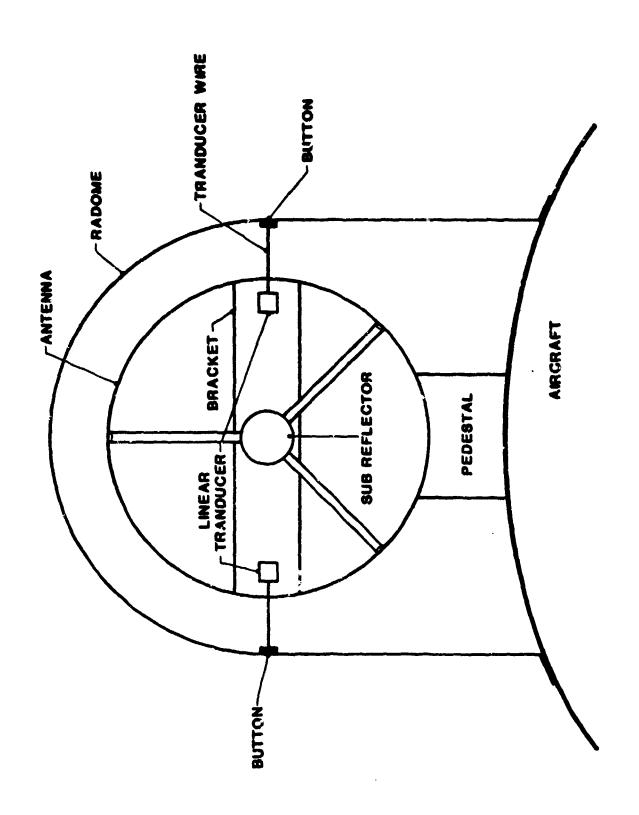


• RESULTS

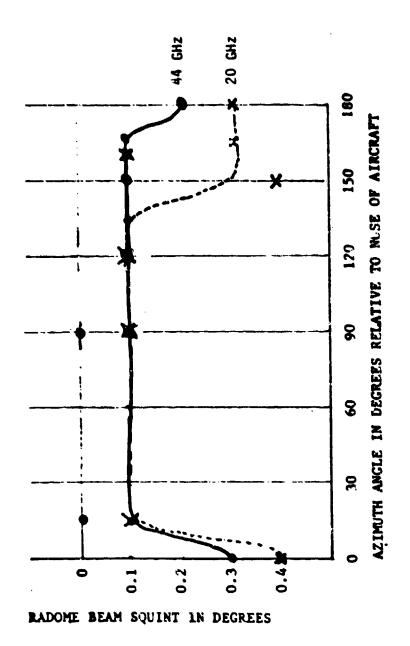
2	RIB TYPE	MAX.	MAX. STRESS	
2	3	DEFLEC. (IN)	(KSI)	M.S.
<	4	.251	4.26	4.07
æ	∢	. 238	4.23	4.10

*ALLOWABLE STRESS = 32.4 KSI, FACTORY OR SAFETY = 1.5

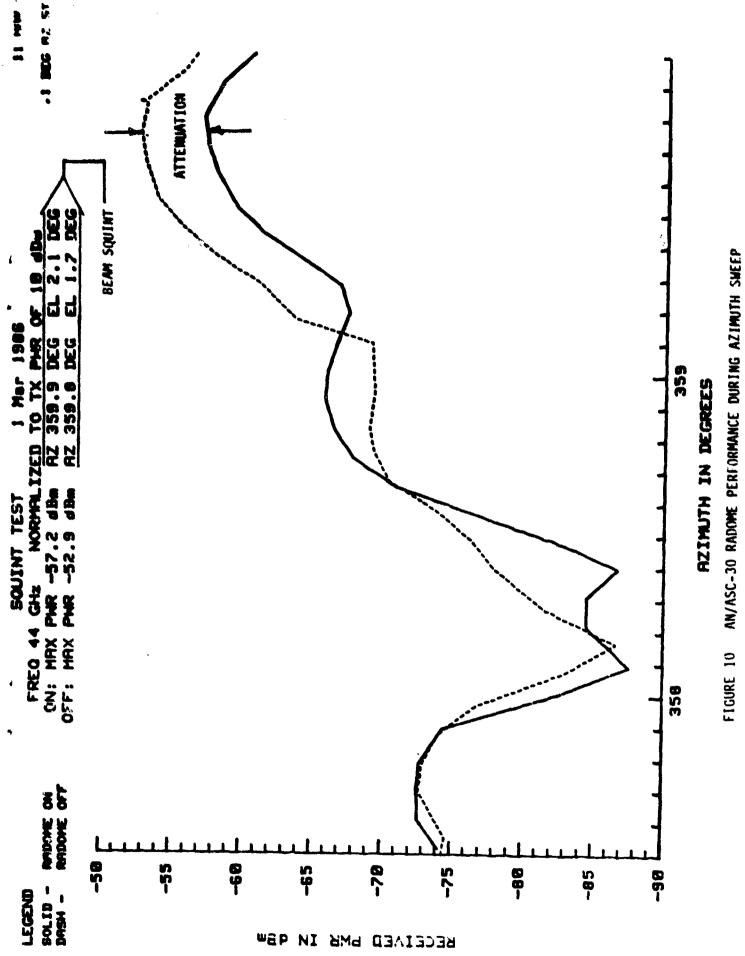
Figure 7 MAXIMUM DEFLECTION OF NASTRAN MODEL



-83-



TRI-BAND RADOME BEAM SGUINT VERSUS AZIMUTH ANGLE Figure 9



-85-

20/44 GHZ FLAT PANEL MEASUREMENTS WITH COATING FIGURE 11

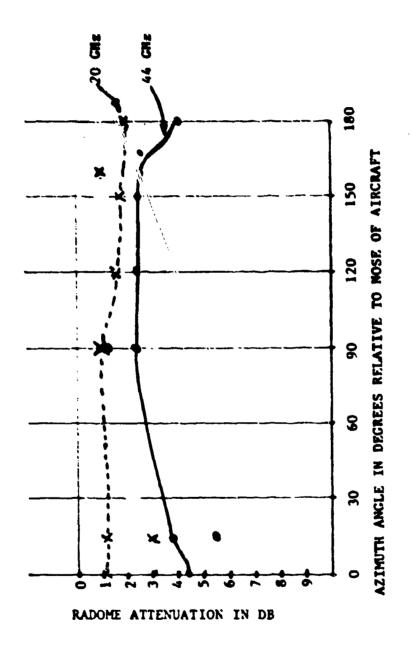
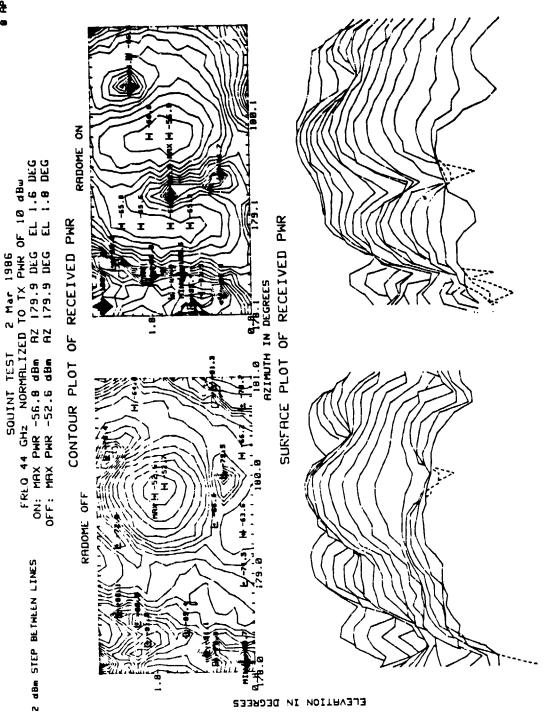


FIGURE 12 TRI-BAND RADOME ATTENUATION VERSUS AZIMUTH ANGLE



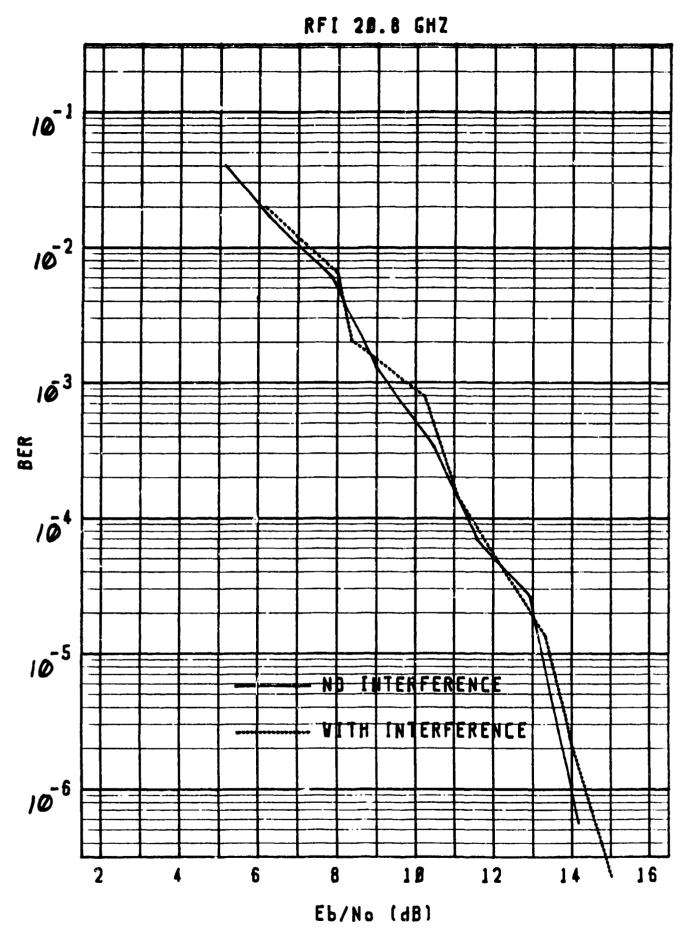


Figure 14 Bit-Error-Rate During Interference Test

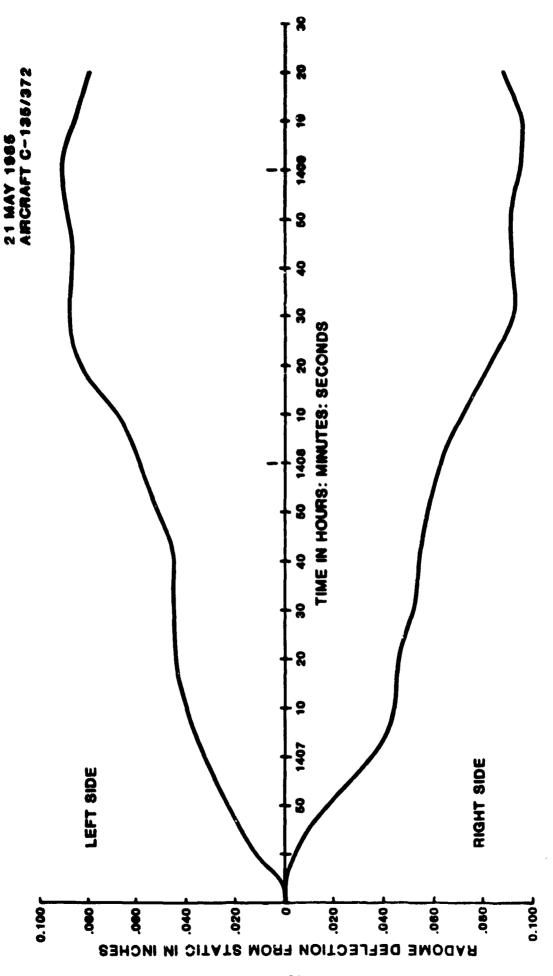


Figure 15 DEFLECTION OF TRI-BAND RADOME DURING TAKE-OFF ROLL

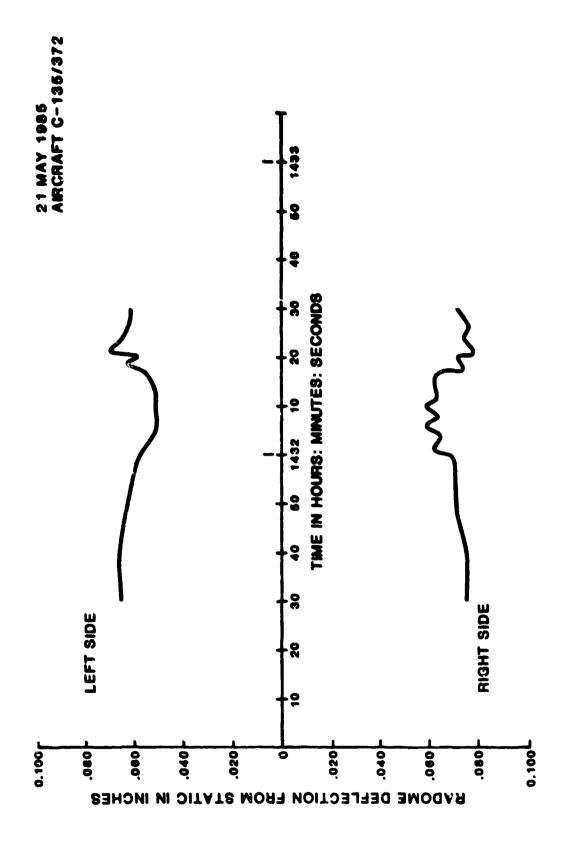


Figure 16 DEFLECTION OF TRI-BAND RADOME DURING 8" LEFT SIDE SLIP

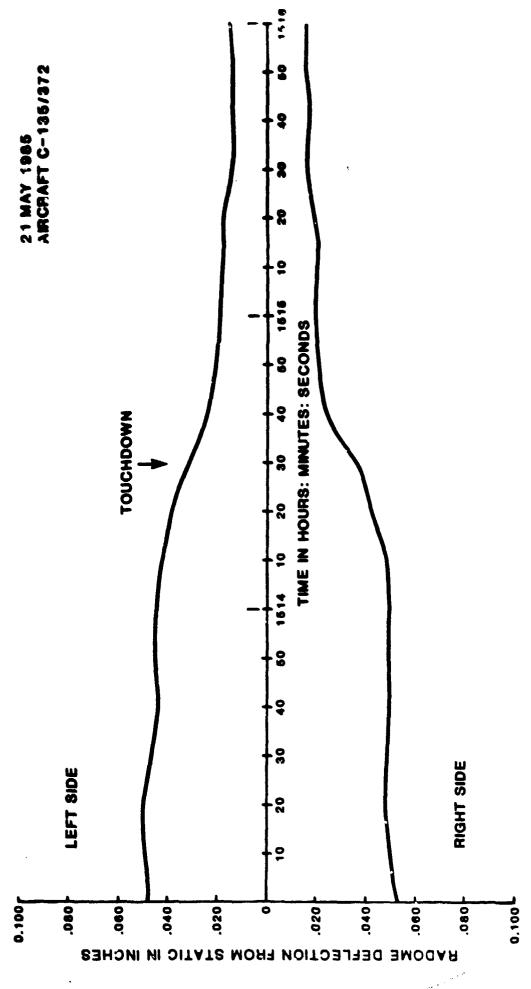


Figure 17 DEFLECTION OF TRI-BAND RADOME DURING LANDING

SIMPLIFIED MMIC ACTIVE APERTURE FEEDING

J. Leon Poirier

Rome Air Development Center Electromagnetic Sciences Division Hanscom AFB, MA 01731



Abstract

MMIC modules of the future offer the possibility for simplifying the feed networks of active aperture phased arrays. In particular, the addition of amplitude control along with the existing phase control would allow the same feed network to be used in the transmit and receive modes even though the two require grossly different aperture tapers. This is easily accomplished by using the amplitude control in the modules to provide the weighting required to produce low sidelobe receive beams.

Specific examples in which amplitude control is implemented with digital attenuators are examined. The effect of the attenuators on the array output signal-to-noise ratio and that of the amplitude quantization on error sidelobe level are evaluated. The results indicate that the component values needed...total attenuation 20-30 dB, low noise amplifier gains and noise figures 20-30 dB and 3-4 dB respectively, and quantization of 2-6 bits... are readily achievable in current GaAs technology. With these, active aperture monopulse arrays with sidelobe levels of -20 to -50 dB below the peak of the mainbeam may be designed with greatly simplified feed networks.

1. INTRODUCTION

Monolithic Microwave Integrated Circuit (MMIC) transmit/
receive modules make possible new phased array antenna architectures. This paper examines the possible simplification of the

feed networks of a monopulse radar array when the flexibility of an MMIC module is fully utilized. In particular, using the module's internal amplitude control will allow a single beamformer to be shared between the transmit and receive modes even though the amplitude taper for each mode is dramatically different.

The circuit arrangement of a typical MMIC module is shown in Figure 1. It is made up of a power amplifier PA, a low noise amplifier LNA, a phaser P, a variable attenuator A, a controller, and a system that selects between the transmit and receive mode. In the transmit mode, the T/R switches provide a connection from the input of the module through the phaser, the PA, and the circulator to the antenna. On receive, the signal path is through the LNA and the PA is turned off to conserve power. In both modes, the phaser is set to the appropriate phase, selected by the controller in response to a command, to produce a beam in the desired direction.

A column of an antenna system of a low sidelobe monopulse radar array antenna is shown in Figure 2a. The system uses a module at each element and three feed networks to produce a transmit, a low sidelobe sum, and a low sidelobe difference beam. The column outputs are further combined in appropriately weighted azimuth beamformers. Notice that the common input/output port on the module must be duplexed with an external switch or circulator to connect it to the appropriate beamformer on transmit

and receive. Also, a power divider is needed in each channel to split the received signal between the two beamformers. The upper and lower halves of the array are added or subtracted to produce the three beams in the vertical plane.

When each module has amplitude control, the arrangement shown in Figure 2a can be simplified. Instead of using the amplitude control only for channel matching and scan correction for conformal arrays, it can also be used to generate the illumination function for one of the receive beams. In this way, one beamformer can be shared between the transmit and receive modes thereby eliminating one of the receive beam feed networks.

Figure 2b shows an antenna system in which the module and antenna have been more closely integrated. Here only two beamformers are needed instead of three. One of these is uniformly tapered and the other is specially modified to produce a low sidelobe difference pattern from the signals that have been corrected to produce a low sidelobe sum beam. The former is used for both transmit and receive. In the transmit mode, it operates exactly as before and delivers a cophased, equal amplitude signal to each module's common input/output terminal. On receive, however, the module amplitude control is activated and adjusts the amplitude of each module's received signal before feeding into the beamformer to produce a low sidelobe Taylor or similarly weighted sum beam at the network's output. Since the signals for the

difference beam are derived from these tapered sum signals, the difference beam feed network must be specially weighted to accomodate these input signals to produce ultimately the required difference weighting function at the Δ channel output.

It now remains to investigate the practicability, limitations, and impact on module design of incorporating the idea of a shared beamformer into an antenna system.

2. SYSTEM CONSIDERATIONS

2.1 Aperture Weighting

The element signals, after passing through the LNA are appropriately attenuated and appear at the module output with a low sidelobe taper distribution. When these outputs are combined in the uniform beamformer network, the beamformer output will be the low sidelobe E pattern. However, the difference channel signals must also be derived from these weighted module output signals. The beamformer weighting necessary to recover a low sidelobe difference pattern is chosen according to the rule

$$k_{\mathbf{q}} = k_{\Delta \mathbf{q}}/k_{\Sigma \mathbf{q}} \tag{1}$$

where k_{Σ} and k_{Δ} are the required sum pattern and difference pattern weights respectively.

An example of the relative weightings for n=4, SLL = -30 dB Taylor Σ and Δ patterns for a 64 element linear array are shown in Figure 3. Equation (1) was used to calculate the modified

weighting represented by the dashed curve that is needed to convert the Taylor distribution into the similarly characterized Bayliss distribution.

2.2 Range Of Attenuation

The range of adjustment of the attenuator that is necessary depends on the SLL of the design. In general, the lower the sidelobe level, the greater the range of amplitudes required across the array to produce the taper. The curves in Figure 4 show the range in attenuation required to achieve various sidelobe levels for several \overline{n} values for Taylor weighting 1^{-3} . For example, an $\overline{n}=6$, SLL = -40 dB design requires a maximum caper attenuation of about 19.4 dB relative to the center element. Thus, if the taper is implemented by attenuators, then the attenuator must have a range of 20 dB. It is apparent that the maximum taper weight is not a sensitive function of \overline{n} and the maximum attenuation A of the attenuator, may be conveniently approximated by

$$A = (11/15)(SLL + 20) - 5 db$$
 (2)

represented by the dashed line in the figure. Thus the attenuator value for a Taylor weighted aperture depends only on the sidelobe level of the design. Equation (2) is represented by the dashed line in the figure.

2.3 Amplitude Quantization Error

The value of attenuation produced by each module will be quantized. The error sidelobes due to quantization of the element amplitudes must be less than the sidelobe level SLL of the design. The rms error sidelobe level due to phase and amplitude errors can be found from the expression

$$SLL_{rms} \approx (\sigma^2 p + \sigma^2 A)/(1 - \sigma^2 p) M \eta_t$$
 (3)

where σ^2_P and σ^2_A are the variances of the total phase and amplitude errors from all sources respectively, M the number of elements, and η_t the aperture taper efficiency. It should be noted that M and η_t in Eq. (3) apply to the entire aperture. For example, a rectangular aperture of Q rows and P columns would make M = QP and $\eta_t = \eta_{tQ} \eta_{tP}$. The total variances σ^2_P and σ^2_A are equal to the sums of the variances from all contributing sources of the phase and amplitude errors respectively. The variance due to a phase shifter quantization of B bits is $\sigma^2_{Pl} = \pi^2/(3\times 2^{2B})$. For an attenuator of B' bits and total attenuation A (in dB)

$$\sigma_{A1}^2 = 10^{A/10}/(12 \times 2^{2B}). \tag{4}$$

Other sources of phase and amplitude errors include mismatch, power division and element position errors.

The taper efficiency for a linear array of Q elements is evaluated with the expression

$$n_{t} = \begin{array}{ccc} Q & Q & Q \\ \lambda & \lambda & a_{q}a_{p}/Q & \lambda & a_{q}^{2} \\ \alpha = 1 & p = 1 & \alpha = 1 \end{array}$$
 (5)

where the a_q are the element weights. The results for a linear Taylor weighted array are plotted in Figure 5 for several values of \overline{n} . It is apparent that n_t is not a sensitive function of \overline{n} but depends chiefly on SLL. For convenience and later use, n_t for a linear Taylor tapered array is approximated by

$$n_t = 0.96 \exp[(SLL + 20)/92.2].$$
 (6)

Equation (6) can now be used with Eq. (4) to evaluate the error sidelobe level of Taylor weighted linear arrays for various amplitude quantization levels using Eq. (3). The calculations assume that the only error is that due to the amplitude quantization. The value of A was obtained from Eq. (2). The results are plotted in Figure 6 as a function of SLL. Inspection of the figure shows that for a 64 element array with SLL = -40 dB, a five bit quantization of the 20 dB attenuator is needed to achieve an rms error sidelobe level SLL_{rms} = -38 dB. To this would be added the effects of the other sources of error to arrive at the ultimate, error sidelobe level from all sources.

For a similarly characterized 64×64 array, M = QP = 4096. From Eq. (6), $\eta_t = \eta_{tQ} \eta_{tP} = 0.60$, and from Eq. (2) A = -20 dB. Here we assume the column outputs are in a conventional Taylor weighted beamformer. Using these values in Eqs. (4) and (3) gives $B^* = 3$.

The effect of the attenuator quantization on the antenna patterns is shown in Figure 7. The right half of Figure 7 shows the error free pattern for a \overline{n} = 4, SLL = -30 dB, 64 element linear array. The left half of the figure shows the degradation in the pattern when the taper setting attenuator is quantized to four bits. The patterns are symmetrical about the mainbeam because the aperture taper and the quantization errors as well are symmetrically distributed.

The quantization errors also effect the difference pattern. The modified Bayliss weighting computed from Eq. (1) is error free. However, the Taylor weighted output signals from the modules are correct only to within the attenuator quantization LSB. Therefore the actual signals presented to the difference channel beamformer are errored. The difference patterns that result from Taylor weighted element signals applied to a modified beamformer are shown in Figure 8. The right and left halves of Figure 8 show the error free and four bit level patterns respectively. The patterns are symmetrical because of the taper and errors are symmetrical about the center of the aperture. Because

of this, the depth of the notch is not affected by the quantization.

It should also be noted that the gains of the patterns are somewhat lower than expected. However, Figure 3 shows that the peaks of the Taylor and Bayliss distributions occur at different aperture locations. Because of this, the Taylor weights must be reduced by a factor of about 0.72 during the application of the modified Bayliss weights that results in an additional loss in gain of about 3 dB in the difference pattern. This additional loss could be eliminated by providing a separate attenuator for the A channel. In this case, the power division for the two sum channels would occur ahead of the attenuators so that the output weighting could be independently controlled.

2.4 Signal to Noise Ratio

A sketch of a generalized active array is shown in Figure 9. Each channel contains a low noise amplifier LNA, a digital phase shifter P, and a digital attenuator A. All other circuit channel losses including the insertion losses of the phase shifter, the attenuator, and the beamformer are lumped into L. The signal power at the output of the array may be found by first summing the complex voltage contributions v_q from each element to obtain the output V as

$$V = \sum_{q=1}^{Q} v_q \varepsilon_q q_q k_q l_q \exp[j \dot{v}_q]$$
 (7)

where $\mathbf{g}_{\mathbf{q}}$ is the voltage gain of the LNA, $\mathbf{a}_{\mathbf{q}}$ the voltage attenuation of the attenuator, $\mathbf{k}_{\mathbf{q}}$ the beamformer relative voltage coupling coefficient ($\mathbf{k}_{\mathbf{q}}$ maximum = 1). $\mathbf{l}_{\mathbf{q}}$ the fixed voltage attenuation of the channel, and $\mathbf{\theta}_{\mathbf{q}}$ the total phase shift (including that of the phaser) of the channel. The output power S may be found from

$$S = VV^* = \frac{Q}{L} \frac{Q}{v_q v_p^* g_q g_p^* a_q a_p^* k_q k_p^* l_q l_p^* \exp[j(\theta_q - \theta_p)]}$$
(8)

Similar expressions can be written for the noise contributions⁵. However, since the internally generated noise is independent from channel to channel, the power for terms for $q \neq p$ is zero. Thus, the noise power N may be expressed directly in terms of the channel noise power input N_q as

$$K = \frac{Q}{L} K_q G_q A_q L_q [F_q + (1 - A_q L_q) / A_q L_q G_q] K_q$$
 (9)

where $g_q = g_q g_q^*$ and F_q are the power gain and noise figure of amplifier q respectively. The noise figure of the attenuation of the channel is set equal to the reciprocal of its attenuation⁶. $K_q = k_q k_q^*$ is the power coupling coefficient of the beamformer.

Equations (8) and (9) can now be used to find the output S/N ration of an antenna system in terms of the input S_i/N_i ration for a wide variety of array configurations. For a lossless array

in the mainbeam direction without amplifiers or attenuators and a uniform beamformer, $v_q = v$, $v_p^* = v$, $a_q = 1$, $1_q = 1$,

$$S/N = (S_1/N_1)Q.$$
 (10)

Allowing for equal circuit losses $l_q l_p = L < 1$ in each channel results in the expression

$$S/N = (S_i/N_i)LQ.$$
 (11)

The effect of circuit losses is apparent. To reduce the impact of losses on the S/N ratio, a low noise amplifier may be inserted into the system at each element. Then Eqs. (8) and (9) give

$$S/N = (S_i/N_i)Q/[F + (1 - L)/LG].$$
 (12)

For a wide range of values, S/N depends principally on the noise figure of the amplifier and thus attenuation in the array components is not as important. In fact for LG >> 1,

$$S/N = (S_{i}/R_{i})Q/F.$$
 (13)

For low sidelobe tapered arrays, the improvement in $\rm S_i/N_i$ is not as great as for uniform arrays because the taper efficiency of the array reduces the signal power S. Also, the edge elements, for which attenuation is large compared to the gain of the amplifier, introduce proportionally more noise when

the taper is set by attenuators and the beamformer coupling is uniform.

This can best be seen by inserting Eq. (5), the aperture taper efficiency n_t into Eq. (8). Then, an array with a uniform beamformer ($K_q = 1$), the same amplifier in each channel ($G_q = G$ and $F_q = F$), the same total losses in each channel ($L_q = L$), and the aperture weighting determined by attenuators A_q would display a signal to noise of

$$S/N = \{(S_{i}/N_{i})Qn_{t}/F\} \underset{q=1}{\overset{Q}{\downarrow}} A_{q}/\underset{q=1}{\overset{Q}{\downarrow}} A_{q}[1 + (1 - A_{q}L)/A_{q}LGF].$$
 (14)

When $A_qLG >> 1$, S/N becomes

$$S/N = (S_i/N_i)Qn_t/F.$$
 (15)

Thus Eqs. (14) and (15) for tapered arrays correspond respectively to Eqs. (12) and (13) for uniform arrays.

It is convenient to write Eq. (14) as

$$S/N = (S_i/N_i)Qn_t n_s/F$$
 (16)

where the aperture noise suppression efficiency η_s is defined as

$$\eta_{s} = \sum_{q=1}^{Q} A_{q} / \sum_{q=1}^{Q} A_{q} [1 + (1 - A_{q}L)/A_{q}LGF].$$
 (17)

 $\eta_{\rm S}$ represents the additional reduction in S/N caused by the noise contributed by the array components. $\eta_{\rm S}=1$ for a lossless uniform array without amplifiers or attenuators ($\Lambda_{\rm Q}=1$, G=1, F=1, L=1) and $\eta_{\rm S}=1$ for the same but lossy array ($\Lambda_{\rm Q}=1$, G=1, F=1). The aperture noise suppression efficiency is plotted in Figure 10 for a range of typical values for tapered active arrays. As expected, $\eta_{\rm S}$ decreases with SLL (for a fixed value of G) because increasingly larger attenuation is needed to produce the taper. It is apparent however, that so long as G is sufficiently large compared to A and L the decrease in S/N can be kept small.

2.5 Azimuth Feed Networks

Figure 2a shows the vertical feed network connections. These outputs must now be combined in the azimuth beamformers as shown in Figure 11a. The column index number is P. The weighted sums of the Σ_p outputs for p < 0 and p > 0 are also subtracted to produce the low sidelobe azimuth difference beam $\Sigma\delta$. The Δ_p outputs are similarly divided and combined to produce the elevation difference beam $\Delta\sigma$. The transmit beam T σ combining network is uniformly weighted and interconnects all the transmit vertical beamformers. Thus the input to this network is ultimately equally divided among every element in the array. The elevation difference-azimuth difference $\Delta\delta$ beamformer at the bottom of Figure 11a is used for adaptive nulling arrays and not normally provided as an output.

It is apparent that a fully implemented low sidelobe array requires three elevation beamformers and a mode transfer switch at each of P columns and five azimuth beamformers. Together, these produce a total of five beams. The setup in Figure 11a can be used with the array systems in either Figure 2a or 2b since each has three separate outputs. However, the shared beamformer arrangement can also be applied to the azimuth To and Eo channels thereby eliminating an azimuth beamformer and P mode transfer switches at the cutputs of the vertical beamformers.

This simplified arrangement is sketched in Figure 11b. The uniformly weighted shared beamformer is used for both the transmit beam and, together with amplitude adjustment in the modules, the Lo receive beam. With this arrangement, the attenuators in the modules are adjusted to form the elevation distribution. Simultaneously, the azimuth weighting is applied by increasing the attenuation in all modules of a column as a function column position. As before, the weighting for the azimuth difference beamformer must be modified because its inputs will have a Taylor or similar weighting.

3. EXAMPLE

As an example, a 64 \times 64 array is implemented with the shared beamformer idea. The total number of elements M = PQ = 4096. The goals are SLL = -40 dB and -30 dB below the peak for the azimuth and elevation planes respectively.

First, the maximum taper required was obtained from Figure 4 or Eq. (2). This determines the value of A. However, in a rectangular array the azimuth and elevation weights, if both set by the same attenuators, must be combined so that A = -32 dB. The azimuth weights could be applied at the column level with P modules. This would increase η_s but complicate the antenna.

The aperture taper efficiency from Figure 5 or Eq. (6) is $n_{\rm t} = n_{\rm t,0}$ $n_{\rm t,p} = 0.69$. However, the aperture noise supression efficiency can be similarly factored only if the azimuth weights are applied at the column outputs. Then from Figure 10, $n_{\rm S} = n_{\rm SQ}$ $n_{\rm SP} = 0.99$ and 0.98 for L = -6 dB and -9 dB respectivley in each beamformer. When the row and column weights are applied with the same attenuator, Eq. (17) must be rewritten as

$$\eta_{s} = \frac{Q}{2} \frac{P}{A_{qp}} / \frac{Q}{2} \frac{P}{Q=1} = \frac{1}{p=1} + \frac{(1 - A_{qp}L)}{A_{qp}LGF}.$$
 (18)

With F = 3 dB and G = 30 dB, $\eta_S = 0.96$ and 0.87 for L = -12 dB and -18 dB respectively. Thus applying the total taper at the element level results in an additional loss of about 1/2 dB in S/N ratio. For the same value of G, lower sidelobe levels would result in a greater loss.

To select the number of quantization bits, we assume that the total error consists of four equal parts due to the phase quantization, other phase errors, the amplitude quantization, and other amplitude errors. Furthermore, we require SLL_{rms} to be 10 dB below the SLL. From Eq. (3) with SLL_{rms} , B' = 7 or B' = 5 respectively depending on where the taper is applied.

4. DISCUSSION

A significant reduction in the complexity of the feed network of MMIC active aperture arrays is possible when the modules have internal amplitude control. In this case, one beamformer can be shared between the transmit and the receive sum channel thereby eliminating one of the three feed networks normally required. The T/R switch or circulator that transfers the module input from the transmit to the receive manifold is eleminated as well. It is apparent that in a large array, the total savings in feed network components is formidable.

The calculations have shown that for a large range of designs, the component requirements are very realistic. For example, LNA gains and noise figures of 30 dB and 3 - 4 dB respectively are adequate and easily achievable. The attenuator requirements, 2-6 bit and 20-30 db range, are also easily implemented with GaAs MMIC technology.

The shared beamformer is applicable to arrays that do not require conopulse processing as well. In this case the two feed networks for each column are replaced by one. In contrast to this, a sequential lobing (instead of monopulse) array could be implemented with a single beamformer 7.

There are many other aspects of MMIC antenna integration that must be evaluated before the full potential for this new technology can be realized. Some of these are elimination of the circulator now required to isolate scan induced active element impedance variation; improved concepts for energy storage; better solutions for heat removal; techniques for array alignment, calibration, and monitoring; architectures for adaptive nulling; and methods reconfiguration to compensate for failures. As never before, the antenna designer, system analyst, user, and the component developer must work as a team to develop the technology for MMIC active aperture antennas of the future.

Acknowledgement

I would like to thank John Antonucci and Edward Staffier for their indispensable help in completing this report. Mr. Antonucci developed the programs for calculating the Taylor and Bayliss array element weights and the array patterns as well. Mr. Staffier operated the computer and produced the computer generated figures in the report.

I also thank Philipp Blacksmith, Daniel Jacavanco, and especially Dr. Peter Franchi for reading the manuscript and offering suggestions for its improvement.

References

- 1. Hansen, R.C. (1964) Microwave Scanning Antennas, Volume I, Academic Press, New York
- 2. Elliot, Robert S. (1981) Antenna Theory and Design, Prentice-Hall, Englewood Cliffs
- 3. Barton, David K. and Ward, Harold R. (1969) Handbook of Radar Measurement, Prentice-Hall, Englewood-Cliffs
- 4. Haupt, Capt Randy L. (1982) Simultaneous Nulling in the Sum and Difference Fatterns of a Monopulse Antenna, RADC-TR-82-274
- 5. Steinberg, Bernard D. (1976) Principles of Aperture and Array System Design, Wiley, New York
- 6. Carlson, Bruce A. (1975) Communication Systems, 2nd Ed., McGraw-Hill, New York
- 7. Skolnik, Merrill I. (1970) The Radar Handbook, New York

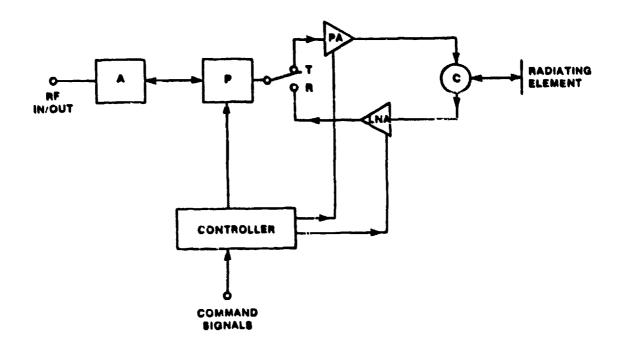
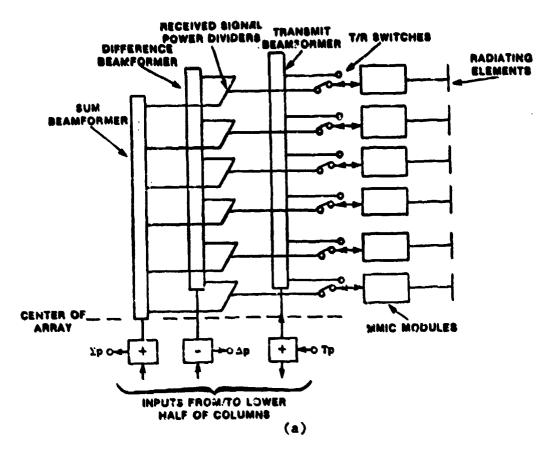
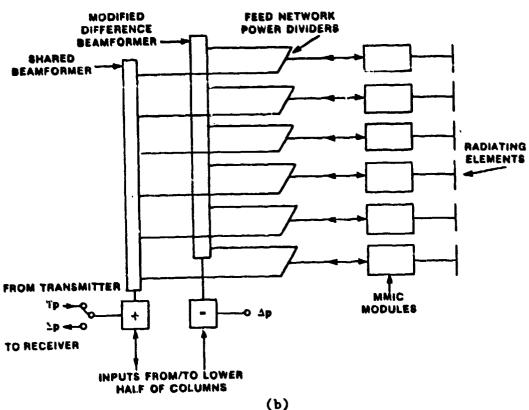


Figure 1. Typical MMIC Transmit/Receive Module





2. Vertical Antenna Networks for Monopulse Radar. (a) Conventional Arrangement and (b) Shared Beamformer Arrangement

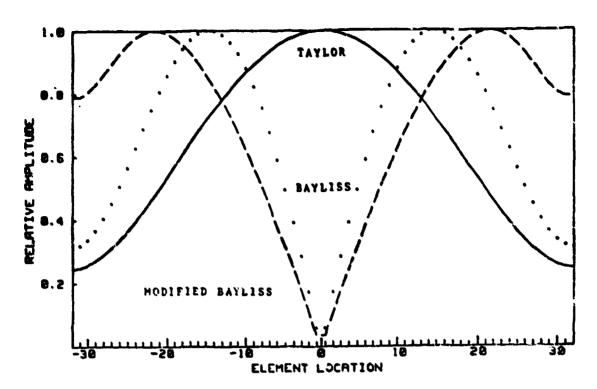


Figure 3. Comparison of Element Weights for Taylor, Bayliss, and Modified Baylist Distributions. $\bar{n}=4$, SLL = -30 dB, and Q = 64

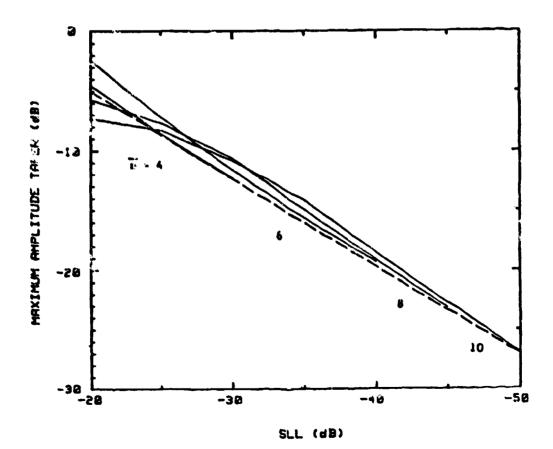


Figure 4. Maximum Element Taper for Linear Taylor Weighted Arrays

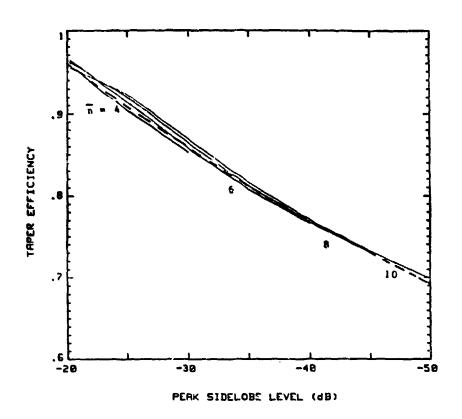


Figure 5. Taper Efficiency for Linear Taylor Weighted Arrays

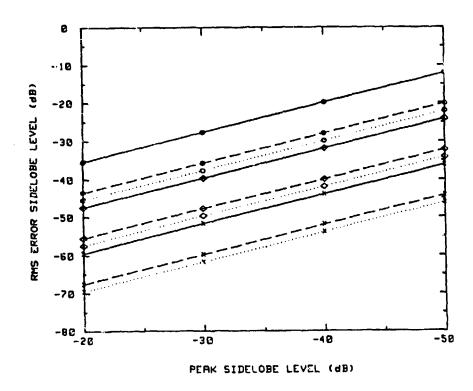


Figure 6. RMS Error Sidelobe Level for Linear Taylor Weighted Arrays

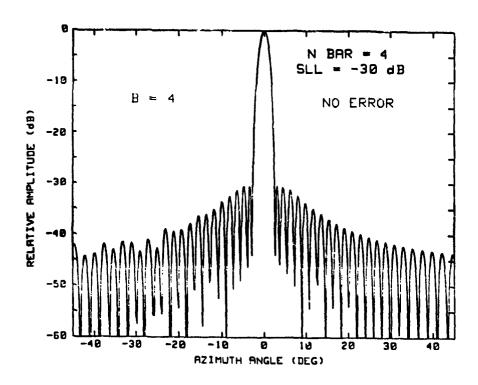


Figure 7. Effect of Amplitude Quantization on Sum Channel Patterns 64 element array with $\,\lambda/2$ spacing

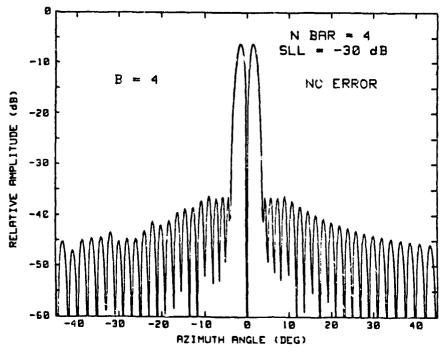


Figure 8. Effect of Amplitude Quantization on Difference Pattern. 64 element array with $\,\lambda/2\,$ spacing

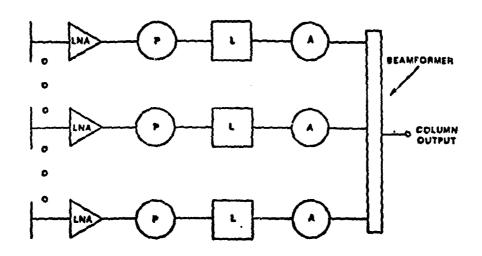


Figure 9. Sketch of Active Aperture Array

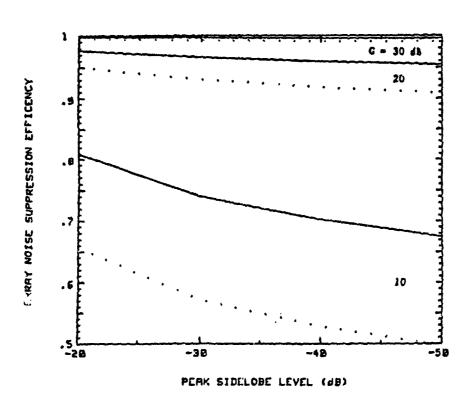
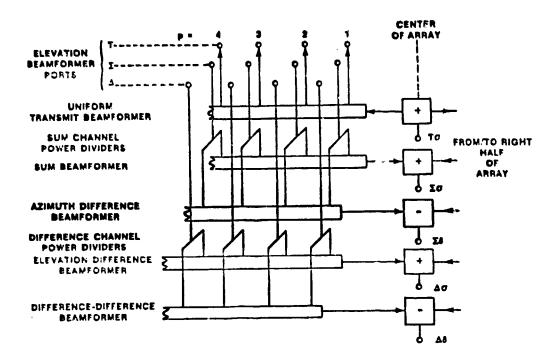


Figure 10. Aperture Noise Suppression Efficiency for Taylor Weighted Array. Q=64, F=3 dB, and spacing is $\lambda/2$. Solid curves L=-9 dB



ELEVATION BEAM PORTS

SHARED P 4 3 2 CENTER OF ARRAY

RIGHT HALF OF ARRAY

SHARED BEAMFORMER

AZIMUTH DIFFERENCE BEAMFORMER

ELEVATION DIFFERENCE BEAMFORMER

(b)

(a)

Figure 11. Azimuth Antenna Networks for Monopulse Radar Array. (a) Conventional Arrangement and (b) Shared Beamformer Arrangement



APS-MORKSHOP ON CHARACTERIZATION
OF MMIC DEVICES FOR ARRAY ANTENNA

EDITED BY

JERRY SMETANA RAJ MITTRA NASA LEWIS RESEARCH CENTER UNIVERSITY OF ILLINOIS

CONTRIBUTING AUTHORS

NICK LAPRADE BRYAN EDWARD AMIR ZAGHLOUL BERNARD GELLER THOMAS APEL RCA, ASTRO ELECTRONICS GE, ELECTRONICS LAB COMSAT LABS COMSAT LABS HAC, MICROWAVE PRODUCTS DIV.

INTRODUCTION

The IEEE AP-S ADCOM is attempting to expand its educational, tutorial and information exchange activities as a further benefit to all members. To this end, ADCOM will be forming specialized workshops on topics of interest to its members.

The first such workshop on *Characterization and Packaging of MMIC Devices for Array Antennas* was conceived. The workshop took place on June 13, 1986 as part of the 1986 International Symposium sponsored by IEEE AP-S and URSI in Philadelphia, PA, June 9-13, 1986. The workshop was formed to foster the interchange of ideas among MMIC device users and to provide a forum to collect and focus information among engineers experienced and interested in the topic.

After brief presentations by the panelists and comments from attendees on several subtopics, the group was divided into working committees. Each committee evaluated and made recommendations on one of the subtopics. Finally, the attendees reconvened to discuss each of the committees' recommendations. The subtopics were:

- 1. Reproducibility and Reliability
- 2. Transitions
- 3. Bias, Control Lines and Thermal Dissipation
- 4. Packaging Concepts
- 5. Characterization

The following sections will present the findings of the workshop attendees.

REPRODUCIBILITY AND RELIABILITY

Recommendations:

1. Standardization

Three items are identified where the implementation of standards should lead to MMIC products of greater reproducibility. First the need for a procurement document extending the methods of MIL STD 883 into the realms of microwave and millimeter wave testing has been identified. Features such as band specific test configurations and fixturing, along with calibration methods, are desirable. The standard procurement document should also revisit the screening and burn-in requirements for lot qualification and acceptance within MIL-STD-883 to assure applicability to MMIC devices of increasing complexity which possibly contain interfaces that include optical, mm wave, and giga-bit rate digital control signals.

Second, a set of standard processing steps, common among foundries, is recommended. The existence of common processing steps for band-specific technologies would lead to a set of specifications which are highly reproducible. Coupled to the first recommendation, a set of standard processing steps, in place throughout the foundry community, would make it possible to apply MMIC devices to high reliability applications without the

costs incurred from repetitively life testing when a specific circuit is procured from multiple sources.

The third point, linked closely to the first two, recommends close cooperation throughout the industry in materials and device testing. By controlling the material entering the MMIC process, and maintaining close agreement on the testing of devices which have completed the process, the MMIC marketplace can be provided with parts which may be purchased in an efficient and agreeable manner.

2. MMIC Application

Three areas where reproducibility and reliability are important beyond the MMIC device processing were identified in the application of these devices. Specifically, high volume applications such as active antenna arrays, were considered. First, the array design which applies MMIC devices should seek to minimize the number of media between the GaAs material and free space. In this way the tolerances associated with each discontinuity, such as substrate-to-substrate, microstrip-to-finline-to-wave-guide, etc., would have minimum impact on the reproducibility of the element design. Second, automated MMIC die attach and bonding techniques should be employed. would serve to diminish the human introduced variabilities in the antenna element manufacturing process. Finally, a much improved set of computer models is required to serve the manufacturing requirements. For example, a revision to current modeling of the spiral inductor has been proposed by Krafcsik and Dawson in their recent (IEEE 1986 MMIC Symposium - MTT-S) paper entitled "A Closed Form Expression For Representing The Distributed Nature of The Spiral Inductor." The present CAD tools are inadequate for MMIC design, let alone the type of tolerance analyses that reproducible wafer processing demands. As the modeling improves the variabilities in lithographic processes can be investigated without the cost incurred from high volume wafer production. This is admittedly a few years away. However, the application of circuit modeling to the manufacturing of both MMIC devices, and the circuit structures into which they are mounted, should be considered in terms of committing to production only those designs which can be demonstrated as inherently reproducible.

3. MMIC Compensation

The third recommendation assumes that MMIC devices in certain applications will always exhibit a degree of variation, unit-to-unit, which will fall outside system constraints. It is recommended that for cases where reproducibility cannot be achieved at a reasonable cost there be provisions within the design made to compensate. Compensation by electronic tuning, by closed loop adjustment of key parameters such as bias, or open loop compensation possibly using digital techniques, are candidates for the applications where an MMIC design can include provisions for external adjustment through automated means. An example of this is a phased-array, where a large number of elements vary in their absolute insertion phase. In this case the design could provide for electronic phase trimming to compensate for the non-reproducible nature of the antenna/MMIC element.

TRANSITIONS

The issue of transitions covers all types of connectivities between MMIC devices and other media in the antenna assembly. Figure 1 shows an example of an MMIC circuit embedded in the feed network of an antenna array. The following are some of the transitions encountered in the assembly of MMIC circuits.

1. MMIC/Waveguide Transitions

The assembly shown in Figure 1 indicates that the transition from MMIC to waveguide is made through an MIC line. Several MIC/waveguide transitions appeared in the literature in the last two decades. Three such transitions are shown in Figures 2, 3,4 and 5. In Figure 2, a ridgeline transformer matches the impedance of the waveguide to that of the microstrip line [1]. The dimensions of the four-step transformer are such that the last step touches the microstrip line. The van Heuven transition [2] shown in Figure 3 orients the MIC vertically inside the waveguide and uses an anti-podal finline transition. Both transitions of Figures 2 and 3 allow transmission in one mode in the waveguide. Another transition which uses a finline structure is shown in Figure 4 where the finline transformer acts as a transition from the waveguide to a slotline [3]. A balun is then used to couple the balanced slotline to the unbalanced microstrip line. In a slightly different configuration, shown in Figure 5, the slotline is coupled directly to the MIC line which is printed on the other side of the substrate and uses the common ground plane of the slotline and finline. The finline transitions have the advantage of supporting two orthogonal polarizations if two transitions are munted perpendicular to each other in a square or circular waveguide as shown in Figure 6.

2. MMIC/MIC STEP

transition from the MMIC circuit to the MIC line is done through a scontinuity step as shown in Figure 7. The lines in the two media are connected via a wire bond. The change in dielectric constant, line width, and substrate thickness creates a discontinuity which has to be characterized.

3. Wire Bonding Steps

As shown in Figure 7 wire bondings, or ribbons are needed to connect the MMIC to MIC lines. Wire bonds are also used to connect two MMIC circuits as indicated in Figure 1. The right length and width of the wire bond or ribbon has to be identified.

4. MIC/Stripline

In some applications striplines are used as the main transmission medium for low loss and light weight. In such cases a transition from the MIC to stripline is required. A sketch of this transition using multiple steps is shown in Figure 8.

5. Packaged MMIC Assembly in MIC Circuits

If the MMIC circuit is available in a packaged form, its connection to the MIC circuit will form another transition. The package may have output leads which are soldered to the MIC lines as shown in Figure 9.

6. MMIC Circuits Fed by Optical Fibers

With the advent of optical fibers as efficient means of transmission, a transition from such fibers to the MIC and MMIC circuits is needed. This one is not fully covered in the literature yet and lends itself mainly to future systems.

7. Reference

- [1] M.V. Schneider et al., "Microwave and Millimeter Wave Hybrid Integrated Circuits for Radio Systems," BSTJ, July-August 1967, pp. 1703-1726.
- [2] J. van Heuven, "A New Integrated Waveguide-Microstrip Transition," <u>IEEE TRANSACTIONS</u>, Vol. MTT-24, March 1976, pp. 144-146.
- [3] B. D. Geller and A. I. Zaghloul, "An MMIC/MIC-to-Waveguide Transition for Single- and Dual-Polarization Systems," 1984 IEEE MTT-S International Microwave Symposium, San Francisco, CA, May 30 June 1, 1984. pp. 412-413.

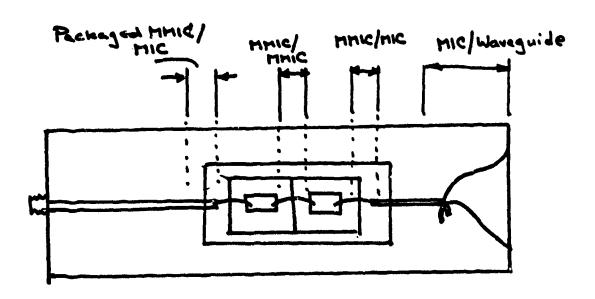


Figure 1 Different Transitions Encountered in a Typical MMIC Assembly

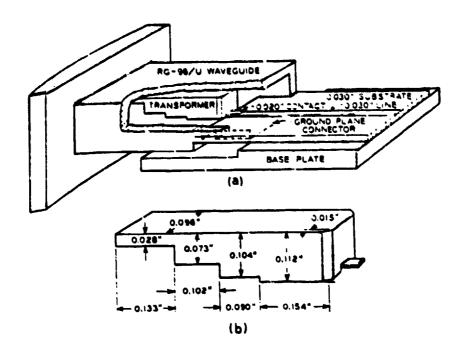
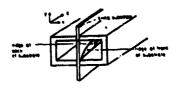
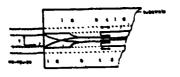


Figure 2 Ridgeline MIC/ Waveguite Transition [1]





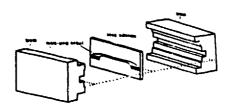


Figure 3 Van Heuven Transition [2]

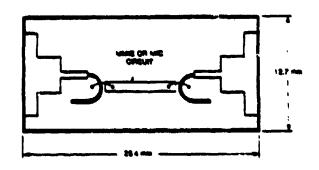


Figure 4 Finline MIC/Waveguide Transition with Balun [3]

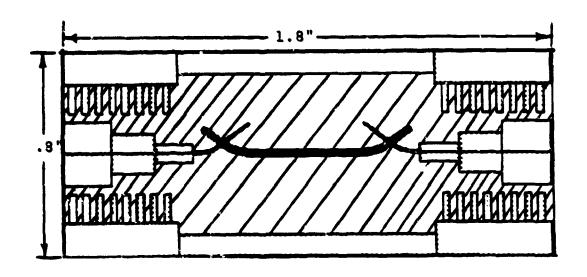


Figure 5 Finline MIC / Waveguide Transition with Slot to MIC Coupling

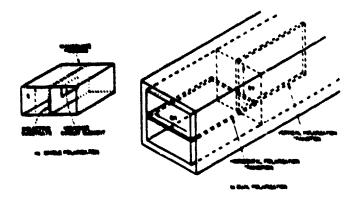


Figure 6 Use of Finline MIC/Waveguide Transition for Single and Dual Polarizations [3]



Figure 7 MMIC/MIC Transition, General Case with Different Dielectric Constants and Different Substrate Thicknesses

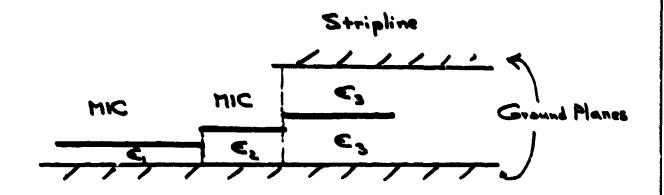


Figure 8 Stepped MIC/Stripline Transition



Figure 9 Packaged MMIC to MIC Transition

BIAS, CONTROL LINES, AND THERMAL DISSIPATION

The objective of this subcommittee was to discuss the issues pertaining to the distribution of prime power (bias), control signals, and the removal of excess heat in large arrays employing active monolithic circuitry at the elemental level. When considering how these systems may be best integrated into the array antenna, it comes to mind that there are at least six systems which may be competing for array volume:

- a. RF Signal Distribution
 - o Transmitter
 - o Receiver
 - o Local Oscillator
- b. RF Calibration Loop
- c. Prime DC Power (Bias) Distribution
- d. Elemental Module Control Signal Distribution
 - o Phase Shifter
 - o Variable Gain
 - o T/R Switching
- e. Heat Removal
- f. Mechanical Support

While some of these systems occur in all arrays, others are unique to active groups.

The prime DC power distribution system must accommodate multiple voltages and sometimes a large amount of total current. To simplify this distribution system, the monolithic circuitry should be designed for operation off common voltages. If these circuits can be operated in "DC series," then the prime power can be distributed at higher voltages and therefore lower total currents. Such a system necessitates monolithic circuit designs with capacitively coupled RF grounds, the ability to stand off high DC voltages, and the fusing to a closed state in the event of failure. An additional issue associated with the prime power distribution system is EMI arising from switching transients.

The complexity of the control signal distribution system is a function of the array performance requirements, the degree of circuit control at the elemental level, and the extent of distributed processing. If a "controller" which determines phase shifter and gain states is incorporated with each elemental module, then the control signal distribution system can be greatly simplified. The use of fiber optics or optical "flood lighting" to distribute control signals can potentially reduce the volume required for this system. With laser diode and detector technology compatible with GaAs MMIC fabrication techniques, we should investigate how these devices may be best combined.

The ability to remove excess heat generated by the monolithic active circuitry may indeed determine the density at which this circuitry may be employed in the array. Within an elemental module, the largest thermal gradients often occur across the GaAs substrate of the active circuitry. If the MMIC devices can be flip-chip mounted, as is done for discrete devices, then heat can be removed much more efficiently from the device channel region. Realizing a good chip carrier to MMIC RF transition with flip-chip mounting may require the circuitry to be designed in formats such as coplanar waveguide.

The volume demands associated with attempting to colocate the systems enumerated above may be alleviated by multiplexing some of the systems. Doing so can also reduce array weight, decrease cost, and even enhance reliability. As an example, in a constrained RF feed system employing stripline, it is feasible to multiplex the RF signal, a serial format control signal, and one prime power voltage on the stripline center conductor. In a waveguide RF feed system, the guide may also be used to conduct excess heat from MMIC devices. In arrays using space—feed for RF signal distribution, control signals may be optically distributed to the elemental modules in a "flood light" fashion.

PACKAGING CONCEPTS

This section summarizes the conclusions and recommendations of the subcommittee on Packaging Concepts at the 1986 AP-S Workshop.

Active element packaging plays a crucial role in the performance, cost, and reliability of array antennas. The "package" considered here may contain individual, hermetically sealed MMIC devices or complete subsystems, such as transmitter or receiver, or even transitions and radiators. The performance is determined, to a large extent, by how well the MMIC circuic/package/array composite is designed and modeled and to what extent interaction between all three levels has been accounted for. The cost aspect may dictate the number of elements in the array or the level of performance to which each element is designed. Reliability enters the picture through appropriate thermal and mechanical design, provision for built-in-test capability, and shielding.

Although MMIC design and processing technology is progessing rapidly, standards for such characteristics as chip thickness, size, DC bias and control, mounting technique, or even transmission medium still do not exist. The immaturity of the technology, therefore, makes it difficult to apply uniform standards to packaging techniques. The Committee, nevertheless, attempted to define the major considerations which should be taken into account in the design of an MMIC package or in the establishment of specifications or standards for MMIC packages.

1. Level of Integration

The MMIC level of integration may range from the basic functional block, such as an amplifier or mixer, to the complete active element on a single GaAs chip. A high level of integration will generally result in better performance and higher reliability because of a reduced number of RF interfaces and bonds, and lower cost (if chip yields can be kept reasonable). In addition, overall

size can be minimized because of reduction in "package overhead" and shared housekeeping functions such as bias, control, and BITE (Built-In Test Equipment). As the level of integration rises, however, care must be taken to assure compatibility of all the circuits which co-habit the package.

2. RF Ports

These can range from the "conventional" microstrip to coplanar waveguide (CPW), finline, twin-strip, or even optical waveguide. Compatibility must obviously be guaranteed between different chips or one would need to resort to interface media, such as coaxial connectors—an undesireable alternative.

Of the above transmission media, finline and twin-strip are considered balanced and have the advantage that they can transition easily to waveguide or dipoles. In addition, they allow operation of power amplifiers in a push-pull mode, which, when coupled with Class B FET operation, has definite advantages in efficiency.

Testing of the packaged circuits by the antenna system integrator will generally require standard package connectors or a standard test fixture into which the package can be dropped. The latter is the more likely scenario since the circuit supplier will need to develop a test fixture as part of his circuit development.

3. Environmental

The issues in this category are mechanical compatibility, ruggedness, thermal conductivity, hermeticity, and chemical compatibility. Mechanical compatibility includes issues such as chip mounting technique (solder, eutectic, epoxy, etc.), package mounting technique (all the above plus mechanical pressure) and thermal expansion compatibility. High thermal conductivity may be required in applications in which significant power is dissipated, such as power amplifiers. This can be achieved by using high thermal conductivity metals, such as copper, aluminum, or various alloys, or ceramics such as beryllia or boron nitride as chip carriers or baseplates.

The final considerations, hermeticity and chemical compatibility, depend on the degree and type of passivation used on the GaAs chip and on the outgassing properties of the materials used in the package.

4. RF Performance

RF performance is determined primarily by the quality of the RF circuit design and processing. The packaging technique will, however, affect performance through RF losses, bandwidth alteration and propagation delay associated with the package, connectors, parasitic reactive element, and feedback effects.

Optimal system performance will be achieved if the RF circuit designed has sufficient information on the factors noted above during the design phase to include them (and compensate for them, if necessary) in the circuit model.

5. Shielding

This area encompasses both ionizing and non-ionizing radiation considerations including radiation hardness, RFI, and electromagnetic pulse effects. Assuming that the proper measures were taken in the design and processing of the MMIC to minimize deleterious effects from these sources, the remainder of the overall system resistance is determined by the packaging technique. Consideration must be given to the choice of materials and their effect on ionizing particles and charge storage in the package. A good RF grounding and bypass technique is essential to both protect the circuit from physical destruction and from interfering with other circuits via the DC bias and control lines.

6. Test Ports

Test ports are required in order to evaluate circuit performance both prior to system integration and during operation. These may be in the form of RF ports which deliver a sample of an RF signal to some monitor point, or in the form of DC or digital signals which contain required information about the state of the system. All the considerations noted above under RF Ports and Shielding apply here. The primary negative effect of the inclusion of test ports into the package is to increase its size and complexity.

In summary, the Committee tried to highlight those major considerations which must be taken into account in the design of MMIC packages for array antennas. The recognition of these areas as potential problems is intended to stimulate better exchange of information between the various disciplines involved in the design of the system and allow the design of RF circuits, packages, and systems which optimize overall performance. The establishment of standards for packages is still premature, but ongoing work in this area will soon lead to "de-facto" standards based on good designs which encorporate most of the above considerations.

CHARACTERIZATION

The techniques available for RF characterization of MM1C devices fall into three general categories: optical, RF probes, and planar fixtures. In order to discuss the relative merits of these techniques, it is first necessary to consider who is doing the characterization, and which needs are driving the activity. On one end of the "pipeline" is the device manufacturer, and on the other is the system manufacturer. In some cases, both may be different profit centers within the same parent organization. It is important to note that their needs and priorities often differ. Consider Figure 1. The device manufacturer clearly is concerned with characterization of wafers and diced chips. He may provide packaged devices to his system customer, but not necessarily. The system manufacturer clearly must test mounted chips. However, he may have received devices in chip form and performed the die-attach himself, but not necessarily. Since mounted chips which are integrated into a system must perform to the full subsystem specification, testing at this level is driven by performance. At the wafer and chip level, the primary consideration is cost. Testing here must be no more than is necessary to assume acceptable yields at the subsystem and system level.

The appropriate chip level tests, after a wafer has been qualified, are DC parameters on a 100% basis, and RF parameters on a sample basis. Appropriate RF data includes scalar parameters such as gain and return loss. However, some applications will require phase information. Traceability to the wafer must be maintained for high reliability applications.

For packaged devices, the full complement of DC and RF tests are necessary. These tests are clearly application driven. Traceability should be maintained here, as well.

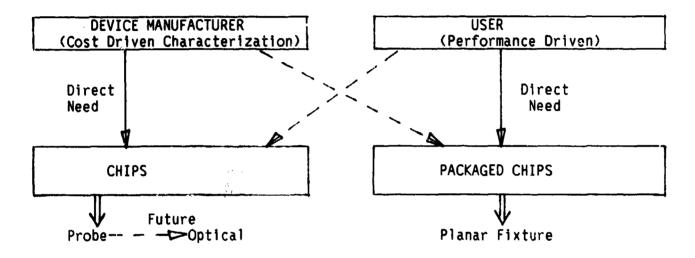


FIG. 1 CHARACTERIZATION NEEDS CAN DIFFER

Chip level RF tests are currently being performed on a nondestructive basis up to 26 GHz with wafer probe techniques. Presently, measurements on chips above 26 GHz is being performed in planar fixtures, which are usually in a waveguide environment. However, chips tested in this way are not re-usable after the test. Furthermore, the assembly is costly and not typically re-usable as a fixture for other chips. Optical sampling techniques are currently being investigated by several groups [Bloom, Stanford University; Hammond, Los Alamos National Laboratory; Marou, University of Rochester]. Potentially, these non-invasive/ non-destructive techniques offer a means of device characterization through 100 GHz.

At the present time, a standardized package approach doesn't exist for devices above Ku band. Typically, millimeter-wave assemblies are constructed on a planar substrate which is permanently mounted in a section of waveguide. Typical transitions from planar media to waveguide include:

- a. E-plane probe with back short,
- b. Tapered fin-line, and
- c. Stepped or tapered ridge guide.

This is the same approach as is being employed in the characterization of individual chips in planar fixtures. If planar fixtures are approached properly, a standardized approach to MMIC packages, above 20 GHz, could

result. That is, the fixture and package are designed together, and the package becomes \underline{part} of the fixture.

In order to discuss the characterization of devices in a standardized package, some attributes of such a package were assumed by the characterization committee. The details of the package approach were left to the package committee. The assumptions are as follows:

- a. Package media allows coplanar interface to chip. Balanced (e.g., CPS or slotline) or unbalanced (e.g., CPW or slabline) options both remain open.
- b. The same coplanar interface can be used to provide interpackage connections where several "packaged" circuits must be interfaced.
- b. The package can be waveguide interfaced or RF probed.

These assumptions are not overly restrictive, since considerable latitude remains in the particular media and interface selection.

The consensus which was reached on RF characterization techniques is as follows:

- a. RF coplanar probing techniques should be employed wherever applicable. The upper frequency limit for these techniques is expected to continue to push upward. Probing allows rapid, repeatable and low cost data acquisition from wafers, chips, and packages. Power device characterization can be obtained by pulse testing with an RF probe.
- b. Fixture tested packages must be designed together with the fixture. A coplanar interface to the chip and fixture must be provided by the package, since discontinuities are thereby minimized.
- c. Integrated optical sampling techniques are expected to play a more significant role in the future characterization of chips, since the chip interface is eliminated.

The criteria which were considered in these recommendations are repeatability, characterization time, cost, thermal path, and post characterization limitations (i.e., is the device usable by the system after test).

CONCLUDING REMARKS

The workshop on "Characterization and Packaging of MMIC Devices for Array Antennas," provided a forum both for exchanging information on the current status of development of MMIC devices and packaging and for identifying the need for future developments. Opinions of the five subcommittees and their recommendations for future developments have been collected and integrated in this report. It is hoped that these summaries and recommendations will be useful to workers engaged in research and development of the various aspects of Monolithic Microwave and Millimeter Wave Integrated Circuits.



APERTURE COUPLED PATCH ANTENNAS AND ARRAYS

Daniel H. Schaubert and David M. Pozar Department of Electrical and Computer Engineering University of Massachusetts elambda(0)/ Amherst, MA 01003

Phased arrays of microstrip patch antennas are being studied extensively for millimeter wave applications, in which the feeds for several elements including the T/R modules might be integrated onto a single GaAs substrate. It is hoped that this integrated method of fabrication will improve performance and reduce the cost per element in large arrays. Many investigators are finding, however, that patch arrays on GaAs do not perform as well as they would on a lower permittivity substrate. Also, the area available in the unit cell (generally (10/2) by (10/2)) is not sufficient to place the radiators and all of the circuit components on a single surface. The aperture coupled patch antenna permits the use of a low & substrate for the antenna, and GaAs for the active circuits. An intervening ground plane isolates the feed network from the radiating face of the afray, and undesirable via connections are not required. This paper describes an eight-element linear array of aperture coupled patches that is designed for E-plane scanning. Element and array performance are discussed. An aperture coupled patch with a perpendicular feed also is described. This arrangement allows the feed circuit to occupy as much depth behind the array as needed. The impedance and radiation patterns of the element are typical of other patch antennas.

1.0 INTRODUCTION

Microstrip antennas have been popular elements for planar and conformal arrays. A traditional means of fabricating these arrays that takes maximum advantage of the economies of printed circuit fabrication involves the layout of radiating elements and a feed network on a single surface of a

(epsilon(n))

grounded substrate. This minimizes the size and weight of the total array and requires the installation of only one coaxial connector to feed the array, thus reducing the cost. However, the microstrip feed network radiates small amounts of power that can degrade the sidelobe and polarization characteristics of the array. Also, the radiators and feed lines occupy much of the available area, leaving little space for the phase shifters that are required for beam steering. Furthermore, for monolithic phase shifters, the substrate must be GaAs, which is not a desirable substrate for the radiators. ¹

Most of these problems can be alleviated by using a two-layer structure that has the radiating elements and their substrate on one side of a ground plane and the feed network and its substrate on the other. In the past, arrays fabricated in this fashion have utilized a via connection probe at each element in order to transfer power from the feed network to the radiators. However, these via connections are increasingly difficult to fabricate as the frequency increases. Also, the use of GaAs as a feed substrate complicates the fabrication.

A useful alternative to the via connection probe is aperture coupling.^{2,3} In this configuration, power is coupled from the microstripline feed to the radiating patch through an electrically small aperture in the ground plane (see Fig. 1). No electrical connection is required and the performance is relatively insensitive to small errors in the alignment of the two circuits. Single elements have performed well at frequencies as high as K_u band.⁴

The objectives of this paper are (i) to present the performance of an 8-element linear array of aperture coupled patches that was designed to demonstrate the use of this type of element in a phased array that utilizes a (simulated) monolithic feed network, and (ii) to present an alternative aperture coupled geometry that offers some potential benefits compared to the original design. The next section describes the 8-element array, presents the performance of various elements in the array and mutual impedance data, and finally shows the overall array perofmance. The third section describes a perpendicular feed geometry and presents some ideas for its use in phased arrays.

2.0 EIGHT-ELEMENT ARRAY OF APERTURE-COUPLED PATCHES

The primary objective of this array is to demonstrate that an array of aperture coupled patches with PTFE substrate for the antennas and high permittivity substrate ($\epsilon_r = 10.2$ to simulate approximately GaAs) for the feed network can be used as an integrated, phase-steered array at EHF. Rather than to operate at EHF where measurements and phase shifting are difficult, a scaled model was built at 5 GHz. Tolerance studies have shown that misalignment of the feed network on the order of 10 % of the patch length by minimal effect on the performance of the antenna elements, so that the scale model should be representative of the results that can be achieved at 20 or 25 GHz. The use of 25-mil Duroid 6010.2 for the feed substrate simular approximately 5-mil GaAs at 25 GHz, and the 60-mil

Duroid 5380 antenna substrate is 0.025 λ_o thick at the operating frequency. The dimensions of the array are given in Figure 2. In a monolithic feed version, phase shifters would be fabricated on GaAs, but the antenna tested here has microstriplines (approximately λ_o long) that connect to the feed network through coax-to-microstripline transitions.

2.1 ELEMENT CHARACTERISTICS

The input impedance, referenced to the center of the coupling slot, of an isolated element is shown in Figure 3. The element is well matched at 5 GHz. The input impedance of a typical element in the array (measured with the other elements terminated in 50 ohms) is shown in Figure 4. The return of loss plots of some of the elements (referenced to the coaxial input connector) are shown in Figure 5, where the worst case return loss at 5 GHz is about 12 dB. Mutual coupling is approximately -20 dB between adjacent elements of the array and drops to -30 dB for center-to-end element coupling (see Table 1).

E-plane radiation patterns of several elements are shown in Figures 6 and 7. The unused elements are terminated in 50 ohms. The expected mirror symmetries are evident, otherwise the patterns exhibit the broad beamwidth and endfire levels of approximately -10 dB that are typical of patch radiators. Some pattern irregularities and scattering behind the ground plane, which was approximately $4\lambda_o \times 2\lambda_o$, are seen, but the patterns are generally good

and should result in useful array patterns over a fairly wide range of scan angles.

2.2 ARRAY CHARACTERISTICS

Radiation patterns of the array were obtained by feeding the elements with equal—amplitude, in—phase signals. This was accomplished by using a commercially available 8-way power divider connected to the array by equal lengths of semi-rigid coaxial cable. The return loss of the array measured at the input to power divider is shown in Figure 8. The VSWR is less than 2:1 over the frequency range 4.9-5.2 GHs. E-plane radiation patterns at four frequencies are shown in Figure 9. The 20-dB front-to-back ratio implies that the slot apertures in the ground plane do not radiate significantly on the feed side. The sidelobes are a little higher than one would expect for a uniform distribution and they exhibit some asymmetries, but the patterns are generally good. It appears that the performance of the aperture coupled patch in small arrays will be about the same as that of the probe-fed patch, but the fabrication may be simpler.

A scan blindness can occur in aperture coupled arrays due to the surface wave on either the antenna substrate or the feed substrate. However, the blindness caused by the low permittivity antenna substrate is very near to endfire. Also, the blindness caused by the GaAs feed substrate occurs at scan angles greater than 80° for thicknesses up to $0.02 \lambda_{\circ}$ and element spacings of

0.5 λ_{σ} . Therefore, scan blindness induced by the GaAs substrate should not limit the scan range of practical antennas at frequencies below 50-80 GHs.

3.0 ARRAY GEOMETRY WITH A PERPENDICULAR FEED SUB-STRATE

Another design that uses separate substrates for the radiating elements and active circuitry is shown in Figure 10. In this case a vertical substrate holding the radiating elements is fed by a number of parallel feed substrates. Coupling is again through apertures in the ground plane of the antenna substrate. This design also allows the use of a low dielectric constant substrate for the radiating elements and a separate semiconductor substrate for the active circuitry, similar to the two-sided geometry, and so has the same advantages in relation to scan blindness/bandwidth performance and shielding of spurious radiation or coupling. In addition, this architecture has a number of other advantages.

First is the fact that the feed substrate can be of virtually unlimited size, since there is not immediate restriction on the "depth" dimension away from the vertical antenna substrate. Waveguide phased arrays usually use this depth dimension to a similar advantage. The geometry also permits a modular construction, where feed modules could conceivably be plugged in to recepticles on the antenna substrate.

This design also allows efficient heat transfer from the ground plane of the feed substrate. At millimeter wave frequencies low device efficiency requires efficient heat transfer from active circuitry. The unobstructed ground plane of the feed substrates allows such heat removal to take place, while the embedded ground plane of the two-sided design makes heat removal more difficult.

Finally, such a geometry would lend itself well to space-fed phased array lens designs, which may be of interst for some applications. This could be implemented by having antenna substrates at both ends of the feed substrates. It does not appear, however, that this geometry would be useful if dual polarization were required.

The array with perpendicular feed substrates depends on the feasibility of feeding a single patch through an aperture with a microstrip line on a perpendicularly oriented substrate. Such a geometry is shown in Figure 11, and has been verified experimentally, but no theory has been developed beyond simple arguments.⁵

Figure 12 shows a Smith chart plot of the measured input impedance of a model at 2.2 GHs. This case used antenna and feed substrates both with $\epsilon_r = 2.55$, but a higher dielectric constant substrate could be used for the feed, as well. Figure 13 shows measured E- and H-plane radiaton patterns for this antenna. Most of the back lobe radiation is due to the use of a small ground plane, and scattering from the connecting cable.

The geometry in Figure 11 shows a direct connection from the feedline to the top of the aperture; the two ground planes are also in electrical contact. Another version of the perpendicularly fed antenna excites the aperture by proximity coupling, eliminating the need for a direct connection of the feedline.

4.0 SUMMARY

Aperture coupled microstrip antennas offer some potential advantages in phased arrays compared to probe-fed and microstripline-fed patches. A linear eight-element, E-plane array of patches using the two-sided approach has been fabricated to demonstrate the use of this technique in small arrays. The array performed well. An alternative configuration that provides more space for feed circuits utilizes a perpendicular feed substrate. Single elements of this type have been fabricated and tested, and arrays could be built.

References

- Posar, D.M. and D.H. Schaubert, "Comparison of Architectures for Monolithic Phased Array Antennas," Microwave Journal 29 (No. 3): 93—104.
- Posar, D.M., "Microstrip Antenna Aperture Coupled to a Microstripline," Electronics Letters, 21:49—50.
- Sullivan, P.L. and D.H. Schaubert, "Analysis of an Aperture Coupled Microstrip Antenna," IEEE Trans. Antennas and Propagation, to appear August 1986.

- 4. Schaubert, D.H., R.W. Jackson and D.M. Posar, "Antenna Elements for Integrated Phased Arrays," Proc. 1985 Antenna Applications Symposium, Univ. of Illinois.
- Buck, A.C. and D.M. Posar, "An Aperture Coupled Microstrip Antenna with a Perpendicular Feed," Electronics Letters 22:125—126.

Table 1. Mutual Coupling in Array

$P_L = 1.78 \text{ cm}$ $\epsilon_r^{ant} = 2.22$ $\epsilon_r^{feed} = 10.2$	$5 ext{ GHz}$ $P_W = 2.54 ext{ cm}$ $d^{ant} = 0.159 ext{ cm}$ $d^{feed} = 0.064 ext{ cm}$	s = 3.0 cm
	$ S_{ij} (dB)$	$\angle S_{ij}(deg)$
S41	-30.7	-79
S ₄₂	-24.8	102
S ₄₃	-21.6	-46
S_{45}	-22.1	-52
S ₄₆	-27.0	103
S ₄₇	-30.3	-110
S40	-31.8	70

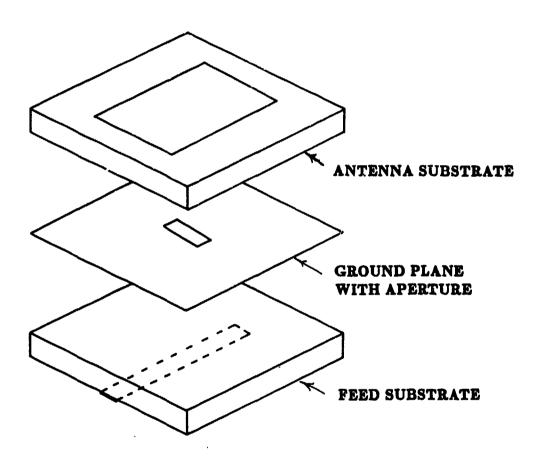


Figure 1. Aperture coupled microstrip patch antenna element.

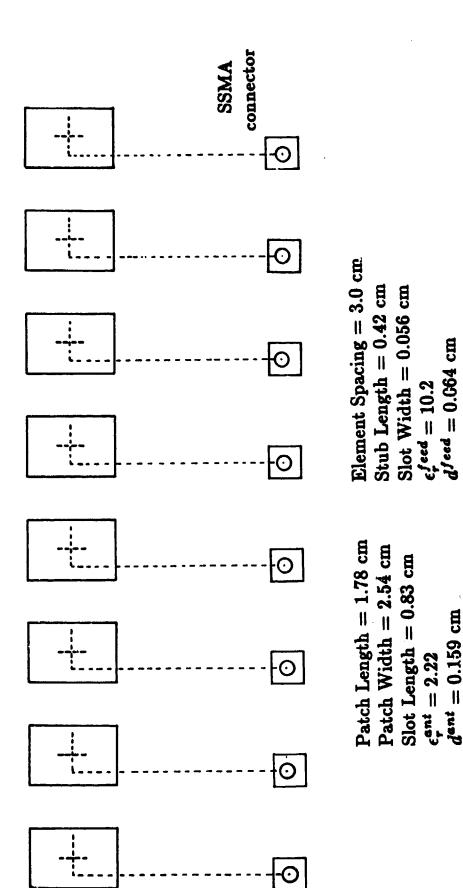


Figure 2. Eight-element, E-plane array.

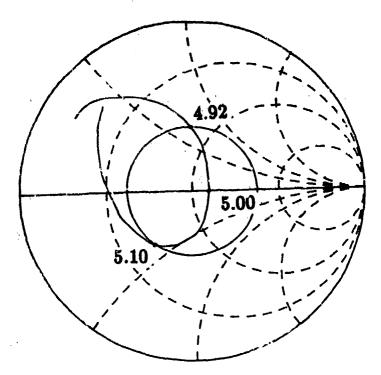


Figure 3. Input impedance of isolated element, 4.5-5.5 GHz. Circle indicates VSWR=2.

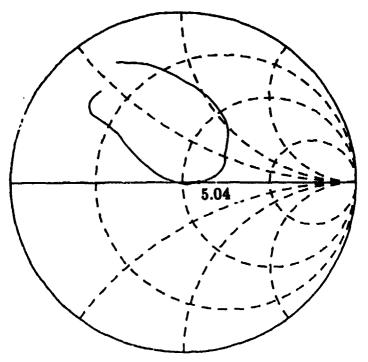
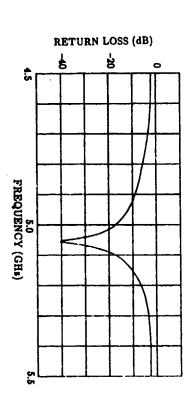


Figure 4. Input impedance of element 6 in the array. Other elements terminated in 50 ohms.

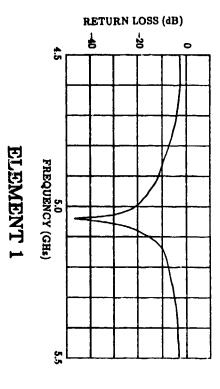


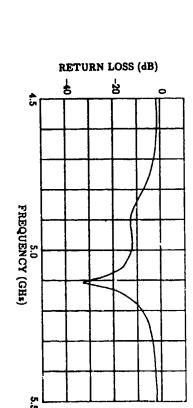
ELEMENT 3

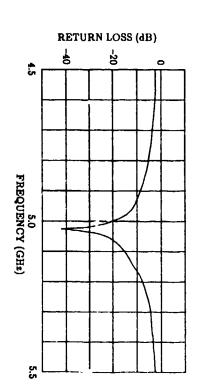
Figure 5.

Return loss of elements 1, 2, 3 and 4 measured at the coaxial connec-

ELEMENT 4



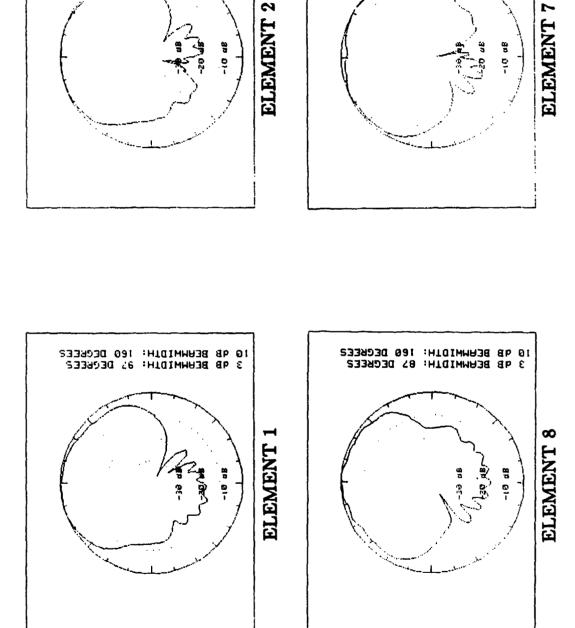




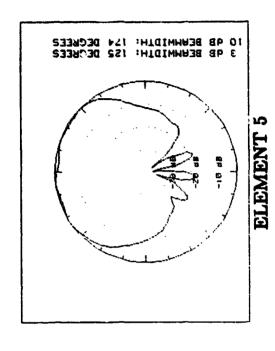
ELEMENT 2

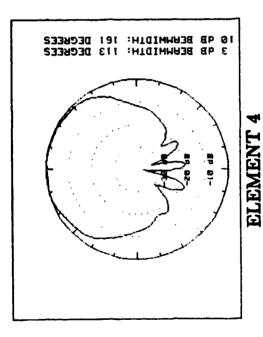
3 AE BEANNIDIN: 133 DEGREES

3 48 BERNMIDTH: 118 DEGREES

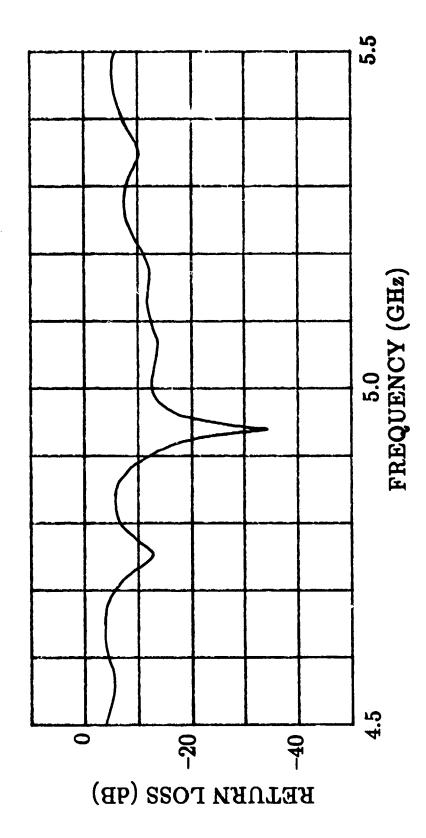


E-plane patterns of end elements in array at 5.0 GHz. Unused elements terminated in 50 ohms. Figure 6.





E-plane patterns of central elements in array at 5.0 GHz. Unused elements terminated in 50 ohms. Figure 7.



Return loss of 8-element array at input to coaxial power divider. Figure 8.

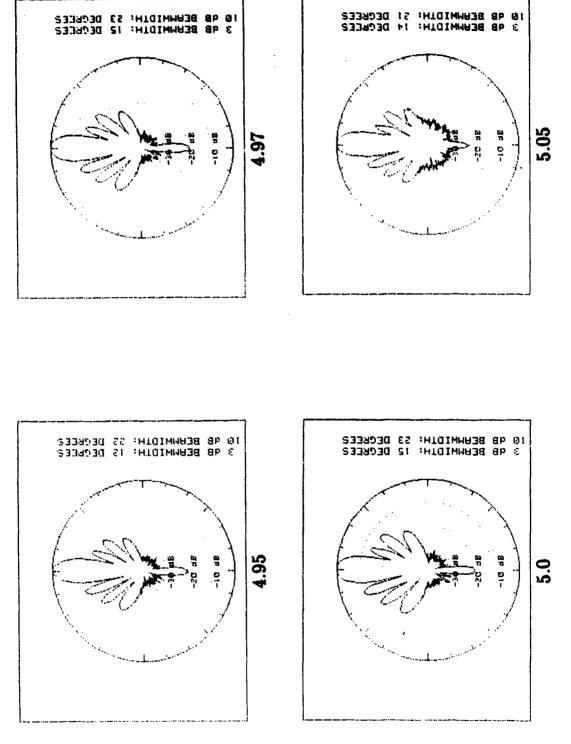


Figure 9. E-plane radiation patterns of 8-element array.

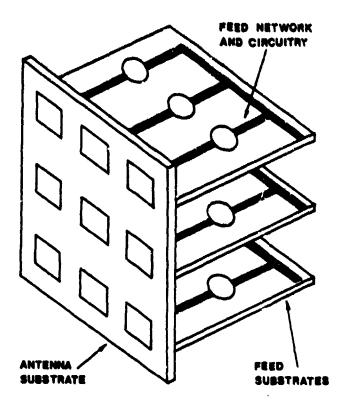


Figure 10. Integrated phased array configuration using feed substrate perpendicular to radiating element substrate.

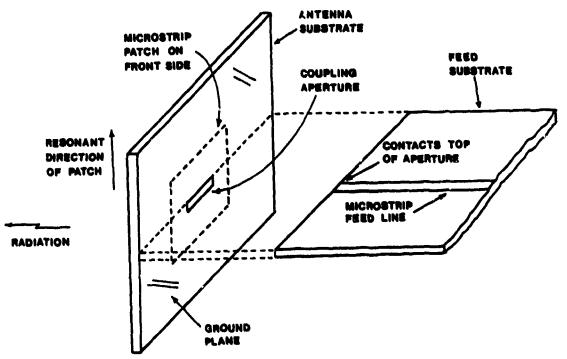


Figure 11. Geometry of isolated microstrip antenna fed through aperture with microstrip line on perpendicularly oriented feed substrate.

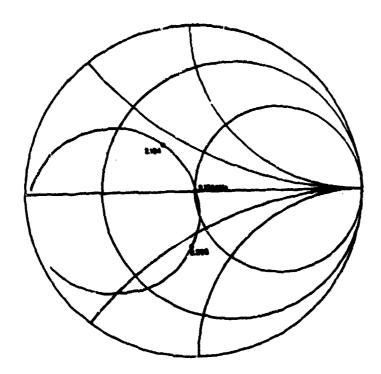


Figure 12. Smith chart plot of measured input impedances of perpendicularly fed microstrip antenna with aperture coupling.

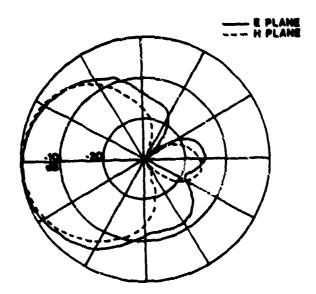


Figure 13. Measured radiation patterns of perpendicularly fed microstrip antenna with aperture coupling.



Phased Array Antenna Pattern Optimization with Failed Elements

B.F. Colline II, 2.H. Lewentowicz, A.J. Terruoli, Jr. Electrical Engineering Department
Air Force Institute of Technology
WPAFB, Ohio 45433

ABSTRACT

This paper discusses several methods of optimizing the pattern of a phased array antenna. Two methods, the gradient search algorithm method and the null displacement technique were shown to be applicable to optimizing a phased array with failed elements. The results of the study show how the pattern can be optimized depending on the scalar cost function and constraints chosen and what effects varying the complex weight of the array elements has on the pattern.

1. INTRODUCTION

1.1 <u>Background</u> - The primary advantage of mounting a phased array antenna on a satellite is the potential of scanning the main beam, reducing the sidelobes or improving the signal to noise ratio by varying the amplitude and phase of the current on each of the elements. The major disadvantage of mounting a phased array antenna on a satellite is that once the system is space-borne, it isn't very maintainable. If for some reason an element no longer performs its designed function, the pattern will generally degrade, i.e., the gain of the array will decrease, the main beam

will widen and the sidelobes will increase. A few element failures can be tolerated, especially if the elements which fail are positioned on the outer edges of the array, but as the failures become excessive, the problem worsens. This paper discusses several methods of compensating for the failed elements of an array by varying the complex weight of the currents on the remaining elements.

- 1.2. Assumptions It is assumed that the exact position of all the working elements are known, the elements are excited with the correct emptitude and phase or not at all and the elements will fail in clusters (due to asteroids or space debris), rows (due to power supply or computer failure) or randomly. Also, the satellite will be at an altitude which requires a \pm 15° scan to cover the area of interest. This assumption will ease the requirement of controlling all the sidelobes and also allow a 0.7 λ interelement spacing, thereby reducing the effects of mutual coupling. Finally the pattern is defined to be optimized if the average power in the sidelobes of interest (\pm 15°) minus the average power in the mainlobe is minimized.
- 1.3 <u>Development</u> The array entenna pattern is optimized by using an optimization algorithm and by using null displacement [1,2]. The optimization algorithm is the most straight forward approach because the rules for optimization can be defined more precisely. However such a program may take too long to converge especially for an array of several thousand elements. The null

displacement technique may be implemented using discrete fourier transforms and therefore may be quicker. Other optimization technique considered include thinned array analysis [3-6], eigenvalue methods [7,8], and adaptive array analysis [4,9]. These techniques either modified variables not applicable to this case (such as element position or phase shifters in nulling trees), or required perturbation of the weights of the failed elements. Also considered was time modulation of each element's current amplitude [10]. This method requires more complex circuitry and weight, frequency modulates a representation of the array pattern and may limit bendwidth.

2. ANALYSIS

- 2.1 Gradient Search Algorithm Given a cost function G(u) with N parameters, the location of the minimum (or maximum) cost is desired. A necessary condition for the minimum is that the gradient of G(u) vanish at the stationary point. Inflection stationary points can be eliminated algorithmically. Although global optimality is not guaranteed, experience and intuition help assure that the minimum reached is optimal. This is especially true for problems where the parameter space is tightly constrained by physical limitations. A maximum-decent gradient-search algorithm is used in locating the optimal cost.
- 2.1.1 <u>Cost Function and Gradients</u> The first step in applying an optimization algorithm is to define the scalar cost function which must be minimized. To find a balance between the

main lobe and side lobes, the cost function chosen is:

or

G(u)=
$$\int_{-Lim}^{Lim} |P(u)|^2 du - (1+s_1) \int_{-Bw}^{|P(u)|^2} |P(u)|^2 du$$

where

$$P(u) = \sum_{i=0}^{N-1} w_i \exp[jkdui],$$

s₁ = scaling factor to increase or decrease the importance of main beam power,

$$Bw = \sin \left(\frac{1}{.7N}\right) * 0.5,$$

 $\lim = \sin(15^{\circ})=0.26$,

$$kd = \frac{2\pi}{\lambda} (0.7\lambda) = 1.4\pi,$$

 $w_1 = a_1 \exp(j\phi_1),$

 $u = \sin \theta$,

and N = number of elements.

After integrating, the cost function becomes:

$$G(u) = \sum_{n=0}^{N-1} \sum_{m=0}^{N-1} w_n w_m^{+} H_{nm}$$
 (1)

where

$$H_{nm} = 2 \text{ Lim Sa(kd(n-m)Lim)}-2(1+s_1)Bw Sa(kd(n-m)Bw).$$

The gradient vector, which is the partial derivative vector of the cost function with respect to the amplitude and phase of the current exciting each element, is:

$$\frac{\partial G}{\partial g_{k}} = \sum_{m=0}^{N-1} 2 a_{m} \cos(\phi_{k} - \phi_{m}) H_{km}$$
 (2a)

and

$$\frac{\partial G}{\partial \phi_K} = \sum_{m=0}^{N-1} -2 a_K a_m \sin(\phi_{K} - \phi_m) H_{Km}. \tag{2b}$$

2.1.2 <u>Search Method</u> - The second step of optimization is to define the method of traveling towards the minimum. The algorithm chosen begins by finding an initial gradient and the point along the initial gradient direction where the dot product of it and the next gradient at that point equals zero. This guarantees the steepest descent. To converge to that point, the step size is iteratively determined by:

new step = old step
$$(1 + 0.9 \cos \alpha)$$
 (3)

where α is the angle between the initial gradient vectors and the next gradient vectors. When new step equals old step, $\alpha=90^\circ$, the dot product of the two gradient vectors equals zero and the next

gradient vector becomes the initial gradient vector.

Theoretically, (3) will converge to the point of interest regardless of the initial step size. However, the step does oscillate around the perpendicular intersection of the two gradient vectors. To minimize the oscillations, the algorithm counts the number of consecutive cycles and chooses a new gradient vectors if the number of cycles become excessive.

2.1.3 Results Using Gradient Search Algorithm

2.1.3.1 Amplitutude Only Perturbations - The optimization algorithm was initially run on a linear array with no failures using amplitude only perturbations. The resulting distribution (fig la) approached the ideal described by Dolph [11]. Figure 2a shows the improved pattern versus the pattern for an array with a uniform distribution. The algorithm was run again for an array with failed elements. The results are shown in figures 1b and figures 2b. It is important to note that each pattern is normalized or

$$|P(u)|_{\text{max}} = 1.$$

This requires the maximum current on the optimized array to be 30% greater than the maximum current on the uniform array. This is an improper condition, for if one element is capable of handling a greater current, then all elements should be equally capable.

After the algorithm was modified to constrain the amplitude of the

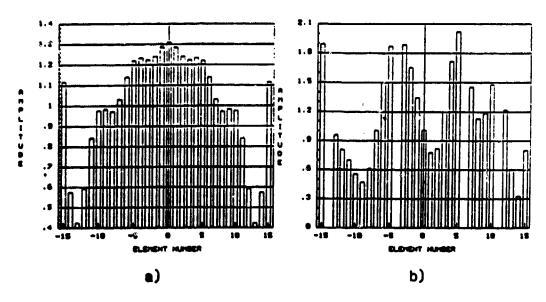


Figure 1. Amplitude distribution of a 31 element array as determined by gradient search algorithm a) without failures; b) with failures

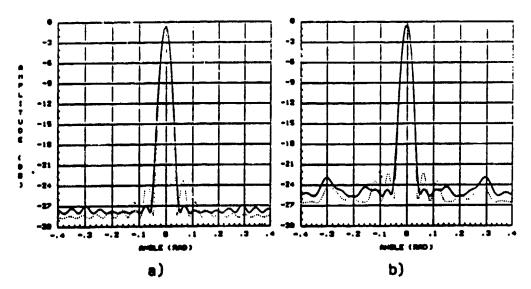


Figure 2. Comparison of normalized array pattern from uniform amplitude distribution (...) vs. gradient search amplitude distribution (....) a) without failures; b) with failures.

current on each element, the tests were repeated. In each case the algorithm stepped up to the constraint boundary - in order to minimize the cost function, all elements should be at their maximum current handling capabilities. Only in the case of limited power should amplitude tapering (as power management) be used.

2.1.3.2 Phase Only Pertubations - Optimizing the antenna pattern using phase only pertubations has been done by Voges and Butler [12] and Shore [13]. Just as in the amplitude only optimization case, phase only optimization is a nun-linear function of the phase parameters. Shore's cost function for phase only optimization is similar to the cost function used in (1). The difference is Shore's work includes the sum of the squared weight perturbations, which will minimize the required phase variations. Equation (1) becomes:

$$G(u) = \sum_{n=0}^{N-1} |w_n - w_{0n}|^2 + s_2 \int_{-0.26} |P(u)|^2 du - (1+s_1) \int_{-\theta w}^{\theta w} |P(u)|^2 du$$

and the phase gradient is:

$$\frac{\partial G}{\partial \phi_k} = 2a_k^2 \sin(\phi_k) - s_2 \sum_{m=0}^{N-1} a_m a_k \sin(\phi_k - \phi_m)$$

where

$$\underline{\mathbf{w}} = [\mathbf{w}_0, \mathbf{w}_1, \dots, \mathbf{w}_{n-1}]^{\mathsf{T}}$$
 (optimized weights),

 $\underline{\mathbf{w}_0} = [\mathbf{w}_{0_0}, \mathbf{w}_{0_1}, \dots \mathbf{w}_{0_{n-1}}]^T$ (original weights),

In all cases; full or partial erray, constrained or unconstrained perturbations, the cost function was optimized when the phase of all the elements equaled zero. The major reason for this is that the area of interest is relatively large and is even-symmetric but phase perturbations cause odd symmetric changes in array patterns. If the area of interest wasn't so large, optimization may occur [IA] using non-zero phase shifts.

2.2 Null Displacement

- 2.2.1 Characteristics of the Z-Transform The roots (zeros) of the z-transform of an array factor can be moved by varying the complex weight of the currents on each element. The zeros, if on the unit circle of the z-plot, represent a null in the antenna pattern. If the zero is not on the unit circle, the pattern will dip at the location of the zero, but will not null (Fig 3). Also, the closer the zeros are to each other, the lower the peak power of the lobe between them. Apparently, the cost function (1) would be minimized if the zero corresponding to nulls beside the main lobe were held constant and all the other zeros were moved into the ± 150 range.
- 2.2.2 <u>Effect of Complex Weight Perturbations</u> To observe the effects the amplitude and phase of the complex weight have on the

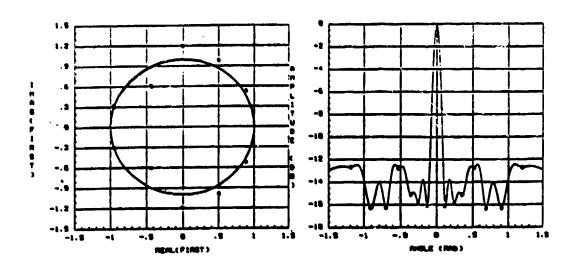
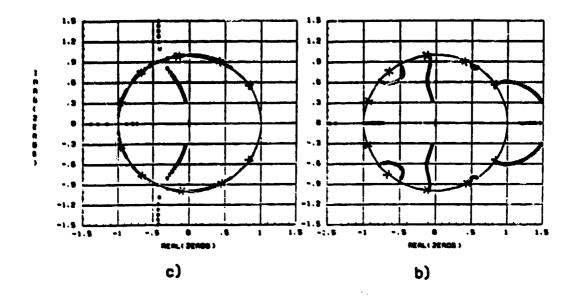


Figure 3. Example of effect of zero placement on array pattern.

zeros, the "root locus" was plotted.

2.2.2.1 <u>Amplitude Perturbation</u> - Figure 4a shows that as the amplitude of the current is increased evenly for a pair of elements, the zeros move towards the z-plot which would result from having only those two elements. As expected, the zeros move in an even fashion. If the current amplitude of a pair of elements is varied oddly, figure 4b results. This shows that the array pattern will be even symmetric but the main lobe will be nulled out. Finally, if the current of only one element is varied (fig 4c) the zeros temporarily travel off the unit circle as the current goes from zero to the value of the other currents, and then head off toward infinity or zero. With all the zeros at the limits, the antenna pattern is that of an isotropic radiator.



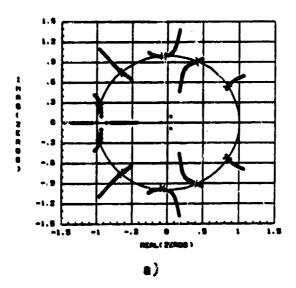


Figure 4. Zero travel due to amplitude perturbations of selected elements of an 11 element array a) even (elements (-3,3)) b) odd (-3,3) c) single (4).

- 2.2.2.2 <u>Phase Perturbations</u> The behavior of the zeros is not as apparent with phase pertubation as it is with amplitude perturbations. From figure 5 these observations can be made:
- 1. The further out the perturbed element is the greater its effect on the main lobe and near in side lobes.
- 2. The pattern created by varying the phase of an element on one side of an array will be the flip side of the pattern created by varying the phase of the opposing element on the other side the of array.
- 3. Zeros from an even and single element phase perturbation are more constrained to a particular angle whereas zeros from an odd phase perturbation are more constrained to the unit circle.
- 4. All zeros travel in the same direction as their complex conjugates. For instance if one zero is moving in the direction of increasing angle, then so is it's complex conjugate (i.e., odd symmetric)
- 5. Zeros traveling due to phase pertubations always travel in loops (in other words, $2\pi = 0$).
- 2.2.3 Modifying the Pattern Gaushell [1] has shown that a desired pattern can be synthesized by first deciding which nulls to move, changing the placement of the zeros and taking the z-transform of the resulting polynomial to find the required complex weight. In other words:

$$\underline{w}_{0} = Z^{-1} \{E(z) H(z)\} \tag{4}$$

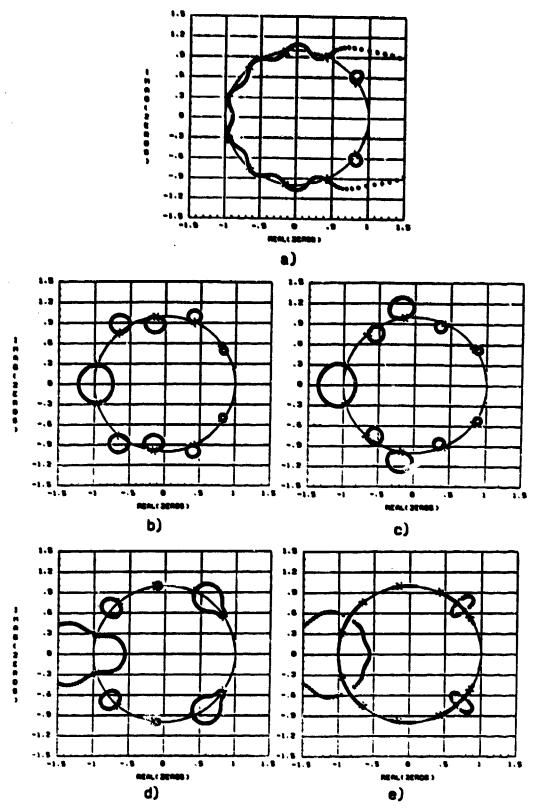


Figure 5. Zero travel due to phase perturbations of selected elements of an 11 element array. a) single (-5); b) single (-1), c) single (1); d) even (-3,3); e) odd (-3.3).

or
$$\underline{w}_{n} = Z^{-1} \{E(z)\} + h(n)$$

where

 $H(z) \leftrightarrow h(n) =$ the original array coefficients and

$$E(z) = \frac{(1-y_1z^{-1})(1-y_2z^{-1})}{(1-z_1z^{-1})(1-z_2z^{-1})}$$

= the ratio of new zero positions (y_i) to old zero positions (z_i) .

The model (4) is only applicable to full arrays. Further study is required to determine the feesibility of comparing the z-plot of a full array to the z-plot of a partial array, including a factor with E(z) to account for the difference and proceeding, as proposed by Gaushell, from there. Equation 4 would then be

$$\underline{w}_{1} = Z^{-1} \{E_{0}(z) E(z) H(z)\},$$

where $E_0(z)$ characterizes the effects of failed elements. This study would determine what complex weights are needed to create the desired pattern.

3. CONCLUSION

Optimizing the pattern of a phased array antenna with failed elements will improve the performance and reliability of the dependent system. Many optimization techniques were considered, including thinned array analysis, adaptive array analysis, time modulation of each element's current amplitude, gradient search,

and null displacement. The former two methods were applied because of their adaptability to periodic, thinned arrays. For the gradient search technique, the cost function to be minimized was defined as the average power of the near in aidelobes minus the average power of the main lobe. Using the gradient search algorithm to find the optimum current amplitude and phase on each claments showed:

- If the total power available is constrained, the amplitude distribution approaches the Dolph-Chebyshev distribution.
- If all elements have the same capacity, and if sufficient total power is available, all elements should be excited at their maximum output.
- 3. The phase of the currents on all the elements should be 0°. For the null displacement technique, varying the amplitude of the current on an element caused the pattern to change in an even fashion and varying the phase of the current on an element caused the pattern to change in an odd fashion. Further study is required to verify an algorithm for displacing the zeros of a periodic thinned, array in such a way as to improve the array pattern.

REFERENCES

- Gaushell, D. "Synthesis of Linear Antenne Arrays Using Z-Transforms," <u>IEEE Trans Antennes Propag.</u>, <u>AP-19</u>: 75-80 (January 1971)
- Davies, D.E.N. "Independent Angular Steering of Each Zero of the Directional Pattern for a Linear Array," <u>IEEE Trans</u>
 Antenna Propag., AP-15: 296-298 (March 1967).
- Skolnik, M.I. "Nonuniform Array," Chapter 6 in <u>Antenna Theory</u>,
 <u>Part I</u>, edited by Collin and Zucker, New York: McGraw Hill,
 1969.
- 4. Steinberg, B.D. <u>Principles of Aperture and Array System</u>
 <u>Design</u>, New York: John Wiley and Sons, Inc., 1976.
- 5. Schjeer Jacobsen, H. and Madsen, K. "Synthesis of Nonuniformly Spaced Arrays using a General Monlinear Minimex Optimization Method," <u>IEEE Trans Antennas Proper</u>., <u>AP-24</u>: 501-506 (July 1976).
- 6. Lo, Y.T. "Random Periodic Arrays, "Radio Sci., 3: 425-436 (May 1968).
- 7. Shore, R.A. <u>Sidelobe Sector Nulling with Minimized Weight</u>

 Perturbations, RADC-TR-85-40, AD A118695 (March 1985)
- 8. Cheng, D.K. "Gain Optimization for Arbitrary Antenna Arrays,"

 IEEE Trans Antenna Propeg., AP-13; 973-974 (November 1965).
- 9. Applebaum, S.P. "Adaptive Arrays," <u>IEEE Trans Antenna Propeq.</u>,
 AP-2A: 585-598 (September 1976).

- 10. Kummar, W.H. et al. "Ultra-Low Sidelobes from Time
 Modulated Arrays," <u>IEEE Trans Antenna Propen</u>., <u>AP-11</u>: 633-639

 (November 1963)
- 11. Dolph, C.L. **A Current Distribution For Broadside Arrays
 which optimizes the Relationship Between Beam Width and
 Side-Lobe level, ** Proceedings of the IRE, 34: 335-348 (June 1946)
- 12. Voges, R.C. and Butler, J.K. "Phase Optimization of Antenna Array Gain with Constrained Amplitude Excitation," <u>IEEE Trans</u>
 Antenna Propag., AP-20: 432-436 (July 1972).
- 13. Shore, R.A. <u>Sidelobe Sector nulling with Minimized Phase</u>

 <u>Perturbations</u>, RADC-TR-85-56, AD A157085 (March 1985)
- 14. Shore, R.A. "Nulling at Symmetric Pattern Locations with Phase Only Weight Control," <u>IEEE Trans Antenna Propag.</u>, <u>AP-32</u>: 530-503 (May 1984).



WIDE-BAND, DOUBLE-TUNED MICROSTRIP ELEMENTS

David R. Tanner and Paul E. Mayes
Electromagnetics Laboratory
Dept. of Electrical and Computer Engineering
University of Illinois
Urbana, Illinois 61801

Abstract-Hicrostrip antennas are popular because of their inherent versatility as low profile multifunctional antennas. Their few disadvantages, however, include a narrow frequency bandwidth for single-mode operation. This has led to the development of dual-band elements for dual-frequency operation. To achieve a continuous bandwidth of operation from elements displaying an inherently resonant behavior, however, requires two or more resonant modes capable of producing similar radiation patterns with a similar quality factor. In addition, the feed system must be capable of exciting these modes in a manner that produces a smooth transition between mode; (without intervening stop bands). This paper describes the realization of an element supporting two such modes whose resonant frequencies can be made as close to one another as desired. In addition the element is completely monolithic and realized without the use of shorting pins or plated-through holes which inherently raise a resonant fraquency and therefore increase the element dimensions in free space wavelengths. The equivalent circuit of the element is derived from a cavity model that includes mode coupling.

1. INTRODUCTION

One of the disadvantages of resonant microstrip antennas is their inherent narrow impedance bandwidth. This disadvantage has led several researchers to explore various ways of increasing the bandwidth. The nonresonant traveling-wave microstrip antennas are not plagued with this problem and are not the concern in this paper.

One obvious approach to increasing bandwidth is to lower the Q-factor of the resonance. For a thin cavity antenna radiating a given power, the resonant electric field and stored electric energy are inversely proportional to the cavity thickness. Thus the half-power bandwidth (1/Q) is roughly proportional to the element thickness. The advantage of this method is that the element structure remains simple. However, microstrip lines can become overly wide to maintain the same impedance level on a thicker substrate. A coaxially fed element suffers from an increase in inductive feed reactance (contribution of higher order modes) proportional to element thickness. Also, a patch element on a substrate of thickness greater than 0.1 dielectric wavelengths has been shown to loose as muc! as 30% of the input power to the dominant TM to z (where z is the substrate normal) surface wave supported by the grounded dielectric substrate [i]. It hardly needs to be said that a thicker element also sacrifices

the conformability that would otherwise be obtained from a thinner one.

Another approach to bandwidth enhancement is by appending a reactive matching network. The most successful of these [2,3] appear to be networks of low order (typically 3 or fewer elements). The Q of the resonant mode places a fundamental limitation [4] on the bandwidth attainable with a matching network. Care must be taken to avoid excessive stored energy in stubs leading to narrower bandwidths and increased losses.

Bandwidth can also be enhanced by the addition of coupled radiating elements. Various combinations of parasitic and driven elements were studied by [5,6]. However, little concern was shown for the difficulty in realizing a stable radiation pattern over the impedance bandwidth. Weakly coupled parasitic elements are more likely perturbed by an array environment and thus fewer approximations can be made in the analysis of arrays. For phased array applications it appears that greater pattern stability will be achieved with fully driven elements.

Dual-band microstrip antennas are another approach to increasing bandwidth. They serve as a good example of a design which takes advantage of the natural mode structure supported by a microstrip antenna.

In the dual-band approach [7] one or three slots were cut in a rectangular patch to lower the (0,3) mode frequency, while a number of shorting pins were used to raise the (0,1) mode frequency. By increasing the slot lengths and number of pins, the ratio of resonant frequencies was varied from 3 to 1.31. Apparently considerable effort was placed in obtaining a lower ratio for continuous-band operation since an alternative method obtaining a ratio of 1.07 was claimed. The alternative method consisted of a microstrip patch reactively loaded on a radiating edge with a wrapped around transmission line. Such reactively loaded elements were studied later [8,9,10] and also exhibited dual-band performance. By loading the patch at an interior point (where feed inductance was smaller) with a shorted stub just under two wavelengths long, the separation in resonant frequencies was reduced to 3.7% of midband frequency [10], corresponding to a ratio of 1.037. However, continuous-band operation was not achieved.

The principle behind reactive loading is simply illustrated by considering the reactance seen at the load port of the patch [8,10]. Looking toward the antenna one sees the parallel resonant mode reactance X_p in series with the feed reactance (due to higher order modes) associated with this port. Thus the parallel resonant mode is effectively loaded by a reactance X_s consisting of the feed reactance in series with the transmission line stub.

Since the two reactances X_g and X_p appear in series, the condition for resonance of the loaded structure is $X_p = -X_g$. If the parallel-resonant frequency (f_p) of the mode reactance (X_p) approximately coincides with the series resonant frequency (f_g) of the effective load reactance (X_g) , then this condition is satisfied at two frequencies, f_- and f_+ , such that $f_- < f_p < f_+$. To bring these frequencies closer together, the slope of X_g with frequency is increased by increasing the stub characteristic impedance and the stub length by additional half wavelengths. While the frequency separation is decreased, apparently the Q's of the loaded modes are increased due to additional stored energy in the longer stub.

This paper describes a new wide-band microstrip antenna for linearly polarized phased array applications. The specific applications in mind are arrays consisting of a single thin layer (typically 0.03 dielectric wavelengths) where bandwidths in excess of 10% are desired. Of course, given the luxury of thicker or multiple layers, additional bandwidth can be expected. Some of the important considerations addressed which distinguish this work are:

 The realization of two modes with nearly identical linear polarizations, radiation patterns and Q-factors, obtained without reactive series resonator loading.

- 2. The resonant frequency ratio of the two modes can be made as close to 1.0 as desired without the use of shorting pins or plated through holes.
- 3. The realization of a feed system allowing a smooth transition between modes without introducing an intervening stop band.
- 4. The impedance properties of the antenna are described by a nearly degenerate cavity model that includes mode coupling through radiation losses.

2. DESCRIPTION OF THE DOUBLE-TUNED ELEMENT

The double-tuned element is a microstrip antenna suitable for linearly polarized phased arrays. It can operate with stable impedance and pattern characteristics over a continuous frequency band that is more than three times that of a single-mode microstrip antenna of the same thickness.

A feature which is fundamental to the antenna performance is the realization of two resonant modes, each capable of radiating a nearly identical linearly-polarized far-field pattern with approximately the same quality factor (Q). With this approach the resonant frequencies (f_- and f_+) of the two modes can be made as

close to one another as desired. To achieve the enhanced bandwidth capabilities, the normalized separation in resonant frequencies is adjusted to approximately satisfy

$$2(f_{+}-f_{-})/(f_{+}+f_{-})\approx B/Q$$
 (1)

where B is a number from about 2 to 3 depending on the desired mismatch.

Assuming that two modes can be found which radiate approximately identical patterns, a cavity model [11] predicts the principal-polarized components of the far-field of each mode are excited approximately in the ratio

Ş١

$$E_{-} / E_{+} = \frac{(f_{+} - f(1 - J/2Q)) A_{-}}{(f_{-} - f(1 - J/2Q)) A_{+}}$$
 (2)

where the scalar products $A_- = \langle J, \bar{Q}_- \rangle$, $A_+ = \langle J, \bar{Q}_+ \rangle$, and J is the exciting vertical current density. \bar{Q}_+ and \bar{Q}_- are mode functions describing the vertical electric field of the two dominant modes in a thin cavity antenna. The mode functions are real and assumed orthonormal with signs such that equal coefficients would imply additive broadside radiation. At midband

frequencies (f = (f₊ + f₋) / 2) the ratio E_- / E_+ should approximately equal $e^{j\theta}$, $0 \le |\theta| \le \pi/2$, in order to achieve an aiding contribution from each mode to the far field. To achieve this relationship, the factors in (2) imply the phase of A_- / A_+ must be an odd multiple of π (i.e. artiphased).

3. FEALIZATION OF MODES WITH SAME POLARIZATION

The search for a structure able to support two linearly polarized modes at the same frequency led to the arrangement of four patches shown in Figure 1. The geometry has four planes of reflection symmetry, is invariant under rotation by multiples of w/2, and is eight-fold degenerate at the (0,1) mode resonant frequency of a square microstrip patch. Such a degenerate structure has eight linearly independent eigenvectors which are nonunique since an arbitrary linear combination of them yields a new (dependent) eigenvector. From the eight dimensional space spanned by eight independent eigenvectors, an orthogonal set of eigenvectors can be found by the Gram-Schmidt process.

The particular set of eigenvectors used here can be designated as an even or odd function of x or y, and further as either azimuthal or radial. The two linearly polarized modes shown in Figure 1 shall be referred to as the even-odd-azimuthal (EOA) and the even-odd-radial (EOR) modes of the four patch

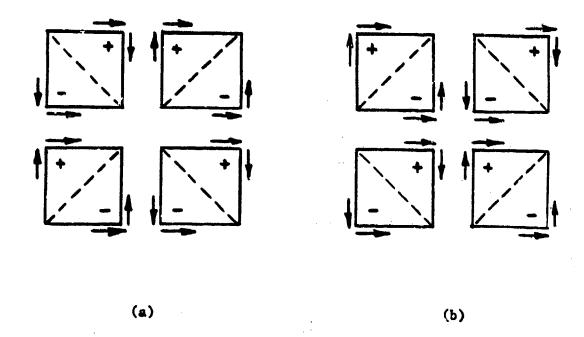


Figure 1. The two vertically polarized modes supported by the four-patch element, (a) azimuthal mode, (b) radial mode. The sign of the rf patch voltage with respect to the ground plane is denoted by + or -. The dashed lines denote a nodal plane (E-wall). The distribution of radiating magnetic currents for each mode is shown by arrows along the patch edges.

element. The azimuthal mode is characterized by a nodal line (E-wall) extending radially through each patch. The radial mode is characterized by a nodal line extending azimuthally through each patch.

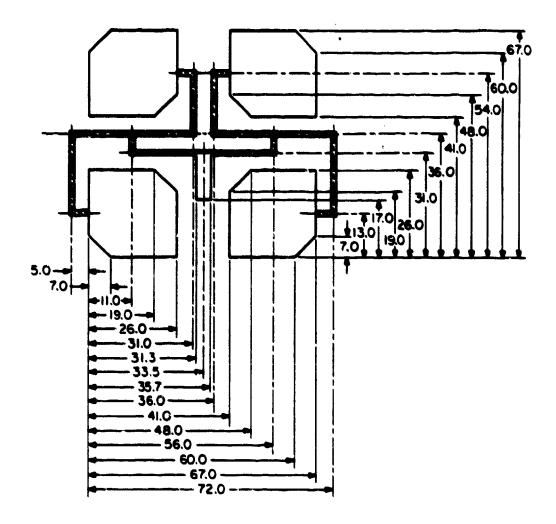
The effective radiating magnetic current associated with each mode is shown with arrows along the patch edges in Figure 1. For both modes it is readily seen that the x-directed currents will produce a broadside far electric field which is linearly polarized in the y direction. Similarly for either mode it is seen that the far-field contribution from the undesired y-directed current cancels in the broadside direction. In fact the contribution from the y-directed current completely cancels in the principal planes which is a characteristic similar to the radiation of the (0,1) mode of a single rectangular patch.

It should be noted that the EOA and EOR modes can be realized with a similar arrangement of four identical patches of a different, but degenerate shape. Examples of alternative structures are, four circular patches arranged in a square, or a single annulus divided into four sectors (each being degenerate).

The degeneracy between the azimuthal and radial modes can then be split in one of several ways to yield the two modes shown in Figure 1 as eigenfunctions associated with different eigenvalues. The degeneracy can be split by trimming the radial or azimuthal corners of the patches to raise the resonant frequency of the radial or azimuthal mode, respectively. Another approach is to cut a small radial or azimuthal slot in the center of each patch to lower the resonant frequency of the azimuthal or radial mode, respectively. The former method is easier to implement. However, the latter method (which lowers a resonant frequency) has the advantage of keeping the element electrically smaller.

4. FEED SYSTEM DESIGN

To maintain excitation symmetry a corporate feed system was chosen to produce four identical excitation currents. Corporate feed systems (based on equal time delay) are known to provide good excitation phase stability with frequency. However, from equation (2) it was shown that an aiding far-field contribution from the two modes at midband is achieved by an excitation current satisfying the requirement that $\langle J, \delta_- \rangle / \langle J, \delta_+ \rangle \approx -1$. Thus the appropriate feed point on each patch is located where the two modes are equal in magnitude but opposite in sign. This theory led to the corporate feed system and first prototype double-tuned element shown in Figure 2.



Notes: Midband frequency is 3.55 Ghz. Substrate is 1/16 inch Rexolite 2200, $\epsilon_{\rm P}$ = 2.62 All dimensions above are in millimeters. All microstrip feedline is 1.2 mm in width (100 Ω), except the input line is as indicated (50 Ω).

Figure 2. A double-tuned modular element with corporate feed system for equal midband excitation of the two linearly polarized modes shown in Figure 1.

5. PROTOTYPE CONSTRUCTION AND TESTING

The first prototype was constructed as four patches (approximately one inch square) on a Rexolite 2200 substrate of 1/16 inch thickness. The substrate thickness was 0.03 dielectric wavelengths at the nominal resonant frequency. The reflection coefficient was measured with an HP8510 network analyzer at the plane of the first T-junction before and after splitting the degeneracy.

According to the theory, very little radiation occurs for the chosen excitation before the degeneracy is split, because the two modes are phased to cancel near broadside yielding a low radiation conductance at the driving point. After the degeneracy is split the cancellation is not complete and the element begins to radiate broadside, thus raising the driving point conductance and giving rise to a "dent" in the S₁₁ locus. Further separation of the two resonant frequencies causes the "dent" to transform to a "cusp" which transforms to a "loop" as the separation is increased. The midpoint of the "loop" corresponds to the highest radiation conductance as seen through the feed system (and feed inductance). The resulting S₁₁ locus and SWR after trimming the radial corners is shown in Figure 3. The locus is characterized by a double-tuned response as shown in the measured SWR. The bandwidth

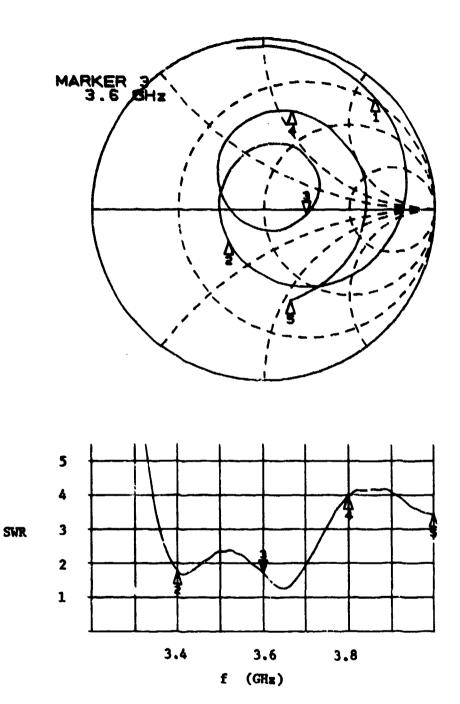


Figure 3. The measured s_{11} locus (above) and SWR (below) of the first prototype element shown in Figure 2. The markers 1-5 denote 0.2 GHs frequency intervals.

(SWR < 3) achieved using double-tuning is about 11 \times (3.36 to 3.74 GHz) at 3.5 GHz.

The pattern stability achieved is indicated by the measured patterns at frequencies 3.4, 3.5, 3.6 and 3.7 GHz. Figures 4 and 5 show the measured patterns in the H-plane (β = 0) and E-plane (β = 1/2) for 0 and β components of electric field in a spherical coordinate system.

6. PATTERN ANALYSIS AND EQUIVALENT CIRCUIT

The radiation pattern for each mode can be derived from the Fourier transform of the aperture magnetic current distribution. Since the two modes are defined as linear combinations of (0,1) and (1,0) modes in each patch, the transform can be expressed as the sum of the transforms of the (0,1) and (1,0) mode current each weighted by appropriate array factors. Thus the current transform of the azimuthal and radial modes can be written as

$$\vec{E}_A = 2 \cos(ud) \cos(vd) \vec{E}_{01} + 2 \sin(ud) \sin(vd) \vec{E}_{10}$$
 (3)

$$\mathbf{R}_{\mathbf{R}} = 2 \cos(\mathbf{ud}) \cos(\mathbf{vd}) \mathbf{R}_{01} - 2 \sin(\mathbf{ud}) \sin(\mathbf{vd}) \mathbf{R}_{10}$$
 (4)

where $u=k\sin\theta\cos\phi$ and $v=k\sin\theta\sin\phi$ are the transform variables, 2d is the patch spacing, and k_{01} and k_{10} are the transforms of the magnetic currents for a single square patch.

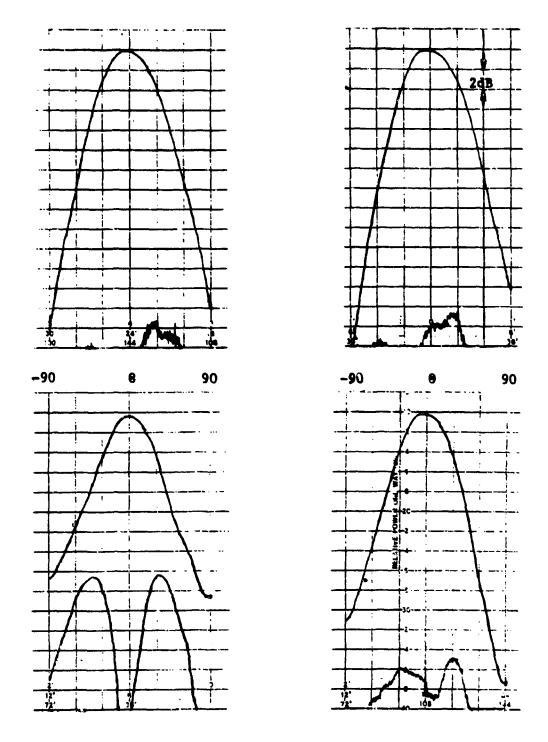


Figure 4. The measured E-plane (upper figures) and H-plane (lower figures) elevation patterns at 3.4 GHz (left figures) and 3.5 GHz (right figures). Principal polarization and cross polarization are shown in each case.

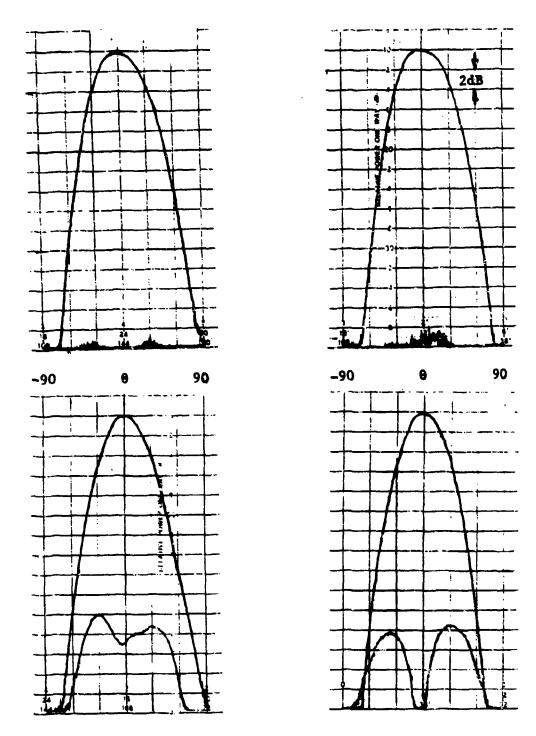
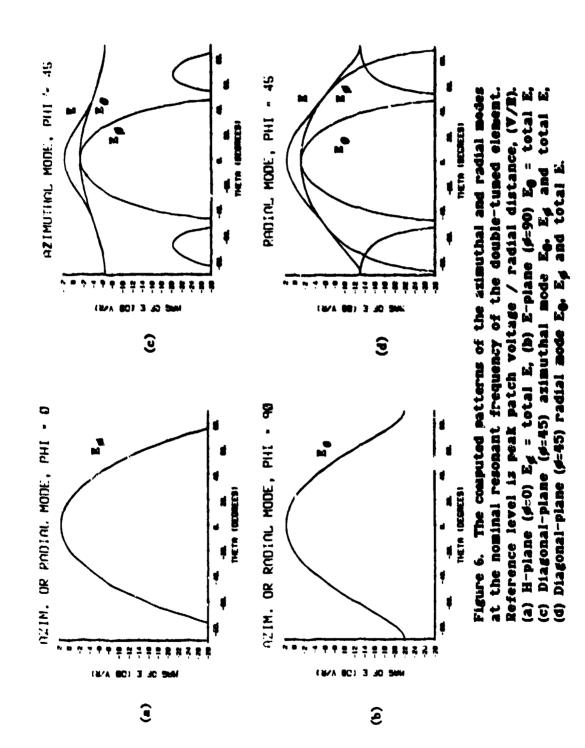


Figure 5. The measured E-plane (upper figures) and H-plane (lower figures) elevation patterns at 3.6 GHz (left figures) and 3.7 GHz (right figures). Principal polarization and cross polarization are shown in each case.

Equations (3) and (4) readily show that the two modes have identical patterns in the principal planes. Also, if cross-polarized radiation is defined as that polarization radiated by the (1,0) mode, then such radiation is confined near the diagonal planes at angles far from broadside. Over midband frequencies the sum of the azimuthal and radial modes furtizer suppresses the contribution from the (1,0) modes. To better understand the antenna behavior, the radiation patterns at the nominal resonant frequency are shown for each mode in the H-, E- and diagonal planes in Figure 6.

Further analysis of the antenna in the vicinity of a near degeneracy shows that the idealized asimuthal and radial modes of a lossless cavity model are strongly coupled by exterior radiation (losses). This phenomenon is a familiar effect in the theory of waveguides and cavities which have wall losses, but would otherwise be degenerate if lossless [12]. The effect is that the lossless modes are coupled by the wall losses, resulting in lossy modes which are no longer degenerate. In the double-tuned antenna considered here, the degeneracy has deliberately been split. However, the modes are still coupled due to substantial mutual coupling loss. Thus the radiation loss can be represented by a positive definite radiation conductance matrix G and its associated quadratic form in terms of mode voltages. The stored energy is also represented by a quadratic form which is



approximately diagonal if the exterior stored energy is much less than the internal, and the lossless modes are orthogonal. The mode-coupled cavity model shown in Figure 7 is derived in a manner analogous to the usual cavity model [ii]. The new model removes the strong dependence of the mode conductance on frequency that occurs if the usual cavity model is applied to a nearly degenerate case. The ideal transformers are introduced to remove the dependence of the mode capacitance and inductance on the feed point location. In absence of mode coupling the new model becomes identical to the usual model. It is of interest to note that the nearly square patch often used for circular polarization is an example of a cavity where the nearly degenerate (0,i) and (1,0) modes are not coupled by either wall losses or radiation.

The reactive circuit elements in Figure 7 can be computed in the usual manner [!1,13]. The radiation conductance matrix is computed from far-field integration of the Poynting vector for an arbitrary set of mode voltages (coefficients). The computed Q-factors due to radiation loss are 39 and 48 for the azimuthal and radial mode, respectively. For comparison, the Q of a single square patch supporting the (0,1) mode is 42. Thus it appears that the Q's of the two modes are not exactly alike as hoped, but are not significantly higher than that of a single square patch. Also, the mutual conductance G_{AR} contributes additional loss not accounted for in the individual mode Q's. This additional loss

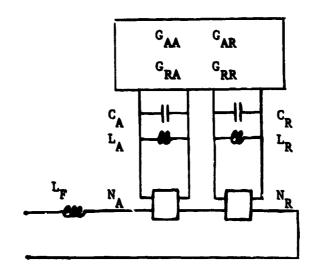


Figure 7. The driving point equivalent circuit for the double-tuned element with azimuthal and radial mode coupling (corporate feed system not shown).

accounts for more bandwidth than would be estimated from the Q's alone.

7. CONCLUSIONS AND FUTURE WORK

The theory for a double-tuned continuous-band antenna was presented based on a cavity model with mode coupling due to radiation. An approach to the realization of two modes which radiate nearly identical polarization over a broadside pattern was demonstrated. Rather than beginning with two desired modes and attempting to force their resonant frequencies together, the approach began with a degenerate structure of sufficient degree such that two desired modes would remain after appropriately splitting the degeneracy. The two modes were excited using a corporate feed system designed to satisfy the "phase condition" for continuous-band operation. For additive far-field contributions of the two modes at midband, the feed points are located where the mode functions are about equal in magnitude, but opposite in sign. This result suggests that had the feed point been otherwise located in the dual-band elements described by Wang and Lo [7] and also by Richards, Davidson and Long [10], radiation could be possible at frequencies between two closely spaced resonances.

Also, it is believed that the mode-coupled cavity model could explain other phenomenon that are observed in a microstrip cavity. For instance, when the dominant mode is not strongly excited by a particular feed arrangement, the new model predicts that the dominant mode could also be excited indirectly through mode coupling. Heglecting the coupling in this case is expected to cause some error in the computation of radiated power and input conductance. Subsequent investigation shows that the (0,1) and (even,odd) modes of a rectangular patch exhibit such coupling.

8. ACKNOWLEDGEMENT

The authors would like to express their gratitude to the RCA Government and Commercial Systems, Missile and Surface Radar Division, Moorestown, NJ for funding this research.

REFERENCES

- Davidovits, M. and Lo, Y. T. (1956) Input impedance of a probe-fed circular microstrip antenna with thick substrate, <u>IEEE Trans. on Antennas and Propagation</u> 34 (No. 7):905-911.
- Paschen, D. A. (1983) Broadband microstrip matching techniques, <u>Froc. of the Antenna Application Symp.</u> Paper presented at Robert Allerton Park, University of Illinois, Urbana IL.
- 3. Mayes, P., Tanner, D., Waller, R., Drewniak, J., Smurlo, T., Boris, A. and Kunkee, D. (1985) Some broadband, low-profile antennas, <u>Proc. of the Antenna Applications Symp.</u> Paper presented at Robert Allerton Park, University of Illinois, Urbana IL.
- 1. Matthaei, G. L., Young, L. and Jones, E. M. T. (1964)

 Microwave filters, impedance-matching networks, and coupling

 structures, McGraw-Hill Book Co., New York.
- Kumar, G. and Gupta, K. C. (1984) Broad-band microstrip antennas using additional resonators gap-coupled to the radiating edges, <u>IEEE Trans. Antennas and Propagation</u> 32 (No. 12):1375-1379.
- 6. Kumar, G. and Gupta, K. C. (1985) Directly coupled multiple resonator wide-band microstrip antennas, IEEE Trans. Antennas and Propagation 33 (No. 6):588-593.

- 7. Wang, B. F. and Lo, Y. T. (1984) Microstrip antennas for dual-frequency operation, <u>IEES Trans. Antennas and Propagation</u> 32 (No. 9):936-943.
- 8. Richards, W. F. and Lo, Y. T. (1984) A simple theory for reactively loaded microstrip antennas, <u>IEEE Antennas and Propagation Soc. Symp. Dig.</u> pp. 259-262, Paper presented in Boston, MA.
- 9. Richards, W. F. and Long, S. A. (1984) An experimental investigation of loaded microstrip antennas, <u>IEEE Antennas</u> and <u>Propagation Soc. Symp. Dig. pp. 263-266</u>, Paper presented in Boston, MA.
- 10. Richards, W. F., Davidson, S. E. and Long, S. A. (1985)

 Dual-band reactively loaded microstrip antenna, <u>IEEE Trans.</u>

 <u>Antennas and Propagation</u> 33 (No. 5):556-561.
- 11. Richards, W. F., Lo, Y. T. and Harrison, D. D. (1981) An improved theory for microstrip antennas and applications, IEEE Trans. Antennas and Propagation 29 (No. 1):38-46.
- 12. Gustincic, J. J. (1963) A general power loss method for attenuation of cavities and waveguides, <u>IEEE Trans. Microwave Theory and Techniques</u> 11 (No. 1):83-87.
- 13. Richards, W. F. and Lo, Y. T. (1983) Theoretical and experimental investigation of a microstrip radiator with multiple lumped linear loads, <u>Electromagnetics</u> 4 (No. 3-4):371-385.



PRACTICAL EXAMPLES OF INTEGRAL BROADDAND MATCHING OF MICROSTRIP ANTENNA ELEMENTS

D. A. Paschen
Ball Aerospace Systems Division
Boulder, CO 80306

ABSTRACT

A general discussion of techniques for enhancing the bandwidth of microstrip antenna elements was presented at this symposium in 1983. Since that time many forms of broader bandwidth microstrip antenna elements have been fabricated at Ball Aerospace Systems Division (BASD). The purpose of this paper is to discuss those types of microstrip elements which have been broadbanded through the use of an integral matching network. The integral network is part of the actual element and this eliminates the requirement for additional printed circuit or lumped element matching networks. This simplified form of wide bandwidth microstrip element is currently finding use in moderate bandwidth arrays being built at BASD.

1.0 INTRODUCTION

The demand for elements in the L-Band frequency range which cover both of the Global Position Satellite (GPS) frequencies L1 (1575 MHZ) and L2 (1227 MHZ) is extensive. The additional requirement for coverage of the NDS frequency L3 (1381 MHZ)

would require an element bandwidth of approximately 25%. Microstrip elements have many benefits which would make them attractive for use in these medium bandwidth applications; however, the operating bandwidth has typically been much less than the required 25%. It is the purpose of this paper to describe a technique which will extend the bandwidth of microstrip elements to 30% and beyond. The technique and the modifications can be built into the element feed so that no external matching circuit layers or components are required.

2.0 DESIGN TECHNIQUE

A simple model for a thick microstrip patch is shown in Figure 1. The inductance L_2 is caused by the length of probe required to feed the patch. The model is closely related to a two stage bandpass figure as shown in Figure 2. The simple addition of a series capacitor would allow the inductance L_2 to be resonated at the center frequency. If L_2 can be varied, the series resonant combination can be made to optimally enhance the bandwidth of the basic patch which is fixed for a given thickness and dielectric constant. The input impedance of a typical thick microstrip patch based on the model is shown in Figure 3. The point P_1 is actually the center frequency of the parallel tank circuit. The value of the R_L in the model is 90 ohms by inspection, and the value of L_2 can be found easily by

$$V_{ij} = 60/\omega_0 \text{ H} \tag{1}$$

where ω_0 is the radian frequency at point P_1 . Since the microstrip

patch has a built-in impedance transformer, resistance R_L can be varied by the position of the probe. The 1.8:1 VSWR bandwidth of this patch, when optimized, will be between the two radian frequencies ω_1 and ω_2 which are also determined by inspection. The curves in Figures 4 and 5 are useful in finding the optimal component values L_2 and L_2 for the two stage filter model. The curve in Figure 4 shows that a 1.8:1 VSWR (0.35 db loss) gives a N=2 decrement of 0.65. Figure 5 gives the following values:

$$g_1 = 1.50$$

 $g_2 = 0.46$
 $g_3 = 1.80$

The following equations are then used.

$$c_1 = \frac{g_1}{R_1 (\omega_2 - \omega_1)}$$
 (2)

$$L_1 = \frac{1}{\omega_0^2 c_1} \tag{3}$$

$$L_2 = \frac{g_2 R_L}{\omega_2 - \omega_1} \tag{4}$$

$$c_2 = \frac{1}{\omega_0^2 L_2} \tag{5}$$

$$R_{IN} = R_L/g_3 \tag{6}$$

The calculated value of R_{IN} is 50 ohms as would be expected. L_1 and C_1 give the component values for the patch model, and L_2 and C_2 give

the optimal values for the matching circuit. Figure 6 shows the patch input impedance from the model in Figure 1 with the inductance L_2 removed. Figure 7 shows the input impedance of the optimally broadbanded patch based on the model in Figure 2.

The comparison between the actual value of L_2 and the desired value of L_2 will show whether the probe inductance from direct feeding as shown in Figure 8 needs to be increased or decreased. The inductance can be decreased by making the probe diameter increase, and the inductance can be increased by making the probe diameter smaller or by coiling if large increases are required as shown in Figure 9.

The capacitor C₂ can also be implemented as part of the feed by capacitively coupling to the actual path. Figure 10 shows parallel-plate and cylindrical forms. Other possibilities include annular rings etched into the attachment point in the element, various other etched capacitors, or various other mechanical forms of capacitive coupling between the element and the feed probe.

An element was designed using the technique described above for use over the two GPS bands L1 and L2 and the NDS band L3 and is shown in Figures 11 and 12. The element is currently in use on an electronically switched spherical array (ESSA) antenna system³ designed to produce six independent beams. The actual input impedance of this element is shown in Figure 13 for a single port of the dual probe circularly polarized element; the coupler which provides the orthogonal power division is normally built into the

element but was removed for this measurement. Linear E-plane radiation patterns for the three bands are shown in Figures 14 through 16 and the peak gain has been increased considerably at the band edges over an unmatched version. The squinting of the main beam is one limitation of this technique although compensation is possible in most arrays.

3.0 CONCLUSION

The broadband matching technique described was used in the design of the L-band element for use in a multibeam ESSA antenna system. The 1.8:1 VSWR bandwidth was 25%, and 2:1 VSWR bandwidth was greater than 28%. The matching network was integral to the feed of the element so that no additional layers of circuitry were required for broadbanding. In addition, the radiation properties were reasonable over the bandwidth of operation.

4.0 REFERENCES

- Paschen, D.A., "Broadband Microstrip Matching Techniques",
 1983 Antenna Application Symposium, Allerton, IL.
- 2. Matthaei, G. L., Young, L. and Jones, E. M. T., (1964)

 <u>Microwave Filters, Impedance-Matching Network and Coupling</u>

 Structures, McGraw-Hill, New York, pp. 123, 127.
- 3. Taylor, T. H. Jr., "Electronically Sterrable Spherical
 Array Provides Multiple Beam Coverage of a Hemisphere", 1982
 Antenna Applications Symposium, Allerton, IL.

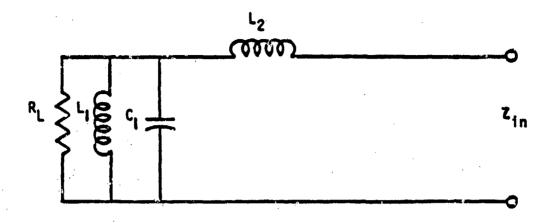


Figure 1. Microstrip Patch Model

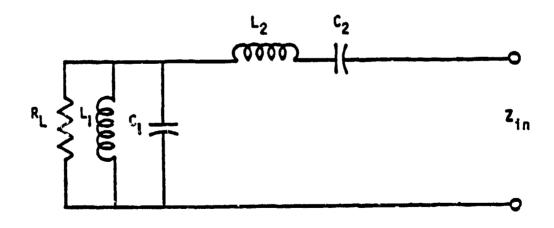


Figure 2. Bandpass Filter (N = 2)

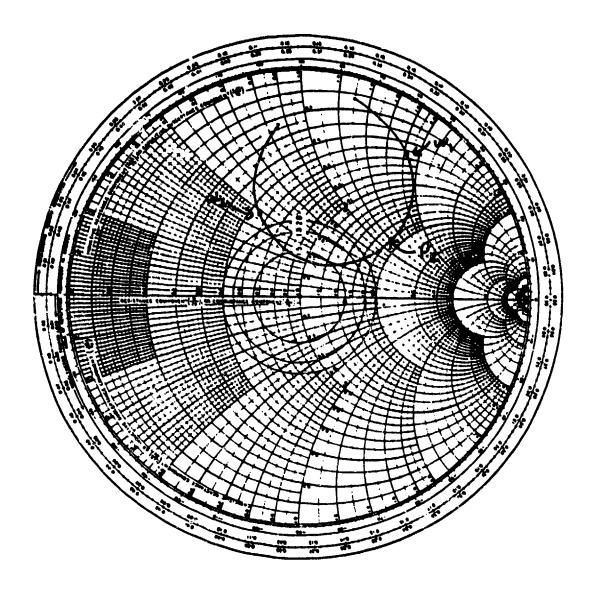


Figure 3. Typical Input Impedance of Thick Patch

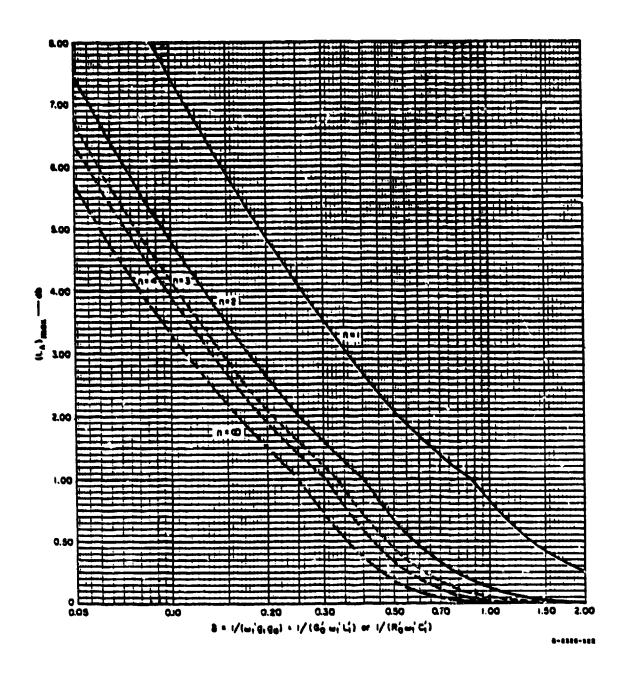


Figure 4. Maximum Insertion Loss Versus Decrement (1)

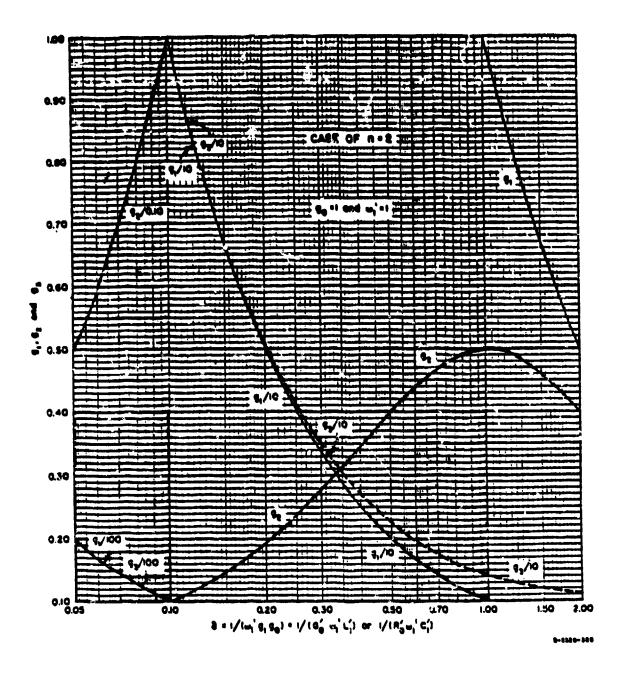


Figure 5. Element Values Versus δ for N = $2^{(1)}$

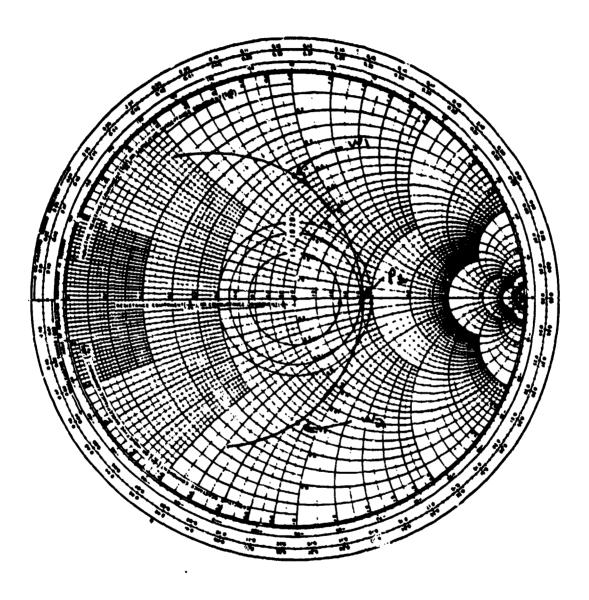


Figure 6. Patch Impedance Without Probe Inductance

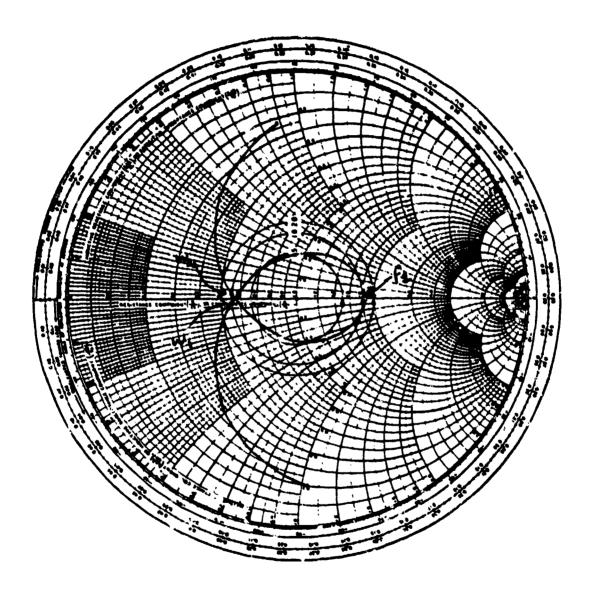


Figure 7. Input of Impedance of Broadbanded Patch

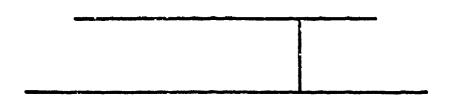


Figure 8. Direct Fed Patch

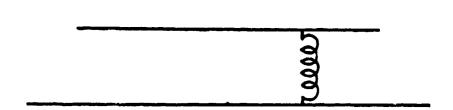


Figure 9. Increased Inductance

Parallel - Plate

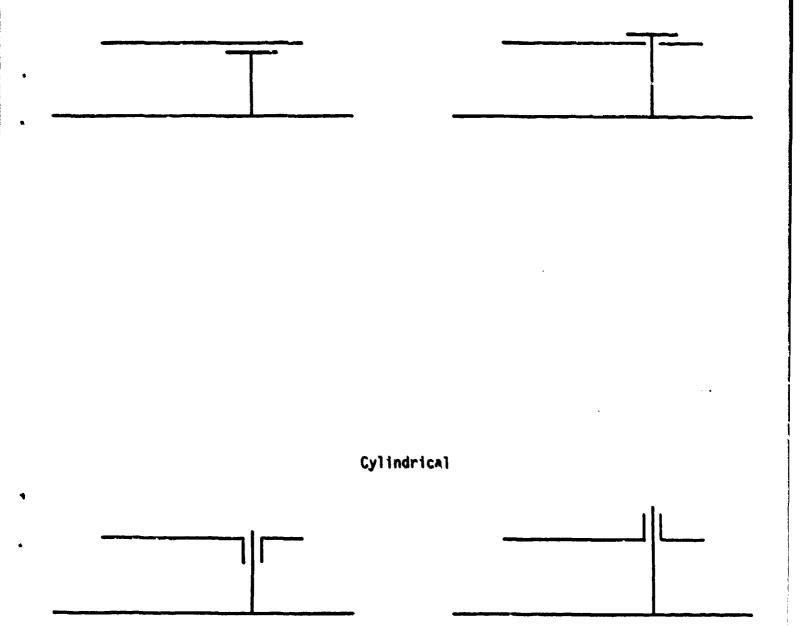
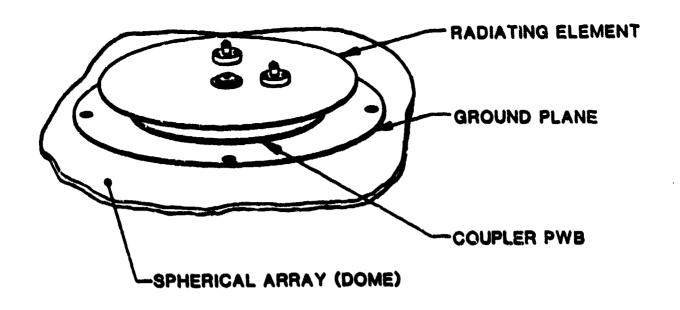
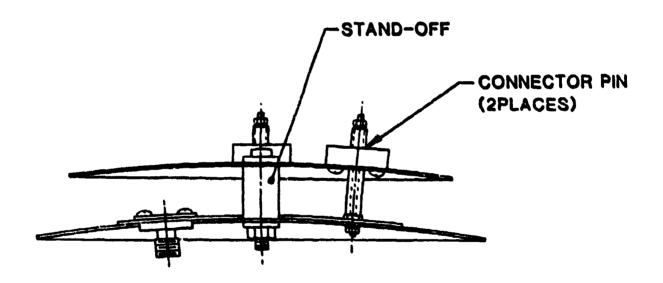


Figure 10. Four Methods of Integral Series Capacitance





CROSS-SECTIONAL VIEW

Figure 11. GAS Element Views

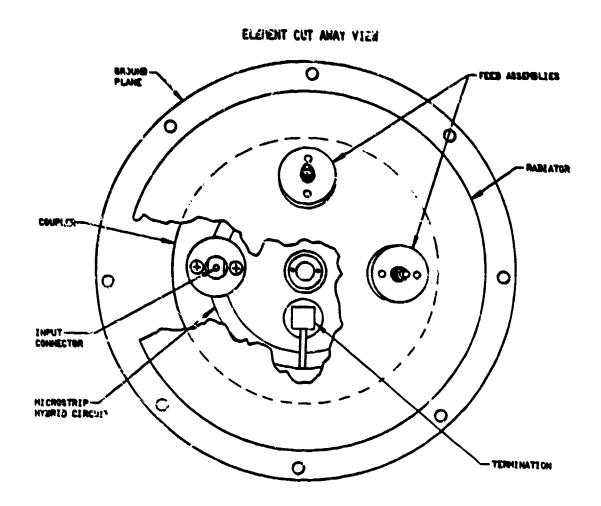


Figure 12. GAS Element Details

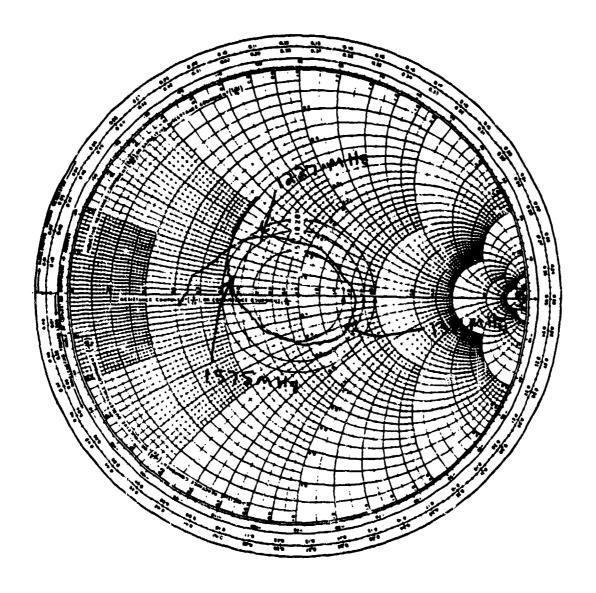


Figure 13. GAS Element Input Impedance

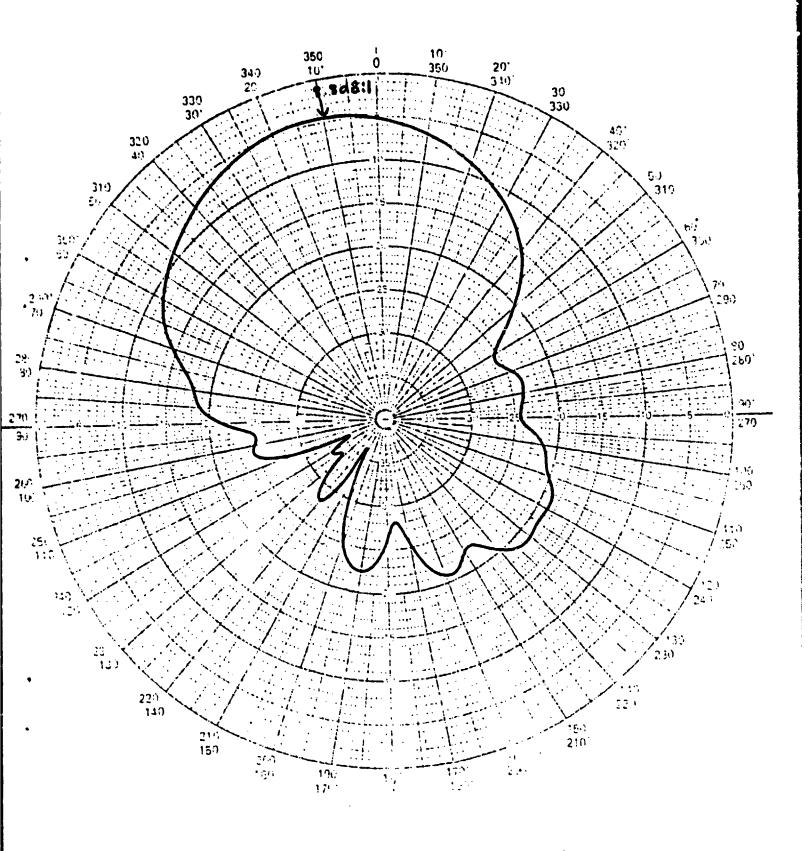


Figure 14. Linear Radiation Pattern at 1227 MHz

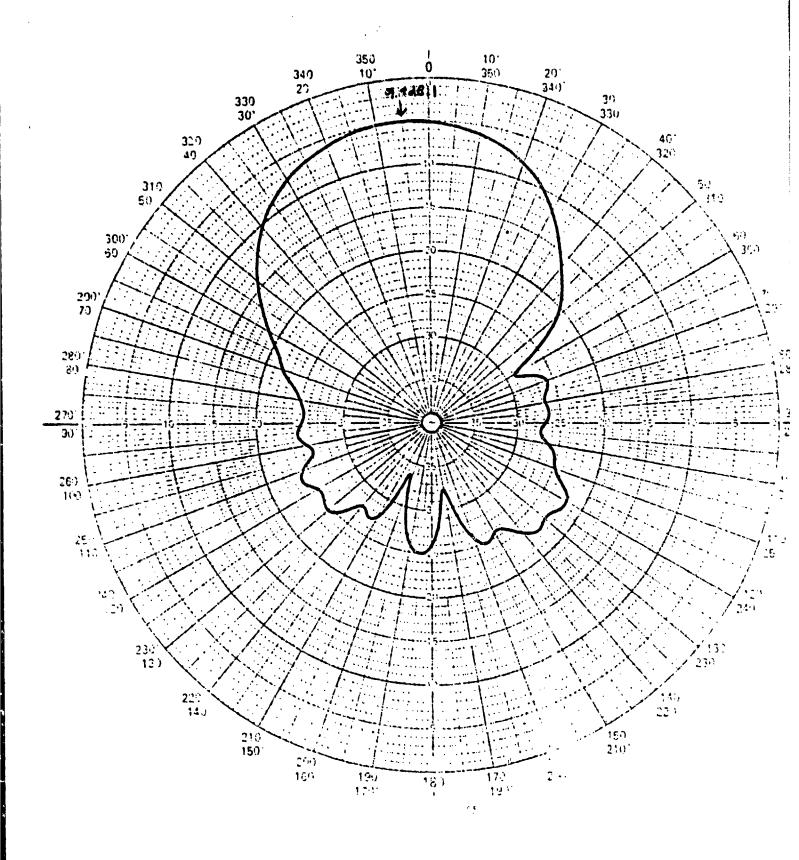


Figure 15. Linear Radiation Pattern at 1381 MHz

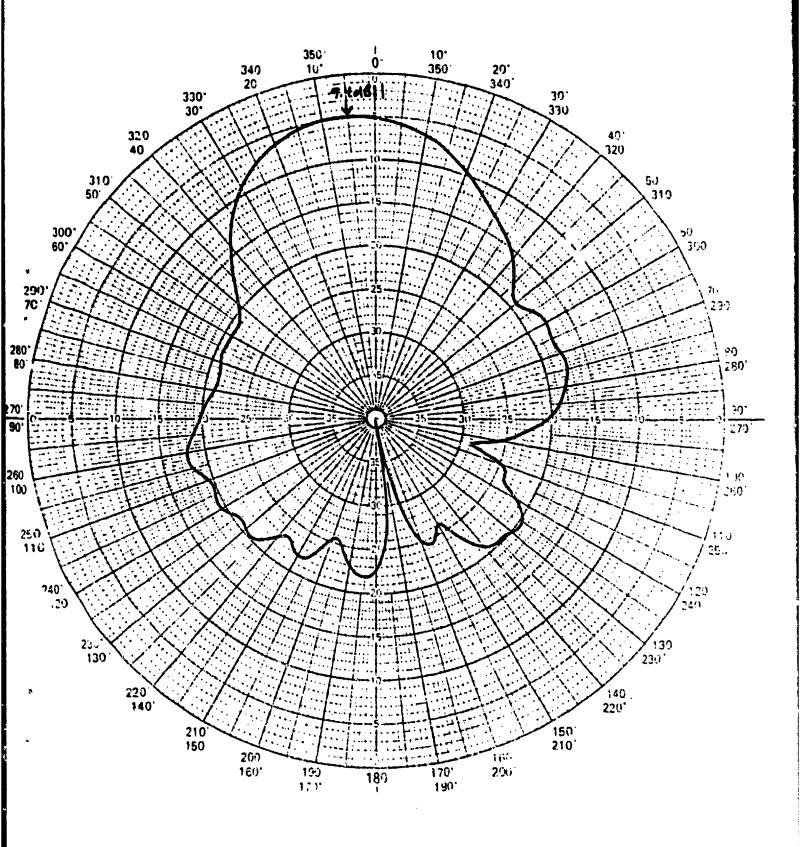


Figure 16. Linear Radiation Pattern at 1575 MHz

PRINTED DIPOLE RADIATING ELEMENTS FOR MONOLITHIC MILLIMETER VAVE PHASED ARRAYS

By: Daniel E. Rees and Brian J. Edward

Blectronics Laboratory

General Blectric Company

Syracuse, New York

ABSTRACT

Monolithic microwave integrated circuits (MMICs) are presently being developed for millimeter wave phased array radars and communications systems. Incorporating monolithic active circuftry into these arrays greatly increases system performance and cost effectiveness as well as overall flexibility and reliability. To achieve this system performance, radiating elements are needed which are efficient, exhibit broad band— and beamwidths, are lightweight, low in cost, and that are directly integratable with monolithic circuitry.

This paper focuses on our current work with K_a- and V-band microstrip fed dipole radiators with balun structures printed on fused silica substrates, which may be directly integrated with MMICs, and reports on an eight dipole-element line array using a space-feed for element illumination. The elements exhibit broad beamwidths and therefore are compatible with wide scan-angle phased array radars, and their VSWR is less than 2:1 over bandwidths in excess of 20%.

1. INTRODUCTION

Transmit/receive modules employing monolithic integrated circuitry are currently being developed for active millimeter wave phased arrays. Applications for these elemental modules include ground based phased array radar, airborne radars, spacebased radars, EW systems, missile guidance systems, and satellite communications systems.

General Electric is presently designing and fabricating modules for high performance millimeter wave arrays. Radiating elements which are efficient, have broad beam— and bandwidths, are light in weight, low in cost, that directly interface with monolithic circuitry, and are integratable into the module package have been developed. This paper focuses on our work with K_R — and V-band printed microstrip fed dipole radiators with balun structures. The design and performance of these elements are described. The integration of the elements with the active circuitry is detailed. A demonstration line array incorporating eight dipoles and a space-feed for element illumination is also described.

2. A PRINTED DIPOLE WITH BALUN RADIATING ELEMENT

a. Radiating Element Selection

The millimeter wave phased array radiating elements must exhibit high efficiencies, broad radiation patterns, high polarization purity, and sufficient operating bandwidths. In addition, the elements must be light in weight, be low in cost,

interface directly with the module active circuitry, and be integratable with the module packaging. Because dipole antennas satisfy all the electrical performance requirements, and a printed implementation fulfills the physical criteria, they have been selected for the active arrays' radiating elements. The printed implementation allows for wide flexibility in the design of the dipole and its balun feed structure.

b. Balun/Dipole Design

The balun concept employed for the feed of the dipole was proposed by Roberts¹ in a coaxial realization, and later expanded to a printed circuit format by Bawer and Wolfe². The coaxial balun structure and its equivalent circuit are shown in Figure 1. Referring to figure 1b, the coaxial transmission line of characteristic impedance $\mathbf{Z}_{\mathbf{b}}$ forms a series open circuited stub with the load impedance, $\mathbf{Z}_{\mathbf{1}}$, while the outer conductors of the coaxial transmission lines having characteristic impedances $\mathbf{Z}_{\mathbf{a}}$ and $\mathbf{Z}_{\mathbf{b}}$ form a shunt short circuited balanced line stub of characteristic impedance $\mathbf{Z}_{\mathbf{a}b}$. From inspection of the equivalent circuit the impedance, $\mathbf{Z}_{\mathbf{i}n}$, of the balun structure is readily expressed as

 $Z_{in}'=-jZ_{b}\cos\theta_{b}+jZ_{1}Z_{ab}\tan\theta_{ab}/(Z_{1}+jZ_{ab}\tan\theta_{ab})$ (1) where θ_{b} represents the electrical length of the open circuited series stub and θ_{ab} represents the electrical length of the short circuited shunt stub. If the electrical lengths θ_{ab} are made equal

$$\Theta_{ab} = \Theta_{b} = \Theta \tag{2}$$

then Z_{in}' becomes

$$Z_{in}' = \underline{Z}_{1} \underline{Z}_{ab}^{2} + \underline{i\cot\theta} [\underline{Z}_{1}^{2} \underline{(Z_{ab} - Z_{b}\cot^{2}\theta) - Z_{b}} \underline{Z}_{ab}^{2}] .$$

$$Z_{ab}^{2} + Z_{1}^{2}\cot\theta$$
(3)

If Θ is selected to be equal to a quarter wavelength in the transmission media, then at that frequency equation (3) reduces to

$$Z_{in}' = Z_i . (4)$$

If the characteristic impedance Z_a is equal to $Z_{in}{}'$, then the input impedance $Z_{in}{}$ is given by

$$Z_{in} = Z_{i} \tag{5}$$

for θ equal to 90° . Alternatively, Z_a can serve as a series transformer to match the impedance Z_{in} , to that of the accompanying circuitry.

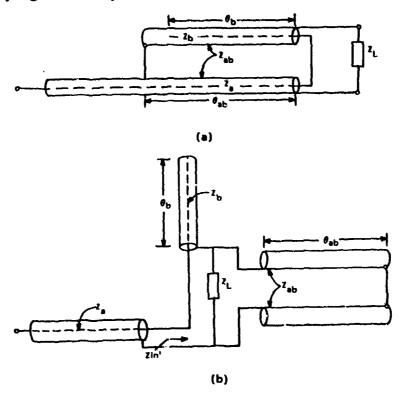


Figure 1. Coaxial Balun Structure (a), and Equivalent Circuit (b).

A printed realization of the balun structure of Figure 1 is The unbalanced coaxial transmission lines depicted in Figure 2. are replaced by substrate supported microstrip conductors. The groundplane for the microstrip conductors are printed so as to form a balanced transmission line analagous to the outer shields of the coaxial line. The width of these balanced line conductors are selected to be at least three times that of the microstrip. With this constraint, standard design equations can be employed to determine the impedances and effective dielectric constants of the microstrip lines. The characteristic impedance of the balanced line may be calculated by modeling the conductors as a pair of coupled microstrip lines on a suspended substrate operating in the The bottom ground plane of the coupled lines is odd mode. considered to be located a relatively large distance with respect to the substrate thickness so that the balanced line impedance becomes equal to twice the calculated microstrip odd mode impedance;

 $Z(balanced\ line) = 2\ Z_{odd}\ (\mu\ strip)\ . \tag{6}$ The effective dielectric constant for the balance line configuration is equal to that calculated for the odd mode coupled microstrip lines;

$$\varepsilon_{eff}$$
 (balanced lins) = $\varepsilon_{eff-odd}$ (μ strip) . (7)

From a practical standpoint, the realizable spacing between the balanced line conductors limits the lower extreme of Z_{ab} while the three times microstrip ground plane width constraint limits the lower extreme of Z_a and Z_b and the upper extreme of Z_{ab} . The

actual characteristic impedances selected for these transmission lines will be influenced by the supporting substrate's dielectric constant and thickness with values between 60 and 1009 being typical.

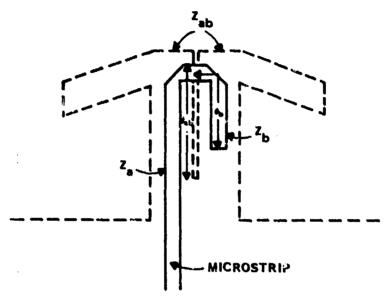


Figure 2. Printed Realization of Balun Structure with Integrated Dipole.

The dipole radiator is directly combined with the balun structure by forming the arms of the dipole as extensions of the balanced line conductors as depicted in the figure.

The length of the open circuited microstrip line, Θ_b , is referenced to the center of the balanced line. The short circuited balanced line length, Θ_{ab} , is referenced to the center line of the dipole arms as shown in Figure 2.

The dipole radiator is positioned a quarter of a free-space wavelength above the arrays' front face ground plane so that

maximum element directivity occurs normal to the array surface. The feed point impedance for a single dipole a quarter of a wavelength above a ground plane was calculated as a function of frequency using a method-of-moments code for wire antennas. Based on the work of Butler³, an equivalent wire radius for the flat printed dipole conductors of one fourth their width was used in the method-of-moments model. Figure 3 reports the calculated feed point impedance versus frequency for a printed dipole having a length to width ratio of eight. The calculated feed point resistance at resonance is approximately 80%.

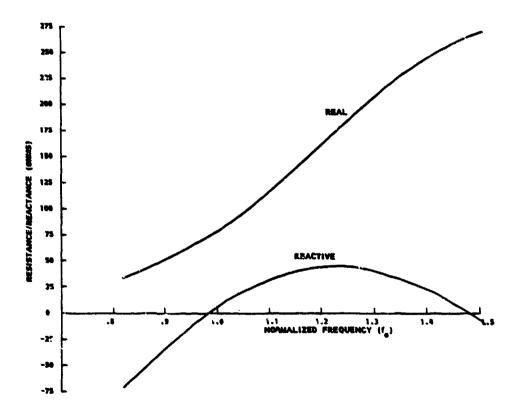


Figure 3. Calculated Feed Point Impedance of Flat Conductor Dipole having Length to Width Ratio of 8, and Located $\lambda_o/4$ Over a Ground Plane.

The balun line lengths, 9_{ab} and 9_{b} , were selected to be 90 electrical degrees at the dipole's resonant frequency and the line impedances, Z_{a} and Z_{b} , were chosen to be equal to the dipole's resonant resistance of 809. Therefore the dipole/balun combination exhibits an input impedance at resonance per equation (5) of

$$Z_{in} = 80Q$$
 .

c. Measured Radiating Element Performance

Radiating elements based on the above described design have been fabricated for both K_a- and $V\cdots$ band. Samples of these elements are shown in the photograph of Figure 4. The K_-band elements are printed on 0.25mm thick fused silica substrate and the V-band elements are fabricated on 0.13mm thick fused silica. Fused silica was selected because it has a low loss tangent (tan δ =0.0001) and its dielectric constant (ϵ _=3.8) results in favorable dimensions for the balanced and microstrip balun lines. In addition, since fused silica is a hard type substrate, it is suitable for integration into the module where hermetic sealing is required and for interfacing with the GaAs active circuitry. Since this particular dipole/balun combination design is centered to the dipole's resonant resistance of 800, a 630 quarter wavelength microstrip transformer was added in series with the input to each of the baluns to facilitate measurement of the impedance matches with 509 test equipment.

The elements are mounted so as to protrude through a 10.16 cm square groundplane. A Wiltron "K" connector provides a coaxial to

microstrip transition for measurement of the K_a-band element and a ridged waveguide to microstrip transition is used for evaluation of the V-band element. Both styles of transitions provide in excess of 20 dB return loss over their respective bands. A K_a-band dipole/balun mounted in its test fixture with groundplane is shown in Figure 5.

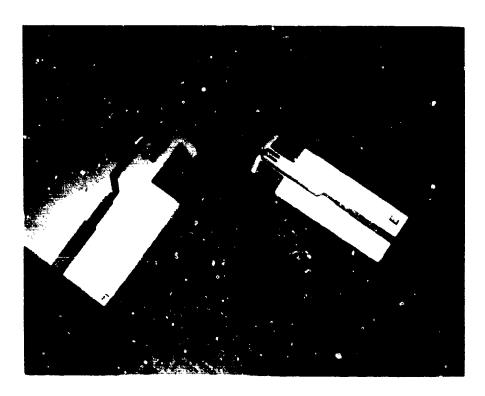


Figure 4. Ka- and V-Band Dipole/Balum Radiating Elements Printed on Fused Silica.

Measured return loss of the K_a - and V-band elements are presented in Figures 6 and 7. The elements exhibit 2:1 VSWR bandwidths on the order of 20%.

The measured E- and H- plane far-field radiation patterns are shown in Figures 8 and 9. For both bands, the elements exhibit a

broad lobe normal to the ground plane and peak gains on the order of 5 dBi.

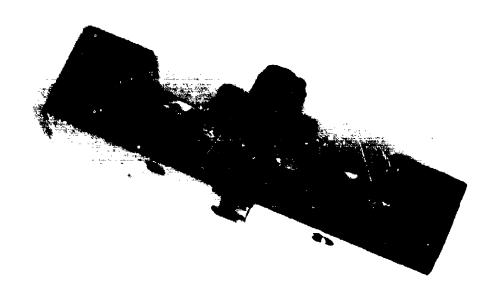


Figure 5. Ka-Band Dipole/Balun Mounted in Test Fixture.

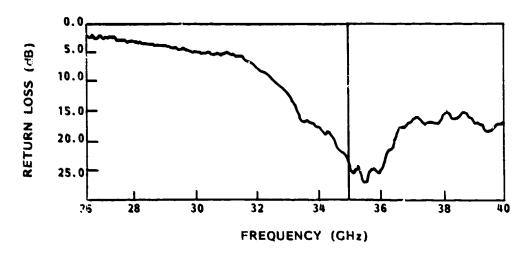


Figure 6. Measured Return Loss of Ka-Band Dipole/Balun.

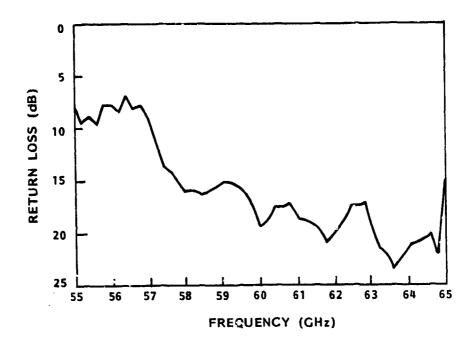


Figure 7. Measured Return Loss of V-Band Dipole/Balun.

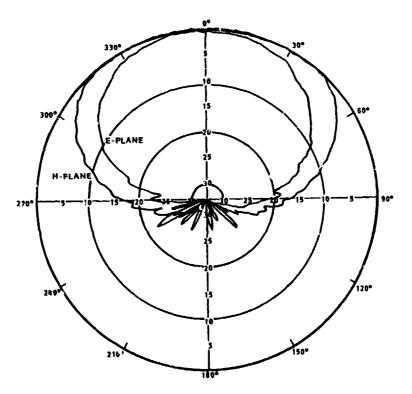


Figure 8. Measured Far-Field Radiation Patterns of Ka-Band Dipole/Balun.

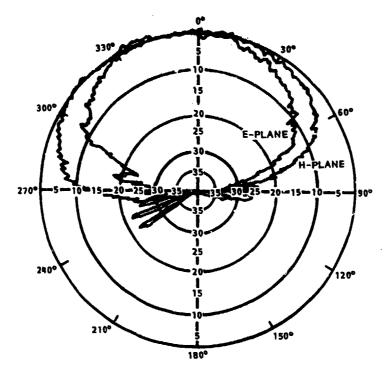


Figure 9. Measured Far-Field Radiation Patterns of V-Band Dipole/Balun.

3. AN INTEGRATED ACTIVE CIRCUITRY/RADIATING ELEMENT ASSEMBLY

To realize high phased array electrical performance, flexibility, and reliability, along with system cost effectiveness, the active elemental module design must be driven by a number of considerations. These include the interconnection of the RF circuitry, the integration of the radiating elements, the distribution of prime DC power and control signals, the removal of excess heat. hermetic sealing, and low cost manufacturability issues. General Electric is currently developing millimeter wave modules which address these issues.

To achieve low production costs and high electrical performance, the quantity of individual components and the number



of interconnects between them must be minimized. An array building-block which incorporates multiple elemental module circuitry with radiating elements into a planar "tray" assembly is illustrated in Figure 10. The tray assembly incorporates a hard substrate with laser tooled cut-outs to accommodate the active monolithic transmit/receive circuitry. Printed onto this substrate are the circuitry RF interconnect lines and the dipole/baluns thus providing direct interconnects between the active circuitry and integration of the radiating elements. Selecting a hard substrate enables glass sealing of ceramic covers to the substrate to form a hermetic package. A second substrate distributes command signals from a controller to the elemental phase shifters and T/R switches. DC power conductors are located on the bottom side of the tray. Each tray is placed onto an array support structure having channels for heat removal fluid.

4. SPACE-FED LINE ARRAY

The physically small element to element spacings and high circuit densities associated with millimeter wave active phased arrays restricts the use of constrained feeds for the distribution of the RF signals. This is particularly true for the case of multi-beam forming feed networks such as when amplitude monopulse beams are required. Space-feeds are therefore an attractive means of distributing RF signals to the elements of an active millimeter wave array when overall depth is unrestricted. The space-feed concept is illustrated in Figure 11. The array acts as a lens with collector and secondary radiating elements focusing energy

from a primary feed. The primary feed may be horn type antennas as illustrated or a small array. The array's illumination taper, efficiency, and spillover are determined by the primary feed's characteristics and the array/feed geometry.

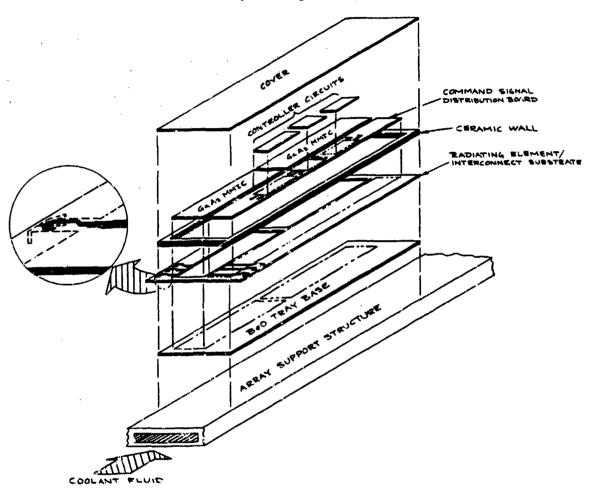


Figure 10. "Tray" Array Building Block Incorporating Multiple

Elemental T/R Modules with Integrated Radiating

Elements, DC Power and Command Signal Distribution

System, and Heat Removal System.

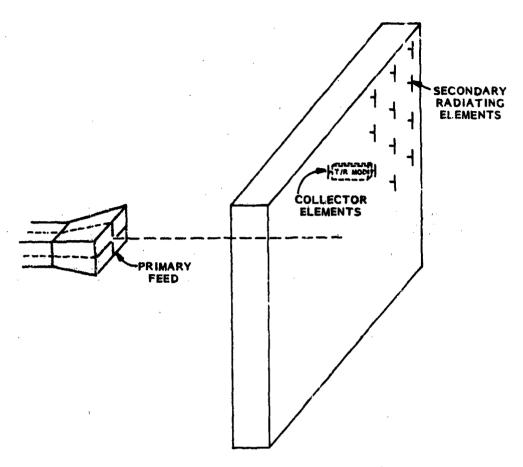


Figure 11. Space-Feed Concept for Active Phased Arrays.

To demonstrate the operation of the printed dipole/balun radiating elements in an array and the feasibility of the space-feed concept, an eight element E-plane space-fed line array was constructed for K_a-band. The array and feed structure are shown in Figure 12. The elements are printed onto a single substrate with the array secondary radiators protruding through the front ground plane. The array collector elements are on the far side of the ground plane in the figure. For the demonstration a single 15 dBi rectangular horn serves as the primary feed. It is located approximately 15cm from the array by an absorber lined shroud.

The line array elements intercept energy from only a small portion of the primary feed's main lobe and are therefore close to being uniformly illuminated. The far side ground plane surrounding the array collector elements is covered by absorber to dissipate the energy which is not intercepted.

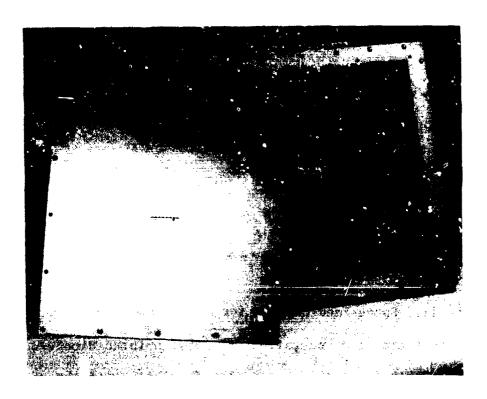


Figure 12. Bight Blement, E-Plane: Space-Fed Line Array for Ka-Band.

An eight element line array substrate is shown in the photograph of Figure 13. The elements are spaced $0.6057\lambda_o$ corresponding to the spacing required for grating lobe free beam scanning to 65° from broadside in a triangular grid planar array. For the single line of elements the grating lobe is incipient in visible space for a scan angle of approximately 41°. The array

shown in the photograph is designed to form a beam at broadside. The microstrip lines which interconnect the collector and secondary radiating elements have lengths which compensate for the spherical phase front of the primary feed. Other substrates have been fabricated with interconnecting line lengths which compensate for the primary feed phase front plus provide radiating element phasings for beam steering to 15, 30, and 45 degrees from broadside.

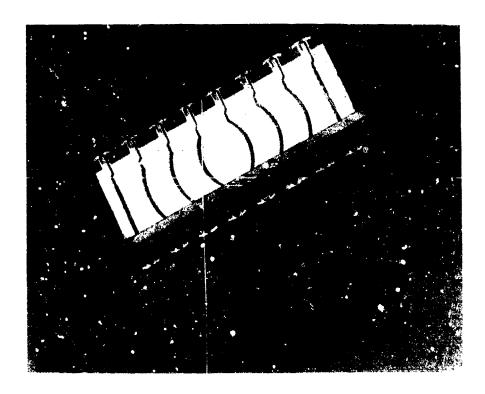


Figure 13. Eight Element Substrate showing Secondary Radiating and Collector Elements, and Phase Compensating Interconnecting Lines.

The measured and calculated far-field E-plane radiation patterns for the K_a -band space-fed line array phased for a

broadside beam are plotted in Figure 14. Excellent agreement exists between the measured and calculated patterns with the measured sidelobe levels being within a small fraction of a dB of the level expected for the nearly uniformly illuminated array.

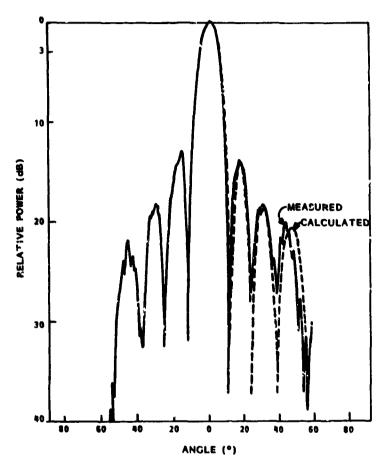


Figure 14. Measured and Calculated B-Plane Radiation Patterns for the Ka-Band Space-Fed Line Array, Broadside Beam.

The measured main lobe patterns for the E-Plane scanned beams are presented in Figure 15. The levels, which are normalized to the broadside meam, and cate the in-place element power pattern is on the order of $\cos^{3/2}\theta$.

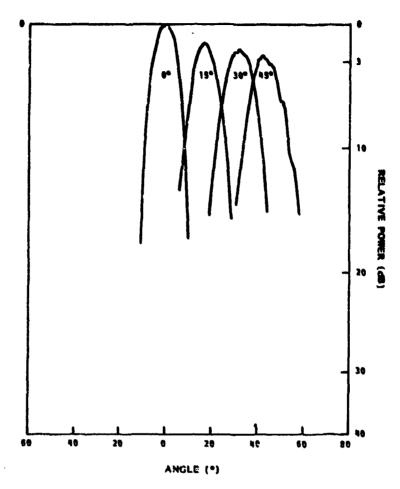


Figure 15. Measured Main Lobe Radiation Patterns for the Ka-Band Space-Fed Line Array, E-Plane Scanned Beams.

5. SUMMARY

A microstrip fed printed dipole with integrated balun has been described. This antenna is efficient, exhibits broad band- and beamwidths, is lightweight, low in cost, and may be directly interconnected with monolithic circuitry and integrated with their packaging. This antenna is ideally suited as a radiating element in millimeter wave phased arrays where active circuitry is

employed at the elemental level. The performance of this design has been demonstrated at both K - and V-band frequencies.

Space-reeding is an attractive method for the distribution of RF signals in millimeter wave arrays. The feasibility of this concept with the dipole/balun employed for both collector and secondary radiating elements has been demonstrated with array beams being formed at and scanned off broadside.

6. REFERENCES

- 1. Roberts, V.K. (1957) A New Wide Band Balun, Proceedings of the IRE, Vol. 45 (no. 12):1628-1631.
- Bawer, R. and Wolfe, J.W. (1960) A Printed Circuit Balun for Use with Spiral Antennas, <u>IRE Transactions on Microwave Theory</u> and Techniques, Vol. MTT-8 (No. 3):112-119.
- 3. Butler, C.M. (1982) The Equivalent Radius of Narrow Conducting Strip, IEEE Transactions on Antennas and Propagation, Vol. AP 30 (No. 4):755-758.

AD-P005 404

A Design Concept for an MMIC Microstrip Phased Array

Richard Q. Lee, Jerry Smetana, and Roberto Acosta Lewis Research Center Cleveland, Ohio

Prepared for the 1986 Antenna Applications Symposium cosponsored by the University of Illinois and the Rome Air Development Center Monticello, Illinois, September 17-19, 1986



A DESIGN CONCEPT FOR AN MMIC MICROSTRIP PHASED ARRAY

Richard Q. Lee, Jerry Smetana, and Roberto Acosta National Aeronautics and Space Administration Lewis Research Center Cleveland, Ohio 44135

1. ABSTRACT

abla A conceptual design for a microstrip phased array with monolithic microwave integrated circuit (MMIC) amplitude and phase controls is described. The MMIC devices used are 20 GHz variable power amplifiers and variable phase shifters recently developed by NASA contractors for applications in future Ka band advanced satellite communication antenna systems. The proposed design concept is for a general NxN element array of rectangular lattice geometry. Subarray excitation is incorporated in the MMIC phased array design to reduce the complexity of the beam forming network and the number of HMIC components required. proposed design concept takes into consideration the RF characteristics and actual physical dimensions of the MMIC devices. Also, solutions to spatial constraints and interconnections associated with currently available packaging designs are discussed. Finally, the design of the microstrip radiating elements and their radiation characteristics are examined.

2. INTRODUCTION

NASA Lewis Research Center has an on-going program to develop monolithic microwave integrated circuit (MMIC) devices for satellite communication applications in the 20 and 30 GHz frequency bands. In parallel with this activity, research efforts have been focused on the development of active phased array technology making use of these MMIC devices. The advantages of active phased arrays with amplitude and phase control at each radiating element or subarray are well known. In addition to electronic beam steering at nanosecond switching speed, an MMIC phased array can provide adaptive nulling of interfering signals and dynamic compensation of a distorted wavefront. To investigate and demonstrate the feasibility of MMIC phased array concepts, NASA Lewis is currently developing an MMIC phased array feed system using horn radiators and waveguide beam-forming networks with the MMIC devices placed inside waveguide housings. 2 An active phased array with MMIC devices in waveguide housings, however, does not offer any significant improvement in weight, size, and cost advantages. Recent research efforts on MMIC phased array have led to multi-layer planar structure design concepts where the radiating elements. MMIC devices. RF power distribution and logic control networks are deposited on different substrate layers. 3 To our knowledge, a total system integration based on such design concepts

has not yet been realized to date. This paper discusses some considerations and constraints relating the MMIC microstrip phased array designs. Based on these considerations, a conceptual design for a MMIC phased array composed of modular microstrip subarray is proposed.

3. ARRAY DESIGN CONSIDERATIONS

Some considerations in active phased array designs are spatial constraints, interconnections, heat dissipation, and cost. At high frequency, the physical size of the microstrip antenna is generally too small to allow direct amplitude and phase control at each element. With the currently available packaging designs for the 20 GHz transmitting module as depicted in figure 1, the overall dimensions of the MMIC devices are larger than a single microstrip patch element. If MMIC devices were placed at each element, the element spacing would be large, and grating lobes would be generated. The spatial constraint may require the use of modular subarray as radiating elements. When an active phased array requires thousands of radiating elements, cost is an overriding factor due to low production yields and high costs for the RF characterization of MMIC devices. The design concept developed by NASA Lewis uses modular subarray instead of individual radiating elements. The subarray modular approach reduces the cost and the complexity of the beam-forming network by reducing the number of MMIC devices required.

Another critical issue is that of heat removal. The projected efficiency for a power amplifier is typically less than 20 percent. The MMIC devices on substrate boards often generate excess heat causing warping and device malfunctions. To prevent excessive heating, MMIC devices are placed on separate substrate boards and proper thermal heat sinks for the MMIC devices are provided.

The multi-layer design approach requires very precise board alignment in electrically connecting several layers containing radiating elements, logic control circuit and beam-forming network. The interconnection of large quantities of MMIC devices and microstrip patch elements pose formidable topology and mutual coupling problems in active phased array designs. The complexity of high-level integration requires innovative feeding technique and proper choices of array architecture and beam-forming network design. Electromagnetic coupling techniques and optical beamforming network concepts are currently being considered by NASA Lewis as viable approaches to these problems. ⁵

4. ARRAY DESIGN CONCEPT

Figure 2 shows a design concept of an MMIC microstrip phased array. The MMIC amplitude and phase control modules are mounted on a small rectangular substrate panels with RF power and logic control lines extending to the edges. The panels are inserted vertically into a properly designed bracket connecting the

radiating element layer to the RF power distribution layers at both end. With MMIC devices mounted on individual substrate panels, the proposed array configuration allows device characterization as well as easy replacement of faulty devices. Furthermore, the existence of large spacing between adjacent MMIC panels alleviates heat dissipation difficulties. A thermal sink is generally required for multiple beam operations where several sets of amplitude and phase controls are placed on the same substrate panel. Figure 3 illustrates a scheme for heat removal using graphite aluminum (GR/AL) heat pipe. GR/AL is a composite material with the property of lightweight, low coefficient of thermal expansion and high thermal conductivity. NASA Lewis is currently supporting development of such material for space applications.

The spatial and interconnect problems delineates the choice of subarray-type configuration. Figure 4 shows four modular subarray configurations currently under investigation. Subarray (a) is a corporate fed 2 by 2 rectangular subarray. Subarray configurations b, c, and d all have a driven center element and surrounding parasitic elements. The parasitic subarray configurations have the potential advantages of lower feed losses, reduced feed line radiation, lower sidelobes, and increased bandwidth. Experimental investigations are being carried out to study the circuit and radiation characteristics of these

subarray configurations. Figure 5 shows the typical radiation patterns of a 2 by 2 rectangular subarray and a 3 by 3 parasitic subarray along with that of a single microstrip patch.

The use of electromagnetic coupling between the feed line and the radiating element through an aperture will greatly simplify the interconnect problem. An aperture-coupled microstrip antenna with a perpendicular feed has been investigated and proven feasible. This technique is particularly attractive for use in the excitation of the parasitic subarrays. However, further study and investigation is required to improve the coupling efficiency.

5. CONCLUSION

A conceptual design for a microstrip phased array with currently available MMIC amplitude and phase control devices has been described. The proposed design addresses the problems of spatial constraints, interconnections and heat removal. Although, the hardware and fabrication techniques for the MMIC phased problems system may already exist, much work still needs to be done to reduce the complexity of MMIC control and interconnectivity while achieving good performance.

REFERENCES

- 1. Acosta, R.J., (1986) "Compensation of Reflector Surface Distortions Using Conjugate Field Matching," in IEEE 1986
 Antennas and Propagation. International Symposium Digest, Vol. 1, IEEE, New York, pp. 259-263.
- Smetana, J., Kascak, T.J., and Alexovich, R.E., (1986) MMIC Antenna Tachnology Development in the 30/20 Gigahertz Band. NASA TM-87192.
- 3. Mailoux, R.J., (1986) Fhased Array Architecture for Millimeter Wave Active Arrays, Microwave J., 29:317-124.
- 4. Schell, A.C., (1986) Trends in Phased Array Development,
 Microwaye J., 29:36-35.
- 5. Kunath, R.R. and Bhasin, K.B., (1986) Optically Controlled

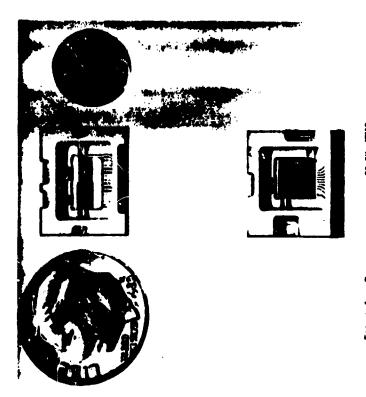
 Phased Array Antenna Concepts Using GaAs Monolithic

 Microwave Integrated Circuits, NASA TM-87229.
- Lo. Y.T., et al. (1986) Study of Microstrip Antennas,
 Microstrip Phased Arrays and Microstrip Feed Networks,
 (RADC-TR-77-406) UILU-ENG-77-2265.

7. Buck, A.C., Pozar, D.H., (1986) Aperture-Coupled Microstrip

Antenna With a Perpendicular feed, <u>Electron</u>. <u>Lett.</u>,

22:125-126.



GUNE 1. - PACKAGING DESIGNS FOR ZO GHZ MIC DEVICES.

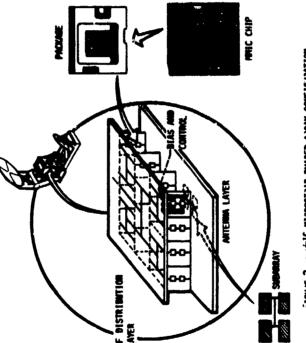
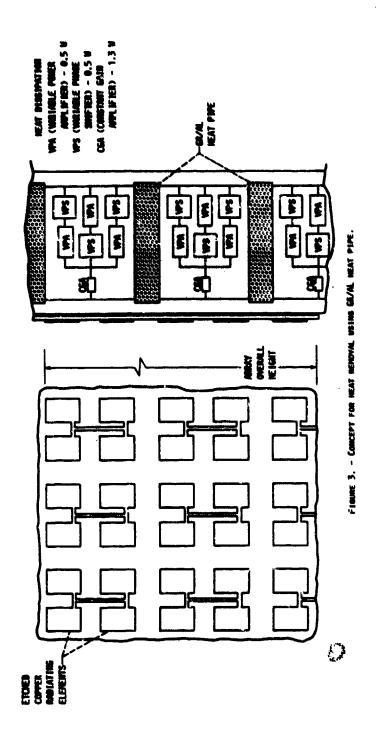
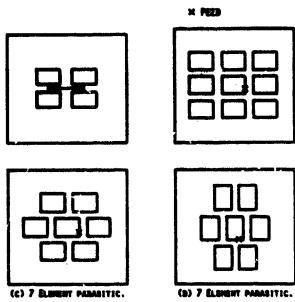
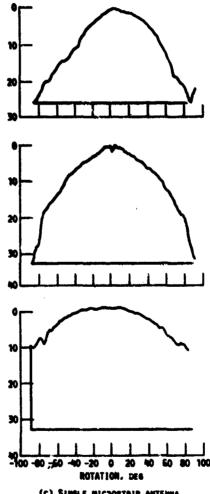


FIGURE 2. - IMIC MICROSTAIP PHASED AARAY CONFIGURATION.





Floure 4. - Subannay conflourations.



(C) SINGLE MICROSTRIP ANTENNA.
FIGURE 5. - E PLANE RADIATION PATTERNS.



AD-P005 405

MUTUAL ADMITTANCE BETWEEN SLOTS IN CYLINDERS OF ARBITRARY CROSS SECTION SHAPE

A. F. Peterson and R. Mittra

Electromagnetic Communication Laboratory

University of Illinois

Urbana, IL

ABSTRACT

Both the proper design of slot arrays and the positioning of multiple antenna arrays on a common surface require an accurate estimate of the mutual coupling between individual slot elements. To date, the analysis of mutual admittance has been undertaken for slot elements in simple shapes such as circular cylinders, cones, and spherical surfaces. Limited attempts have also been made to treat more general surface shapes using asymptotic methods. In an effort to extend this type of analysis to arbitrary geometries, the present investigation considers a numerical solution for the mutual coupling between individual, finite-sized slots in an infinite, conducting cylinder of arbitrary cross section. Both axial and circumferential slots are considered.

The problem of determining the mutual coupling is posed in such a manner as to make it amenable to convenient numerical solution. This is done by using the equivalence theorem to replace the source slot by magnetic currents radiating in the presence of the closed cylinder. Next, the original three-dimensional problem is replaced by a series of equivalent two-dimensional problems via the use of the Fourier transform in the axial direction. The magnetic field integral equation, which is used to solve for the problem of scattering by an arbitrarily shaped cylinder.

domain. The mutual impedance is computed from the knowledge of the numerical solution for the current density on the cylinder. The results obtained via the use of this approach are found to be in good agreement with the available data for circular cylinders. It appears from this initial study that the method is practical to apply for cylinder circumferences up to or exceeding ten wavelengths. The method is also generalizable to cylinders with surfaces that satisfy an impedance boundary condition.

1. INTRODUCTION

Both the proper design of slot arrays and the positioning of multiple antenna arrays on a common surface require an accurate estimate of the mutual coupling between individual slot elements. To date, the analysis of mutual admittance has been undertaken for slots on ground planes [1], on cones [2], [3], on circular cylinders [4] - [8], and on spherical surfaces [9]. Limited attempts have also been made to treat more general surface shapes [10], [11]. These approaches are based on analytical or asymptotic methods, and are not easily generalized to more complicated geometries. In an attempt to extend this type of analysis to arbitrary geometries, the present investigation considers a numerical solution for the mutual coupling between individual slots in an infinite, conducting cylinder of arbitrary cross section shape. In general, numerical solutions involving electrically large three-dimensional structures are cumbersome and inefficient. Furthermore, tradeoffs that can greatly improve the efficiency usually do so only at the expense of accuracy in the results. Therefore, one goal of the present study is to identify the degree of accuracy attainable in practice from the numerical procedure and assess the overall efficiency of the approach. Since extensive results have been tabulated for circular cylinders [5], these will be the initial focus in order to judge the accuracy of the method.

Two cases will be considered: coupling between two circumferential slots and coupling between two axial slots. The slots are assumed to be waveguide-fed apertures excited with the TE10 waveguide mode, with no higher-order modes included in the model. (A recent investigation has included the effects of higher-order modes, and concluded that the true mutual coupling is generally slightly smaller than that predicted under the above assumption [9].) Under this assumption, the aperture field of the source slot can be expressed as

$$E = \hat{z} \left[\frac{2}{h_A w_A} \right]^{1/2} \cos \left(\frac{\pi t}{w_A} \right) \tag{1.1}$$

for the circumferential slot and

$$E = \hat{t} \left[\frac{2}{h_A w_A} \right]^{1/2} \cos\left(\frac{\pi z}{w_A}\right) \tag{1.2}$$

for the axial slot, where the origin of the coordinate system is located at the center of the slot, as depicted in Figure 1.

Under the above assumption, the mutual admittance for the circumferential case is defined

$$Y_{AB} = -\left[\frac{2}{h_B w_B}\right]^{1/2} \int_{\frac{-h_B}{2}}^{\frac{h_B}{2}} \int_{\frac{-u_B}{2}}^{\frac{w_B}{2}} \cos\left(\frac{\pi t'}{w_B}\right) J_z(h', t') dh' dt' \tag{1.3}$$

where the integral is taken over the aperture of slot B, and J_z is the current density induced on the cylinder when slot B is short-circuited (closed by a perfect conductor) and slot A is excited by the assumed field of Equation (1.1). Similarly, for the axial case the mutual admittance is defined

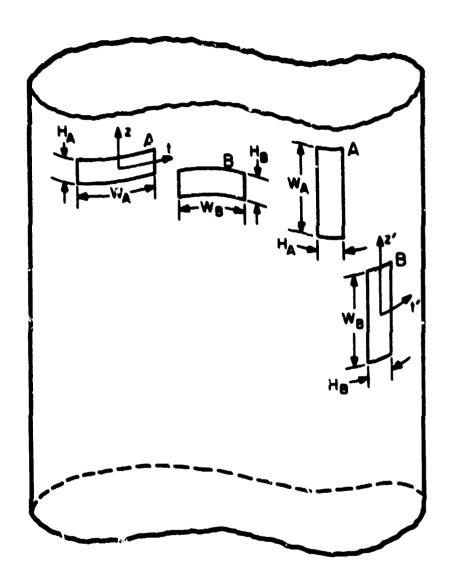


Figure 1. Geometry showing two axial slots and two circumferential slots in a cylinder of arbitrary shape.

$$Y_{AB} = -\left(\frac{2}{h_B w_B}\right)^{1/2} \int_{-h_B}^{h_B} \int_{-w_B}^{-w_B} \cos\left(\frac{\pi z'}{w_B}\right) J_i(h'.z') dh'dz'$$
 (1.4)

where J_t is the transverse current density induced on the cylinder by the assumed field of Equation (1.2), with slot B short-circuited. The current densities can be found after solving for the fields of an equivalent magnetic source defined

$$K_{eq} = E \times \hat{n} \tag{1.5}$$

For the circumferential slot field of Equation (1.1).

$$K_{eq} = \hat{t}K_t = \hat{t} \left[\frac{2}{h_A w_A} \right]^{1/2} \cos\left(\frac{\pi t}{w_A}\right)$$
 (1.6)

For the axial slot field of Equation (1.2),

$$K_{eq} = \hat{z}K_z = -\hat{z} \left[\frac{2}{h_A w_A} \right]^{1/2} \cos\left(\frac{\pi z}{w_A}\right)$$
 (1.7)

These equivalent magnetic currents, radiating in the presence of the infinite cylinder, produce the same exterior fields and currents as the original slot with aperture fields described by Equations (1.1) and (1.2). Thus, the problem of computing the mutual coupling between slots A and B reduces to that of finding the currents induced upon a closed, infinite conducting cylinder by a finite impressed source K_{eq} . Once these currents are found, the mutual admittance between slot A and any other slot location can be computed using Equations (1.3) and (1.4).

To simplify the task of determining the currents induced upon an infinite cylinder by a finite source, the problem can be posed in the Fourier transform domain. The Fourier transform is defined

$$F_{z} \{H(z)\} = \tilde{H}(\gamma) = \int_{-\infty}^{\infty} H(z) e^{-j\gamma z} dz$$
 (1.8)

The inverse Fourier transform is

$$F_{z}^{-1}\left\{\tilde{H}(\gamma)\right\} = H(z) = \frac{1}{2\pi} \int_{-\infty}^{\infty} \tilde{H}(\gamma) z^{\gamma z} d\gamma \qquad (1.9)$$

Applied to the unknown currents, the Fourier transform converts functions of 't' and 'z' to functions of 't' and the transform variable ' γ '. Because the cylinder is invariant with respect to z, the unknown current density at each value of γ can be found independently. Thus, the original three-dimensional problem reduces to the superposition of uncoupled two-dimensional problems, which are more amenable to numerical solution.

In spite of the simplification resulting from the decoupling of the equations mentioned above, we are still faced with the task of solving the two-dimensional problem over the infinite continuum spanned by the variable γ . In practice, we are forced to work with a finite number of discrete values of the spatial frequency, i.e., γ_0 , $\gamma_{\pm 1}$, ..., $\gamma_{\pm N}$. As is well known from signal analysis [12], when a Fourier transform is combined with an evenly-spaced sampling process, the result is equivalent to working with the Fourier transform of a periodic extension of the original function of z. We can think of the above approach as being equivalent to replacing the original problem (which involved a single source slot) by one involving a periodic array of source slots. This analogy allows a better grasp of the approximations introduced by sampling in the transform domain.

The period of the fictitious source array must be sufficiently large so that the coupling between the fictitious slots and slot B will be insignificant compared to the coupling from slot A to slot B. In addition, discrete values of γ must be included up to the point where truncation does not introduce numerical inaccuracy. After

solving for the transform currents over a sufficient range of y, the inverse transform can be computed explicitly according to the equation below

$$J(t,z) = \frac{\Delta \gamma}{2\pi} \left| \tilde{J}(t,0) + 2 \sum_{n=1}^{N} \tilde{J}(t,n\Delta \gamma) \cos(n\Delta \gamma z) \right|$$
 (1.10)

to produce the spatial currents at the desired locations for the admittance calculation. In Equation (1.10), we have assumed that the original source distribution is centered at z=0 and is symmetric in z

In summary, we have posed the mutual coupling problem in an arbitrarily-shaped cylinder in such a manner as to make it amenable to numerical solution. The equivalence theorem is used to replace the source slot by magnetic currents radiating in the presence of the closed cylinder. The desired three-dimensional problem can be represented by the superposition of two-dimensional problems via the Fourier transform. The equations can be discretized directly in the transform domain, which introduces a fictitious periodicity in the spatial domain. However, the formulation does require that the two-dimensional problem be solved at a number (perhaps a large number depending on the relative location of the source and secondary slot) of spatial frequencies. The extent of the necessary spectrum, the period size, and other aspects concerning the modeling procedure will be determined by numerical experimentation.

2. COUPLING BETWEEN AXIAL SLOTS

The framework for constructing a numerical solution for the mutual admittance between slots was developed above. The primary task is to find the electric current density induced in the vicinity of the secondary slot by the equivalent magnetic current representing the source slot. For axial slots, only the transverse electric current density J_t is required for the admittance calculation. A

suitable equation for the transverse electric current density is the magnetic field integral equation (MFIE), which enforces the boundary condition that the total magnetic field at the surface of the cylinder is proportional to the electric surface current density according to

$$\hat{n} \times H = J \tag{2.1}$$

The MFIE can be expressed

$$H_z^{inc}(t,z) = -J_t(t,z) - \hat{z} \cdot curl \int \hat{t}(t') J_t(t',z') \frac{e^{-jkR}}{4\pi R} dt'dz' \qquad (2.2)$$

where

$$R = \sqrt{[x(t) - x(t')]^2 + [y(t) - y(t')]^2 + (z - z')^2}$$
 (2.3)

and where H_z^{in-} represents the \hat{z} -component of the magnetic field produced by the equivalent magnetic current K_z if the magnetic current was radiating in free space. Equation (2.2) is a convolution in the variable z. and an application of the Fourier transform in conjunction with the convolution theorem [12] yields

$$\tilde{H}_{z}^{iac}(t,\gamma) = -\tilde{J}_{t}(t,\gamma) - \hat{z} \cdot curl \int \hat{t}(t')\tilde{J}_{t}(t',\gamma)\tilde{G}(\rho;k,\gamma) dt'$$
where [13]

$$\tilde{G}(\rho; k, \gamma) = F_z \left\{ \frac{e^{-jk\sqrt{\rho^2 + z^2}}}{4\pi\sqrt{\rho^2 + z^2}} \right\}$$

$$= \begin{cases}
\frac{1}{4j} H_0^{(2)} (\rho\sqrt{k^2 - \gamma^2}) & k^2 > \gamma^2 \\
\frac{1}{2\pi} K^0 (\rho\sqrt{\gamma^2 - k^2}) & \gamma^2 > k^2
\end{cases}$$
(7.5)

and

$$\rho = \sqrt{[x(t) - x(t')]^2 + [y(t) - y(t')]^2}$$
 (2.6)

Equation (2.4) is identical in form to the conventional two-dimensional integral equation for scattering from a conducting cylinder, with the exception that the wavenumber k has been replaced by

$$k_{t} = \sqrt{k^2 - \gamma^2} \tag{2.7}$$

The incident magnetic field can be computed from the expression

$$\tilde{H}_{z}^{inc}(t,\gamma) = \frac{k^{2} - \gamma^{2}}{jk \, \eta} \int_{t \log \Delta} \tilde{K}_{z}(t',\gamma) \, \tilde{G}(\rho;k,\gamma) \, dt' \qquad (2.8)$$

where η is the intrinsic impedance of free space. ρ is defined in Equation (2.6), and \tilde{K}_z is the Fourier transform of Equation (1.7).

The preceding discussion introduced the idea of replacing the original source slot by a periodic repetition of slots, in order to discretize the transform domain. If the spatial period is P_z , the sampling interval in the transform domain is fixed at

$$\Delta \gamma = \frac{2\pi}{P}.\tag{2.9}$$

Equation (2.4) can be solved approximately by converting it to a matrix equation of finite order, using the method of moments [14]. The cylinder cross-section can be modeled by the superposition of flat strip-cells, and the unknown electric current density can be replaced by a finite expansion of the form

$$\tilde{J}_{i}(t,\gamma) \cong \sum_{n=1}^{M} j_{in}(\gamma) p_{n}(t)$$
 (2.10)

where p_n (t) denotes a subsectional pulse basis function

$$p_n(t) = \begin{cases} 1 & \text{if } t \in \text{cell } n \\ 0 & \text{otherwise} \end{cases}$$
 (2.11)

The integral equation of (2.4) can be enforced approximately at the centers of each of the cells in the model to yield an M-th order matrix equation. The solution of this system of equations gives an approximation to one harmonic of the unknown current density.

The moment-method approach employed here has been adequately discussed elsewhere [14]. [15], and the details of the numerical implementation will be omitted. However, two additional points deserve mention. The first concerns the modeling of the source. It is convenient to model the source slot with the same cells that comprise the model of the cylinder, although this is not at all essential to the approach. In the axial case, the source is constant in the variable t, and can be represented by the same type of pulse expansion used in Equation (2.10). The second point concerns the evaluation of the integrals arising in the matrix elements. Since closed-form expressions for the integrals of the type appearing in Equation (2.4) are not often available, some form of numerical integration is necessary to accurately evaluate the elements of the moment-method matrix. In this case, many of the matrix elements can be accurately determined by single-point integration. For those elements of the matrix representing closely spaced cells, experimentation determined that single-point evaluation does not produce accurate enough numbers. A Romberg integration algorithm [16] was used to compute the closely-spaced terms.

The total solution for the current density as a function of z is obtained by solving the matrix equation for each harmonic and superimposing the transform currents according to Equation (1.10). This indicates that the coupling between a single source slot and a multitude of secondary slots can be calculated

simultaneously using the currents produced by a single source configuration (provided that the spatial period is selected large enough to accommodate all the secondary locations). The admittance calculation follows from Equation (1.4). Since this calculation also requires a numerical integration over the current, it is necessary to evaluate J_t at several points throughout each secondary slot.

3. COUPLING BETWEEN CIRCUMFERENTIAL SLOTS

The treatment of coupling between circumferential slots is similar to that of the axial case. However, the circumferential case is slightly more complicated because the equivalent magnetic current of Equation (1.6) excites both \hat{t} and \hat{z} components of electric current on the cylinder. Although only the \hat{z} component is used in the admittance calculation, the solution process involves both components of electric current density. Coupled magnetic field integral equations for this problem are given as

$$\tilde{H}_{z}^{inc}(t,\gamma) = -\tilde{J}_{t}(t,\gamma) - \hat{z} \cdot curl \int \hat{t}(t') \tilde{J}_{t}(t',\gamma) \hat{G}(\rho;k,\gamma) dt' \qquad (2.1)$$

$$\tilde{H}_{t}^{inc}(t,\gamma) = \tilde{J}_{z}(t,\gamma) - \hat{t}(t) \cdot curl \int \hat{z} \tilde{J}_{z}(t',\gamma) \tilde{G}(\rho;k,\gamma) dt'$$

$$-\hat{t}(t) \cdot curl \int \hat{t}(t') \tilde{J}_{t}(t',\gamma) \tilde{G}(\rho;k,\gamma) dt'$$
 (3.2)

where the "incident" fields on the left-hand side of the equation are those produced by the equivalent magnetic source of Equation (1.6), radiating in the absence of the cylinder. These expressions are

$$\tilde{H}_{z}^{inc}(t,\gamma) = \frac{\gamma}{k \eta} \int_{slot A} \left\{ \frac{\partial}{\partial t'} \tilde{K}_{t}(t',\gamma) \right\} \tilde{G}(\rho;k,\gamma) dt'$$
(3.3)

$$\tilde{H}_{t}^{inc}(t,\gamma) = \frac{k^{2}}{jk \eta} \int_{slot A} \tilde{K}_{t}(t',\gamma) \, \tilde{G}(\rho;k,\gamma) \, dt'$$

$$+ \frac{\frac{\partial}{\partial t}}{jk \eta} \int_{slot A} \left\{ \frac{\partial}{\partial t'} \, \tilde{K}_{t}(t',\gamma) \right\} \tilde{G}(\rho;k,\gamma) \, dt' \qquad (3.4)$$

where \tilde{G} is defined in Equation (2.5).

The equation for the transverse component of the current is decoupled from the other, and this suggests that we first solve Equation (3.1) for J_i . Subsequently, the axial component can be found from the Equation (3.2). Because the treatment of the circumferential case requires the solution of two integral equations, which translates into the solution of two matrix equations for each value of γ , the process is less efficient than in the axial case.

As explained in Section 2, the cylinder under consideration can be modeled by a superposition of flat cells. Again we consider replacing the unknown current density by an expansion in piecewise constant basis functions, and enforce the equations at the center of each cell in the model. At each value of γ , we first set up and solve a matrix equation for an approximate solution to Equation (3.1). With the exception of the source term given in Equation (3.3), this equation is identical to that discussed for the axial slot case. Once the transverse current density is found, we set up and solve a second M-th order matrix equation to find the axial current density. In the second case, we include the known transverse current density as an additional source. Finally, the total currents on the cylinder are found from superimposing the harmonics according to Equation (1.10).

For convenience, the source slots were represented with some of the same cells that model the cylinder surface. Although the source varies in a sinusoidal manner in the variable t, a piecewise-constant representation was used for simplicity. As mentioned above, it is necessary to evaluate integrals numerically to construct the

M-th order matrix and the right-hand side. In some cases, single-point evaluation is sufficiently accurate; in other cases a Romberg algorithm was used.

4. PRELIMINARY RESULTS

Computer programs were developed in FORTRAN to treat each of the two cases described above. Although these codes are configured to treat arbitrarily shaped cylinders, the focus of this initial study was confined to circular cylinders, in order to gauge the accuracy and efficiency of the method employed.

Consider the axial slot case. Table 1 shows numerical results for the mutual admittance between two slots in a circular cylinder having radius equal to one wavelength. Each slot is 0.5 by 0.214 wavelengths in size. 88 cells are used to model the cylinder for the moment-method approach, and the spatial period is fixed at 15.5 wavelengths. Parameters z_0 and ϕ_0 indicate the spacing between the source and secondary slot along the axis and circumference, respectively. Table 2 shows data from the literature [5] for comparison, for the same size cylinder with similar slots (these were 0.5 by 0.2 wavelengths). Note that it appears from Table 2 that the asymptotic data is not very accurate for this particular cylinder, which is to be expected since the radius is not large compared to the wavelength. The agreement between the numerical solutions and the exact (modal expansion) appears excellent.

Similar data for the circumferential case is shown in Tables 3 and 4, for a cylinder of one wavelength radius modeled with 88 cells. The slot dimensions are 0.5 by 0.2 wavelengths, and the spatial period was 18.5 wavelengths. In this case, the agreement is not as good as it was with the axial case. It is felt that additional care needs to be taken with the numerical modeling of the source slot (i.e., eliminate the piecewise constant representation of the source distribution) in order to improve the accuracy.

TABLE 1

Numerical solution for the mutual admittance between axial slots in a circular cylinder with radius of one wavelength. The slot sizes are 0.5 by 0.214 (wavelengths). The distance between the centers of the slots is given in terms of (x_0, ϕ_0) where x_0 is in wavelengths and ϕ_0 in degrees. This numerical solution used a spatial period of 15.5 wavelengths.

20	\$ 0	$ Y_{AB} $, dB	$arg(Y_{AB})$, degrees
0.5	0	-72.6	19.5
1.0	o	-86.8	-176.0
2.0	0	-101.0	-175.0
0.0	45	-78.3	144.0
0.5	45	-82.5	104.0
1.0	45	-90.0	-2.3
2.0	45	-101.0	67.2

TABLE 2

Exact (mcdal) and asymptotic data from reference [5] for comparison to Table 1.

Data for slots of size 0.5 by 0.2 wavelengths in circular cylinder with radius of one wavelength. (Modal data only available for a few cases)

			(exact)	(asymptotic)		
20	φ ₀	IYABİ, dB	arg(Y _{AB})	IYABI. dB	arg(Y _{AB})	
0.5	0	N/A	N/A	-70.1	25	
1.0	0	-87.1	-171	-86.7	-173	
2.0	0	-100.0	-174	-99.4	-177	
0.0	45	N/A	N/A	-74.9	130	
0.5	45	N/A	N/A	-79.1	90	
1.0	45	-89.2	2	-87.3	-15	
2.0	45	N/A	N/A	-99.8	49	

TABLE 3

Numerical solution for the mutual admittance between circumferential slots in a circular cylinder with radius of one wavelength. The slot sizes are 0.5 by 0.2 wavelengths. The slot spacings are given in terms of (z_0, ϕ_0) where z_0 is in wavelengths and ϕ_0 in degrees. This numerical solution used a spatial period of 18.5 wavelengths.

20	Φ0	IYAB I. dB	$arg(Y_{AB})$, degrees
0.5	0	-68.3	-119
1.0	0	-73.2	68
20	0	-79.4	71
4.0	0	-87.7	74
0.0	45	-82.8	-117
0.5	45	-83.8	105
1.0	45	-82.8	-48
2.0	45	-84.6	-11
4.0	45_	-90.1	17

TABLE 4

Exact (modal) and asymptotic data from reference [5] for comparison to the data of Table 3. Data for slots of size 0.5 by 0.2 wavelengths in circular cylinder of one wavelength radius. (Modal data not available for all cases)

			(exact)	(asymptotic)		
20	φυ	IYAB I. dB	arg(YAB)	YABI. dB	arg(YAB)	
0.5	0	-67.9	-117	-67.7	-117	
1.0	o	-72.5	67	-72.3	68	
2.0	0	-77.5	68	-77.2	70	
4.0	0	-82.2	66	-82.1	68	
0.0	45	N/A	N/A	-86.7	-110	
0.5	45	N/A	N/A	-85.9	130	
1.0	 45	-82.3	-26	-82.7	-24	
2.0	45	N/A	N/A	-82.6	9	
4.0	45	N/A	N/A	-85.2	32	

For the data presented here, the equivalent spatial period was chosen to be at least six times the maximum slot spacings in z. Errors on the order of 3 dB or more were observed for examples with smaller period sizes. For all of the test cases run to-date, the mutual impedance appears to stabilize to a value once terms up to $\gamma=20$ are included in the inverse transform of Equation (1.10). In fact, for slot separations involving nonzero ϕ_0 , a much smaller value of γ appears sufficient. For the admittance calculation, five point integration was used to compute Equations (1.3) and (1.4).

The computer execution times needed for the above calculations vary with the spacings between slots (the necessary spatial period and the associated sampling interval in γ), whether the axial or circumferential case is being used, and the number of terms retained before truncation in γ . As a rough guideline, data collected to date required between one and five minutes of execution time (per source slot) on the CDC CYBER 175, or two to ten hours on an AT&T 6300 desktop personal computer. It is felt that cylinder geometries up to about ten wavelengths in circumference can be treated within this execution time range. Of course, if desired, much larger cylinders could be treated with a corresponding increase in memory and execution time requirements.

5. ADDITIONAL DISCUSSION

While the numerical procedure outlined in this paper can not hope to compete with the accuracy of exact modal solutions or the efficiency of asymptotic approaches for the treatment of circular geometries, it is easily extendible to cylinders that are arbitrarily shaped. The numerical solution can also be used to treat cylinders with finite surface conductivity using an impedance type of boundary condition [17]. In general, an impedance condition will cause coupling

between transverse and axial components of current, and require the solution of a larger order matrix at each stage than required for the perfect conductor case.

The method proposed here is not without limitations, however. First, in comparison to the asymptotic methods the numerical scheme typically requires a much larger amount of computation time to obtain an accurate solution. Second, the magnetic field integral equation used for the formulation occasionally suffers from nonuniqueness problems associated with cylinders that are also resonant cavities. The non-uniqueness problem can be avoided by the use of the combined field formulation [18].

It appears from this preliminary study that it is feasible to approach the mutual coupling problem in the manner outlined above. The tradeoff between accuracy and efficiency may limit the method in practice to the treatment of cylinders with circumferences on the order of tens of wavelengths, yet no other technique exists with complete flexibility as to the surface shape. Future work will concentrate on the improvement of the accuracy for the circumferential case and the resolution of some of the potential problems discussed above.

6. REFERENCES

- [1] Commatas. C. G. and J. N. Sahalos (1983) Mutual coupling and radiation patterns of two slots asymmetrically located on a square plate. *IEEE Trans.*Antennas Propagat. AP-31:531-535.
- [2] Golden, K. E., G. E. Stewart, and D. C. Pridmore-Brown (1974) Approximate techniques for the mutual admittance of slot antennas on metallic cones, *IEEE Trans. Antennas Propagat.* AP-22:43-48.
- [3] Lee. S. W. (1978) Mutual admittance of slots on a cone: solution by ray

- technique, IEEE Trans. Antennas Propagat. AP-26:768-773.
- [4] Stewart, G. E. and K. E. Golden (1971) Mutual admittance for axial rectangular slots in a large conducting cylinder, *IEEE Trans. Antennas Propagat*. AP-19:120-122.
- [5] Lee, S. W., S. Savini-Naini, and R. Mittra (1977) Mutual admittance between slots on a cylinder, Electromagnetics Laboratory Report No. 77-8, UlLU-ENG-77-2549, Dept. of Electrical and Computer Engineering, University of Illinois, Urbana, IL.
- [6] Lee. S. W. and S. Savini-Naini (1978) Approximate asymptotic solution of surface field due to a magnetic dipole on a cylinder, *IEEE Trans. Antennas* Propagat. AP-26:593-598.
- [7] Bird, T. S. (1984) Comparison of asymptotic solutions for the surface field excited by a magnetic dipole on a cylinder, *IEEE Trans. Antennas Propagat*.

 AP-32:1237-1244.
- [8] Bird, T. S. (1985) Accurate asymptotic solution for the surface field due to apertures in a conducting cylinder, IEEE Trans. Antennas Propagat. AP-33:1108-1117.
- [9] Inami, K., K. Sawaya, and Y. Mushiske (1982) Mutual coupling between rectangular slots antennas on a conducting concave spherical surface. IEEE Trans. Antennas Propagat. AP-30:927-933.
- [10] Pathak, P. H. and N. Wang (1981) Ray analysis of mutual coupling between antennas on a convex surface, IEEE Trans. Antennas Propagat. AP-29:911-922.
- [11] Lee, S. W. (1982) A review of GTD calculation of mutual admittance of slot conformal array, *Electromagnetics* 2:85-127.
- [12] McGillem, C. D. and G. R. Cooper (1974) Continuous and Discrete Signal and System Analysis, Holt, Rinehart and Winston, Inc., New York.

- [13] Gradshteyn. I. S. and I. M. Ryzhik (1980) Table of Integrals, Series, and Products, Academic Press, New York, pp. 472.
- [14] Harrington, R. F. (1982 Reprint) Field Computation by Moment Methods, R. E. Krieger, Malabar, FL.
- [15] Andreasen, M. G. (1964) Scattering from parallel metallic cylinders with arbitrary cross sections. *IEEE Trans. Antennas Propagat.* AP-12:746-754.
- [16] Cheney. W. and D. Kincaid (1980) Numerical Mathematics and Computing,
 Brooks/Cole Publishing, Monterey, CA.
- [17] Andreasen, M. G. (1965) Scattering from cylinders with arbitrary surface impedance, *Proc. IEEE* 53:812-317.
- [18] Mautz, J. R. and R. F. Harrington (1978) H-field, E-field, and combined-field solutions for conducting bodies of revolution, A.E.U. 32:157-163.



A TECHNIQUE FOR LOW SIDELOBES IN MONOPULSE PLANAR ARRAY ANTENNAS

Anders G Derneryd ERICSSON RADIO SYSTEMS AB S-431 26 Molndal, Sweden

Abstract

Conventional monopulse planar arrays designed for low sum sidelobe levels suffer from high sidelobes in the two difference patterns. The monopulse function is obtained by combining the outputs of the four quadrants in a monopulse comparator, hence the amplitude tapering is the same for the sum and the two difference modes. The phase reversal and the amplitude discontinuity when forming the difference modes causes the high difference sidelobe levels.

This paper discusses a technique to accomplish low sum and difference sidelobe levels without going into a complex feed design.

The basic idea consists of creating a hole in the difference excitation functions at the center of the array. This results in a smoother projected linear distribution. The technique is realized with a passive lossles feed network.

A computer simulation of a monopulse planar array is presented. An improvement of 7 dB in the difference sidelobe level is demonstrated without affecting the sum pattern.

1 INTRODUCTION

In order to obtain great pracision in search— and track radars it has been found desirable to utilize monopulse antennas. In such a system a sum mode and two spatially orthogonal difference modes are provided to derive the angular location of the target.

A widely used antenna for phase monopulse technique is the planar slot array. The antenna aperture is divided into four quadrants and the monopulse function is obtained by combining the four outputs in a monopulse comparator. The sum pattern is achieved with all quadrants added in phase and the difference patterns are achieved with pairs of quadrants added in phase reversal. The amplitude tapering of the antenna excitation is thus the same for the three modes.

Theoretically, the three excitations can be independently tapered since they represent orthogonal functions. However, the required feed network is usually considered too complex to make a practical design attractive at least for a slotted waveguide antenna.

This paper presents a technique to simultaneously realize low sum and difference sidelobe levels without going into a complex mechanical design.

INDEPENDENT EXCITATION CONCEPTS

2

A tradeoff between the optimum sum and difference beam performance is required when the three monopulse modes are not independent of each other. Assume that an optimum sum pattern is choosen then the sidelobe levels of the two difference patterns are unsatisfactorily high because of the abrupt phase discontinuity between pairs of quadrants. Similarly, when the design is optimized for the elevation difference pattern both the sum and the azimuth difference patterns will experience high sidelobe levels. This dilemma is illustrated in figure 1.

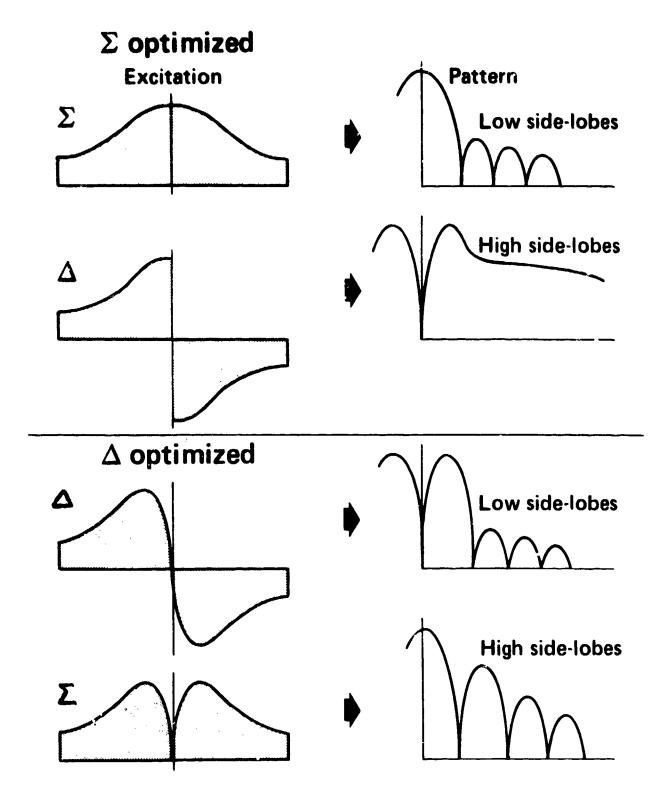


Figure 1 Excitation functions and corresponding radiation patterns of a conventional monopulse array antenna.

A compromise is not a very good solution either since the optimum excitations of the three modes are vastly different. However, a technique has been suggested (reference 1) for a planar waveguide fed slot array. The compromise design is created by taking the average of the slot offsets and slot lengths for the three optimum modes. This technique permits improvement in the difference pattern sidelobe levels at the cost of some degradation in the sum sidelobe level.

In stripline—fed slot arrays a rather complex feed network can be employed in order to improve the performance of the three monopulse modes (reference ?). Each quadrant is partitioned into a number of subarrays which can be independently excited for the three modes. For each set of four symmetrically located subarrays, a sum and two difference signals are created with separate monopulse comparators. All sum signals are then combined to form a total sum signal atc. Thus there are three separate networks to individually optimise the weighting of the subarrays for the three modes independently. This is gained at the expense of some increased loss and of going into a multilayer circuit design.

A complete independent realization of the three monopulse modes requires control of the amplitude and the phase of each element or pair of elements. A network that permits that has been presented (reference 3). A nested feed concept has been employed for a 112 element primary feed array. The need to perform a tradeoff between the three modes is eliminated at the cost of using a great number of stripline boards and coaxial cables.

3 IMPROVED SIDELOBE PERFORHANCE

An optimum sum amplitude excitation and an optimum difference amplitude excitation differ mainly close to the center of the array as seen in figure 1. The optimum difference excitation has an amplitude blockage or hole at the center besides the usual phase reversal. An improved difference amplitude excitation is thus obtained by subtracting power from the optimum sum excitation at the center of the array.

A practical technique is to design the array for an optimum sum mode and physically divide the array into five subarrays. First one part is created at the center of the antenna while the rest is equally divided into four parts. See figure 2. A conventional monopulse comparator is connected to the outputs of these four subarrays to form a sum and two difference channels.

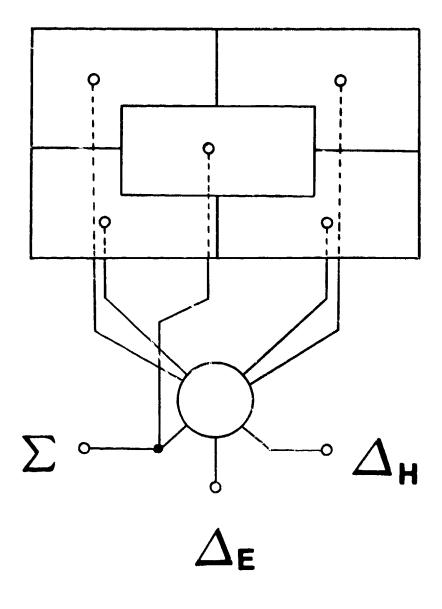


Figure 2 Improved monopulse array antenna

The center subarray is coupled in phase directly to the sum channel of the comparator to form a total sum channel. Hence, all subarrays are active and the optimum sum amplitude excitation is choosen as in a conventional monopulse array antenna.

The difference channels are formed with only four subarrays active thereby excluding the center part. The size of the center subarray controls the difference patterns and it can be adjusted without affecting the sum mode. Since part of the antenna and feed network are common for both the sum and the different modes these are not completely independent.

However, this new feed method provides a monopulse antenna having good radiation patterns and in which the monopulse modes are separately designed for optimum performance.

The extra lossles feed network that is necessary is very simple and it can be realizable both in waveguide and stripline technology.

COMPUTER RESULTS

The technique just described has been used to design a circular monopulse suot array having 148 elements. The diameter of the antenna is 300 mm and the interelement spacing is 20 mm. The design frequency is 10 GHz.

A 25 dB circular Taylor distribution is desired for the sum mode. Typical calculated cuts of the sum and difference modes are given in figure 3 for a conventional monepulse slot array. The sum sidelobes are below -25 dB and the neak difference sidelobes are only -14 dB below the sum beam peak.

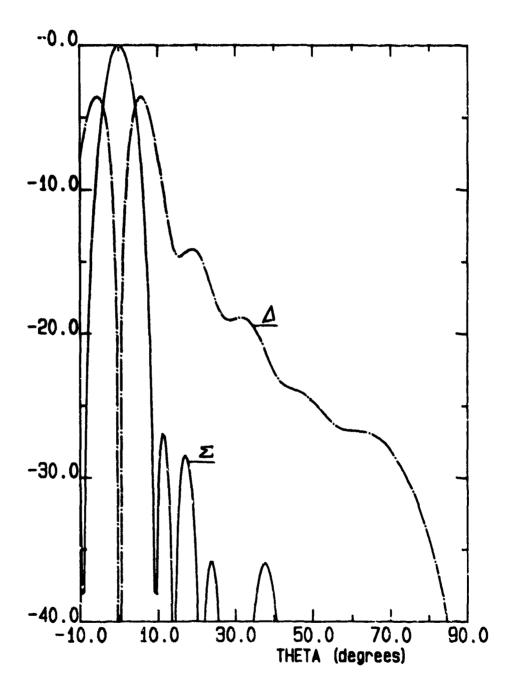


Figure 3 Computed radiation patterns of a conventional monopulse array antenna.

An improved difference pattern is achieved by introducing a fifth subarray at the center of the antenna. The size of the center part controls the difference sidelobe levels. The maximum sidelobe level along the H-plane has been calculated for different sizes at the center part. The result is plotted in figure 4. The sidelobe level decreases with increasing size until the diameter of the center part is about 0.4 of the accenna diameter. Thus it is possible in this example to improve the difference sidelobe level up to 7 dB by excluding the center part of the antenna when forming the difference modes.

An example of partitioning the monopulse array antenna is given in figure 5. The introduced center part is cross shaped and it has a diameter of 120 mm. This corresponds to about 16 % of the total area of the antenna. The same Taylor distribution as before is used giving an unaffected sum pattern. However, the center part of the array is not used in the difference channel thus creating a dip in the projected linear amplitude distribution. Calculated cuts of the sum and the difference patterns are shown in figure 6 for the improved monopulse slot array. The sum sidelobe levels are as before but the peak difference sidelobe is lowered to -21 dB. An improvement of 7 dB in the difference sidelobe levels is thus achieved.

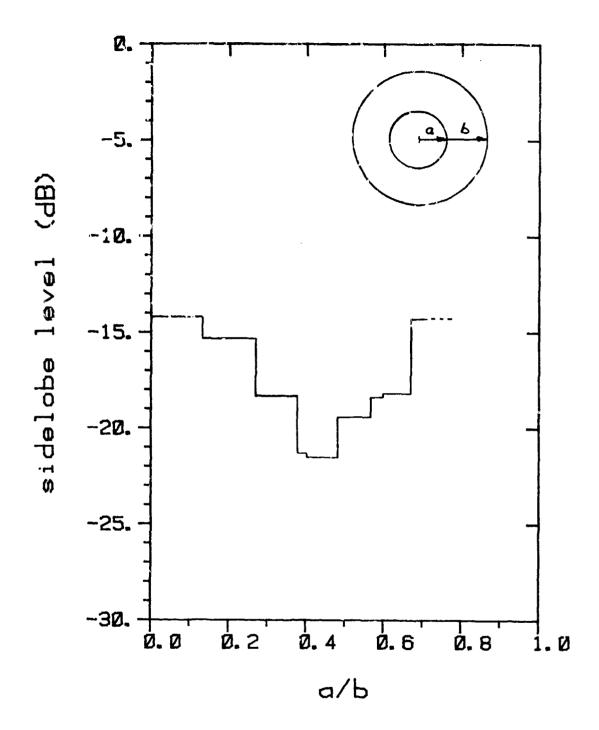


Figure 4 Calculated maximum difference sidelobe level along the H-plane.

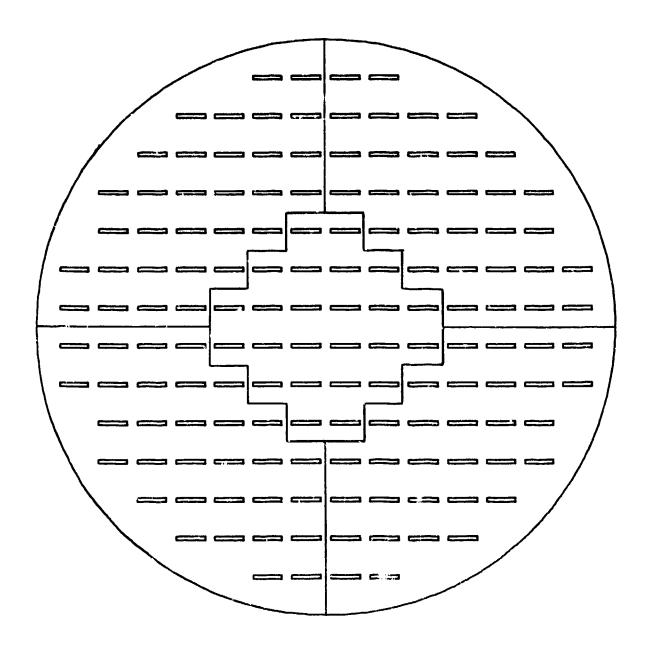


Figure 5 Example of partitioning a monopulse array antenna.

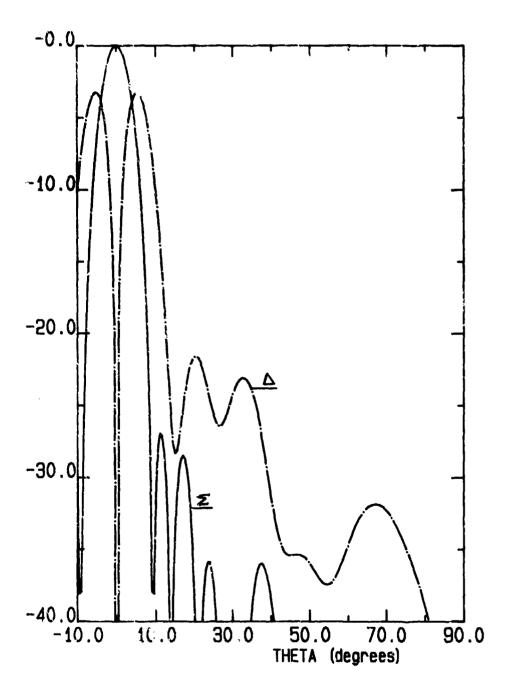


Figure 6 Calculated radiation patterns of an improved monopulse array antenna.

5 CONCLUSTON

A technique has been described which permits improvement in the difference pattern sidelobe levels for a planar slot array. This is achieved by introducing a fifth center subarray in a conventional four quadrant monopulse array. This center subarray is coupled directly to the sum channel and it is not used when forming the difference channels. Thus sum and difference modes are designed separately for optimum performance. The technique is realized with a passive lossles feed network.

6 REFERENCES

- Schaftner J.H., Kim D and Elliott R.S.,

 "Compromises among optimum sum and difference
 patterns for planar waveguide-fed slot array",

 Alta Frequenza, vol. L, pp 312 319, Nov Dec 1981
- Josefsson L, Moeschlin L and Sohtell V, "A monopulse flat plate antenna for missile seeker", Proc Military Electronics Defense Expo, Wiesbaden, Sept 1977
- Pizette S and Toth J, "Monopulse antenna networks for a multielement feed with independent control of the three monopulse modes", Proc IEEE MTT-S

 Symp, pp 456 458, 1979

PHASED ARRAY ANTENNA FOR SPACE SHUTTLE ORBITER

Shayla E. Davidson

NASA Lyndon B. Johnson Space Center

Houston, Texas

ABSTRACT

The National Aeronautics and Space Administration is developing a distributed phased array antenna at the Lyndon F.

Johnson Space Center as a possible upgrade for the Space Shuttle Orbiter S-band phase modulation communications system. The antenna consists of an eight-element transmit section, eight-element receive section, and a single L-band receive element.

The antenna design is constrained by the existing Orbiter system and space environment. The solution to the interface design problems led to an antenna system which provides improved link margins and yet supports previous operational configurations.

This paper describes the system development, antenna hardware, and the interface considerations which led to the final design.

1. INTRODUCTION

The S-band phased array antenna is being developed to provide a proof of concept for a possible upgrade to the quad antenna currently being used for the S-band phase modulation (PM) communication system on the Space Shuttle Orbiter. The Orbiter

has historically exhibited less than desirable link margins with this system, and a phased array antenna is one solution to this problem. The phased array antenna also uses solid state components, which do not have the arcing problems of the current antenna.

The current antenna consists of two crossed dipole antennas that can be switched to produce two beams. The Orbiter has four of these antennas mounted in the forward fuselage (Fig. 1), hence the name "quad antennas." Depending on which quadrant the signal is in, the antenna system utilizes one of the four antennas in one of the two beam positions, during normal operation. The current antenna thus limits the Orbiter to eight beam positions for full spherical ocverage. Antenna coverage is at least 3 dB

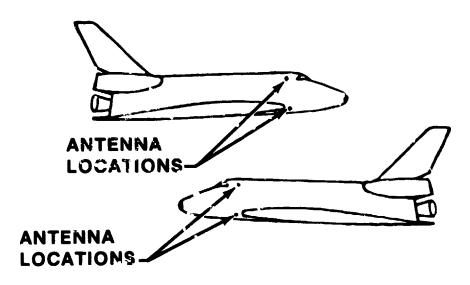


Fig. 1 S-band quad antenna placement on Space Shuttle Orbiter.

for only 50% of the sphere. Because the power is generated via a traveling wave tube amplifier before distribution to the antennas, the switches at the antenna locations to control the beam position are mechanical. These switches have demonstrated arcing problems on past Orbiter missions.

2. SYSTEM DEVELOPMENT

The original phased array antenna system design was a passive phased array with no active components at the array level. An active component is defined as one requiring direct current (dc) power to operate, such as an amplifier. The addition of active amplifiers for both transmit and receive functions significantly improved the calculated link margin of the phased array antenna and also allowed the power amplifier and preamplifier to be removed from the S-band PM system. This concept had been investigated previously, but the heat load at the antenna was too high to be dissipated passively. A new design was initiated in 1984 because of advances in amplifier technology that promised a reduced heat load, making the possibility of flying an active array again feasible.

The initial 1984 phased array antenna design called for a 16-element active array. The design included a microprocessor controller for selecting the antenna beam and setting the phase shifters. Each element would be part of an electronic chain

consisting of a phase shifter, a circulator after the phase shifter to isolate the transmit and receive paths, a high power amplifier (HPA) for the transmit path, an isolator to protect the output of the HPA, a second circulator to isolate the transmit and receive paths at the antenna port, the antenna element, a filter for the receive path, and a low noise amplifier (LNA) for the receive path. Each phase shifter would be connected to a 16-way power divider to bring the combined signals to the single radiofrequency (RF) port which presently exists in the quad system configuration.

Further system studies identified microstrip antenna elements as the best element candidate because of the low profile. The only disadvantage was an inherently narrow bandwidth which would not cover the entire band from 1.7 to 2.3 GHz. A study of alternate system configurations led to the concept of separating the transmit and receive functions in the array, thereby removing the requirement for the two circulators. The narrow bandwidth of the microstrip element also protects the receive path, which deleted the requirement for a filter, since the isolation between transmit (2.2175 and 2.2875 GHz) and receive (2.0419 and 2.1064 GHz) is now provided by the system configuration. The reduced area of the individual transmit and receive arrays is compensated for by the reduction in path loss due to the removal of the

circulators and filters. A single element at 1.75 GHz was designed to cover the requirement for 1.7767 and 1.8318 GHz for the Space Ground Link System. A triplexer is included to combine the transmit, S-band receive, and L-band receive on the single RF port.

The eight-element receive and transmit subarrays are oriented so that there are four elements in the roll plane and two elements in the pitch plane. This placement allows for three beams across the pitch plane (180° from nose to tail) and seven beams across the roll plane (45° from the ton to side or side to bottom). The three-bit phase shifters result in a phase resolution of 45°, which results in 21 beams per antenna (Fig. 2) or 84 beams per Orbiter. The narrower beamwidths significantly improve the directivity and, therefore, gain of the antennas. The phased array antenna has a calculated gain of 13 dB on boresight and 9 dB when scanned ±90° off boresight, which does not include element gain. The effective isotropic radiated power of the antenna will vary from 26.7 dBW on boresight to 24 dBW when scanned 70° from boresight. Antenna coverage is calculated to be 10 dB over 85% of the sphere.

A schematic of the array is shown in Fig. 3. The radiating elements, triplexer, and microprocessor controller were designed

and fabricated in-house. The HPA's, LNA's, power divider/
combiner and phase shifter subassembly, and active limiter were
purchased. The operating temperature range for all components
was specified as -25° to +65° C, and the nonoperating temperature

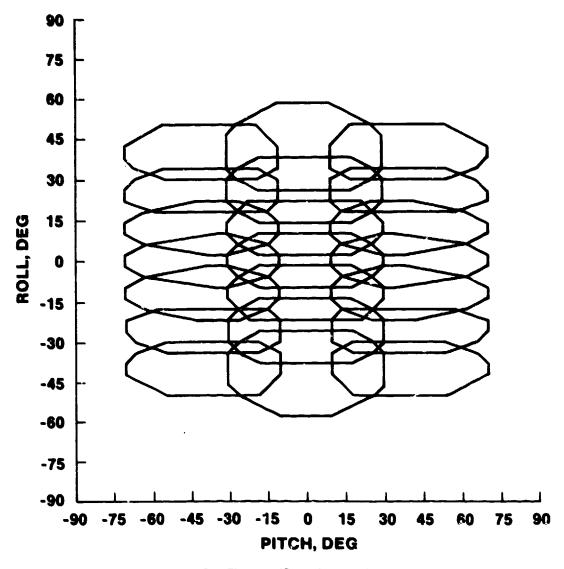


Fig. 2 Three dB gain contour.

range was specified as -65° to +100° C. The array components are discussed individually in the following section.

3. ARRAY COMPONENTS

The radiating elements for the S-band phased array antenna consist of 17 microstrip elements: 8 transmit, 8 receive, and 1 L-band receive for the Space Ground Link System frequencies.

Each element is designed as a rectangular microstrip patch with a corner feed. The two orthonormal modes thus excited provide right hand circular polarization. The antenna elements are fabricated from a 0.3175 cm thick Rogers 5880 duroid substrate. Element spacing in the pitch plane is every 0.47 wavelength and in the roll plane is every 0.56 wavelength. The layout is shown in Fig. 4. Element voltage standing wave ratios (VSWR's) range

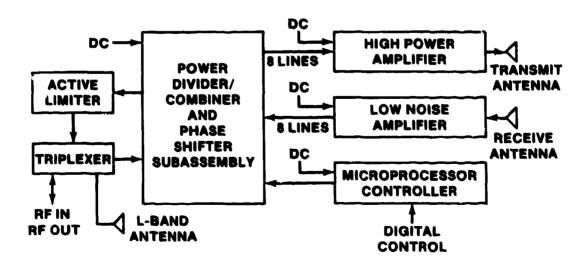


Fig. 3 Phased array antenna schematic.

from 1.15:1 to 1.5:1. The peak gain of the elements ranges from 4.4 to 7.3 dB.

The triplexer for the S-band phased array antenna is required to separate the transmit, receive, and L-band receive paths.

This triplexer consists of a common RF port for the antenna RF connector, a circulator to separate transmit and receive, a matching network to combine the received signal from the 5-band LNA's and the L-band element, bandpass filters for each receive frequency, and isolators for each receive frequency (Fig. 5).

The isolators and circulator provide channel isolation, and the circulator also reduces the insertion loss in the transmit path

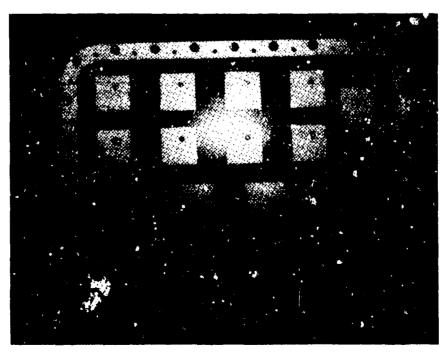


Fig. 4 Radiating aperture layout.

and therefore improves the transmit link margin. A transmit bandpass filter is included, because the initial design did not include the circulator, and transmit signals were therefore required to go through the matching network. With the addition of the circulator, the transmit bandpass filter is no longer required and is therefore connected to a 50 ohm load. For each path, the VSWR's are 1.13:1 or better, and the highest insertion loss is 2.9 dB between the common output and the S-band receive input, which does not significantly degrade the link margin since this loss is after the LNA's in the receive path. Isolation is 75 dB from the common input to the receive inputs and greater than 20 dB from the receive inputs to the transmit output.

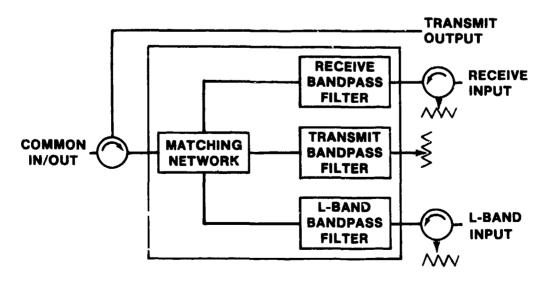


Fig. 5 Triplexer block diagram.

Isolation is greater than $48~d\mathbb{B}$ from the transmit output to the receive inputs.

The microprocessor controller for the S-band phased array antenna sets the phase shifters based on the desired pointing angle and returns telemetry data. Roll and pitch angles are compared to a data list which determines the beam. The phase shifter bit pattern for this beam is then output to the phase shifters. The microprocessor returns telemetry consisting of the selected beam number, microprocessor health data, one of the HPA temperatures, and a flag for the HPA RF power levels. The data exchange occurs every 2 sec, which means that it takes 16 sec to poll all of the eight HPA temperatures.

The HPA's are placed in the transmit paths to raise the power just before the antenna elements. Each three-stage amplifier was specified to produce 7 W RF output at the transmit frequencies and be at least 30% efficient. When these amplifiers were tested at -25°, +23°, and +65° C, the highest temperature tended to produce a slightly low output power (6.62 W minimum, instead of 7 W). Efficiencies range from 32.0% to 42.5%. Circulators are included internally on the input and output of each HPA to allow the HPA to operate with a VSWR of any magnitude and phase, on either input or output. The HPA temperature and detected RF output power level are provided as dc voltages.

The LNA's are included in the S-band phased array antenna to reduce the noise figure and increase the signal-to-noise ratio. There are eight LNA's, one for each of the eight receive elements. The candidate LNA was placed in the Electronic Systems Test Laboratory Orbiter S-band PM receive configuration. The bit error rate was improved by 1 dB when the Orbiter S-band pre-amplifier was replaced with the candidate LNA. The LNA's for the array were therefore ordered with gain tolerances from 35.0 to 36.5 dB and a 1.5 dB noise figure. Actual test data show that the LNA's have noise figures of 1.28 dB maximum and a maximum VSWR of 1.8:1. The total power dissipated by all eight units is 9.62 W.

The 16 phase shifters, 8-way power divider, and 8-way power combiner for the antenna are integrated into a single subassembly that requires less volume and provides a lower insertion loss because of the direct connections from the phase shifters to the power divider and power combiner ports. Insertion losses are 12.9 dB maximum and VSWR's are 1.52:1 maximum. The minimum isolation is 18.7 dB.

An active limiter is inserted in the receive path of the antenna to protect the Orbiter S-band transponder from excess RF energy. The device limits the RF power to -25 dBm in the receive

path between the power combiner and the triplexer and is reflective when limiting.

4. ORBITER INTERFACES

The existing cavity in the Orbiter must be used for the S-band phased array antenna, since fabricating new holes in the Orbiter structure and routing new cables would be too costly. The cavity was therefore defined as the maximum available envelope for the phased array. The current antenna does not utilize all of the cavity, so a study was performed to define the limits of the cavity. It was found that the cavity was smaller toward the front of the Orbiter, and that the upper and lower cavities differ. The antenna housing for the upper right antenna based on the cavity dimensions is shown in Fig. 6. All of the antenna components must be mounted in this housing, as shown in Fig. 7. The phased array antenna requires one more connector than the current antenna, so the connectors on the housing had to be placed to fit through the hole in the skin in the Orbiter during mounting.

The phased array antenna is designed to be cooled passively, since it is impossible to route cooling lines to the antenna locations without modifying the Orbiter structure. The phased array antenna can dissipate a maximum of 94 W of heat using cooling straps tied to the frame of the Orbiter.

The phased array antenna requires pointing angles in roll and pitch to set the correct phase shifter bit pattern. This information is generated in the Orbiter antenna management software and can be routed to a multiplexer/demultiplexer (MDM). The phased array antenna interfaces with the MDM via a digital control line. Telemetry from the phased array antenna is also passed through the MDM.

The Orbiter has the capability of allowing the crew or ground control to select one of the existing eight antenna beams. To maintain this function, the phased array antenna has a mode which mixics the fore or aft beam of the current antenna if the



Fig. 6 Antenna housing for upper right phased array antenna.

pointing angles are not present on the digital control line.

The current antenna has only 28 V do power supplied to it. The phased array antenna requires a variety of do power levels for its active components. Rather than convert the do power at the antenna location and generate additional heat, the do power is converted in the Orbiter avionics bay, and separate do power lines are then routed to the antenna locations.

The phased array antenna requires less input power than the current antenna, since the power level is boosted at the antenna elements by the HPA's on transmit and the LNA's on receive. For this reason, the preamplifier and power amplifier in the S-band



Fig. 7 Phased array antenna components mounted in housing with walls removed.

PM system can be removed for the phased array antenna system.

This saves power and also leaves more room in the avionics bay
for other avionics system components.

5. CONCLUSIONS

The phased array antenna will maintain a better link margin during all modes of operation than the current antenna and has produced a more efficient system requiring less power. The phased array antenna will provide 10 dB over 85% of the sphere, compared to 3 dB over 50% of the sphere for the current antenna. In addition, the arcing problem of the current antenna has been overcome and additional benefits of more room in the avionics bay will be achieved. Current estimates predict that the phased array antenna system will be half as expensive as the current antenna system.

Final assembly and testing is planned for the remainder of 1986 with environmental tests occurring in early 1987. The results of all these tests will then be presented to the Space Shuttle Projects Office with specifications for an operational system and final recommendations. The decision whether to retrofit the existing Orbiters or to include the phased array design on future Orbiters can then be made.

86:EE33:034:Text NASA-JSC

A HEMISPHERICALLY SCANNING X/KA BAND MIRROR ANTENNA

Kurt Hollenbeck Dr. Oren Kesler

Texas Instruments, Inc. Antenna Department McKinney, Texas

Overview:

Texas Instruments, under contract to Naval Surface Weapons Center (NSWC), has delivered the first proof of concept, prototype X and Ka band Mirror Scanning Antenna to the Navy. This antenna is a candidate for the Navy's new generation of ship self defense vieapon systems and culminates over two years of work by Texas Instruments' Antenna Department.

Several unique operational features are offered by the Mirror Scanning Antenna. These features include full hemispherical scan coverage, simultaneous X and Ka band dual plane monopulse tracking, rapid scan rates, variable scan modes, high Ka band power handling ability, and an integral weather tight protective radome.

These features allow the Mirror Scanning Antenna to be used for shipboard tracking of multiple incoming low flying, low observable aircraft and sea skimming missiles. The dual frequency capability allows incoming threats to first be located with the broader beam of the X band signal then accurately tracked with the narrow beam high power Ka band signal. The high Ka band power can then be used to

exploit slight surface irregularities on a low observable target to further enhance target tracking against the sea clutter environment. Rapid scanning allows several targets to be tracked at once giving the Navy multiple tracking channels from a single antenna. Variable scanning modes allow an optimum scanning method to be used depending on the target classification, sea clutter environment and target trajectory. The rugged integral radome protects the system from the harsh ship deck environment.

Antenna Operation:

The Mirror Scanning Antenna consists of four main components. These components, shown in figure 1, are the hydraulic gimbal, the dual band feed, the parabolic radome/transreflector and the twist reflecting mirror.

The antenna system, in the transmit mode, operates under the following principles. Energy which is linearly polarized leaves the feed horn and strikes the parabolic transreflector. Embedded in the transreflector is a wire grid that is parallel to the direction of the incident linearly polarized electric field. Upon striking the grid, the spherical wave front from the feed is collimated by the reflection from the parabolically shaped transreflector. The reflected energy then travels back toward the twist reflector mirror structure. The energy impinging upon the twist reflector mirror is then reflected back toward the transreflector with the linear polarization rotated by 90 spatial degrees. When this re-reflected energy strikes the

transreflector grid it is polarized perpendicular to the grid and thus passes through the transreflector and out into space.

To achieve a scanning beam from this antenna it is only necessary to move the twisting mirror structure to an angle other than along the transreflector axis. When the polarization twisting mirror is gimbaled, the reflected energy from the transreflector is moved through space at twice the angle of the twisting mirror. This two to one angle advantage allows the antenna beam to be scanned to 90 degrees while only moving the twisting mirror structure to 45 degrees. It is this two to one angle advantage which allows the Mirror Scanning Antenna to rapidly track multiple targets that are widely spaced.

Antenna Requirements:

To fulfill the mission of ship self defense, the Mirror Scanning Antenna must meet certain requirements. These parameters include complete he mispherical scan coverage, 10% instantaneous frequency bandwidths centered around 9.0 GHz and 35.0 GHz, narrow beamwidths, moderate sidelobe levels and high power handling capability at Ka band. These design parameters and their desired performance goals are listed in Figure 2.

The need to handle average power levels of 10 Kilowatts and peak power levels of 100 Kilowatts at 35.0 GHz required special attention in the design of the antenna. It was necessary to pressurize the waveguide feed assembly to prevent high power dielectric breakdown and subsequent arcing. In order to pressurize the feed

assembly, a high power ceramic feed radome was placed over the open end of the feed horn. In addition to feed pressurization, the entire teed assembly was surrounded by water jackets for cooling purposes. Low loss, high temperature dielectric materials were used to insure that the transreflector and twist reflector would not burn up during high power operation.

Hardware Description:

Hydraulic Gimbal:

The hydraulic gimbal for the Mirror Scanning Antenna was designed and fabricated by Dr. L. H. Russell from Naval Surface Weapons Center. The gimbal uses hydraulic actuators to apply torque to the upper and lower gimbal arms. The gimbal arms are attached to the mirror plate of the antenna through spherical bearings. The gimbal is shown in figure 3. As the gimbal arms are move, the mirror plate is also moved and the antenna is scanned. Using this hydraulically actuated gimbal scheme, the mirror plate can be moved to any location from 0 to 48 degrees with an accuracy of 0.01 degrees. The speed and precision of this gimbal mechanism allow the antenna to accurately track multiple targets throughout a hemispherical region of coverage.

Dual Band Feed Assembly:

The Mirror Scanning Antenna uses a X/Ka dual band four lobe monopulse multimoded feedhorn. The multimoded feedhorn was chosen over a conventional four horn feed for improved performance between the sum and difference channels. This improved performance is the result of batter power distribution to the reflector as well as keeping the sum and difference channels at the reflector's focal point.

The feedhorn assembly consists of eight main sections: the adapter block, comparators, Ka band waveguide adapter section, X/Ka waveguide combiner section, waveguide extension section, X/Ka waveguide adapter section, feedhorn/moder section and the feedhorn radome. These sections are surrounded by water jackets which are linked together using standard 0.25" copper tubing. The feedhorn assembly sections are shown in figure 4. Electrical operation of the feed is based on a four channel monopulse waveguide run feeding a multimoded feedhorn section. The monopulse processing is done in a waveguide comparator which is located at the input to the feed assembly. When power is delivered to the feed assembly, it is divided four ways in the comparator and fed to the multimoded feedhorn in four separate waveguide runs.

Each of the four waveguide runs must be of equal electrical length for proper phase summation. As the input power enters the multimoded horn, each pair of input waveguides are tapered up to the moder junction. At the moder junction, the energy which was constrained inside the waveguide pair transfers abruptly into the multimoded cavity of the horn. For signals which are fed into the moding cavity in phase, the TE₁₀ modes of the input waveguides transforms to TE₁₀/TE₃₀ waveguide modes at the moder junction to

form the antenna sum beam. For signals which are fed 180 degrees out of phase, the TE_{10} input waveguide modes transform to form the moding cavity TE_{20} antenna difference channel mode. This mode forming is shown in Figure 5.

The feedhorn assembly for the Mirror Scanning Antenna combines both the X and Ka multimoded horns into one unit. This was done for two reasons. First, it keeps both the X and Ka feedhorns located at the focal point of the parabolic transreflector and thus yields coincident beams. Second, it allows the feed assembly to fit within the size limitations put forth by the hydraulic gimbal mechanism.

Twist Reflector:

The twist reflector is a 60 inch diameter circular gimbaled flat plate which steers the antenna beam in space. The twist reflector acts both as a reflecting mirror and a polarization rotation device. In the center of the twist reflector, a hole is cut to allow the feed assembly to protrude through. This is shown in Figure 6.

The function of the twist reflector is to reflect the incident E field with a 90 degree spatial polarization rotation. This is accomplished by orienting the twist reflector grid wires at 45 degrees with respect to the transreflector grid lines. The field that is incident on the twist reflector then has half of its energy oriented parallel to the wires, while the other half of the energy is oriented perpendicular to the twist reflector wires. The polarization twist is accomplished by phase

shifting the reflected parallel energy by 180 degrees in time phase with respect to the perpendicular reflected energy. This phase shift is a result of the small metallic wires which act as inductive shunt susceptance elements.

The twist reflector circuits are etched on a 0.0025" thick copper clad fiberglass sheet. There are two layers of circuits spaced apart by one layer of honeycomb. Another honeycomb layer separates the circuits from the aluminum groundplane of the mirror support structure. A cross-sectional view of the twist reflector circuit is shown in Figure 7.

Radome/Transreflector:

The radome and transreflector are integrated into a single structure. The shape of this structure consists of a cylinder with a parabolic top and a circular mounting flange. A smooth arc is used to transition between the cylindrical wall and the parabolic top.

The radome consists of two fiberglass skins separated by a low density honeycomb core. This sandwich design allows the radome to pass both the X and Ka band frequencies with an efficiency greater than 90%. The radome sandwich structure transitions into the electrically opaque solid fiberglass mounting flange area at the base.

The parabolic transreflector consists of a grid of parallel metal lines 0.005" wide spaced apart by 0.015". These metal lines are embedded 0.005" into the inner radome skin over the 40 inch diameter parabolic section. The orientation of the grid is aligned with the

principal polarization from the feedhori? El field. The grid section is made up of 16 pie shaped sections and one circular section at the top. Each of these sections was etched flat with curved grid lines so that once placed on the parabolic tool the locally parallel lines would project as straight lines.

The radome transreflector is painted with a white flourelastomeric hydrophobic paint. This paint helps to reduce solar heat loads inside the radome and also prevents rain and sea water from degrading the antenna performance. The completed transreflector mounted on the Mirror Scanning Antenna is shown in Figure 8.

Testing:

Mirror Scanning Antennas have the unique property of having their linear polarization rotate with the beam scan angle. This rotation property makes testing and target tracking more difficult than for a standard reflector antenna. In this case, the hemispherical scan limits accentuate this property. Therefore, in order to be able to take useful test data, and later successfully track targets, a mathematical solution to the polarization rotation, with scan angle, was developed.

To solve the transformation and to compute the antenna polarization, a mathematical model was constructed which consisted of a 3x3 coordinate transformation matrix. The input polarization to this matrix was a simple unit vector located along the -Y axis (0, -1, 0). From here, the known polarization behavior along the major axes and

the 45° axes was modeled in the 3x3 matrix. This was programmed on the computer and the on axis performance was verified. Further study of the polarization behavior showed that the behavior of the polarization at all angles could be modeled as three separate rotations of the polarization vector. The coordinate system for this rotation is shown in Figure 9-a. The rotation order is as follows: first alpha (α), then beta (β), and finally gamma (γ). The first rotation, α , rotates the original coordinate system about the z-axis so that the angle θ now appears as a rotation about the new x'-axis (Figure 9-b). The second rotation, β , causes the original z-axis to become coincident with the normal to the rotated polarization vector (Figure 9-c). The final rotation, γ is about the new z"-axis of the rotated coordinate system and is the inverse to the first rotation (Figure 9-d). The final transformation matrix is listed below.

$$T = \begin{bmatrix} \cos \gamma \cos \alpha - \sin \gamma \cos \beta \sin \alpha & \cos \gamma \sin \alpha + \sin \gamma \cos \beta \cos \alpha & \sin \gamma \sin \beta \\ -\sin \gamma \cos \alpha - \cos \gamma \cos \beta \sin \alpha & -\sin \gamma \sin \alpha + \cos \gamma \cos \beta \cos \alpha & \cos \gamma \sin \beta \\ \sin \beta \sin \alpha & -\sin \beta \cos \alpha & \cos \beta \end{bmatrix}$$

The antenna was tested for 2 months on a 2000' long range. The antenna, mounted on top of a 90-foot test tower is shown in Figure 10. The associated cables coming out of the antenna are for the hydraulic lines, the gimbal computer control lines and the RF signal cables. The hydraulic pumps, which powered the antenna gimbal, were located at the base of the tower while the gimbal computer controller was located in the control room at the top of the tower.

The range measurements were made to quantify the antenna performance at both X and Ka frequency bands over many different scan angles. To quantify the antenna performance, measurements included beamwidth, sidelobe level, null depth, cross polarization, gain and X/Ka band beam coincidence. These measurements were conducted at 20 different scan angle positions for 6 frequencies, (3-X band, 3-Ka band), in both the principal E and H plane of the antenna. In addition to these measurements, a single pattern was measured in a non-principal plane to confirm off axis performance of the antenna. At the end of the 2 month testing period, over 500 individual antenna patterns had been taken.

To successfully test the antenna, a pre-determined set of antenna range positioner coordinates was computed for every scan angle measured. These coordinates were based on the previously solved polarization rotation transformation and enabled the antenna to be measured in the principal E and H plane. The solution of these range positioner coordinates required the creation of a complete

mathematical model of both the range gimbal movement and the antenna polarization transformation. Once this model was completed, a conjugate gradient method of solution was applied. This then gave a unique solution for pointing the antenna beam down range with the correctly oriented polarization needed to achieve the required principal E and H plane patterns. Figure 11 shows the coordinate system used for range testing as well as the beam angles associated with each beam position number.

The beam positions tested were chosen to gain maximum information about the antenna performance. Because it was felt that the antenna performance would be symmetric throughout the hemisphere, intensive testing was done only in one quadrant. Outside of this quadrant, only select beam positions were looked at to verify the expected symmetric performance of the antenna. The quadrant chosen for intensive testing was determined by the direction the Navy oriented the system during their target tracking experiments.

Testing Results:

Results of the range testing show that the beamwidth, sidelobe levels, null depth and gain do not change significantly over the hemispherical scan angles. However, significant changes were seen in the cross polarization with scan angle. These changes are the direct result of the transreflector polarization filter effect near zenith scans and the degrading twist reflector performance at horizon scans. Because the majority of the antenna parameters remain well behaved

versus hemispherical scan, a representative set of antenna patterns is shown in Figures 12 and 13.

Looking at the representative antenna patterns, it is noted that the 9.0 GHz sidelobe levels are a very high 9 dB below the main beam. For 35.0 GHz, the sidelobe levels are better but still high at about 13 dB below the main beam. These high 9.0 GHz and 35.0 GHz sidelobe levels are the direct result of extensive blockage from the hole in the twist reflector mirror plate. In addition to blockage, the poorer X band sidelobe levels are caused by the use of a non-optimum X band feed aperture layout and improper X band focusing. The non-optimum X band feed layout, selected in the design trades, is the result of placing the Ka band feed between the two X band feeds. Improper X band focusing resulted because the phase centers of the X and Ka feedhorns were not co-located. The optimum focal location for the feed was therefore based on the Ka band signal to optimize its performance. Each of the causes of the high sidelobe levels has been analyzed and much lower sidelobes are expected after the necessary rework is completed.

Antenna sidelobe levels, beamwidths, cross polarization and gain levels were measured throughout the hemisphere. These parameters are plotted in Figure 14 for 9.0 GHz and Figure 15 for 35.0 GHz. Looking over the data, it is seen that except for cross polarization, antenna performance remains well behaved over all hemispherical scan angles. This well behaved performance, even over such a large

scan volume, is one of the strong features of the mirror scanning antenna. Because the antenna achieves scan simply by moving a flat reflecting mirror, there are no unusual performance variations of the sidelobes, gain or beamwidth levels throughout the hemisphere.

One parameter which does vary drastically with scan angle is cross polarization. The apparent erratic cross polarization performance is the result of two factors. First, the polarization filtering effects of the transreflector are lost for theta scan angles over 70 degrees. Second, the twist reflector circuits were designed to give maximum performance over theta scan angles from 0 to 60 degrees to reduce the antenna VSWR. Therefore, the cross polarization performance variation with scan angle is a combined result of the transreflector and twist reflector circuit operation. It is seen that the worst case cross polarization occurs at theta = 90 degrees (horizon scan) for any phi angle. It is feit that with new analytical tools which are now available, the twist reflector cross polarization performance can be greatly improved in the future.

The monopulse error slope was computed using the delta/sum ratio plotted verse scan angle. After the error slopes for the 21 beam scan positions were computed and plotted, they were condensed to give an error slope envelope. This envelope represents the bounds of the error slope curve as the antenna scans throughout the hemisphere.

Figures 16 and 17 show the typical error slope curves for 9.0 and 35.0 GHz respectively. Studying the error slope envelope curves, it is

seen that the linear region extends over the +/- half power beamwidth points for both frequency bands. Within this linear region the envelope for all hemispherical scans narrows. This shows that throughout the hemisphere, the antenna performance remains nearly constant.

An overview of the measured performance of the antenna versus the performance goals is shown in Figure 18. Most of the causes of the performance degradation have been located and analyzed. The two areas of the antenna which need to be upgraded for performance improvement include the feed assembly and reduction in the twist reflector blockage. Improvements in these two areas will be initiated in a performance upgrade program.

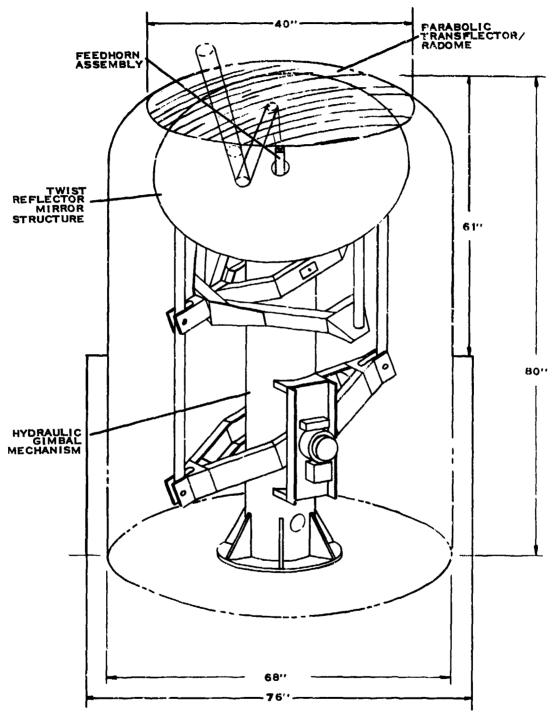


FIGURE 1 MIRROR SCANKING ANTENNA MAIN COMPONENTS

PARAMETERS	PERFORMANCE
	GOALS
CENTER FREQUENCY	9.0 GHZ
BANDWIDTH	8,55 - 9,45 GHZ
PEAK POWER (SUM CHANNEL INPUT)	1 60 KW
AVERAGE POWER (SUM CHANNEL INPUT)	1 KW
HALF POWER BEAM WIDTH (9.0 GHZ)	2.30*
MAXIMUM SIDELOBE (9.0 GHZ)	-20 DB
AVERAGE HIGHEST SIDELORE (9.0 GHZ)	-20 DB
INPUT VSWR (9.0 GHZ)	SUM CHANNEL 1.3:1 DIFFERENCE CHANNEL 1.5:1
CENTER FREQUENCY	35,0 GHZ
BANDWIDTH	33.25 - 36.75 GHZ
PEAK POWER (SUM CHANNEL INPUT)	100 KW
AVERAGE FOWER (SUM CHANNEL INPUT)	10 KW
HALF POWER BEAM WIDTH (35.0 GHZ)	0.6°
MAXIMUM SIDELOBE (35.0 GHZ)	-20 DB
AVERAGE HIGHEST SIDELOBE (35.0 GHZ)	-20 DB
INPUT VSWR (35.0 GHZ)	SUM CHANNEL 1.3:1 DIFFERENCE CHANNEL 1.5.1

FIGURE 2 ANTENNA PERFORMANCE GOALS



FIGURE 3 HYDRAULIC GIMBAL ASSEMBLY

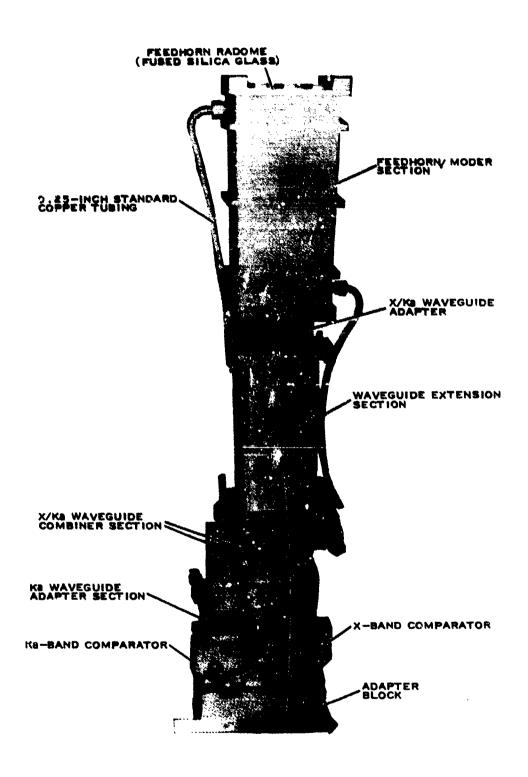
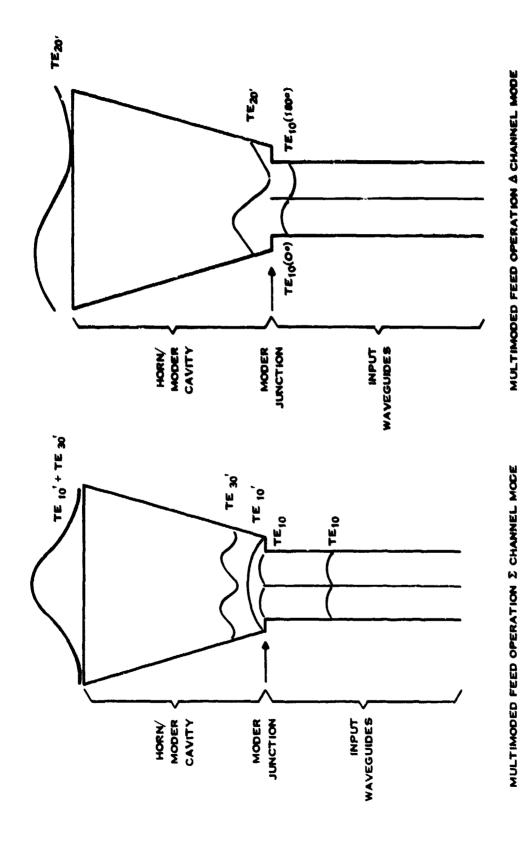


FIGURE 4 FEEDHORN ASSEMBLY SECTIONS

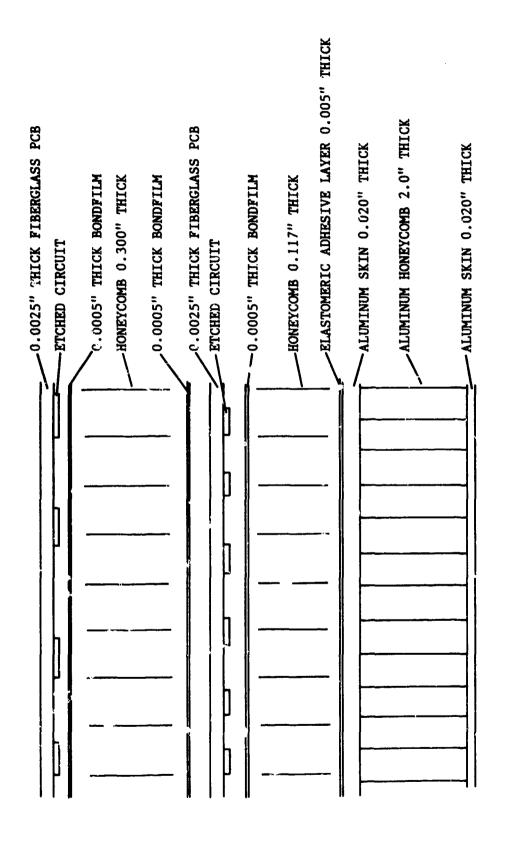


Z AND A MODE FORMING

FIGURE 5

ř

TWIST REFLECTING MIRROR WITH FEED HOLE CUTOUT



TWIST REFLECTOR CROSS-SECTIONAL VIEW

FIGURE 7

-327-

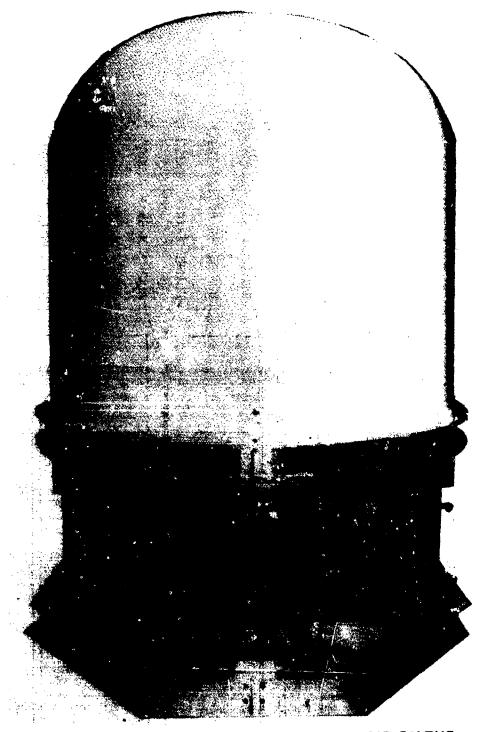
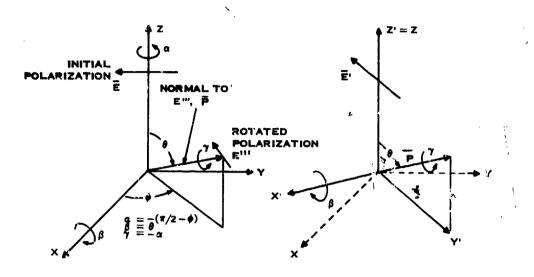
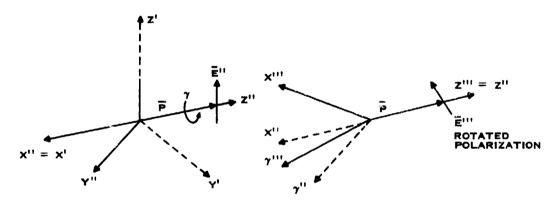


FIGURE 8 TRANSREFLECTOR MOUNTED ON THE MIRROR SCANNING ANTENNA



(A) ORIGINAL COORDINATE SYSTEM

(B) COORDINATE SYSTEM AFTER FIRST ROTATION ABOUT α .



(C) COORDINATE SYSTEM AFTER SECOND ROTATION ABOUT $\boldsymbol{\beta}$.

(D) COORDINATE SYSTEM AFTER THIRD ROTATION ABOUT γ .

FIGURE 9 COORDINATES FOR POLARIZATION ROTATION TRANSFORMATION

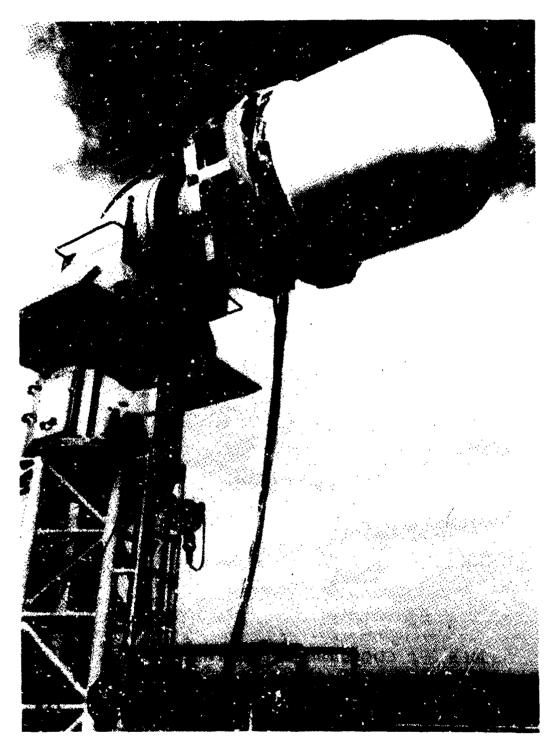
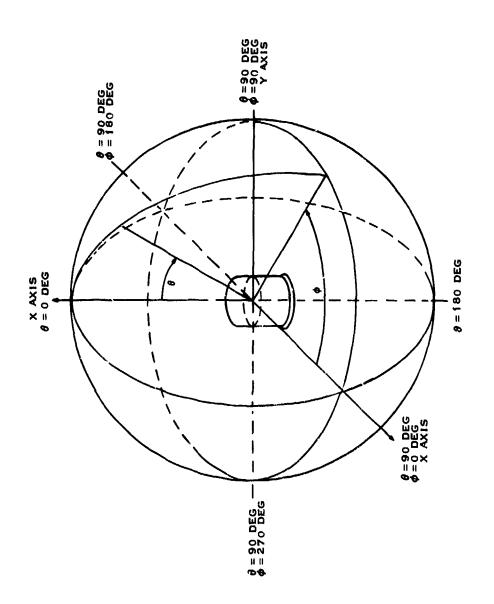
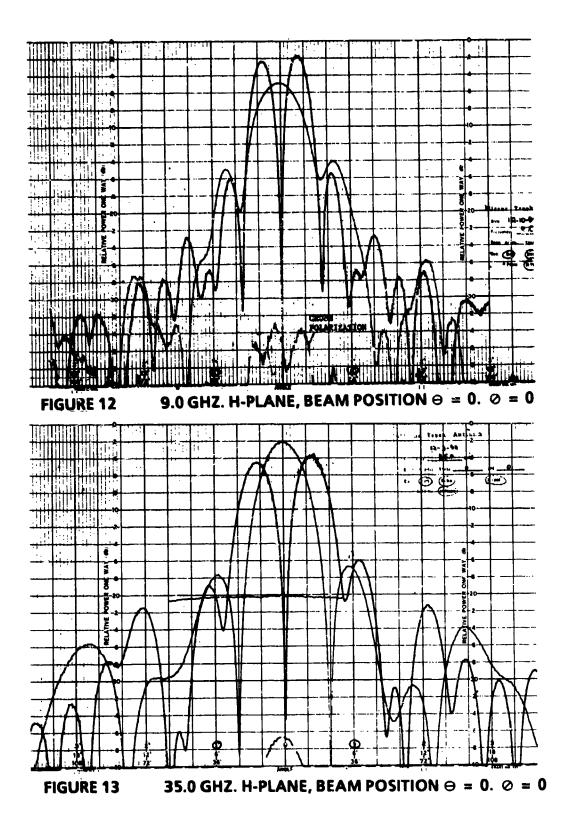


FIGURE 10 ANTENNA ASSEMBLY MOUNTED ON TOP OF THE RANGE

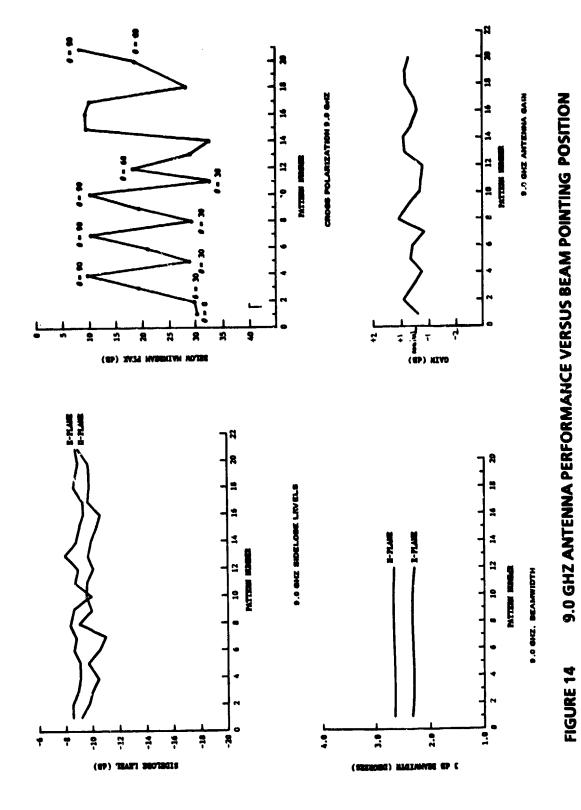
BEAM	•	•	٥	0	0	96	06	06	270	270	270	45	45	315	315	45	180	225	45	4.5	225	315
OŽ V	0	۰	30	9	06	30	9	06	Ė	09	06	30	09	30	9	06	06	06	45	67.8	09	06
PAJMEER		-	Ν.	3	4	r	9	7	80	6	01	-	12	13	14	15	91	17	18	19	20	21



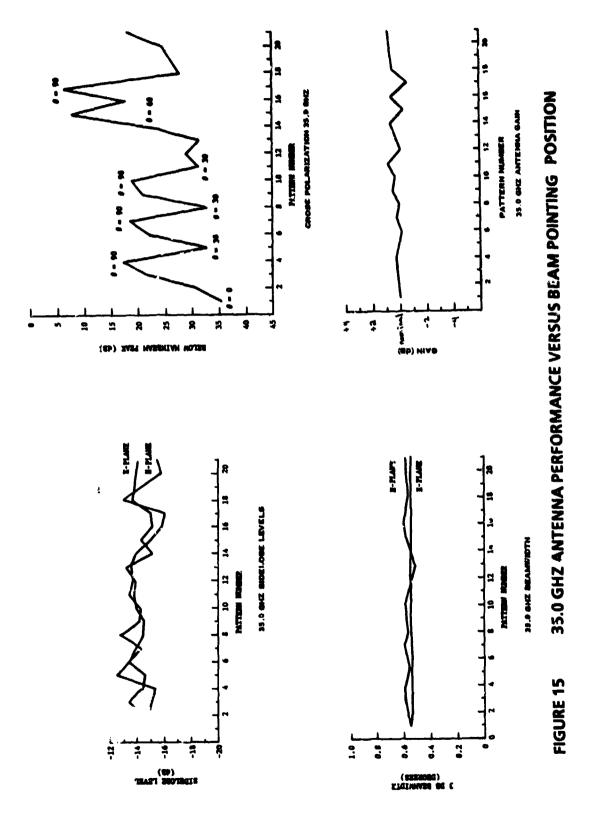
BEAM POINTING ANGLES & COORDINATE SYSTEM DEFINITION FIGURE 11

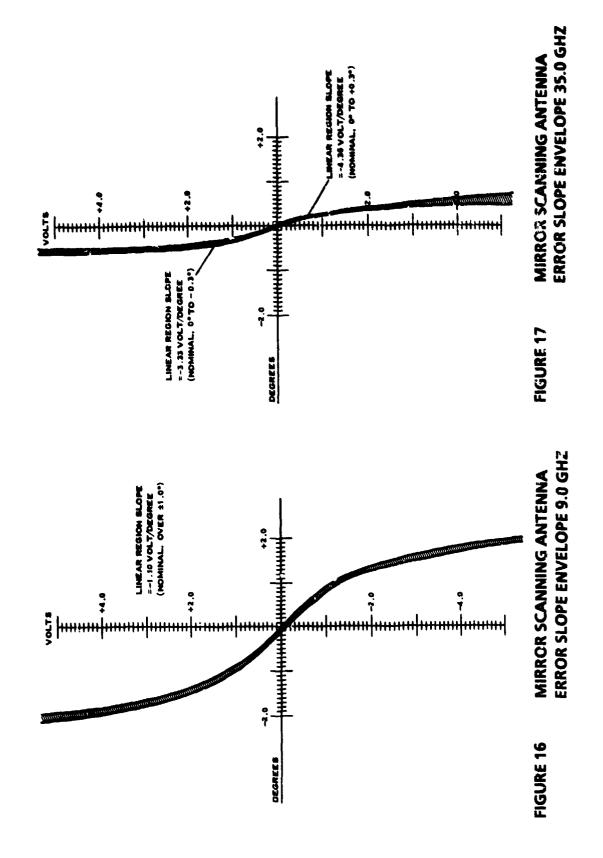


--332-



-333-





GOALS VS ACTUAL PERFORMANCE

		PREFORMANCE	
PARAMETERS	GOAL	MEASURED WITHOUT FEED RADOME	MEASURED WITH FEED RADOME
CENTER FREQUENCY	9.0 GHZ	9.0 GHZ	9.0 GHZ
BANDWIDTH	8.55 - 9.45 GHZ	8.35 - 9.45 GHZ	8.55 - 9.45 GHZ
PEAK POWER (SUM CHANNEL INPUT)	160 KW	160 KW ¹	160 KW ¹
AVERAGE POWER (SUM CHANNEL INPUT)	1 KW	i KW i	ı KW¹
HALF POWER BEAM WIDTH (9.0 GHZ)	2.30°	E-PLANE 1.92" H-PLANE 3.8"	E-PLANE 2.33" H-PLANE 2.65"
MAXIMUM SIDELOBE	-20 DE	E-PLANE -7.9 DB H-PLANE -9.0 DB	F-PLANE -15.0 DB H-PLANE -8.0 DB
AVERAGE HIGHEST SIDELORE (\$.0 GHZ)	-20 DB	E-PLANE -9.8 DB H-PLANE -9.8 DB	E-PLANE -16.0 DB H-PLANE -8.2 DB
INPUT VSWR (9.0 GHZ) (MAXIMUM VALVE PROM APPENDIX G 9.0 GHZ)	SUM CHANNEL 1.3:1 DIFFERENCE CHANNEL 1.5:1	BUM CHAMMEL 1.49.1 DIFFERENCE CHAMMEL 1.65:14	NOT WEASURED
CENTER FREQUENCY	35.0 GHZ	35.0 GHZ	35.0 GHZ
BANDWIDTH	33,25 - 36,75 GHZ	33.25 - 36.75 GHZ	33.25 - 36.75 GHZ
PEAK POWER (SUM CHANNEL INPUT)	100 KW	30 KW ¹	100 KW ¹
AVERAGE POWER (NPUT)	10 KW	3 KW ¹	10 KW ¹
HALF POWER BEAM WIDTH (35.0 GHZ)	0.5*	E- AND H-PLANE 6.56"	E- AND H-PLANE 0.56"
MAXIMUM SIDELOSE (35.0 GHZ)	-20 DB	E-PLANE -13.4 DB	E-PLANE -13.0 DB
AVERACE HIGHEST SIDELOBE (35.0 GHZ)	-20 DB	E-PLANE -14.0 DB H-PLANE -14.2 DB	E-FLANE -14.4 DB H-FLANE -12.2 DB
INPUT VSWR (35.0 GHZ) (MAXIMUM VALVE FROM APPENDIX G 35.0 GHZ)	SUM CHANNEL 1.3:1 DIFFERENCE CHANNEL 1.5.1	SUM CHANNEL 1.33:1 DIFFERENCE CHANNEL 1.25:14	NOT MEASL TED

1 DESIGNED FOR BUT NOT TESTED

FIGURE 18



FIGURE 19

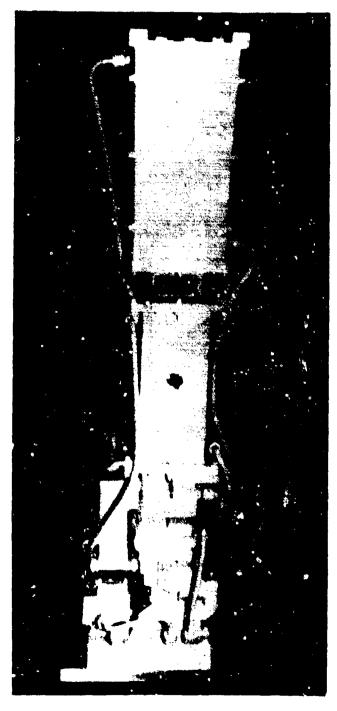


FIGURE 20

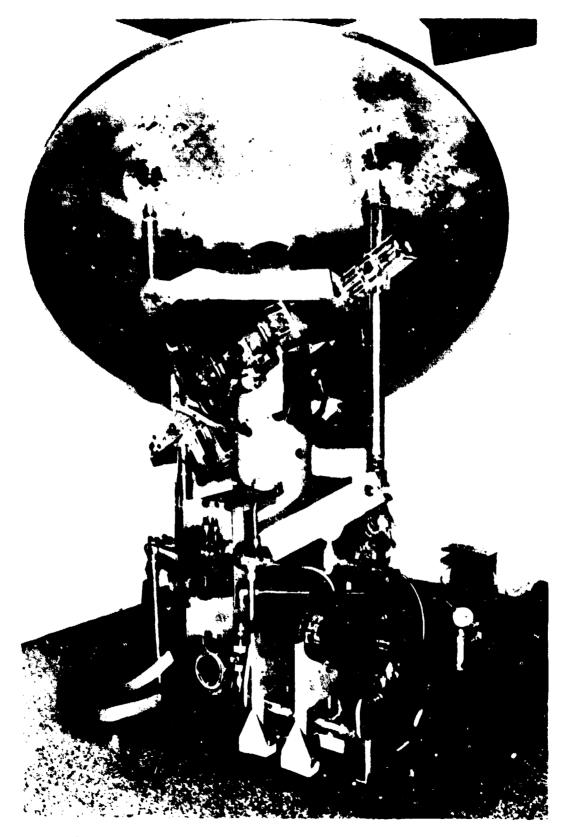


FIGURE 21

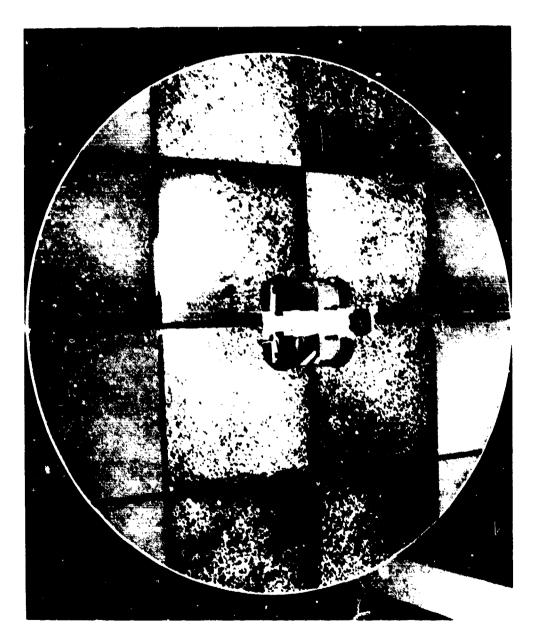


FIGURE 22

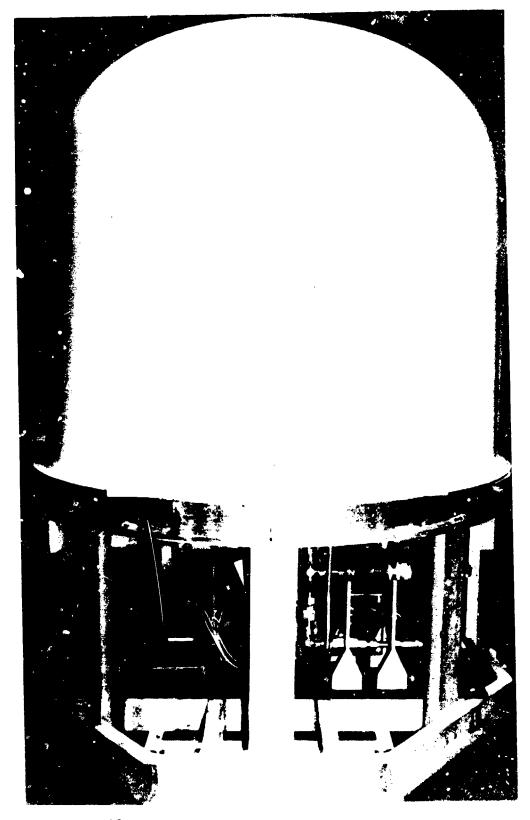


FIGURE 23

AD-P005 409

A LIGHTWEIGHT CONSTRAINED LENS FOR WIDE ANGLE SCAN IN TWO PLANES

Daniel T. McGrath, Capt, USAF Rome Air Development Center Electromagnetic Sciences Division Hanscom AFB, MA 01731

Abstract

A new design principle has been used to construct a three-dimensional constrained lens whose planar front and back faces are arrays of microstrip patches. The two arrays face in opposite directions and have a common ground plane. Each back face element is connected to a front face element by a short length of microstrip line and a feed-thru hole in the ground plane. The lengths of those transmission lines is a function of radius, with the longest in the center. Wide-angle focusing is achieved by the addition of a second geometric degree of freedom - the back face elements are not directly behind their corresponding front face elements, but are displaced radially, with the amount of displacement also varying as a function of radius.

The experimental model is a 20" diameter lens with a 40" focal length and 8 GHz center frequency. Scanning to ±30° was demonstrated with no observable aberrations in either the E plane or the H plane other than the feed horn's astigmatism. The overall efficiency is approximately 29%.

This paper will discuss the general two-degree-of-freedom lens design and its specific embodiment in this microstrup constrained lens. Experimental data will be presented to show its scanning characteristics, losses, and potential improvements.

1. INTRODUCTION

Constrained lenses have not been considered for many antenna applications because they are heavy and difficult to produce. A notable exception is the printed circuit Rotman lens [1], which unfortunately, forms beams in only one plane. This paper introduces a new design for a three-dimensional bootlace lens that is very lightweight, yet is capable of scanning wide angles in two planes simultaneously.

The entire lens structure is 1/8" thick, comprised of two 1/16" printed circuit boards, each of which is a microstrip patch array containing 283 elements in an equilateral-triangular lattice. The two arrays, which are the lens front and back faces, have a common ground plane and face in opposite directions. Each pair of array elements, one on the front and one on the back, is connected by two short lengths of microstrip transmission line and a feed-thru pin going through the ground plane. Radiation from a feed positioned benind the lens is captured by the back face elements and routed along the transmission line paths, then re-radiated by the front face elements.

The lengths of the transmission lines is different for each pair of elements, and is a function of radius. A second geometric "degree of freedom" is applied in order to give the lens good wide angle focusing: The back face elements are not directly behind their front face counterparts, but are displaced radially, with the amount of displacement also varying as a function of radius from the lens center.

The experimental model is a 20"-diameter lens with a 48" focal length. The quality of its 5° beam remains good when the feed is mechanically scanned to 30° in both the E and H planes, which shows that, consistent with theory, it is free of significant scanning aberrations. Since the lens design has no axial variation (it is symmetric in \$\psi\$), these results would hold in any diagonal scan plane as well. Hence, an array feed positioned behind the lens could produce well-focused beams in all directions within a large cone-shaped scan region.

2. GENERAL DESIGN PRINCIPLES

Our microstrip constrained lens is a practical embodiment of the two-degree-of-freedom planar lens discussed in [2]. In order that both front and back lens faces be flat, there are only two geometric degrees of freedom available with which to attempt to achieve wide-angle focusing. Those degrees of freedom are the length of transmission line joining pairs of elements and the relative locations of front and back face elements. A cross-sectional view of the lens is shown in Figure 1 - note that the back face elements are not directly behind their front face counterparts. Finding equations for the line lengths and element locations is a straightforward matter of assuming two perfect focal points at $(z,r)=(-F\cos\theta_0,\pm F\sin\theta_0)$ and equating path lengths from either point through the center of the lens and through an arbitrary point away from the center of the lens. This procedure results in the following expressions for the back face element

locations ρ and line lengths W [3:46]:

$$\rho = r \left[\frac{F^2 - r^2 \sin^2 \theta_0}{F^2 - r^2} \right]^{1/2} \tag{1}$$

$$W = F + W_0 - .5(F^2 + \rho^2 - 2\rho F \sin \theta_0)^{1/2} - .5(F^2 + \rho^2 + 2\rho F \sin \theta_0)^{1/2}$$
 (2)

For a three-dimensional lens, equations (1) and (2) remain the same, but r and ρ are now the radial coordinates in the front and back faces, respectively, as illustrated in Figure 2. The best choice for the focal angle is $\theta_0=0$, which forms a single on-axis focal point. In the three-dimensional lens, that yields the largest scan region for any given maximum path length error. This lens design is theoretically capable of maintaining low sidelobe patterns within a solid angle 36 beamwidths across [2].

There is a wide latitude to choose the type of radiating elements and transmission lines. For example, open-ended wave-guides with coaxial lines, folded dipoles with parallel-wire lines aand microstrip slots with stripline transmission lines are a few possibilities. We have chosen microstrip patch radiators with microstrip transmission lines because that construction offers the ultimate in light weight and fabrication ease. It is the planar geometry of the two lens surfaces that makes the microstrip lens possible.

3. THE MICROSTRIP CONSTRAINED LENS

The details of the MCL's construction are illustrated in Figure 3, which shows a single pair of elements, one on the front

face and one on the back face. The entire structure is two printed circuit boards, one double-side clad and one single-side clad. The double-sided board forms the aperture side array and the common ground plane, and the single-sided board forms the back face array. There are small apertures in the ground plane to allow the feed thru pins to go through without touching the ground plane. Figure 4 shows the mask layout for the front face. Note that the transmission lines all have different lengths. Figure 5 is the back face mask. We have developed an algorithm that determines the correct layout for each transmission line depending on its length and the relative positions of the elements, and incorporated it into the same computer program that uses a Calcomp (a) flatbed plotter to draw the mask artwork.

The lens elements are fairly standard rectangular microstrip patch radiators, approximately b=.49 $\lambda_0/\sqrt{\epsilon}$ long and a=.65b wide, designed using the transmission line model [4]. The transmission lines have characteristic impedance of 71 Ω , and are inset into the patch for a good impedance match. Figure 6a shows a single patch element in a test fixture, with measured return loss and radiation pattern in 6b and 6c, respectively.

Figure 7 is a photograph of the completed antenna. The two printed circuits comprising the lens are mounted in a Lexan B holder attached to a mounting plate as shown in Figure 8. The feed horn is suspended behind the lens so that its phase center is at the focal point. Table 1 gives complete design parameters.

4. PERFORMANCE

Two versions of the MCL were constructed, each on epoxyfiberglass circuit board material. The significant difference
between the two was the orientation of the feed thrus: the first
version's feed thrus are exactly as shown in Figure 3 - the
transmission line continues on in the same direction after the
feed thru; while in the second version, the lines reverse direction at the feed thru. The first version has better radiation
patterns, but the second version has higher gain. However, both
maintain good quality beams at wide scan angles.

4.1 First Version

We obtained very good radiation patterns with this first version. Figure 9 is an overlay of the on-axis beam and the 10° , 20° and 30° scanned beams. The gain is falling as the feed is scanned because of the feed illumination (in this instance an 8° diameter conical horn): The focal length varies with scan angle as shown in Figure 10 [3], and the feed must be moved closer to the lens when it is scanned, and will therefore illuminate less of the aperture (in other words, the aperture efficiency is dropping with scan angle). The usual $\cos \theta$ scanning loss also contributes to this gain decrease. There is some astignatism evident in the patterns of Figure 9 (the first sidelobe is blended into the side of the main beam), which is caused mainly by the feed horn itself. Franchi [4] found the phase centers of this particular horn in the E and H planes are approximately 4° apart.

The measured gain of this antenna was 18.2 dBi. Since the

maximum gain of a 19"-diameter aperture is 32.1 dBi, this leaves 13.9 dB of losses to account for. As pointed out earlier, the 8" conical horn feed provides a very steep aperture taper with a -10dB edge illumination, corresponding to 4.1 dB taper loss. The measured gain of the feed horn itself was 1.3 dB less than the theoretical gain from King [5]. Therefore, 8.3 dB of loss is directly attributable to the lens, and it must have an overall efficiency of 15%.

There are only three identifiable loss mechanisms in microstrip lens: attenuation in the transmission lines; active mismatch of the microstrip arrays; and reflection from the feed From previous measurements of microstrip transmission thrus. lines on Epoxy-fiberglass, we know that the average line loss in this lens will be 1.5 dB. The feed thru reflection loss, on the other hand, is 4.4 dB, which we have determined by the following Figure 11 is the pattern of the lens with a broadprocedure: beam feed (a single 8 GHz microstrip patch), scanned to 1.5%. That scan angle is just enough that the feed does not block the energy reflected from the lens back face. Note that the back lobe is 2.5 dB higher than the front lobe, and it is focused! The only way this back lobe could be focused is if it reflected from the feed thrus instead of the lens back face (the feed thru pins are usually located at the midpoints of the transmission lines and the wave incident from the feed reflecting back from the feed thrus will have undergone a time delay proportional to from eq. (2), and will therefore form a focused beam the

radiating in the backward direction. In essence, the structure is working both as a lens and as a reflectarray.) Since the reflected beam is 2.3 dB higher than the transmitted beam through the lens, the loss due to feed thru reflections must be 4.4 dB. This reflection loss was considerably lower in the second lens version because the feed thru design was more efficient.

4.2 Second Version

The second version MCL was identical to the first except that the transmission lines reversed directions at the feed thru points. (This was actually due to a fortuitous fabrication error in which the back face was etched with the mask negative upside down. Fortunately, the feed thru locations were generally symmetric about the lens center line, and there was only one pair of elements that were misaligned and cannot be connected electrically.) The back lobe is approximately 4 dB lower than the main beam, hence the feed thru reflection is only 1.5 dB. This reduced loss is evident in 2.9 dB higher measured gain from the second version (29% overall efficiency).

Radiation patterns are shown in Figures 12 and 13 for H plane scan and E plane scan, respectively for lens version #2. The feed used in these two cases was a 4.7"x6.0"-aperture pyramidal horn. There is no deterioration in the pattern when the lens scans to $\pm 30°$ away from the lens axis in either plane. The wide angle scanning in two planes demonstrates an essential feature of the lens: since there is no ϕ -variation in the design, it can scan to wide angles in any ϕ plane.

5. POTENTIAL IMPROVEMENTS

Our intent in building and testing this lens was to verify the relevant concepts of (1) the "two-degree-of-freedom lens" design and (2) its embodiment in this "microstrip constrained lens." For expediency we made some tradeoffs that hurt the overall antenna performance (gain and sidelobe levels). In future versions, we will need a better feed thru design, a patch element design that minimizes the active array reflection coefficient, use of a low-loss printed circuit material (such as PTFE), a shorter focal length to prevent spillover and a better feed to lessen the taper loss and provide a low-sidelobe illumination.

Obviously, given the much higher gain of the second lens version, the feed thru design is very critical. The relative angle between the two transmission lines seems to affect its reflection. We suspect that the diameter of the shorting pin, the diameter of the hole in the common ground plane, and the diameter of the "pad" on the end of the line are also important. It will take some a perimentation to establish the optimum feed thru design.

We have not considered the effect of an active mismatch at the lens face, although it is usually critical to lens performance. The patch element used was designed as an isolated antenna, and is not actively matched to the array environment. The result will be a mismatch loss at each face, causing added reflections that contribute to the back lobe and reduce the gain at wide scan angles.

The Epoxy-fiberglass material we used is inexpensive, but lossy. For the same length of transmission lines, a PTFE mater-ial would reduce the line losses from 1.5 03 to .5 dB. Future versions will use the more expensive microwave laminates now that we know the pitfalls in the fabrication process.

6. CONCLUSIONS

We have used a new design principle, that of the two-degree-of-freedom planar lens, to construct a three-dimensional constrained lens consisting entirely of two printed circuit boards. The two versions of the lens we constructed focused a good quality beam to ±30° in both the \$\phi=0°\$ and \$\phi=90°\$ planes. The better of the two versions had an overall efficiency of 29%. The most significant loss mechanisms were the feed through pins connecting front and back face elements, active array reflection and transmission like attenuation. In future versions of the microstrip constrained lens, we plan to use an optimized feed-thru design (to be found experimentally) to reduce the reflection at those junctions, and a low-loss laminate to lower the transmission line loss.

The results from this first model of an entirely new type of lens are quite promising. It is extremely light and quite inexpensive, yet is capable of scanning to wide angles in all planes of ϕ . Those qualities should justify its use in antenna applications for which lenses have not previously been considered.

REFERENCES

1 !

- 1. D. H. Archer, "Lens-Fed Multiple Beam Arrays," Microwave Journal, Sep. 1984, pp. 171-195.
- 2. D. T. McGrath, "Planar Three-Dimensional Constrained Lenses," <u>IEEE Trans. Antennas and Propagation</u>, vol. AP-34, Jan. 1986, pp. 46-50.
- 3. K. R. Carver and J. W. Mink, "Microstrip Antenna Technology," IEEE Trans. Antennas and Propagation, Jan. 1981.
- 4. P. R. Franchi, "Simple Expressions for the Phase Centers of Small Horn Antennas," <u>Proc. 1985 Antenna Applications Symposium</u>, RADC-TR-85-242 Vol. 2, ADA-165-535.
- 5. A. P. King, "The Radiation Characteristics of Conical Horn Antennas," <u>Proc. IRE</u>, vol. 38, pp. 249-251, 1968.

Table 1. MCL Design Parameters

Aperture Radius	7.5"
Focal Length	40"
Frequency	8.0 GHz
Beamwidth on axis	5.16°
Element Spacing, front face	δ _χ =.75λ ₀ =1.1045" δ _γ =.45λ ₀ = .9583"
Material Thickness Dielectric Constant E _{eff} at 8GHz	Epoxy-Fiberglass (FR4) 1/16" 4.4 3.444
Element Length Width Inset	Rectangular Patch .3272" .4572" .095"
Transmission lines Width Impedance, Zo	.060" 71Ω

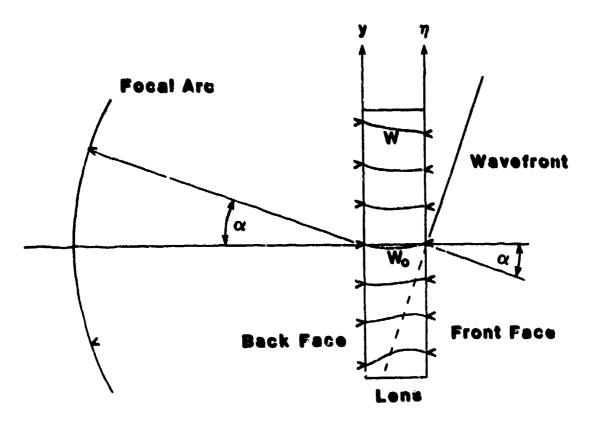


Figure 1. Linear Two-Degree-of-Freedom Lens

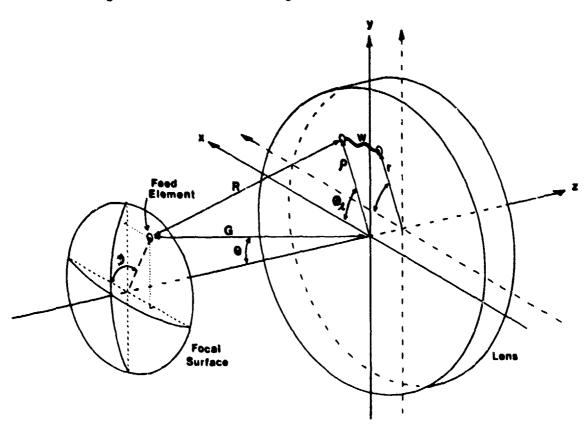


Figure 2. Planar Two-Degree-of-Freedom Lens with Concave Array Feed

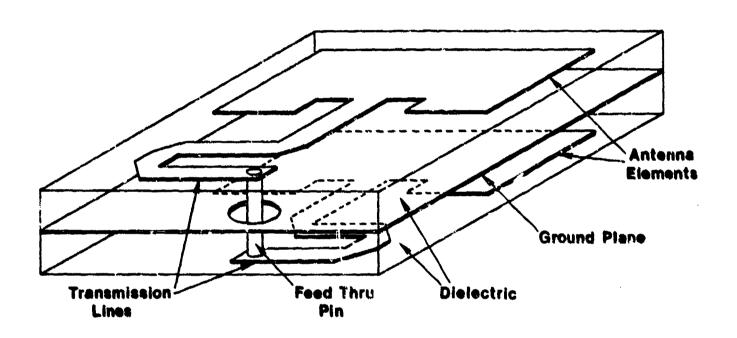


Figure 3. Detail of Interconnection Between Faces of the Microstrip Constrained Lens

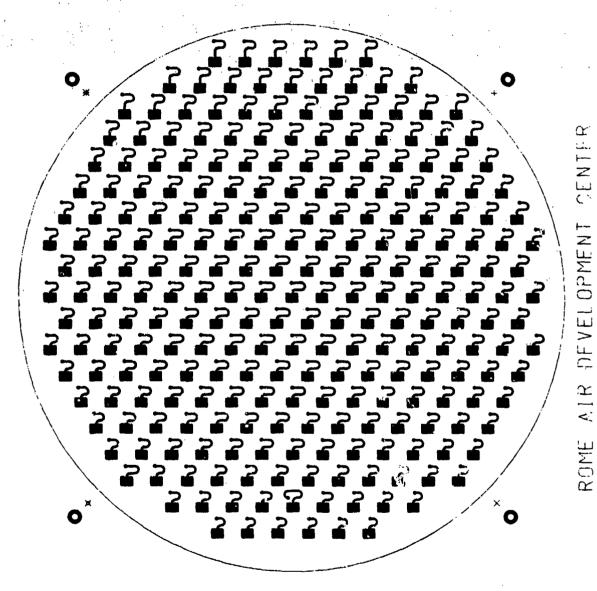


Figure 4. Front Face Mask Artwork

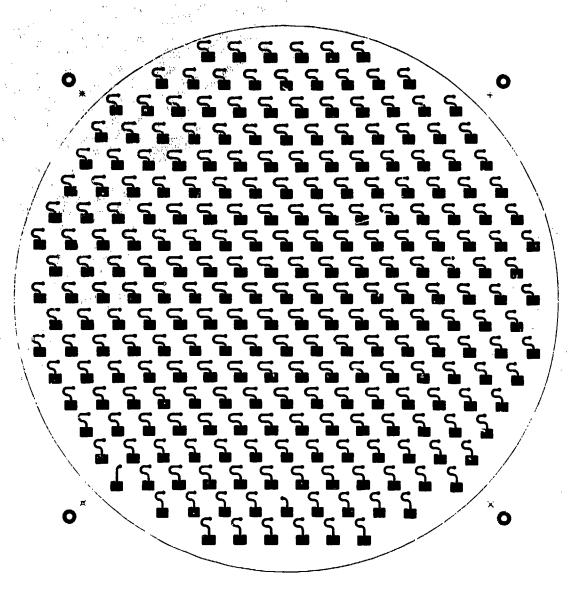


Figure 5. Back Face Mask Artwork

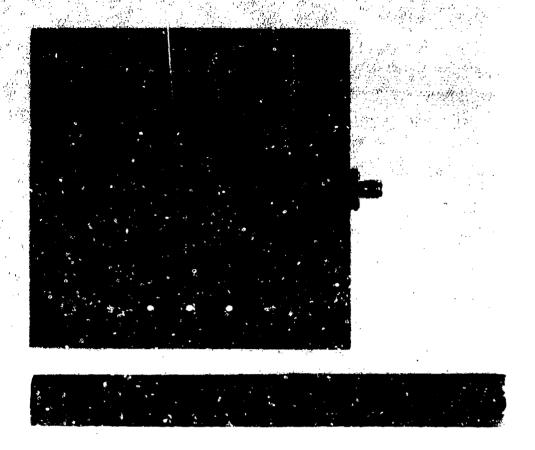
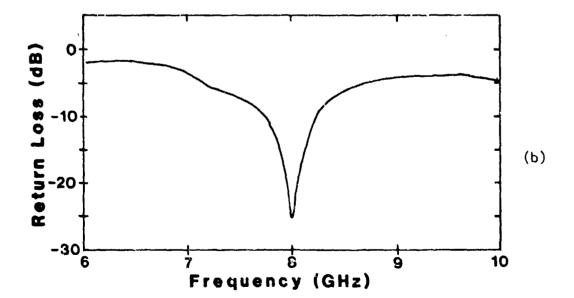


Figure 6. Inset-Feed Microstrip Patch Radiator
a) Photograph of Element in Test Fixture (above)
b) Measured Return Loss vs. Frequency (below)
c) Measured Radiation Patterns (next page)



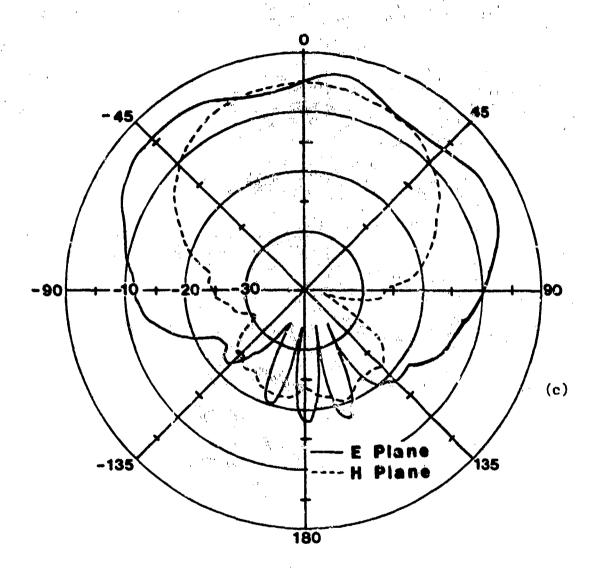




Figure 7. Microstrip Constrained Lens (First Version) with Pyramidal Hern Feed

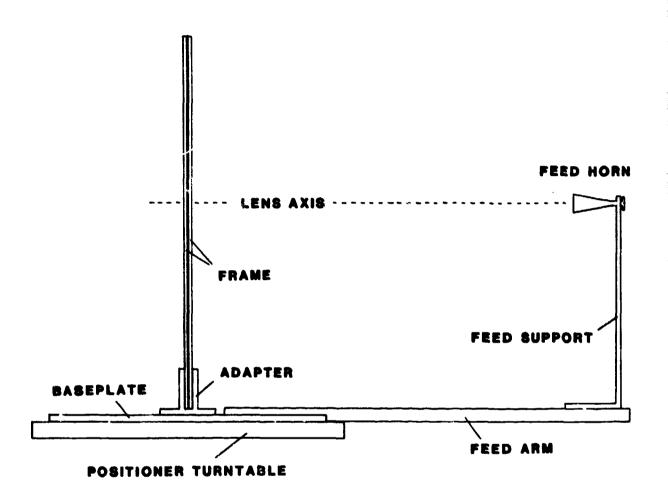


Figure 8. Test Fixture (Side View)

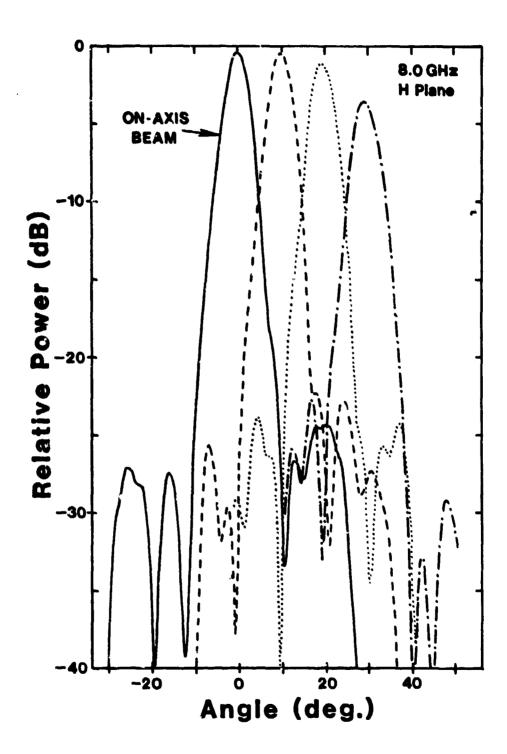


Figure 9. Scanned Patterns of MCL #1 with 8" Conical Horn Feed

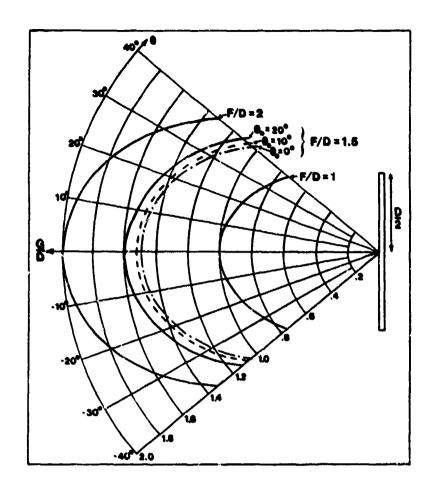


Figure 10. Shape of the Minimum-R.M.S. Error Focal Arc for Various Focal Lengths

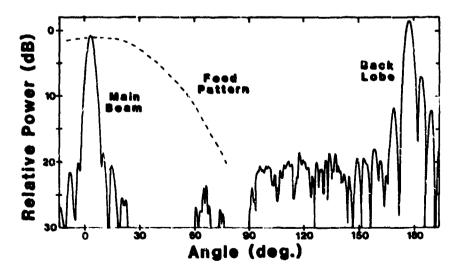


Figure 11. H Plane Pattern of MCL #1 Scanned to 1.5° Showing Back Lobe (Microstrip Patch Feed)

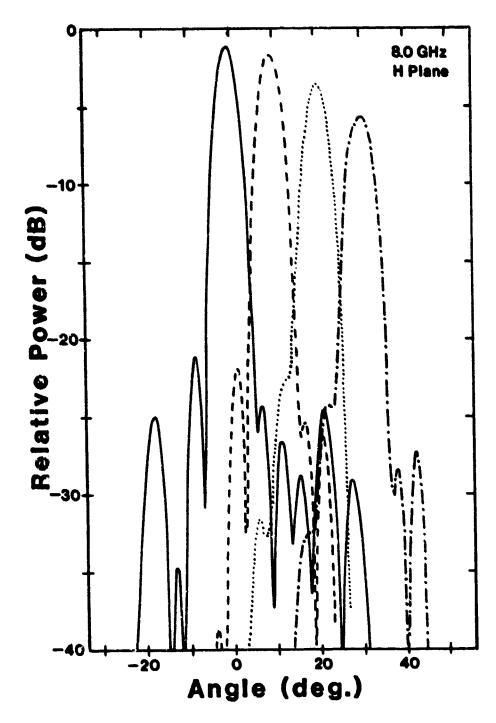


Figure 12. H Plane Scanned Patterns of MCL #2

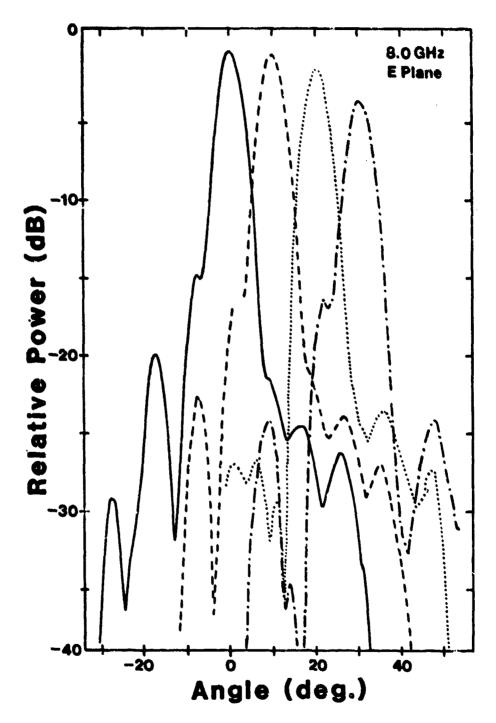


Figure 13. E Plane Scanned Patterns of MCL #2

*U.S. GOVERNMENT PRINTING OFFICE: 1987-700-800-30819